Turbulence control for drag reduction with active wall deformation

by

Dipl. Masch.-Ing. ETH Henrik Koberg

Department of Aeronautics
Imperial College of Science, Technology and Medicine
Prince Consort Road
London SW7 2BY

This thesis is submitted for the degree of Doctor of Philosophy of the University of London

2007

Abstract

Ecological and economical considerations motivate the search for ways to reduce the skin friction drag in turbulent flows. Several numerical studies have shown that wall shear stress can be lowered at low Reynolds numbers by applying a small amount of wall transpiration. In this study it is investigated how another type of actuation, active wall deformation, could be used to yield a similar effect.

First, discrete time-dependent wall deformation is studied in laminar flow. Lacking background turbulence, the baseflow allows clear identification of the flow perturbation. The analysis reveals that a downward moving actuator is surrounded by a region of negative wall-normal velocity and *vice versa*. Comparably less intuitive are the vorticity fields which often display complicated structures. A similar, subsequent study in turbulent flow shows that, indeed, active wall deformation can restructure wall turbulence.

Based on these findings, a series of experiments were conducted on opposition control. This scheme aims at opposing the velocity sensed away from the wall by imposing velocity of opposite direction at the wall. By locally deforming the wall accordingly, skin friction reductions of up to 15% are observed. Parameters critical to the performance of the control scheme, such as actuation scales and deformation limiters, are identified and analysed. As Reynolds number and actuation scales are much smaller than in practical applications, the results are of limited applicability but encouraging for prospective drag reduction at higher Reynolds numbers.

In a separate study a novel control method based on non-linear global stabilisation of the perturbed Navier-Stokes equations was tested. Using body forcing over the entire domain as actuation, the flow relaminarised.

Acknowledgements

I would like to thank my supervisors, Professor J.F. Morrison and Professor S.J. Sherwin, for their help and contribution as well as the arrangement of funding under EPSRC Grant GR/S20994/01. The computing resources supplied by the Imperial College High Performance Computing Service are also gratefully acknowledged. Thanks goes to Professor Mike Kirby for providing advice on numerical issues.

On a personal basis, I am grateful to Dr. Steffen Stolz for taking the time to introduce me to academic research and to my sisters who helped me to maintain my motivation. A special thanks goes to Alicia for looking after me in the final year and for proof-reading parts of my thesis.

To the British taxpayer

Notation

Symbol	Definition	Units
Roman		
A	amplitude function (eq. (7.5))	./.
$\mathbf{A}, A^i$	additional equation term (eq. (3.34))	./., ./.
$\mathbf{a}$	acceleration	./.
c^i_j, C	transformation coefficients, matrix (eq. (3.14))	./.
D	total differential	./.
E	perturbation energy	./.
E_0	initial perturbation energy	./.
$E_{u_i u_i}$	energy spectra (table 5.2)	./.
e	element number	./.
F_i	highest actuated wavenumber in the ith direction	./.
f	wall deformation (eq. (4.1))	./.
fr^*	frequency of the actuator	$1/s$
G	power gain (eq. (7.4))	./.
$\mathbf{G}, G^i$	pressure operator	./., ./.
g_{ij}	metric tensor (eq. (3.17))	./.
g_D	Dirichlet boundary condition	./.
g_N	Neumann boundary condition	./.
h	time-dependent shape of the actuator ($T(t)X(x)Z(z)$)	./.
i, j, k	general summation indices	./.
$\mathbf{K}$	curvature tensor ($\mathbf{K} = -\nabla_\pi \mathbf{n}$)	./.
k_i	wavenumber in the ith direction	./.
J	Jacobian	./.
J_e	order of the explicit time-integration scheme	./.
J_i	order of the implicit time-integration scheme	./.
L_i	domain size in the ith direction	./.
L^*_c	channel half-height	m

Symbol	Definition	Units
L^{+*}	viscous length (eq. (5.4))	m
$\mathbf{L}, L^i$	linear diffusion operator	$./., ./.$
$\mathbb{L}$	linear partial differential equation	$./.$
M_i	number of solved Fourier modes in the ith direction	$./.$
m_i	Fourier mode in the ith direction	$./.$
N_i	number of actuated Fourier modes in the ith direction	$./.$
$\mathbf{N}, N^i$	non-linear advection operator	$./., ./.$
$\mathbf{n}$	unit outward normal	$./.$
N_{el}	number of elements	$./.$
N_{dof}	number of global degrees of freedom	$./.$
O	order	$./.$
P	polynomial order	$./.$
P	Jacobi polynomial (eq. (3.60))	$./.$
P	pressure averaged over y and z	$./.$
P_{in}	power input (eq. (7.2))	$./.$
p	polynomial number	$./.$
p	pressure	$./.$
Q	flowrate (eq. (3.69))	$./.$
Q	number of quadrature points (eq. (3.62))	$./.$
q	potential source	$./.$
q	polynomial number	$./.$
q	step in time-integration scheme	$./.$
r	radius of the actuator	$./.$
$R_{u_i u_i}$	two-point correlation (table 5.2)	$./.$
Re	Reynolds number	$./.$
Re_{B}	Reynolds number ($u^*_{\text{B}}\ L^*_c\ /\ \nu^*$)	$./.$
Re_{C}	Reynolds number ($u^*_{\text{C}}\ L^*_c/\nu^*$)	$./.$
Re_τ	Reynolds number ($u^*_\tau L^*_c\ /\ \nu^*$)	$./.$

Symbol	Definition	Units
Re_θ	Reynolds number ($u^*_\infty \theta^*/\nu^*$)	./.
Re_δ	Reynolds number ($u^*_\infty \delta^*/\nu^*$)	./.
s	iteration step	./.
s_{ij}	transformation coefficient (eq. (A.8))	./.
S^i	velocity of the ith coordinate (eq. (3.20))	./.
Str_C	Strouhal number ($fr^*\ L^*_c\ /\ u^*_\mathrm{C}$)	./.
Str_τ	Strouhal number ($fr^*\ L^*_c\ /\ u^*_\tau$)	./.
Str^+	Strouhal number ($fr^*\ L^*_c\ /\ (u^*_\tau\ Re_\tau)$)	./.
Str_l	Strouhal number ($fr^*\ y^*\ /u^*_\mathrm{C}$)	./.
T	time function	./.
t	time in cartesian coordinates	./.
$u, v, w, \mathbf{u}, u_i$	velocities in cartesian coordinates	./.,./.,./.,./.,./.
u^*_B	bulk velocity (eq. (5.1))	m/s
u^*_C	centreline velocity (eq. (5.2))	m/s
u^*_τ	friction velocity (eq. (5.3))	m/s
u^*_∞	free-stream velocity	m/s
u_slip	slip velocity	./.
$U, V, W, \mathbf{U}, U_i$	velocities in general coordinates (eq. (3.19))	./.,./.,./.,./.,./.
v	test function	./.
v_S	velocity at detection plane	./.
v_W	wall velocity	./.
$\hat{v_\mathrm{W}}$	unmodified actuation wall velocity	./.
v_LW	lower-wall velocity	./.
v_UW	upper-wall velocity	./.
W	pumping power (eq. (7.3))	./.
w_i	quadrature weights (eq. (3.62))	./.
XZ	time-independent shape of the actuator	./.
$x, y, z, \mathbf{x}, x_i$	Cartesian coordinates	./.,./.,./.,./.,./.

Symbol	Definition	Units
y_{LW}	y-coordinate of the lower wall	./.
y_{S}	y-coordinate of the detection plane	./.
y^+	distance from the wall normalized by L^{+*}	./.
$y_{\max}$	deformation limit	./.
Greek		
α	constant-flowrate force coefficient	./.
α	equation parameter (eq. (3.60))	./.
β	equation parameter (eq. (3.60))	./.
β	time integration coefficients	./.
Γ	circulation	./.
Γ	Christoffel symbol (eq. (3.18))	./.
δ^*	boundary-layer thickness	m
$\delta\Omega$	boundary of Ω	./.
$\delta\Omega_D$	boundary of Ω with Dirichlet conditions	./.
$\delta\Omega_N$	boundary of Ω with Neumann conditions	./.
ϵ	amplitude (eq. (4.3))	./.
ϵ_i	local coordinate (eq. (3.52))	./.
η_i	local coordinate (fig. fig:collapsed)	./.
θ^*	momentum thickness	m
κ_v, κ_y	amplitude-function parameters (eq. (7.11))	./.
μ^*	dynamic viscosity	kg/ms
ν^*	kinematic viscosity (μ^*/ρ^*)	m^2/s
$\xi, \eta, \zeta, \boldsymbol{\xi}, \xi_i$	general coordinates	./., ./., ./., ./., ./.
ϖ	damping factor (eq. (7.6))	./.
ρ^*	density	kg/m^3
σ_i	actuator parameter in the ith direction	./.
$\sigma_{t,\mathrm{C}}$	actuator motion parameter ($u^*_{\mathrm{C}}/L^*_{\mathrm{C}}$)	./.

Symbol	Definition	Units
$\sigma_{t,\tau}$	actuator motion parameter $(u^*_\tau / L^*_{\mathrm{C}})$	./.
$\boldsymbol{\sigma}, \sigma_i$	vorticity-flux	./., ./.
τ	time in general coordinates	./.
Φ	global expansion mode (eq. (3.50))	./.
ϕ	local expansion mode (eq. (3.53))	./.
τ_{Re}	total shear stress	./.
τ_{W}	wall shear stress in x-direction	./.
$\boldsymbol{\tau}_W$	wall shear stress	./.
$[\boldsymbol{\tau}]$	viscous stress tensor	./.
χ	penalty parameter (eq. (7.8))	./.
χ	element transformation (eq. (3.52))	./.
ψ	modified principal functions [57]	./.
Ω	solution domain	./.
Ω_{st}	standard element	./.
$\boldsymbol{\omega}, \omega_i$	vorticity	./., ./.

Symbols

∂Q	partial differential of Q
∇Q	Gradient of Q
$\nabla \cdot Q$	Divergence of Q
$\nabla^2 Q$	Laplacian of Q
$Q_1 \times Q_2$	vector cross product of Q_1 and Q_2
$Q_1 \wedge Q_2$	Q_1 or Q_2
$\|Q\|$	determinant of Q
$\|Q\|$	absolute value of Q
(Q_1, Q_2)	Legendre inner product of Q_1 and Q_2
$\bigcup Q$	set union of Q
$\in Q$	is a member of Q

Symbol	Definition	Units

Subscripts

$Q_{1,2,3,\ldots}$	expansion terms of Q
Q_{flat}	flatness factor of Q
Q_n	wall-normal component of Q
Q_C	non-dimensionalised by u_C^*
Q_τ	non-dimensionalised by u_τ^*
Q_m	Q at the point of maximum deformation
Q_π	tangent component of Q
Q_{rms}	root-mean-square fluctuation of Q
Q_{skew}	skewness factor of Q
Q_v	component of Q due to vertical velocity
Q_{viscous}	viscous component of Q
Q_{m_i}	Q for mode m_i

Superscripts

$\bar{Q}$	average of Q
$\dot{Q}$	rate of change of Q ($\dot{Q} = \partial Q/\partial t$)
Q^*	dimensional quantity
Q^d	diffusion component of Q
Q'	fluctuation component of Q
$\hat{Q}$	polynomial coefficient of Q
$\hat{Q}$	intermediate value of Q
Q^e	Q of element e
Q^δ	approximate solution of Q

Symbol	Definition	Units

Abbreviations

AB	Adams-Bashforth
BMT	Bewley *et al.* [5]
CCS	curvilinear coordinate system
CF	Channelflow 0.9.15 [38]
CFL	Courant-Friedrichs-Lewy
CMK	Choi *et al.* [15]
CN	Crank-Nicolson
DNS	direct numerical simulation
EKS	Endo *et al.* [27]
FCG	Flow Control Group
FFT	Fast Fourier Transform
flat	flatness factor
IBM	immersed boundary method
K	Kellogg [58]
KS	Kang *et al.* [54]
KK	Kuroda and Kasagi [64]
LES	Large Eddy Simulation
LW	lower wall
MEMS	microelectromechanical systems
PDE	partial differential equation
PDF	probability density function
POD	Proper Orthogonal Decomposition
RK	Runge-Kutta
rms	root-mean square
skew	skewness factor
UW	upper wall
WDA	wall deformation actuator

Contents

Abstract **1**

Notation 4

Table of Contents **11**

List of Figures **14**

List of Tables **21**

1 Introduction **23**

2 Literature review on reactive skin friction control of turbulence **29**

2.1 Control Schemes 30

2.1.1 Adaptive schemes 30

2.1.2 Schemes based on physical arguments 31

2.1.3 Schemes based on dynamical systems 33

2.1.4 Optimal and sub-optimal control schemes 33

2.1.5 Linear and non-linear control theory 34

2.2 Actuators 35

2.2.1 Synthetic jets 35

2.2.2 Flap actuators 36

2.2.3 Wall deformation actuators 37

2.3 Improving skin friction control by active wall deformation 41

3 Mathematical framework **45**

3.1 Flow equations and time discretisation 45

3.1.1 Cartesian coordinate system 47
3.1.1.1 The equations 47
3.1.1.2 The time-stepping scheme 48
3.1.2 Time-dependent curvilinear coordinate systems 49
3.1.2.1 The equations 49
3.1.2.2 The splitting scheme 51
3.1.3 Divergence-free coordinate systems 52
3.2 Spectral element methods 54
3.2.1 Galerkin formulation of the one-dimensional Poisson equation 55
3.2.2 One-dimensional expansion basis 56
3.2.3 Extension to two dimensions 61
3.3 Fourier expansion in the third dimension 62
3.4 Constant flow rate 64

4 Laminar channel flow over active wall deformation 66
4.1 Parameters 68
4.2 Vorticity generation 72
4.3 Flow over linearised actuators 74
4.3.1 Linearisation 75
4.3.2 Vorticity flux 78
4.3.3 Flow analysis 81
4.3.3.1 Case 1: Transient motion 81
4.3.3.2 Case 2 and 3: Oscillating motion 89
4.4 Flow over non-linear actuators 91
4.4.1 Coordinate system 91
4.4.2 Vorticity flux 93
4.4.3 Flow analysis 94
4.4.3.1 Case 1: Transient motion 94
4.4.3.2 Case 2: Slow oscillating motion 105
4.4.3.3 Case 3: Quick oscillating motion 107

5 Turbulent channel flow **111**

5.1 Parameters 112

5.2 Statistics 118

5.2.1 Case P6Z32 121

5.2.2 Case P7Z48 122

5.2.3 Case P8Z64 126

5.3 Reynolds number effects 126

6 Turbulent channel flow over active wall deformation **134**

6.1 Parameters 135

6.2 Flow analysis 136

7 Opposition control in turbulent channels by wall deformation **144**

7.1 Standard opposition control 145

7.1.1 Reynolds number effects 147

7.2 Opposition control by wall deformation 148

7.2.1 Restriction in wall deformation 150

7.2.2 Secondary effects of deforming walls 153

7.2.3 Actuation bandwidth 155

7.2.4 Ramifications of using a divergent-free coordinate system . . . 156

7.2.5 Coordinate system 157

7.3 Results 159

7.3.1 Standard opposition control: Case 1 162

7.3.2 Effect of limiting control to lower wall: Case 2 162

7.3.3 Effect of restricting control to small wavenumbers: Case 3, 4, and 5 166

7.3.4 Effect of restricting the deformation: Case 6 173

7.3.5 Effect of using wall deformation to actuate: Case 7 176

7.3.6 Optimising the function restricting the deformation: Case 8, 9, and 10 184

8 Control-theoretic approach to skin-friction reduction **188**

8.1 The Orr-Sommerfeld-Squire system 190

8.2 Transient growth in sub-critical channel flow 190

8.3 Passivity-based control in turbulent channels 192

9 Conclusions and outlook **197**

A Verification of the mathematical theory and its implementation **201**

A.1 Test 1: Passive obstacles in two-dimensional flow 201

A.2 Test 2: Swapping of coordinate axes 203

A.3 Test 3: Interaction between the flow responses of two actuators in two-dimensional flow 203

B Passivity-based control of turbulent channel flow **209**

B.1 Theoretical foundation 209

B.1.1 The small-gain theorem 210

B.1.2 The passivity theorem 210

B.1.3 Application to the Navier-Stokes equations 211

B.2 The controller synthesis problem 215

B.3 Application to channel flow 218

Bibliography **222**

List of Figures

1.1 Envisioned skin-friction drag reduction by wall deformation on aircraft. 25

2.1 Feedback control. 29

2.2 Skin-friction-control techniques 30

2.3 Instantaneous shot of turbulent channel flow at $Re_\tau = 100$ taken from case P7Z48 of Chapter 5. a) Streaks at $y^+ = 5.4$. b) A pair of streamwise vortices in the wall region. As a result of the no-slip condition secondary vortices appear at the wall. 32

2.4 A schematic diagram of a synthetic jet. 36

2.5 a) Dimple actuator; b) Measurement of dimple actuator shape; c) Prototype of MEMS-fabricated dimple actuators. FCG, Imperial College, Dearing *et al.* [23] 39

3.1 Global assembly of element mass matrices. Taken from Karniadakis and Sherwin [57]. 59

3.2 Shape of the expansion modes given in expression (3.61) for a polynomial order of $P = 5$. Taken from Karniadakis and Sherwin [57]. . . 60

3.3 A fourth-order ($P = 4$) two-dimensional quadrilateral expansion constructed from the tensor product of two one-dimensional expansions of order $P = 4$, where $\psi_p^a = \phi_p$ and $(\xi_1, \xi_2) = (\epsilon_1, \epsilon_2)$. Taken from Karniadakis and Sherwin [57]. 61

3.4 Transformation between triangular and quadrilateral elements, where $(\xi_1, \xi_2) = (\epsilon_1, \epsilon_2)$. Taken from Sherwin and Karniadakis [93]. 62

4.1 Geometry of laminar channel flow with wall actuators 67

4.2 Computational mesh. 68
4.3 Time-dependent height $T(t)$, velocity $\dot{T}(t)$, and acceleration $\ddot{T}(t)$. a) Oscillating actuator with $Str_C = 0.1$. b) Transient actuator with $\sigma_{t,C} = 1.44$. 70
4.4 Planes of flowfield. 82
4.5 Case 1: (u'=0.1)-iso-surfaces around dimple. $t = 0.5, 1, 1.5, 2, 3, 7$. . . 84
4.6 Case 1: (-0.1≤u'≤0.1)-contours in xy-midplane. $t = 0.5, 1, 1.5, 2, 3, 7$. 85
4.7 Case 1: (v=±0.01)-iso-surfaces around dimple. $t = 0.5, 1, 1.5, 2, 3, 7$. . 85
4.8 Case 1: (-0.07≤v≤0.02)-contours in xy-midplane. $t = 0.5, 1, 1.5, 2, 3, 4, 5, 6, 7$. 86
4.9 Case 1: (w=±0.01)-iso-surfaces around dimple. $t = 0.5, 1, 1.5, 2, 3, 7$. . 86
4.10 Case 1: (-0.01≤p≤0.01)-contours on lower wall. Circle shows approximately where dimple is located. $t = 1.5$ and 7. 87
4.11 Case 1: (ω_x=±0.1)-iso-surfaces around dimple. $t = 0.5, 1, 1.5, 2, 3, 4, 5, 6, 7$. The y-axis has been stretched by a factor of three. 88
4.12 Case 1: Contours of total spanwise vorticity flux, σ_z, between -0.04 and 0.04 in the xy-midplane. $t = 0.5, 1, 1.5, 2, 3, 4, 5, 6, 7$. 89
4.13 Case 2 and 3: Time-averaged (ω_x=±0.2)-iso-surfaces around dimple for different frequencies. The y-axis has been stretched by a factor of three. 90
4.14 Transformation of a vector in the xy-midplane. a) Cartesian coordinate system. b) Boundary-fitted coordinate system. 92
4.15 Case 1: (u'=±0.1)-iso-surfaces around dimple. $t = 0.5, 1, 1.5, 2, 3, 7$. . 96
4.16 Case 1: (-0.1≤u'≤0.1)-contours in xy-midplane. $t = 0.5, 1, 1.5, 2, 3, 7$. 96
4.17 Case 1: (v=±0.01)-iso-surfaces around dimple. $t = 0.5, 1, 1.5, 2, 3, 7$. . 97
4.18 Case 1: (-0.07≤v≤0.02)-contours in xy-midplane. $t = 0.5, 1, 1.5, 2, 3, 4, 5, 6, 7$. 97
4.19 Case 1: (w'=±0.01)-iso-surfaces around dimple. $t = 0.5, 1, 1.5, 2, 3, 7$. 98
4.20 Case 1: Streamlines and (-0.07≤v≤0.02)-contours in xy-midplane around dimple. $t = 1.5$ and 7. 98
4.21 Case 1: Streamlines and (-0.07≤v≤0.02)-contours in xy-midplane around bump. $t = 1.5$ and 7. 99
4.22 Shear stress at the irregular channel wall. 99

4.23 Case 1: Stress lines on the dimple. $t = 0.5, 1, 1.5, 2, 3.5, 7$. 100
4.24 Case 1: Stress lines on the bump. $t = 0.5, 1, 1.5, 2, 3.5, 7$. 100
4.25 Case 1: (ω_x=$\pm$0.1)-iso-surfaces around dimple. $t = 0.5, 1, 1.5, 2, 3, 4, 5, 6, 7$. The y-axis has been stretched by a factor of three. 101
4.26 Case 1: Streamlines and (-0.05$\leq\omega_x\leq$0.05)-contours in yz-planes around static dimple at $t = 7$. 102
4.27 Case 1: Streamlines and (-0.05$\leq\omega_x\leq$0.05)-contours in yz-planes around moving dimple at $t = 1.5$. 103
4.28 Case 1: (ω_x=$\pm$0.1)-iso-surfaces around bump. $t = 0.5, 1, 1.5, 2, 3, 7$. Flow structures have been stretched by a factor of 3 in the wall-normal direction. 104
4.29 Case 1: Contours of total spanwise vorticity flux at -0.04:0.01:0.04. $t = 0.5 : 0.5 : 2.5, 3.5$, and 7. 105
4.30 Case 2: (-0.07$\leq v' \leq$0.02)-contours in xy-midplane. $t = 1, 2, 3, 4, 5, 6, 7, 8, 9, 10$. 106
4.31 Case 2: (ω_x=$\pm$0.1)-iso-surfaces around dimple. $t = 1, 2, 3, 4, 5, 6, 7, 8, 9, 10$. The y-axis has been stretched by a factor of three. 108
4.32 Case 2: Stress lines on the dimple. $t = 1, 2, 3, 4, 5, 6, 7, 8, 9, 10$. 109
4.33 Case 3: (ω_x=$\pm$1)-iso-surfaces around dimple. $t = 1, 2, 3, 4, 5, 6, 7, 8, 9, 10$. The y-axis has been stretched by a factor of three. 110

5.1 Instantaneous streamwise velocity contours in a cross plane at $Re_\tau = 100$. 111
5.2 Geometry of turbulent channel flow. 112
5.3 Mesh in the streamwise ,x, and wall-normal, y, direction. 116
5.4 Flowrate and its running time average. a) P6Z32; b) P7Z48; c)P8Z64. 119
5.5 P6Z32: a) mean velocity; b) rms velocity fluctuations; c) mean vorticity; d) rms vorticity fluctuations; e) Reynolds stress and total stress; f) spanwise two-point correlation at $y^+ = 5.4$ 123
5.6 P6Z32: a) skewness of velocities; b) kurtosis of velocities; c) streamwise energy spectra at $y^+ = 5.4$; d) spanwise energy spectra at $y^+ = 5.4$124

5.7 P7Z48: a) mean velocity; b) RMS velocity fluctuations; c) mean vorticity; d) RMS vorticity fluctuations; e) Reynolds stress and total stress; f) spanwise two-point correlation at $y^+ = 5.4$ 127
5.8 P7Z48: a) skewness of velocities; b) kurtosis of velocities; c) streamwise energy spectra at $y^+ = 5.4$; d) spanwise energy spectra at $y^+ = 5.4$; e) streamwise energy spectra at $y^+ = 10.1$; f) spanwise energy spectra at $y^+ = 10$ 128
5.9 P8Z64: a) mean velocity; b) RMS velocity fluctuations; c) mean vorticity; d) RMS vorticity fluctuations; e) Reynolds stress and total stress; f) spanwise two-point correlation at $y^+ = 5.4$ 129
5.10 P8Z64: a) skewness of velocities; b) kurtosis of velocities; c) streamwise energy spectra at $y^+ = 5.4$; d) spanwise energy spectra at $y^+ = 5.4$ 130
5.11 Comparison of near-wall turbulence at different Reynolds numbers: $Re_\tau = 100$ (red), 180 (blue), 650 (green), 2000 (magenta). a) mean velocity; b) rms velocity fluctuations; c) rms vorticity fluctuations. All rms values increase with Reynolds number. 132

6.1 Streamlines and (-0.5≤v≤0.5)-contours in xy-midplane around dimple at $t = 0.15$ (72%). Left: Case 1. Middle: Case 2. Right: Case 3. For viewing purposes flow structures have been stretched by a factor of 3 in the wall-normal direction. 138
6.2 Streamlines and (-0.5≤v≤0.5)-contours in xy-midplane around dimple at $t = 0.6$ (100%). Left: Case 1. Middle: Case 2. Right: Case 3. For viewing purposes flow structures have been stretched by a factor of 3 in the wall-normal direction. 138
6.3 Streamlines and (-30≤ω_x≤30)-contours in (y,z)-planes at $t = 0.15$ (72%). Left: Case 1. Middle: Case 2. Right: Case 3. Domain stretched by a factor of 3 in the wall-normal direction. 140
6.4 Streamlines and (-30≤ω_x≤30)-contours in (y,z)-planes at $t = 0.6$ (100%). Left: Case 1. Middle: Case 2. Right: Case 3. Domain stretched by a factor of 3 in the wall-normal direction. 142

6.5 Comparison of root-mean-square velocity fluctuations in Case 2 and absolute velocity perturbations above the centre of the dimple in Case 3. a) $t = 0.15$ (72%); b) $t = 0.6$ (100%). 143

7.1 Schematic diagram of opposition control by wall transpiration. 145

7.2 Schematic diagram of opposition control by wall deformation. 149

7.3 Amplitude A for different values of $\hat{v}_w$ and y_w: a) expression (7.9) at $\chi = 0.01$; b) expression (7.11) at $\kappa_y = -5$, $\kappa_v = -5$, and $f_{max} = 1$. . . 152

7.4 Case1: Two-sided opposition control using transpiration. Case 2: One-sided opposition control using transpiration. Cases 3, 4, 5: One-sided opposition control using transpiration at small wavenumbers. Case 6: One-sided opposition control using restricted transpiration at small wavenumbers. Cases 7, 8, 9: One-sided opposition control using restricted deformation at small wavenumbers. 163

7.5 Case 2 and P7Z48: a) skin-friction drag at lower wall; b) skin-friction drag at upper wall. 164

7.6 Case 2 and P7Z48: comparison of v statistics close to the controlled wall and uncontrolled wall. a) rms; b) skewness; c) flatness. 165

7.7 Case 2: a) mean velocity; b) rms velocity fluctuations; c) mean vorticity; d) rms vorticity fluctuations; e) Reynolds stress and total stress; f) spanwise two-point correlation at $y^+ = 5.4$. 167

7.8 Case 2: a) skewness of velocities; b) kurtosis of velocities; c) streamwise energy spectra at $y^+ = 5.4$; d) spanwise energy spectra at $y^+ = 5.4$; e) streamwise energy spectra at wall; f) spanwise energy spectra at wall 168

7.9 Case 2: (-20$\leq\omega_x\leq$20)-contours and streamlines in (y,z)-plane. The control action at the lower wall has weakened the streamwise vortices and pushed them away from the wall. 169

7.10 Cases 2, 3, 4, and 5: Skin-friction on lower wall for different actuation bandwidths. 170

7.11 Cases 2 and 5: a) rms velocity fluctuations; b) close-up of vertical rms velocity fluctuations at the wall; c) rms vorticity fluctuations; d) energy spectra in spanwise direction at $y^+ = 5.4$; e) energy spectra in streamwise direction at lower wall; f) energy spectra in spanwise direction at lower wall. 171
7.12 Streaks at $y^+ = 5.4$ depicted by contours of streamwise velocity between -2. and 5. a) P7Z48; b) Case 2; c) Case 5. 172
7.13 Cases 5 and 6: a) rms velocity fluctuations; b) close-up of vertical rms velocity fluctuations at the wall; c) rms vorticity fluctuations; d) energy spectra in spanwise direction at $y^+ = 5.4$. 175
7.14 Case 6: probability distribution function of A. a) All events; b) strong events ($v_{\mathrm{rms,w}} > 0.06$). 176
7.15 Case 7 and P7Z48: a) skin-friction drag at lower wall; b) skin-friction drag at upper wall. 177
7.16 Case 7: Instantaneous wall deformation. Scaling in y is exaggerated to show wall structure. 178
7.17 Case 7 and P7Z48: a) mean velocity; b) rms velocity fluctuations; c) mean vorticity; d) rms vorticity fluctuations; e) Reynolds stress and total stress; f) spanwise two-point correlation at $y^+ = 5.4$. 179
7.18 Case 7 and P7Z48: a) skewness of velocities; b) kurtosis of velocities. Case 7: c) probability distribution of A for all events; d) probability distribution of A for strong events ($v_{\mathrm{rms,w}} > 0.06$). 180
7.19 Case 7 and P7Z48: a) streamwise energy spectra at $y^+ = 5.4$; b) spanwise energy spectra at $y^+ = 5.4$; c) streamwise energy spectra at wall; d) spanwise energy spectra at wall. 181
7.20 Cases 7 and 8: probability distribution of A. a) All events; b) strong events ($v_{\mathrm{rms,w}} > 0.06$). 185
7.21 Cases 7 and 9: probability distribution of A. a) All events; b) strong events ($v_{\mathrm{rms,w}} > 0.06$). 185
7.22 Cases 6 and 10: probability distribution of A. a) All events; b) strong events ($v_{\mathrm{rms,w}} > 0.06$). 186

8.1 Evolution of perturbation energy density for two Poiseuille flow simulations at $Re_c = 1500$. The lower curve was obtained from linear simulation and the upper curve from a non-linear simulation. 192
8.2 Channelflow: a) mean velocity; b) rms velocity fluctuations; c) Reynolds stress; d) drag reduction using controller. 194
8.3 a) Drag reduction. b) Amplitude function, A, for Case 4 and Case 5. 196

A.1 a) Computational mesh around the obstacles. b) Error of the flow over passive obstacles in curvilinear coordinates: Contours of vertical velocity between -2E-5 and 2E-5. 202
A.2 (-0.4$\leq v \leq$-0.02)-contours in the middle and (-0.75$\leq v \leq$0.2)-contours on the right at $t = 0.2$. 204
A.3 (-0.07$\leq v \leq$-0.02)-contours in xy-midplane at $t = 0.5, 1, 1.5, 2, 3, 7$. . . . 208

B.1 A generalised feedback loop made up of two elements H_1 andH_2. This block diagram represents the equations $e_1 = H_2 e_2 + w_1$ and $e_2 = H_1 e_1 + w_2$. 209
B.2 The feedback loop for controlled Navier-Stokes 214

List of Tables

2.1 Dimple and bump categories 41

4.1 Simulation parameters. Parameter values in the upper table are common for all cases. rms values are taken at the centre of the actuators. For Case 1 rms values are computed for the time period $0 \leq t \leq 2.4$. Parameters with the symbol τ in the subscript use the friction velocity u_τ^* (expression 5.3) as reference velocity and serve comparison with table 6.1. 72

5.1 Simulation parameters. 115

5.2 Quantities for the statistical analysis of turbulence. 120

6.1 Simulation parameters. rms values are calculated for $0 \leq t \leq 0.23$. . . 137

7.1 Opposition control experiments. Measurements taken over 42.4 time units. 161

7.2 Parameter-value comparison of opposition control simulations using wall deformation. Notice that the implementation of a maximum deformation, $f^+_{\max}$, can vary. 183

8.1 Simulation parameters. 193

Chapter 1

Introduction

The global climate is changing. According to the Intergovernmental Panel on Climate Change (IPCC) global average air temperature near the Earth's surface rose 0.74 ± 0.18°C during the past century and is expected to increase another 1.1 to 6.4°C until 2100 [20]. This can result in rising sea levels and intense weather events and may lead to increasing deaths, displacement, and economic losses. The urgency and magnitude of this problem has made it a priority on political agendas and in scientific research. The cause of climate change remains subject to controversy but the IPCC concludes that it is "very likely" an increase in greenhouse-gas concentrations.

In many countries aviation is the fastest growing emission source of major greenhouse gases, such as carbon dioxide (CO_2). The IPCC estimates that by 2050 aviation will account for 4% of all CO_2 released by human activity. Various measures to reduce emissions are currently discussed. These range from logistical improvements, such as the creation of a common European airspace [29], to new legislation, such as higher taxation on air travel. But if a 50 % cut in CO_2 emissions is to be achieved by 2020, a goal set out by the Group of Personalities [40], effort must be devoted to developing new fuel-saving technologies.

Crucially, reducing fuel consumption also cuts airline costs, which drives the same effort in industry. In fact, with fuel being the second highest cost category after personnel at most airlines [9] its efficient use has become the dominant issue. This situation is likely to persist if oil prices remain high.

The technological goals inspired by ecological and economical considerations can be met by improving energy sources, engines, aircraft weight, and air drag. Of the latter, approximately 50% are caused by skin friction [34]. This percentage is unlikely to decrease in the near future as to date no technologies are available to substantially lower the wall shear stress on commercial aeroplanes. But in the case of very low Reynolds numbers, numerical studies of turbulent channel flow have shown that a reduction in drag is possible. Most of these investigations involved a small amount of wall transpiration [5]. Such actuation can lead to a variety of issues in practical situations. For example, blowing and suction devices are prone to malfunction caused by blockage. An alternative could be the use of local time-dependent wall deformation to actuate the flow. The question if this can produce comparable success defines the focus of this project. The few studies that have been investigating this suggest that it is possible [27, 54, 58] but the potential as well as the limits of this technique are yet to be explored.

In line with common practice for control simulations, the Reynolds number of this study is very low, that is $Re_\tau = 100$. This is far from any flight conditions, which ideally would define the parameter values of this investigation. But the computational costs involved make DNS at realistically high Reynolds numbers unfeasible. The inherent risk of low-Reynolds-number simulations is that the results may be inadequate to predict drag reduction in real-life scenarios. However, theoretical investigations by Iwamoto *et al.* [46] have shown that active feedback control aiming at the near-wall turbulent velocity fluctuations can achieve large drag reduction even at high Reynolds numbers. In fact, no evidence has been produced to suggest otherwise. To be on the safe side, it could be argued that the Reynolds number in DNS should at least be within the "intermediate" range to guarantee absence of obvious low-Reynolds-number effects. However, experimental results suggest that even at high Reynolds numbers turbulent fluctuations close to the wall do not scale with wall units, indicating that a specific threshold for Reynolds-number-independent near-wall turbulence does not exist [78]. The mean flow in contrast, does scale with wall units in the viscous region, even for Reynolds numbers as low as $Re_\tau = 100$.

Flow control may be predetermined or reactive. The latter relies on sensors that

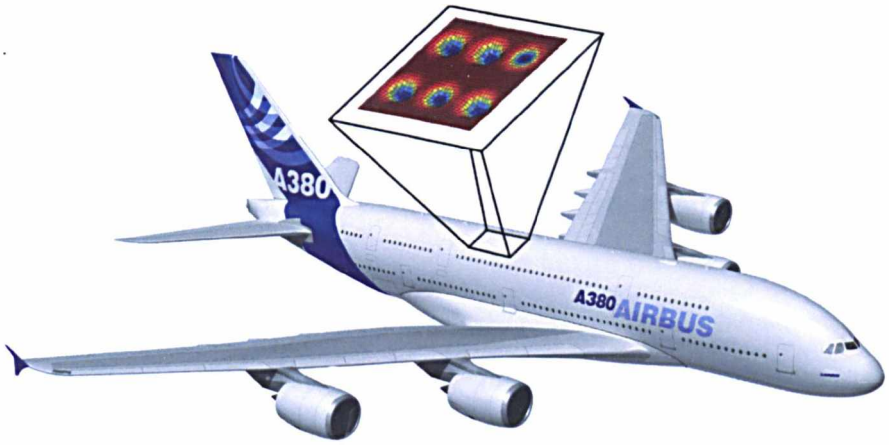


Figure 1.1: Envisioned skin-friction drag reduction by wall deformation on aircraft.

feed a signal to a controller which then determines the necessary actuation. As this is more difficult to implement in a laboratory experiment, predetermined control is usually favored. But the randomness typical in turbulent flows suggests that for best results the actuators should react to events in the flow. Also, it is not unlikely that efficient predetermined schemes can be extracted from results of feedback-control experiments. For example, this could be the case if after the decay of transients a feedback-driven actuation of high regularity emerged. Under these presumptions, this study is focused entirely on reactive control.

For practical applications reactive control strategies pose significant challenges with respect to spatio-temporal scales, that is the size, spacing, and response of actuators and sensors. The control has to take place at least on the scales of the so-called coherent structures. These have been found to be of $O(1\text{mm})$ and $O(1$ kHz) frequencies under typical flight conditions [34]. Although it was not possible to construct such small elements in the past, the pace of development in the field of microelectromechanical systems (MEMS) raises such expectations for the future. This trend is also at the core of the vision underlying this project which is a smart skin consisting of sensors, actuators and a control algorithm that adjusts its local deflection according to adjacent flow events. As shown in figure 1.1 it could be mounted, for example, on the fuselage of an airplane.

Work on active surfaces is also motivated by examples of swimming fishes and

mammals. Some investigators speculate that sharks can actively move the dermal denticles that cover their skin [86]. The indirect evidence for this is that the denticles are connected to muscles underneath the shark's skin. Active regulation of the skin is also considered by some to explain the high swimming speed of dolphins. It was suggested that microvibrations covering the entire body could improve hydrodynamic performance by damping turbulence [87]. However, these theories are subject to controversy. It has been noted that the time scales of the coherent structures are several orders of magnitude less than the minimum response time of the dolphin's skin [33]. Also, drag coefficients for dolphins indicate fully-turbulent boundary layers when gliding [33].

Although novel in the field of skin friction reduction, surfaces with small deformations have had a long history of success in form drag reduction. For example, the spherical shaped dimples on a golf ball introduce disturbances in the surrounding air with minimal pressure loss during flight that promote transition in the boundary layer, thus reducing the size of the wake. As a result, the ball is more easily propelled over longer distances than a smooth ball [3]. The dimpled surfaces on golf balls are passive which means that the flow is modified without external energy input. In contrast, the active wall deformation that is investigated in the present work is adjusted in height over time to control the flow. It belongs to the group of active control techniques that add energy to the flow. Their flexibility makes them good candidates for actuators in many flow control applications.

In the next chapter research on active skin friction control, so far mostly theoretical and numerical, is reviewed. For reasons of clarity, control schemes and actuators are discussed individually. Sensors, the third element of control, are not covered as this would go beyond the scope of this project.

The mathematical framework underlying this study is introduced in Chapter 3. This includes the relatively unknown Navier-Stokes equations in time-dependent curvilinear coordinate systems which facilitate simulations over complicated moving boundaries. A particularly efficient method thereof is introduced which was used for many of the simulations under discussion.

The analysis of results begins in Chapter 4 where the response of laminar flow to

the predetermined motion of a discrete actuator is investigated. A precise identification of the flow perturbations is made possible by the lack of background turbulence. This provides information as to which control strategies are best suited for this type of actuation.

To prepare for turbulent-flow studies, DNS of turbulent channel flow was conducted at different resolutions. In Chapter 5 statistical properties of the flows are verified using well-established references. The comparison explains the choice of a particular resolution that was used as a basis of most of the following turbulent simulations. It offers good balance between accuracy and computational costs.

In Chapter 6 the flow response to predetermined actuation is studied once more, but this time the results are taken from a simulation which was intialised by a fully-turbulent flow field. The analysis is focused on the differences that arise compared to laminar flow and the extent to which wall-deformation actuators can restructure turbulent flow.

The next step was the introduction of feedback control which is documented in Chapter 7. Opposition control was chosen as the control algorithm because it is well-established and widely documented. To use it in conjunction with wall deformation a number of modifications had to be made. Those were added sequentially with a new experiment conducted after each modification. A discussion of the results is also provided in this chapter which reveals factors that are critical to performance.

In the final chapter, 8, a novel control algorithm based on concepts from dynamical systems theory is presented. It was developed by Sharma *et al.* [92] and facilitates the nonlinear global stabilisation of the perturbed Navier-Stokes equation by making the linearised part passive. The synthesised controller was tested using full-domain sensing and actuation and achieved relaminarisation of the flow. Attempts to restrict the actuation to the wall were unsuccessful which motivated the search for alternatives. One is the pursuit of near-passivity by destroying the operator that couples the equations. It is shown that for wall-based actuation this approach is similar to opposition control which is the control algorithm explored in Chapter 7.

The report finishes with the overall conclusions in Chapter 9. The main findings

are summarised and recommendations for future research are given.

To avoid misunderstanding a few points are noted that the reader should bear in mind throughout the entire thesis. First of all, in all simulations involving wall deformation the shape of the wall is entirely dictated by the forcing, meaning the influence of the fluid on the wall is neglected. This approximation is justified for sufficiently stiff actuators and helps to reduce the complexity of the problem significantly. Secondly, to guide the reader efficiently through specific and abstract mathematical formulations as well as discussions of results, clarity is maintained by using the following three notations interchangeably:

$$\begin{aligned}
\mathbf{x} &:= (x^1, x^2, x^3) &:= (x, y, z) \\
\boldsymbol{\xi} &:= (\xi^1, \xi^2, \xi^3) &:= (\xi, \eta, \zeta) \\
\mathbf{u} &:= (u^1, u^2, u^3) &:= (u, v, w) \\
\mathbf{U} &:= (U^1, U^2, U^3) &:= (U, V, W)
\end{aligned}$$

Thirdly, flow quantities are non-dimensionalised differently depending on the flow state. If the flow is laminar the velocity at the centreline of the channel, u_{C}^*, is the reference velocity whereas if the flow is turbulent the friction velocity, u_τ^*, is used. Values can be converted using the two Reynolds numbers Re_{C} and Re_τ whose values are provided in tables 4.1, 5.1, 6.1, and 7.1 for the simulations under discussion. And finally, contour plots are colour-coded in the usual way, where blue refers to low values and red to high values. In most contour plots colour bars are omitted but maximum and minimum values are given.

Chapter 2

Literature review on reactive skin friction control of turbulence

Reactive control schemes consist of three parts: sensors, control algorithms, and actuators. Figure 2.1 shows a schematic diagram of how these parts would be integrated in a smart skin performing feedback control. In the present work the focus is on actuators, in particular wall deformation actuators. Among other factors their design is dictated by the needs of the control algorithm. Actuators that cannot deliver the forcing defined by the control algorithm fail their purpose. Recognising this relation, the review of past and ongoing research in the field of actuators is preceded by an overview of studies on skin-friction control algorithms. The experiments that fall into the latter category usually assume idealised actuation and can therefore be

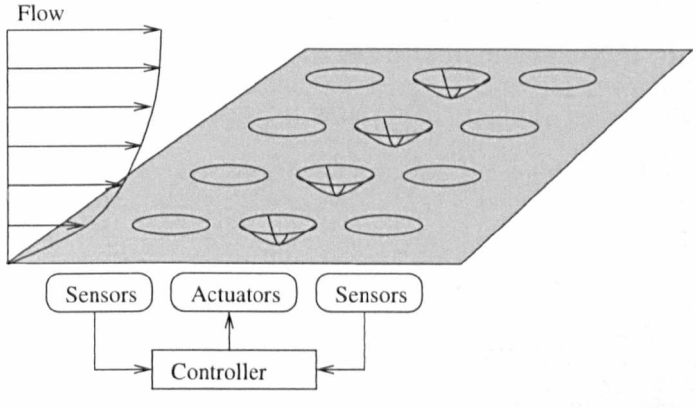


Figure 2.1: Feedback control.

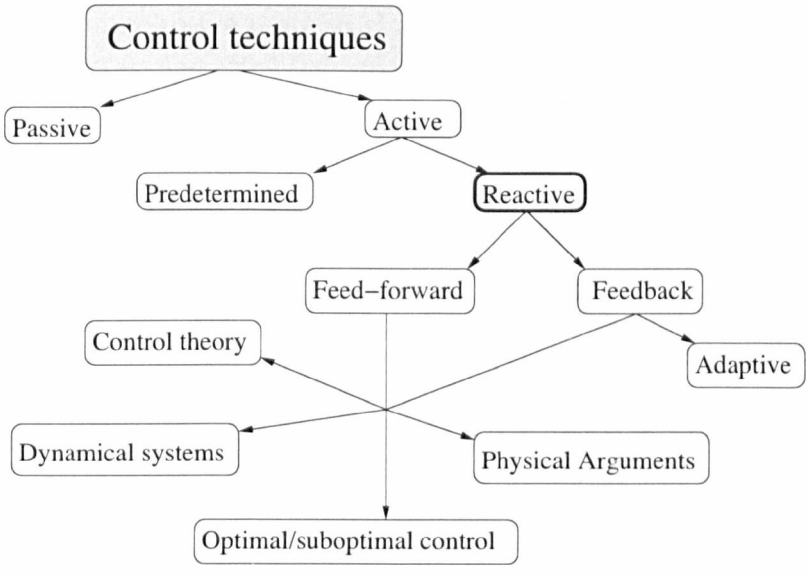


Figure 2.2: Skin-friction-control techniques

clearly distinguished from actuator research. Those few studies where control algorithms are combined with non-ideal actuators are presented in the section covering actuators. Sensing, the third component of reactive control, is equally important but is not subject to discussion as it would go beyond the scope of this project.

2.1 Control Schemes

A comprehensive and popular survey of feedback control schemes was presented by Moin and Bewley [76] and Bewley *et al.* [5]. Their categories, shown in figure 2.2, were chosen according to the extent to which they are based on the governing flow equations. Below, each of them is discussed independently and important examples are given with a view to actuation by wall deformation. Although the schemes are generally feedback all but adaptive ones can also be used in a feed-forward fashion.

2.1.1 Adaptive schemes

Schemes belonging to this class perform system identification and controller determination without using any knowledge of physical processes or the Navier-Stokes

equations but by an adaptive method that tunes parameters for best results.

One of the first numerical studies on adaptive control was carried out by Lee *et al.* [66]. They designed and trained a neural network which was applied in turbulent channel flow at $Re_\tau = 100$. Wall transpiration was used as actuation and the controller was fed by measurements only taken at the wall. As a result the drag fell by roughly 20%. In the laboratory adaptive control was implemented by Jacobsen *et al.* [50], details of which are given in section 2.2.

Adaptive control schemes have shown impressive performance in simple numerical experiments. For complex problems, though, it can be assumed that the ability for those schemes to converge to efficient control is reduced.

2.1.2 Schemes based on physical arguments

The second group consists of methods based on heuristic physical arguments. Their strategy is often to target coherent motions in turbulent flow. According to observations these structures are vortices lying parallel to, and close to the wall oriented in the streamwise direction.

The argument behind this approach is that these streamwise vortices are believed to be linked to the formation of streaks. According to this theory, a low-speed streak is created by lifting slow-moving fluid away from the wall on the updraft side of the vortex while a high-speed streak is produced by the downdraft on the opposite side. The resulting inflectional velocity profile is linearly unstable and produces Reynolds stress. An example of streaks and quasi-streamwise vortices is shown in figure 2.3. It should be noted, though, that the role of coherent structures in the creation of streaks has remained subject to controversy. An alternative explanation for the presence of streaks was brought forward by Chernyshenko and Baig [14] and involves the combined action of non-organised lift-up, mean shear, and viscous diffusion.

Intuitive control laws have the attractive property that they are usually quite simple. This means that the calculation load to determine the control input is rather small, making them very suitable for real-time applications, where time lags must be kept to a minimum. The obvious drawback of schemes based on physical intuition

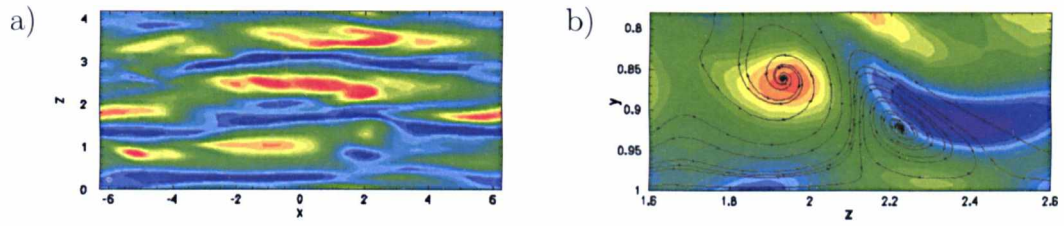


Figure 2.3: Instantaneous shot of turbulent channel flow at $Re_\tau = 100$ taken from case P7Z48 of Chapter 5. a) Streaks at $y^+ = 5.4$. b) A pair of streamwise vortices in the wall region. As a result of the no-slip condition secondary vortices appear at the wall.

is that success is limited by the engineer's understanding of the physical processes.

Physically-intuitive schemes are often based on active cancellation. One of the first and undoubtedly the most well-known was introduced by Choi *et al.* [15]. They used blowing and suction at the wall equal and opposite to the wall-normal component of velocity at $y^+ = 10$, as shown later (figure 7.1). This control approach, termed opposition [41] or out-of-phase v control, reduced the drag by approximately 25% at $Re_c = 1800$. Noting that streamwise vortices lead not only to wall-normal velocity but also spanwise velocity, opposition control was also applied to spanwise velocity. The best result obtained yielded about 30% drag reduction. Applying out-of-phase control to spanwise and wall-normal velocities simultaneously produced nearly the same result.

As with other friction-reducing feedback control schemes, broad implementation of opposition control is currently impossible due to the spatio-temporal requirements of the actuation. But investigators are beginning to use this control scheme in simpler flow settings. For example, Gad-el-Hak *et al.* [36] implemented the scheme to control artificial streaks. Also, experiments using the opposition control scheme were performed by Rebbeck *et al.* [84]. They attempted to selectively cancel the downwash of high-speed fluid during the sweep events. Their results showed that the wall-ward movement of high-speed region during the sweep events was successfully blocked by the wall-normal jet, suggesting that the skin-friction drag of the turbulent boundary layer can be reduced by this control scheme.

Another intuition-based cancellation concept was proposed by Koumoutsakos

[63]. He considered the turbulence control problem in terms of the minimisation of the vorticity flux. Wall transpiration was the actuating mechanism and its strength was calculated explicitly by formulating Lighthill's [68] mechanism of vorticity generation at a no-slip wall. Using wall information only, cancellation of spanwise vorticity flux in a turbulent channel at $Re_\tau = 180$ produced a drag reduction of up to 40%. The control resulted in the absorption of streamwise vortex pairs at the wall. Interestingly it was also observed that after a short transient unsteady spanwise vortical rollers were formed by regular actuator strengths, opening the possibility for predetermined control.

In the present work, both classic opposition control and vorticity flux minimisation, will be considered with respect to wall deformation actuation.

2.1.3 Schemes based on dynamical systems

The algorithms contained in this category are based on dynamical systems theory. Complex turbulent problems may be simplified by decomposing the system into a small number of representative modes using proper orthogonal or other decompositions, in order to obtain a low-dimensional model that is easier to implement for control applications, see Lumley *et al.* [70]. Given the abundance of degrees of freedom in turbulent flow at high-Reynolds numbers, it is certain that any real-world control experiment will feature some model reduction.

2.1.4 Optimal and sub-optimal control schemes

Efficient reactive control laws based on rigid theory can be derived by optimisation. The idea is to minimise a cost function, written to represent the physical problem of interest, by minimising the gradient of the cost functional in the space of the control through an adjoint formulation. Early attempts to implement predictive control with adjoint-based optimisation supposed a short length of the prediction horizon, also called sub-optimal approximation [5, 67]. Such an assumption is primarily made to reduce the computational expense of the control rule. Upon further simplifying the problem by neglecting non-linear terms, Lee *et al.* [67] managed to derive an

analytical control law. Interestingly, the resulting expression produced almost the same distribution of blowing and suction as the control law used in [66], which was created by a neural network.

Bewley *et al.* [5] used optimisation in a predictive control setting to determine controls that effectively reduce the turbulent kinetic energy or drag of turbulent channel flow at $Re_\tau = 100$ and 180. Optimising over a finite prediction horizon, flow relaminarisation, accompanied by a drag reduction of up to over 50%, was obtained using wall transpiration. However, the predictive control algorithm required full-flowfield information and was computationally expensive. Therefore, this algorithm is impossible to implement in a practical setting and should be considered as a benchmark.

2.1.5 Linear and non-linear control theory

Application of linear control theory to the linearised Navier-Stokes equation of transition problems has been made, see Joshi *et al.* [52] and Bewley *et al.* [6]. Researchers are beginning to consider the incorporation of control laws derived by linear control theory in control simulations of the fully non-linear problem of a turbulent flow. This is motivated by numerical results that suggest that the linearised Navier-Stokes equations in a plane channel flow under stochastic forcing can exhibit behaviour reminiscent of the streamwise vortices and streaks characteristic of turbulent flow [30, 31]. Also, it was shown by Kim and Lim [61] that turbulence decays without the linear coupling term of the linearised Navier-Stokes equations.

But linear control techniques, see [6], make certain assumptions about the model error of the linearised model when applied to flow control problems. The model error in the case of the linearised Navier-Stokes equations is the non-linearity. H_∞, the concept underlying control inspired by control theory, assumes that the model error is bounded. The non-linearities, however, are not bounded, but they are conservative. This fact can be exploited to design linear control schemes that give stability with respect to all sizes of perturbation, see Sharma *et al.* [92]. The development of such a controller is undertaken at the Flow Control Group (FCG), Imperial College.

More information on this method is given in Chapter 8.

2.2 Actuators

Currently none of the available actuators could possibly create the kind of dense and uniform small-scale forcing used in most of the control simulations presented in the last section. But intense research is carried out on those that have the potential to meet the requirements in scale, magnitude, and response in the future. As yet, the most promising candidates are synthetic jets, deployable flaps, and wall deformation actuators. An overview of past and ongoing research on these actuators is given in this section with an emphasis upon the latter.

2.2.1 Synthetic jets

The synthetic jet actuator comprises a cavity with a small hole and a membrane, as shown in figure 2.4. This membrane is driven in an oscillatory fashion, usually at its resonant frequency. The actuator operates by alternately sucking and blowing fluid through the small hole and by utilising the fact that the outflow of the orifice is directed while the inflow draws fluid from all sides. The net effect, integrated over many cycles of the membrane motion, is a mass-less jet where no mass but momentum is added to the flow.

An experimental investigation with zero-net-mass-flux jets was made by Rathnasingham *et al.* [83] into the active control of the near-wall region of a turbulent boundary layer at $Re_\tau = 1960$ using a linear active control scheme. The control was applied using a spanwise array of resonant synthetic jet actuators that introduced pairs of streamwise vortices into the time-averaged flow.

Jacobsen *et al.* [50] developed a jet-related actuator, consisting of a piezoelectrically driven cantilever mounted flush with the wall located off-centre over an open cavity. The cantilever was oscillated in and out of a cavity in the surface, resulting in a quasi-steady pair of counter-rotating streamwise vortices and thus a streaky structure. Using an adaptive scheme, the streamwise vortices produced by the actuator were used to cancel the streamwise vortices generated by a cylinder

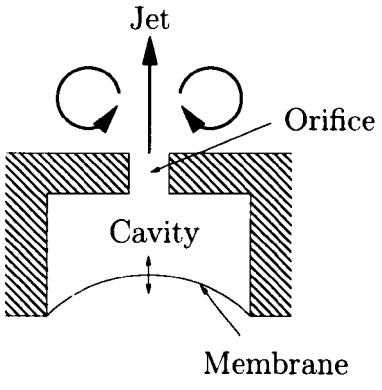


Figure 2.4: A schematic diagram of a synthetic jet.

placed normal to a laminar flow. This idea of cancelling streamwise vortices directly by inducing streamwise vortices of opposite sign is an intuitive cancellation method other than those presented in section 2.1.2. Despite a mismatch in scale between the cylinder-generated disturbance and the actuator control disturbance, the actuator was still able to delay the laminar-turbulent transition. Furthermore the actuator was also used to interact with unsteady low- and high-speed streaks generated by pulsed suction. The actuators were placed to speed up the low-speed streaks and slow down the high-speed streaks. Together with sensors and a control algorithm, the mean of wall shear and its spanwise variation were substantially reduced.

Numerically a similar problem was investigated in [106], where pressure-jump or "puff-jet" actuators were used as actuators to reduce near-wall streak-like structures in a simplified model.

2.2.2 Flap actuators

Tsao *et al.* [103] report the development of a control system based on micro-machined flap actuators for turbulent boundary layer control. The flaps are employed to induce vertical momentum in the sense of opposition control [15]. Experiments were conducted and it was found that the actuators affect the turbulent flow to a significant degree.

2.2.3 Wall deformation actuators

Their robustness against hostile environments makes wall deformation actuators, WDAs hereafter, a very promising candidate for flow control. A WDA can be an active dimple, active bump, or both. A bump on a surface activated by a piezo-electric material underneath was proposed by Lumley [71]. In his configuration, the bump was approximately Gaussian in shape. The laminar flow response of this actuator was then studied by Carlson and Lumley [12]. The results revealed the presence of vortical structures identical to those found in flow over a stationary bump, intensified and stretched by the upward velocity of the boundary. These structures consisted of three pairs of streamwise vorticity regions of alternating sign. During the rise of the actuator, the structures intensified and stretched, assuming more vertical attitudes as they were lifted by the moving boundary. This was followed by an investigation of active control with a Gaussian bump in a turbulent wall layer [13]. Using the same Reynolds number, and the same actuator parameters, simulations were performed in a minimal flow unit, containing a high-, and a low-speed streak in the near-wall region. The actuator was raised underneath the high-speed streak, lifting the fast-moving fluid away from the wall. Although their work is well-reported their results must be interpreted with caution. Their mathematical model was shown by Luo *et al.* [73] to omit some potentially important terms.

A great research effort towards smart skins containing WDAs for reactive control of wall turbulence has been undertaken by a group at the University of Tokyo. Their work is motivated by results from a numerical analysis performed by Endo *et al.* [27]. Using continuous forced wall deformation, velocity sensors away from the wall and opposition control according to Choi *et al.* [15] in turbulent channel flow at $Re_\tau = 150$, a drag reduction of 10% was reported. In this simulation, opposition control was conducted by using the deforming wall rather than wall transpiration to impart the necessary vertical momentum in the near-wall region. Upon substituting the continuous surface actuator with an array of bipolar WDAs the reduction of 10% was surprisingly maintained. However, control simulations at a higher Reynolds number of $Re_\tau = 300$ did not result in any drag reduction for the same size of

deformable actuators [28].

The issue of sensing is not covered in this report but it is worthwhile noting that in some experiments Endo *et al.* [27] estimated the normal velocity away from the wall using wall measurements. This was achieved by considering that the streamwise vortices, which - according to these researchers - account for the normal velocity, create gradients of wall shear stresses through meandering. Using this quantity to estimate the wall-normal velocity, they derived a control scheme that was similar to the one by Lee *et al.* [66, 67] although based on physical arguments rather than sub-optimal theory.

Using a bigger channel, a similar experiment with continuous wall deformation was performed at $Re_\tau = 140$ by Kang *et al.* [54]. Two different control schemes were implemented, opposition control by Choi *et al.* [15], and sub-optimal control by Lee *et al.* [67]. Results showed that 13 to 17% drag reduction was obtained. According to Luo *et al.* [73], however, they omitted the same terms in their mathematical model as Carlson *et al.* [11, 12, 13]. Therefore, their results may be influenced by this omission.

Both studies [27] and [54] achieved less drag reduction than in the case of blowing and suction which produced 22-25% [15, 67]. The differences in performance are commonly attributed to a variety of reasons. The most important is generally considered to be the deformation limiter that has to be imposed on the wall to keep it from deflecting excessively. Another is that opposition control requires the actuators to impart vertical momentum only, whereas surface actuation generates a much more complex flow perturbation, potentially increasing drag. The only certain - though minor - cause of increased skin friction is the growth in surface area that accompanies wall deformation by definition. To date no conclusive evidence has been produced to confirm the first two claims. To quantify the role of the role of these two types of actuation is one of the central goals of this thesis.

A similar numerical experiment was also conducted by Kellogg [58]. Using a different deformation limiter and sensing plane location, Kellogg observed up to 14% drag reduction at $Re_\tau = 100$. Upon substituting the continuous surface with arrayed bipolar WDAs, drag reduction dropped to less than 5%. Interestingly, it

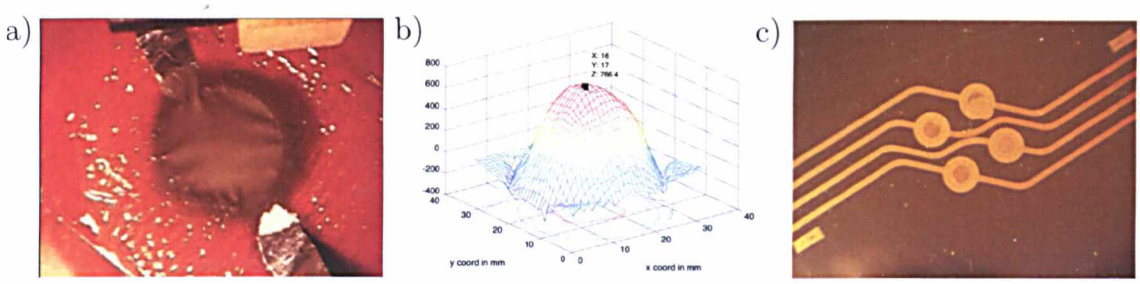


Figure 2.5: a) Dimple actuator; b) Measurement of dimple actuator shape; c) Prototype of MEMS-fabricated dimple actuators. FCG, Imperial College, Dearing *et al.* [23] .

was also observed that oscillating the actuators randomly, the drag was reduced by 0-3% only.

To be suitable for the reduction of skin friction in practical applications, WDAs must facilitate micro-scale actuation. The only existing MEMS-based WDAs known to the author are the microvalve-driven active dimples developed by Patel *et al.* [80]. Other current designs still are on a miniature scale due to the technical difficulties involved. The group at the University of Tokyo, for example, has successfully developed prototypes of electromagnetic and dielectric active bumps of 0.5-1.5 mm in size. Similar efforts are undertaken at the FCG, Imperial College. Frames a and b of figure 2.5 display small moving dimples based on electroactive polymers that have been successfully tested. A MEMS-fabricated prototype of the same principle is currently developed and shown in frame 'c'.

To date only few experimental studies have been conducted on flow over WDAs and none of them was on a micro scale. In most cases the WDAs were simply used as a means to create travelling waves in transitional boundary layer flows.

In 1989 Breuer *et al.* [7] performed an experiment in a laminar boundary layer where pro- and intruding WDAs in the form of pressure-driven membranes were used to cancel partially the three-dimensional large-amplitude disturbance generated by another membrane. In uncontrolled flow at $Re_\delta = 1095$ the disturbance would lead to a turbulent spot. However, the counter-disturbance, located further downstream and generated by an array of eight small membranes mounted next to one another and activated in rapid succession, delayed the breakdown of the disturbance by

about fifty displacement-thickness units when properly phased.

Wilkinson & Balasumbrian [110] investigated the influence of a travelling surface depression in transitional flow. Experiments in low-speed air with an electromagnetically driven wall membrane showed that Reynolds stresses were reduced.

To the author's knowledge only a single experimental study was conducted on localised wall motion in turbulent flow which was performed by Kim *et al.* [17]. Using a pro- and intruding WDA of 20mm in diameter and magnetically driven at frequencies of up to $Str^+ = 0.0129$, the changes in a turbulent boundary layer flow at $Re_\theta = 1870$ were investigated. At high frequencies, the upward motion generated a pair of streamwise vortices, allegedly providing a possibility of generating large-scale streamwise vortices. It should be noted that these vortices are entirely different from the ones found in flow forced by a synthetic jet. First of all they are only found in the phase-averaged field contrary to the quasi-steady vortices generated by a jet. Secondly, they were of a different length scale with a size of just one-seventh of the actuator diameter.

Gaster *et al.* [37] also investigated the velocity field created by an oscillating bump in a turbulent boundary layer. But in their study the actuator was driven at a very low frequency, essentially creating a quasi-static perturbation. The reason for introducing a periodic actuation was experimental, as a static distortion of the flowfield is difficult to measure. These results were later numerically confirmed by Joslin *et al.* [53] using a static bump.

Piston-driven membrane actuators in a laminar water channel have also been investigated at the FCG, Imperial College. Results of previous experiments using active cylindrical depressions are reported in [65], showing the creation of jet-like quasi-steady streamwise vortices at high frequencies time-averaged over many cycles.

In comparing the results from different studies involving discrete local wall deformation, it is important to distinguish between the different types shown in figure 2.1. Dimples and bumps can be either active or passive. The latter has already found widespread use as flow control device as mentioned in the introduction. Despite their long history, passive actuators remain subject to ongoing fundamental research [69] but are not considered in the present study which focuses entirely on active flow

	Dimples and bumps		
Motion	Passive	Active	
Arrangement	Solitary	Arrayed	
Shape	Cylindrical	Spherical	Smooth

Table 2.1: Dimple and bump categories

control. Regarding their arrangement, dimples and bumps can either be solitary or arrayed. For basic flow-response analysis the solitary actuator is often chosen as starting point. But since control of only a selected number of coherent structures is not promising, any real-world control device will probably have to feature close arrays of actuators. Their shape is often dictated by the method of investigation. To avoid discontinuities or even singularities, smooth active surfaces are preferred [12, 13, 27, 28, 54, 58] in numerical simulations. In experimental studies it is the design of the actuator which determines the shape, which can be cylindrical [65], spherical [62, 3], or smooth [22].

2.3 Improving skin friction control by active wall deformation

As mentioned in the last section, skin-friction reductions of up to 17% have been achieved by researchers using active wall deformation as a means to control low-Reynolds-number turbulent flow [27, 28, 54, 58]. The variable results were attributable to the different parameters chosen.

The present project not only aspires to design a test bed for future control experiments but also to improve the results that were achieved to date. Based on past research, some potentially interesting avenues of inquiry are listed below.

- Improving performance while retaining control schemes inspired by wall transpiration.

So far all numerical control experiments used opposition control or linearised sub-optimal control, both designed for wall-transpiration actuation. On one hand the two methods are attractive in their simplicity and practicality but on the other hand they create only modest reductions in drag of about 25%. Given that in theory more than 50% reduction can be attained by relaminarising the flow, other control algorithms might have to be considered. One example of a more efficient control scheme that was also designed for actuation by blowing and suction is optimal control which was shown to be capable of relaminarising the flow when the Reynolds numbers are very low [5]. This improvement in performance came at no extra cost compared to opposition control in the terms of average magnitude of wall transpiration [82]. Even though real-world utilisation of such computationally expensive schemes is nearly impossible, knowledge of their performance in combination with wall motion could be interesting and set a new benchmark.

Improvements to the current designs can also be made through fine-tuning the implementation of wall deformation. To follow the most promising approach to achieve improvements, the parameters most critical to the performance would have to be identified first. One could be for example the deformation limiter that prevents the wall from excessive local growth. The specific kind of mathematical formulation for this restriction should have an influence on the performance.

In the present work both approaches were taken. The fine-tuning of opposition control by wall deformation is discussed in Chapter 7 whereas the search for more efficient velocity-based control algorithms is documented in Chapter 8.

- Tailoring control method to active wall deformation.

  Nearly all of the existing flow control schemes have been constructed with wall transpiration in mind, as discussed above. Instead of adapting control schemes intended for use with wall transpiration to deforming actuators, new control schemes could be invented that are tailored to the advantages and disadvantages of actuation with unsteady, irregular wall geometries. Using discrete wall

deformation actuators merely as sources of wall-normal momentum neglects both the potential uses as well as the possible detrimental effects of the other flow disturbances induced.

For schemes based on intuition this is difficult to achieve as the flow response to deformation is, as will be shown, not intuitive. But for schemes based on mathematical equations the deformation can be taken into account. A first attempt in this direction was made by Berkooz [4]. He derived the control input in a model dynamic system from the time-dependent wall deformation. Alternatively, a neural network could be set up to account for actuation by wall deformation.

In this thesis, reasons will be presented not to pursue this strategy at the current state of knowledge and development.

- Cancelling vorticity flux by active wall deformation.

  Instead of manipulating primitive variables, Koumoutsakos [63] introduced a control scheme that cancels vorticity flux at the wall, thereby achieving 40% drag reduction in a turbulent channel. The scheme involved an explicit formulation to determine the necessary wall transpiration to induce a desired vorticity flux at the wall. In theory this method should be adaptable to actuation using wall deformation. However, as will be seen later, serious difficulties are encountered when trying to derive a formulation for the wall vorticity flux that depends only on the known boundary conditions, unless the boundaries are linearly approximated.

- Creating streamwise vortices by active wall deformation.

  Synthetic jets are popular in the field of skin-friction control for their ability to produce streamwise vortices. In theory, these could be used to cancel pre-existing streamwise vortices and thus suppress the formation of streaks. Whether wall deformation actuators can also produce such structures is an unanswered question which is also investigated in the present work.

  Although not discussed here, examples of coarse, open-loop control simulations

also motivate the design of a device capable of creating streamwise vortices. Schoppa *et al.* [91] report how drag can be reduced by about 20% in a turbulent channel simulation through inducing streamwise vortices much larger than the coherent structures.

Chapter 3

Mathematical framework

This chapter presents the mathematical framework underlying the simulations performed. Its construction can be considered as the first step towards the development of a numerical flow-control test bed.

First, the Navier-Stokes equations are introduced for different coordinate systems in section 3.1. These include the general time-dependent curvilinear system which allows the use of a boundary-fitted mesh in any time-dependent curvilinear geometry. A particular subset thereof was used for most of the experiments in this work. In the same section it is shown how the equations for all coordinate systems are semi-discretised by applying a three-substep splitting scheme. This yields a Poisson equation for the pressure and a Helmholtz equation for each velocity. To solve those time-independent linear partial differential equations the domain is discretised. For two-dimensional problems a spectral element expansion basis is applied as outlined in section 3.2. To extend this scheme to three dimensions the solution is represented by a Fourier expansion in the third direction. This is explained in section 3.3. The last section, 3.4, presents a technique to maintain constant flow rate in the simulation of channel flow.

3.1 Flow equations and time discretisation

The Navier-Stokes equations describe the motion of a Newtonian fluid with constant viscosity μ^* and density ρ^*. In the Cartesian coordinate system these equations are

well-known and widely implemented. But most geometries in this study are channels with irregular and moving walls that require special treatment. By choosing the technique of boundary-fitted meshes to deal with the complex boundaries, the Navier-Stokes equations have to be constructed for time-dependent curvilinear systems.

It should be noted that boundary-fitted meshes are just one technique among many to cope with complex boundaries. For example, an alternative is the immersed-boundary method [58, 32].

Boundary-fitted meshes allow the use of highly-efficient numerical methods, such as globally-spectral discretisation, by creating a canonical geometry in computational space. They are most popular for flow problems with fixed domains but these meshes can be easily adapted to time-dependent geometries. On the downside, the Navier-Sokes equations in a general curvilinear system are much more complex than their Cartesian counterparts. This is because the application of a boundary-fitted mesh essentially reduces the complexity of the geometry by increasing the complexity of the equations. In very complex geometries the extra complexity in the equations outweights the benefits. However, in the specific problem at hand, channel walls deforming in the normal direction only, the equations remain reasonably simple as many terms drop out.

In the following sections three sets of Navier-Stokes equations and the corresponding time-splitting schemes are presented. The first set applies to the Cartesian coordinate system. The second set is coordinate-independent and applies to all possible curvilinear coordinate systems. Hence, it can be used for any system fitted to curvilinear boundaries. The third set is a subgroup of the second formulation and entails all curvilinear systems where the Jacobian of the mapping is uniformly one. It is an interesting subclass that allows very efficient computations when combined with certain time-stepping algorithms. Every simulation in this work, where the displacements of two opposing points at upper and lower wall are identical, are solved using the third set of equations.

The Navier-Stokes equations for curvilinear coordinate systems can be formulated in different ways. One approach is the contravariant tensorial formulation

which can be found for the case of fixed systems in the textbook by Aris [1] or the article by Gal-Chen and Somerville [35]. These tensor equations arise from imposing the conservation of *scalar* mass and of the contravariant components of the *vector* momentum in a general coordinate system (using covariant tensorial differentiation; see expression (3.19) for the definition of contravariant velocities). Generally, these equations are only weakly-conservative and contain eighteen independent geometric quantities for each point. It is this formulation that we adopt here however extended to time-dependent geometries as described by Luo *et al.* [73].

An alternative formulation, one which is strongly conservative, can be obtained by making a general coordinate transformation of the *scalar* Cartesian momentum equations based on the Cartesian components of velocity [105]. This form, also called the semi-Cartesian form, arises from the observation that the Cartesian components of the momentum are conserved and therefore the coordinate transformation of a conservation equation for a *scalar* quantity may be applied to each Cartesian component separately. Using the Cartesian based velocities multiplied by the Jacobian of the transformation as flow variables ensures strong conservation. Furthermore the number of independent geometric quantities is only fifteen. The drawback of using this formulation is that an elaborate procedure for formulating the elliptic pressure equation is required [107].

3.1.1 Cartesian coordinate system

3.1.1.1 The equations

In the Cartesian coordinate system the Navier-Stokes equations are given as

$$\frac{\partial u^i}{\partial x^i} = 0 \,, \tag{3.1}$$

$$\frac{\partial u^i}{\partial t} + u^j \frac{\partial u^i}{\partial x^j} = -\frac{\partial p}{\partial x^i} + \frac{1}{Re} \frac{\partial^2 u^i}{\partial x^j \partial x^j} \,, \tag{3.2}$$

where u^i is the velocity vector in the Cartesian frame, p is the static pressure divided by the density ρ, Re is the Reynolds number, and x^i are the Cartesian coordinates. The nonlinear terms in equation (3.2) have been written in the convective form.

3.1.1.2 The time-stepping scheme

To derive the time-stepping scheme the following operators are defined

$$N^i(\mathbf{u}) = u^j \frac{\partial u^i}{\partial x^j} , \tag{3.3}$$

$$G^i(p) = -\frac{\partial p}{\partial x^i} , \tag{3.4}$$

$$L^i(\mathbf{u}) = \frac{1}{Re} \frac{\partial^2 u^i}{\partial x^j \partial x^j} . \tag{3.5}$$

The momentum equation (3.2) can then be written in the form

$$\frac{\partial u^i}{\partial t} + N^i(\mathbf{u}) = G^i(p) + L^i(\mathbf{u}) . \tag{3.6}$$

Using a semi-discrete formulation, the flowfield can be integrated in time through the following splitting scheme:

$$\hat{u}^i = u^{i,n} + \Delta t \sum_{q=0}^{J_e-1} \beta_q N^i(\mathbf{u}^{n-q}) \tag{3.7}$$

$$\frac{\partial^2}{\partial x^j \partial x^j} p^{n+1} = \frac{1}{\Delta t} \frac{\partial}{\partial x^i} \hat{u}^i \tag{3.8}$$

$$\hat{\hat{u}}^i = \hat{u}^i + \Delta t G^i \left(p^{n+1}\right) \tag{3.9}$$

$$\left(I - \Delta t \gamma_0 L\right) \left(u^{i,n+1}\right) = \hat{\hat{u}}^i + \Delta t \sum_{q=1}^{J_i-1} \gamma_q L^i(\mathbf{u}^{n+1-q}) \tag{3.10}$$

In the first step of this scheme, equation (3.7), the nonlinear terms are calculated and treated explicitly in time by using an Adams-Bashforth time integration scheme to obtain the intermediate velocity $\hat{u}^i$. The order of this time scheme determines the coefficients β_q. By taking the divergence of the semi-discretised form of equation (3.2) and enforcing $\partial u^{i,n+1}/\partial x^i = 0$ the Poisson equation, (3.8), is obtained. Solving this equation yields the pressure at the next time step, p^{n+1}, which can then be used to calculate a new intermediate velocity $\hat{\hat{u}}^i$ through equation (3.9). The splitting errors are minimised by using a mixed implicit/explicit boundary condition for the pressure [56]:

$$\frac{\partial p^{n+1}}{\partial n} = \mathbf{n} \cdot \left[\sum_{q=0}^{J_e-1} \beta_q \mathbf{N}(\mathbf{u}^{n-q}) + \sum_{q=0}^{J_i-1} \gamma_q \mathbf{L}(\mathbf{u}^{n+1-q}) \right] \quad \text{on } \partial\Omega \tag{3.11}$$

Finally, the viscous terms are treated implicitly by solving the Helmholtz equation (3.10) for each velocity component at the next time step, $u^{i,n+1}$. The coefficients γ_q are thus the weights of an Adams-Moulton family of order J_i.

In total, this scheme requires the solution of one Poisson equation and three Helmholtz equations at each time step. Due to the implicit treatment of the viscous terms and the explicit treatment of the non-linear terms, the stability of the latter dictates the time step.

3.1.2 Time-dependent curvilinear coordinate systems

3.1.2.1 The equations

We now consider the contravariant form of the Navier-Stokes equations in time-dependent curvilinear coordinate systems. These systems are based on some transformation that converts the Cartesian system to a system with the same number of coordinates in which the coordinate lines are curved. This transformation is required to be locally invertible at each point. Simple examples of curvilinear systems are cylindrical and spherical coordinate systems.

The super- and subscript now refer to contravariant and covariant behaviour respectively, which are concepts that are explained shortly. For additional information on the derivation of these equations for fixed systems the textbook by Aris [1] is recommended. For details on the extension to time-dependent systems the reader is referred to the article by Luo *et al.* [73].

The time-dependent transformation

$$x^i = x^i(\xi^1, \xi^2, \xi^3, \tau) \tag{3.12}$$

$$t = \tau \tag{3.13}$$

from the Cartesian coordinates $\mathbf{x}$ to the curvilinear coordinates $\boldsymbol{\xi}$ is considered. The transformation matrix is defined by

$$C = \frac{\partial \mathbf{x}}{\partial \boldsymbol{\xi}}, \quad c^i_j = \frac{\partial x^i}{\partial \xi^j}, \tag{3.14}$$

and its inverse by

$$\bar{C} = \frac{\partial \boldsymbol{\xi}}{\partial \mathbf{x}}, \quad \bar{c}^i_j = \frac{\partial \xi^j}{\partial x^i}. \tag{3.15}$$

The Jacobian is

$$J = |C| \ , \tag{3.16}$$

where || denotes the determinant. For the transformation to be locally invertible it is required that $J \neq 0$. The metric tensor, which can be used to measure distance and angle in the curvilinear space, and its inverse are given as

$$g_{ij} = c_i^k c_j^k, \quad g^{ij} = \bar{c}_k^i \bar{c}_k^j \ , \tag{3.17}$$

which leads to the definition of the connection coefficients (or Christoffel symbols of the second kind):

$$\Gamma_{jk}^i = \frac{1}{2} g^{ip} \left(\frac{\partial g_{pj}}{\partial \xi^k} + \frac{\partial g_{pk}}{\partial \xi^j} - \frac{g_{jk}}{\partial \xi^p} \right) \ . \tag{3.18}$$

Vectors that transform from the Cartesian to the curvilinear system through c_j^i, are called covariant, whereas those that transform through the inverse, $\bar{c}_j^i$, are called contravariant. Accordingly, the transformation relationship between the contravariant velocity vector $\mathbf{u}$ in the Cartesian coordinate system and its counterpart $\mathbf{U}$ in the curvilinear coordinate system is

$$u^j = c_i^j U^i, \quad U^i = \bar{c}_j^i u^j \tag{3.19}$$

and the velocities of the moving coordinates are

$$\bar{S}^i = \frac{\partial x^i}{\partial \tau}, \quad S^j = -\frac{\partial \xi^i}{\partial t} \ . \tag{3.20}$$

Using contravariant velocities, the Navier-Stokes equation in a time-dependent curvilinear coordinate system may then be written as follows

$$U_{,i}^i = 0 \ , \tag{3.21}$$

$$\frac{\partial U^i}{\partial \tau} + (U^j - S^j) U_{,j}^i + U^j S_{,j}^i = -g^{ij} p_{,j} + \frac{1}{Re} \left(g^{jk} U_{,k}^i \right)_{,j} \ , \tag{3.22}$$

where the comma in the index denotes covariant differentiation, defined as

$$U_{,j}^i = \frac{\partial U^i}{\partial \xi^j} + \Gamma_{jk}^i U^k \ . \tag{3.23}$$

The equations (3.1) and (3.2) are special Cartesian cases of (3.21) and (3.22).

Using the relationship, $\Gamma^j_{ji} = \Gamma^j_{ij} = J^{-1}\frac{\partial J}{\partial \xi^i}$ [105], and covariant differentiation, one obtains for $U^i_{,i}$:

$$U^i_{,i} = \frac{\partial U^i}{\partial \xi^i} + \Gamma^i_{ik}U^k = J^{-1}\frac{\partial}{\partial \xi^i}(JU^i) \tag{3.24}$$

Substituting equation (3.24) into equation (3.21) yields the simplified mass equation

$$\frac{\partial}{\partial \xi^i}(JU^i) = 0 \ . \tag{3.25}$$

Instead of applying the conservation laws in the general curvilinear system, equations (3.21) and (3.22) can also be obtained through direct transformation of the equations in the Cartesian frame. However, the latter approach is somewhat cumbersome and prone to errors. Direct transformations should be pursued for very simple coordinate systems only.

3.1.2.2 The splitting scheme

To formulate the time-splitting scheme the following operators are defined as

$$N^i(\mathbf{U}) = (U^j - S^j)U^i_{,j} + U^j S^i_{,j} \ , \tag{3.26}$$

$$G^i(p) = -g^{ij}p_{,j} \ , \tag{3.27}$$

$$L^i(\mathbf{U}) = \frac{1}{Re}\left(g^{jk}u^i_{,k}\right)_{,j} \ . \tag{3.28}$$

With these operators equation (3.6) can be used to represent equation (3.22). The solution can then be advanced in time using the scheme

$$\hat{U}^i = U^{i,n} + \Delta t \sum_{q=0}^{J_e-1} \beta_q N^i(\mathbf{U}^{n-q}) \tag{3.29}$$

$$\frac{\partial^2}{\partial\xi^j\partial\xi^j} p_{s+1}^{n+1} = J^{-1}\frac{1}{\Delta t}\frac{\partial}{\partial\xi^i}(J\hat{U}^i) + \left(\frac{\partial^2}{\partial\xi^j\partial\xi^j} - J^{-1}\frac{\partial}{\partial\xi^i}JG^i\right)\left(p_s^{n+1}\right) \tag{3.30}$$

$$\hat{\hat{U}}^i = \hat{U}^i + \Delta t G^i\left(p^{n+1}\right) \tag{3.31}$$

$$\left(I - \Delta t\gamma_0\frac{\partial^2}{\partial\xi^j\partial\xi^j}\right) U_{s+1}^{i,n+1} = \hat{\hat{U}}^i + \Delta t\sum_{q=1}^{J_i-1}\gamma_q L^i(\mathbf{U}^{n+1-q}) + \Delta t\left(L^i - \frac{\partial^2}{\partial\xi^j\partial\xi^j}\right)\left(U_s^{i,n+1}\right) \tag{3.32}$$

The left-hand sides of the elliptic equations (3.30) and (3.32) equations are the same as in the Cartesian case. Hence, the existing solver routines in *Νεκταr* for Cartesian coordinate systems can be retained. However, these equations have been derived by splitting the operator into an invertible part and its remainder, as demonstrated by Carlson *et al.* [11]. Hence, the equations must now be iterated and the right hand side must be updated at each iteration s. This extra loop - plus the great number of additional terms in the fully-expanded equations - make the computations in a general curvilinear system significantly more expensive than in the Cartesian frame. This is a direct consequence of the conservation of mathematical difficulty: using a boundary-fitted coordinate system shifts the complexity from the geometry to the equations.

3.1.3 Divergence-free coordinate systems

One significant disadvantage of the scheme presented in the last section is that the Poisson and Helmholtz equations need to be iterated. This section advocates a special subset of curvilinear coordinate systems that if combined with an increased

portion of explicit time-integration overcomes these problems and leaves all but the first substep of the *Νεκταr* splitting scheme for Cartesian coordinates unmodified.

The first simplification is that the local transformation is such that $J = 1$ which means that the volume of an arbitrary domain element remains constant over time and is equal to the volume in the Cartesian system. In a channel for example, this condition requires that the displacements of two opposite points at lower and upper wall are identical at any given time. Systems that meet this requirement are also termed divergence-free. By substituting the condition $J = 1$ into equation (3.25) one obtains

$$\frac{\partial}{\partial \xi^i} U^i = 0 \,, \tag{3.33}$$

which is identical to the continuity equation in Cartesian coordinates.

The second simplification is that all the terms which are zero in the standard Cartesian form are lumped together in a super-term A^i which is treated explicitly by adding it to the non-linear operator. The operators then simplify to

$$N^i(\mathbf{U}) = U^j \frac{\partial U^i}{\partial \xi^j} + A^i(\mathbf{U}) \,, \tag{3.34}$$

$$G^i(p) = -\frac{\partial p}{\partial \xi^i} \,, \tag{3.35}$$

$$L^i(\mathbf{U}) = \frac{1}{Re} \frac{\partial^2 U^i}{\partial \xi^j \partial \xi^j} \,. \tag{3.36}$$

A full expansion of the super-term A^i is given in Chapter 4 and Chapter 6 for individual cases under investigation. By treating A^i explicitly, the same time-splitting scheme as in the case of a Cartesian coordinate system can be used. Hence,

x^i is replaced with ξ^i and u^i with U^i in equations (3.7) to (3.10) to obtain

$$\hat{U}^i = U^{i,n} + \Delta t \sum_{q=0}^{J_e-1} \beta_q N^i(\mathbf{U}^{n-q}) \ , \tag{3.37}$$

$$\frac{\partial^2}{\partial \xi^j \partial \xi^j} p^{n+1} = \frac{1}{\Delta t} \frac{\partial}{\partial \xi^i} \hat{U}^i \ , \tag{3.38}$$

$$\hat{\hat{U}}^i = \hat{U}^i + \Delta t G^i \left(p^{n+1}\right) \ , \tag{3.39}$$

$$\left(I - \Delta t \gamma_0 L\right)\left(U^{i,n+1}\right) = \hat{\hat{U}}^i + \Delta t \sum_{q=1}^{J_i-1} \gamma_q L^i(\mathbf{U}^{n+1-q}) \tag{3.40}$$

Because this scheme requires no inner-time-step iterations and contains fewer terms than the general one it promises to be more efficient. Therefore, most of the curvilinear-boundary simulations presented in this work will be specifically set up to facilitate the use of this technique. One price paid for this simplification is that the flow geometry is constrained by the condition $J = 1$. Another is that the pressure and viscous components of A^i are treated explicitly. This generates a more stringent stability condition and introduces a divergence error to the approximate solution.

3.2 Spectral element methods

All equation sets in section 3.1 contain an elliptic equation for the pressure and each velocity component. To solve these equations in two dimensions the flowfield is discretised by a spectral/*hp* finite element scheme. The basic concept of this method is demonstrated below through the solution of a one-dimensional Poisson equation. This demonstration comprises the introduction of the Galerkin formulation in section 3.2.1 and the construction of an appropriate expansion basis in sections 3.2.2 and 3.2.3. Supplementary information on this approach can be found in the textbook by Karniadakis and Sherwin [57].

Note that the extension of this scheme to three dimension by using Fourier series in the third direction is presented in the next section.

3.2.1 Galerkin formulation of the one-dimensional Poisson equation

The following illustrates the basic concepts of the Galerkin method considering the example case of the one-dimensional Poisson equation in Cartesian coordinates,

$$\mathbb{L}(u) \equiv \frac{\partial^2 u}{\partial x^2} + f = 0 \ , \tag{3.41}$$

in the domain $\Omega = \{x \mid 0 \leq x \leq L_x\}$. The boundary conditions are specified at the end of the domain and are of Dirichlet and Neumann type, respectively:

$$u(0) = g_D, \quad \frac{\partial u}{\partial x}(L_x) = g_N \ . \tag{3.42}$$

The Legendre inner product (f, g) over the domain Ω is defined as

$$(f, g) = \int_\Omega f(x) g(x) \, \mathrm{d}x \ . \tag{3.43}$$

To construct a weak approximation to equation (3.41), it is multiplied by a test function $v(x)$, which by definition is zero on all Dirichlet boundaries Ω_D. The resulting expression is integrated over the domain Ω so that

$$(v, \mathbb{L}(u)) = \int_0^{L_x} v \left(\frac{\partial^2 u}{\partial x^2} + f \right) \mathrm{d}x = 0 \ . \tag{3.44}$$

Next, equation (3.44) is integrated by parts which yields

$$\int_0^{L_x} \frac{\partial v}{\partial x} \frac{\partial u}{\partial x} \, \mathrm{d}x = \int_0^{L_x} v f \, \mathrm{d}x + \left[v \frac{\partial u}{\partial x} \right]_0^{L_x} \ . \tag{3.45}$$

This formulation is weak in the sense that by having transformed the second-order differential equation (3.41) into the first-order differential equation (3.45) the solution space was enhanced by functions that are C^0 continuous.

By considering that the test functions are defined to be zero on Dirichlet boundaries and implementing the Neumann boundary condition of (3.42) through substitution in (3.45) one obtains

$$\int_0^{L_x} \frac{\partial v}{\partial x} \frac{\partial u}{\partial x} \, \mathrm{d}x = \int_0^{L_x} v f \, \mathrm{d}x + v(L_x) g_N \ . \tag{3.46}$$

To enforce the Dirichlet boundary condition, the solution $u(x, t)$ is defined as a composition of a known function u^D which satisfies the Dirichlet boundary condition

and an unknown homogenous function, u^H, which is zero on the Dirichlet boundaries, so that

$$u^\delta(x,t) = u^H(x,t) + u^D(x,t) \ , \tag{3.47}$$

where

$$u^H(\partial\Omega_D) = 0, \quad u^D(\partial\Omega_D) = g_D \ . \tag{3.48}$$

By substituting equation (3.47) into the weak formulation of the problem given by (3.46), one obtains

$$\int_0^{L_x} \frac{\partial v}{\partial x}\frac{\partial u^H}{\partial x}\,\mathrm{d}x = \int_0^{L_x} vf\,\mathrm{d}x + v(L_x)g_N - \int_0^{L_x} \frac{\partial v}{\partial x}\frac{\partial u^D}{\partial x}\,\mathrm{d}x \ . \tag{3.49}$$

Since u_D is a known function which satisfies the boundary conditions, all terms on the right hand side of equation (3.49) are known. To solve the problem as a finite algebraic system, the approximate solution $u^\delta(x,t)$ to $u^H(x,t)$ and the approximate representation $v^\delta(x,t)$ of $v(x,t)$ are defined as a finite sum of functions,

$$\begin{aligned} u^H(x,t) &= \sum_{i=1}^{N_{dof}} \hat{u}_i(t)\Phi_i(x) \ , \\ v^\delta(x,t) &= \sum_{i=1}^{N_{dof}} \hat{v}_i(t)\Phi_i(x) \ , \end{aligned} \tag{3.50}$$

where $\Phi_i(x)$ are analytic functions, $\hat{u}_i(t)$ are the N_{dof} unknown coefficients, and $\hat{v}_i(t)$ are the test function coefficients that will cancel on both sides upon substitution. By definition both expressions in (3.50) are zero on the Dirichlet boundaries. What makes this weighted-residual method a Galerkin method is that the same expansion functions are used for the approximate homogenous solution, u^H, and the approximate test function v^δ.

3.2.2 One-dimensional expansion basis

Having defined the Galerkin approximation for a linear one-dimensional partial differential equation, it is now followed by the definition of an appropriate one-dimensional expansion basis, again demonstrated in Cartesian coordinates. In the present work the spectral/*hp* element technique is utilised.

In the h-type method convergence is achieved by reducing the size of elements while keeping the polynomial order constant. In the p-type method convergence is achieved by increasing the order of the polynomial in every element while keeping the size of the elements fixed.

The spectral/hp element method permits the combination of both. It facilitates highly-accurate simulations of flow problems that require unstructured discretisation. This can be the case if the geometry is irregular or if a mesh of varying density is desired. Examples of the latter are the laminar simulations presented in Chapter 4 where a fine triangular mesh surrounds the regions close the moving obstacles. A special situation arises when the whole domain is treated as a single element. Then, the p-type method becomes a globally-spectral method, a kind of which is used in Chapter 8 to simulate flow in the simple geometry of a canonical channel.

To implement the h-type method the solution domain, Ω, needs to be subdivided into N_{el} distinct elements, denoted by Ω^e, that is

$$\Omega = \bigcup_{e=1}^{N_{el}} \Omega^e \ , \quad \text{where} \quad \bigcap_{e=1}^{N_{el}} \Omega^e = \emptyset \ . \tag{3.51}$$

Each element Ω^e can be mapped onto the so-called standard element, $\Omega_{st} = \{\epsilon \,|\, -1 \leq \epsilon \leq 1\}$, via the transformation $\chi^e(\epsilon)$, which expresses the global coordinates x in terms of the local coordinates ϵ as

$$x = \chi^e(\epsilon) = \frac{1-\epsilon}{2} x_{e-1} + \frac{1+\epsilon}{2} x_e, \quad \epsilon \in \Omega_{st} \ . \tag{3.52}$$

The Jacobian of this mapping, $J^e = \frac{\partial \chi^e}{\partial \epsilon}$, is constant which is suitable for most of the meshes in this investigation which consist of regular triangles or rectangles. However, when the elements are curved, as in one case presented in section A.1, a higher-order polynomial mapping must be used.

Using the transformation (3.52) the global modes $\Phi_i(x)$ can now be represented in terms of local expansion modes $\phi_p^e(\epsilon)$ by mapping the standard element Ω_{st} to each elemental domain Ω^e. Therefore, one can also express u^δ in terms of $\phi_p^e(\epsilon)$ as

$$u^\delta(x) = \sum_{i=1}^{N_{dof}} \hat{u}_i \Phi_i(x) = \sum_{e=1}^{N_{el}} \sum_{p=0}^{P} \hat{u}_p^e \phi_p^e(\epsilon), \tag{3.53}$$

where P is the polynomial order of the expansion in each element. As there are more local expansion coefficients, $\hat{u}_p^e$, than global expansion coefficients, $\hat{u}_i$, further conditions are required to relate them. These are given by the requirement that the solution at a global point connecting two elements must be the same in both elements, which is equivalent to the enforcement of C^0 continuity of $u^\delta(x)$. This relationship between the local degrees of freedom and the global degrees can be expressed in terms of an asssembly matrix $\mathcal{A}$, such that

$$\begin{bmatrix} \hat{\mathbf{u}}^1 \\ \vdots \\ \hat{\mathbf{u}}^{N_{el}} \end{bmatrix} = \mathcal{A} \begin{bmatrix} \hat{u}_1 \\ \vdots \\ \hat{u}_{N_{dof}} \end{bmatrix} , \tag{3.54}$$

where $\hat{\mathbf{u}}^e = [\hat{u}_0^e, \ldots, \hat{u}_P^e]^T$. Using $\mathcal{A}$, one can perform operations locally within the element and then assemble the global operation. To illustrate this assembly the Galerkin projection of a smooth function $f(x)$ in the domain Ω on the polynomial u^δ,

$$(v^\delta, u^\delta) = (v^\delta, f) , \tag{3.55}$$

is considered, which requires similar assembly procedures as the Galerkin formulation of the Poisson equation (3.49).

In the absence of explicit boundary conditions the polynomials expansions in expressions in (3.50) are used to approximate the solution. Problem (3.55) then becomes equivalent to solving the matrix equation

$$\hat{\boldsymbol{v}}^{\boldsymbol{T}}[\boldsymbol{M_G}\,\hat{\boldsymbol{u}} = \boldsymbol{f_G}] \;\Rightarrow\; \boldsymbol{M_G}\,\hat{\boldsymbol{u}} = \boldsymbol{f_G} ,$$

where

$$\boldsymbol{M}_G[i][j] = (\Phi_i, \Phi_j), \quad \hat{\boldsymbol{u}} = [\hat{u}_1, \ldots, \hat{u}_{N^{dof}}]^T, \quad \boldsymbol{f}_G[i] = (\Phi_i, f) .$$

$\boldsymbol{M}_G$ is also known as mass matrix and can be inverted to determine the solution

$$\hat{\boldsymbol{u}} = \boldsymbol{M_G^{-1}} \boldsymbol{f_G} . \tag{3.56}$$

To find the global mass matrix $\boldsymbol{M}_G$ the element mass matrices $\boldsymbol{M}^e$ are evaluated in the local coordinate, ϵ, according to

$$\boldsymbol{M}^e[p][q] = (\phi_p, \phi_q) = \int_{-1}^{1} \phi_p(\epsilon)\phi_q(\epsilon) J^e \, \partial\epsilon . \tag{3.57}$$

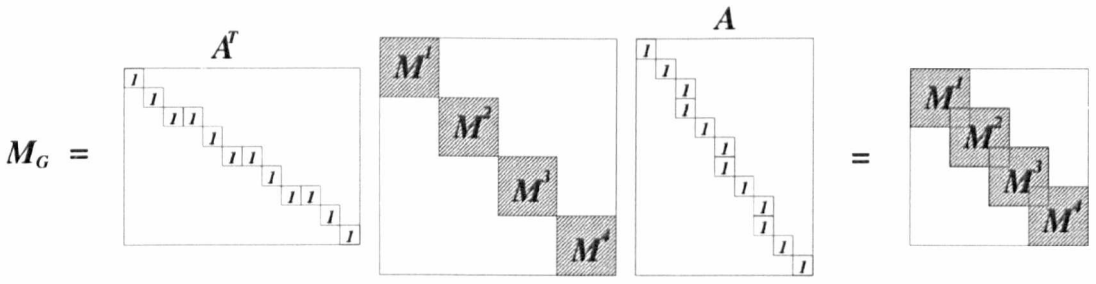


Figure 3.1: Global assembly of element mass matrices. Taken from Karniadakis and Sherwin [57].

These local matrices can then be assembled to a global structure, as illustrated in figure 3.1. Likewise, the local right hand side is given as

$$f^e[p] = (\phi_p, f) = \int_{-1}^{1} \phi_p(\epsilon) f J^e \, \partial\epsilon \ , \tag{3.58}$$

and is assembled through the relation

$$\boldsymbol{f}_G[i] = \mathcal{A}^T \begin{bmatrix} f^1[p] \\ \vdots \\ f^{N_{el}}[p] \end{bmatrix} . \tag{3.59}$$

To implement the p-type method one must define the local expansion modes, ϕ_p. These modes are usually based on Jacobi polynomials $P_P^{\alpha,\beta}(x)$ which exhibit the favorable property of orthogonality. These polynomials are solutions to a singular Sturm-Liouville problem which, in the region $-1 < x < 1$ is written as

$$\frac{d}{dx}\left[(1-x)^{1+\alpha}(1+x)^{1+\beta}\frac{d}{dx}u_p(x)\right] = \lambda_p(1-x)^{\alpha}(1+x)^{\beta}u_p(x), \tag{3.60}$$

with $u_p(x) = P_p^{\alpha,\beta}(x)$ and $\lambda_p = -p(\alpha+\beta+p+1)$.

Using such Jacobi polynomials and guarantying C^0 continuity of the solution across element boundaries the expansion $\phi_p(\epsilon)$ is defined as

$$\phi_p(\epsilon) = \begin{cases} \left(\frac{1-\epsilon}{2}\right) & p = 0 \\ \left(\frac{1-\epsilon}{2}\right)\left(\frac{1+\epsilon}{2}\right) P_{p-1}^{1,1}(\epsilon) & 0 < p < P \\ \left(\frac{1+\epsilon}{2}\right) & p = P \ . \end{cases} \tag{3.61}$$

The modes $p = 0$ and $p = P$ are the boundary modes, which are the only modes which have magnitudes at the ends of the interval. The other modes are interior

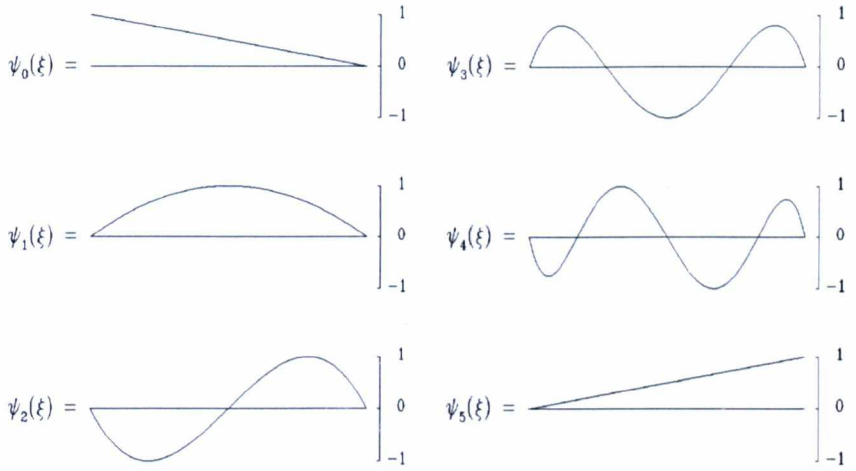


Figure 3.2: Shape of the expansion modes given in expression (3.61) for a polynomial order of $P = 5$. Taken from Karniadakis and Sherwin [57].

modes, and are zero at the boundaries. In the present work the Jacobi polynomial $P_p^{\alpha,\beta}(x)$ with $\alpha = \beta = 1$ is chosen since it proves to maintain a high degree of diagonality in the mass matrix. The normalised modes for P=5 are displayed in figure 3.2.

To complete the implementation of a polynomial basis, one must define methods to perform the mathematical operations of integration and differentiation at an elemental level. Numerical integration is performed by using Gaussian quadrature, which is particularly accurate when integrating smooth functions. It requires the representation of the integrand as a Lagrange polynomial and the definition of a series of integration points upon which the values of the integrand must be known, so that

$$\int_{-1}^{1} u(\epsilon)\partial\epsilon \approx \sum_{i=0}^{Q-1} w_i u(\epsilon_i) \ , \tag{3.62}$$

where w_i are the weights and ϵ_i is an abscissa of Q quadrature points (zeros) within the standard elemental interval. The quadrature points are optimally chosen to permit exact integration of polynomials of order $2Q-1$. Similarly, differentiation is performed through representation by Lagrange polynomials where only the values

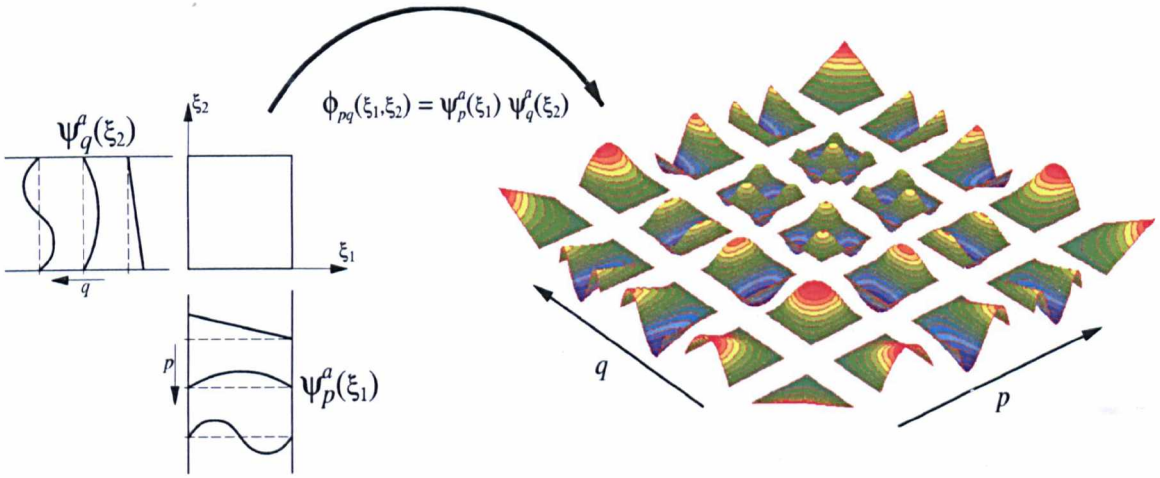


Figure 3.3: A fourth-order ($P = 4$) two-dimensional quadrilateral expansion constructed from the tensor product of two one-dimensional expansions of order $P = 4$, where $\psi_p^a = \phi_p$ and $(\xi_1, \xi_2) = (\epsilon_1, \epsilon_2)$. Taken from Karniadakis and Sherwin [57].

of the derivative at the quadrature points are required.

3.2.3 Extension to two dimensions

Analogous to the construction of a one-dimensional expansion basis, a two-dimensional basis requires the definition of a standard elemental region, Ω_{st}. For a bi-unit square element defined as $\{-1 \leq \epsilon_1, \epsilon_2 \leq 1\}$, the bases are expressed as a tensor product of the one-dimensional basis in each of the two Cartesian direction (ϵ_1, ϵ_2). This is illustrated in figure (3.3) for a polynomial order of P=4 and leads to

$$\Phi_{pq}(\epsilon_1, \epsilon_2) = \phi_p(\epsilon_1)\phi_q(\epsilon_2) \quad 0 \leq p, q; \quad p \leq P_1, \quad q \leq P_2\ , \tag{3.63}$$

where P_1 and P_2 represent the maximum polynomial order in the ϵ_1 and ϵ_2 directions, respectively. This expansion is the most commonly used in quadrilateral elements, which were often used in the present work to discretise the computational domain. But in some simulations, where the domain contained solitary actuators, local refinement in mesh density around the obstacle was required for efficient computing. This was handled by using unstructured meshes and in particular, triangular meshes.

The triangular elements can be related to quadrilateral ones by means of a trans-

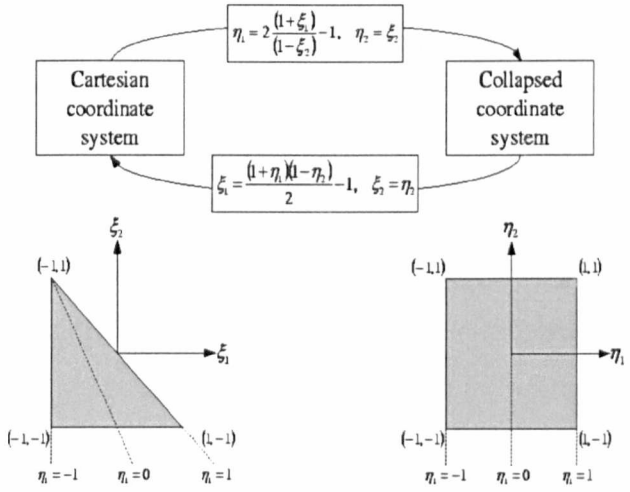


Figure 3.4: Transformation between triangular and quadrilateral elements, where $(\xi_1, \xi_2) = (\epsilon_1, \epsilon_2)$. Taken from Sherwin and Karniadakis [93].

formation, as shown in figure (3.4). Accordingly, the coordinates (ϵ_1, ϵ_2) of the triangular element are being mapped onto the unit-square element with coordinate (η_1, η_2). A two-dimensional expansion basis for triangular elements can then be created from the tensor product of a one-dimensional tensor, $\psi_p^a(\eta_1)$, and a two-dimensional tensor of the form $\psi_{pq}^a(\eta_2)$, which gives

$$\Psi_{pq}^a(\epsilon_1, \epsilon_2) = \psi_p^a(\eta_1)\psi_{pq}^a(\eta_2) \tag{3.64}$$

The exact form of $\psi_p^a(\eta_1)$ and $\psi_{pq}^a(\eta_2)$, known as the modified principal functions, is discussed in the textbook by Karniadakis and Sherwin [57].

3.3 Fourier expansion in the third dimension

An efficient approach to solve a three-dimensional problem is possible when the flow is periodic in one direction. In this approach, spectral elements are only applied

in two directions while a Fourier expansion is used in the third one. This method, which is usually referred to as the spectral element/Fourier method, has advantages compared to the fully-three-dimensional spectral element method. It requires a two-dimensional mesh only and facilitates a more efficient parallelisation.

All three-dimensional simulations in the present work are periodic in the spanwise, z, direction. Hence, the velocity and the pressure field satisfy the symmetry

$$\begin{aligned} \mathbf{u}(x,y,z,t) &= \mathbf{u}(x,y,z+L_z,t) \ , \\ p(x,y,z,t) &= p(x,y,z+L_z,t) \ , \end{aligned} \tag{3.65}$$

where L_z is the spanlength of the domain. The three-dimensional flow variables are then decomposed into a set of $M_z/2$ non-redundant two-dimensional Fourier modes $\hat{\mathbf{u}}_m$ and $\hat{p}_m$, so that

$$\begin{aligned} \mathbf{u}(x,y,z,t) &= \sum_{m_z=0}^{\frac{M_z}{2}-1} \hat{\mathbf{u}}_{m_z}(x,y,t) e^{i\frac{2\pi}{L_z}m_z z} \ , \\ p(x,y,z,t) &= \sum_{m_z=0}^{\frac{M_z}{2}-1} \hat{p}_{m_z}(x,y,t) e^{i\frac{2\pi}{L_z}m_z z} \ . \end{aligned} \tag{3.66}$$

The implementation of a Fourier expansion in the third direction is demonstrated through Fourier-transforming the Navier-Stokes equations in Cartesian form, that is equations (3.1) and (3.2). One obtains the coefficient equations

$$\begin{aligned} \frac{\partial \hat{\mathbf{u}}_{m_z}}{\partial t} &= -\tilde{\nabla} p_{m_z} + \mathbf{L}_{m_z}(\hat{\mathbf{u}}_{m_z}) + \mathbf{FFT}_{m_z}[\mathbf{N}(\mathbf{u})] \ , \\ \tilde{\nabla} \cdot \hat{\mathbf{u}}_{m_z} &= 0 \qquad \text{in} \quad \Omega_{m_z} = 0, \ldots, \frac{M_z}{2} - 1 \ , \end{aligned} \tag{3.67}$$

for each mode m_z of the expansion. $\mathbf{FFT}_{m_z}$ is the m_z^{th}-component of the Fourier transform of the non-linear terms which are evaluated in physical space and can be de-aliased to avoid possible instability. The operators $\tilde{\nabla}$ and $\mathbf{L}_{m_z}(\hat{\mathbf{u}}_{m_z})$ are defined as

$$\tilde{\nabla} = \left(\frac{\partial}{\partial x}, \frac{\partial}{\partial y}, i\beta_{m_z} \right) , \qquad \mathbf{L}_{m_z}(\hat{\mathbf{u}}_{m_z}) = \frac{1}{Re} \left(\frac{\partial^2}{\partial x^2} + \frac{\partial^2}{\partial y^2} - \beta_{m_z}^2 \right) \hat{\mathbf{u}}_{m_z} \ ,$$

where β_{m_z} is the spanwise wavenumber defined as $\beta_{m_z} = \frac{2\pi}{L_z} m_z$. All two-dimensional domains Ω_{m_z} are identical to each other. The only coupling term between the Fourier modes is through the non-linear terms. In consequence, the three-dimensional computation becomes a series of M_z two-dimensional problems that can be computed in parallel by applying the time-splitting scheme to each Fourier mode m_z individually.

3.4 Constant flow rate

The aim of flow control simulations in the present work is to reduce the drag, which can only be measured when the flow rate is held constant. This can be achieved through various methods. A common one is to calculate the necessary pressure gradient by integrating the entire momentum equation. However, this method only works if the time integration is fully-explicit. Since $Nεκταr$ treats the viscous part implicitly other means had to be found to enforce a constant flow rate. The method that was used in the present work is demonstrated on the flow equations in the Cartesian coordinate system but can be applied to any coordinate system.

Enhancing equation (3.6) by the forcing term $\alpha(t)\mathbf{e}_x$ and writing it in vector form together with equation (3.1) one obtains

$$\begin{aligned} \frac{\partial \mathbf{u}}{\partial t} + \mathbf{G}^i(p) - \mathbf{L}(\mathbf{u}) &= \mathbf{N}(\mathbf{u}) + \alpha(t)\mathbf{e}_x \ , \\ \nabla \cdot \mathbf{u} &= 0 \ , \end{aligned} \tag{3.68}$$

where $\mathbf{e}_x$ is the desired flow direction and α is an unknown coefficient. It needs to be determined so that

$$\int_y \mathbf{u} \cdot \mathbf{e}_x \, \mathrm{d}y = Q \ , \tag{3.69}$$

where Q is the specified flow rate. The equations (3.68) can be semi-discretised to

$$\begin{aligned} \frac{\mathbf{u}^{n+1} - \mathbf{u}^n}{\Delta t} + \mathbf{G}^i(p^{n+1}) - \sum_{q=0}^{J_i-1} \gamma_q \mathbf{L}(\mathbf{u}^{n+1-q}) &= \sum_{q=0}^{J_e-1} \beta_q \mathbf{N}(\mathbf{u}^{n-q}) + \alpha \mathbf{e}_x \\ \nabla \cdot \mathbf{u}^{n+1} &= 0 \end{aligned} \tag{3.70}$$

Since $\mathbf{u}^n$ is known from the previous time step the problem is linear and $\mathbf{u}^{n+1}$ and p^{n+1} can be decomposed into two components,

$$\begin{aligned} \mathbf{u}^{n+1} &= \hat{\mathbf{u}}^{n+1} + \alpha \bar{\mathbf{u}}^{n+1} \\ p^{n+1} &= \hat{p}^{n+1} + \alpha \bar{p}^{n+1} \ . \end{aligned} \tag{3.71}$$

Substituting expressions (3.71) into equations (3.70) and comparing coefficient one finds that the governing equations for $\hat{\mathbf{u}}^{n+1}$, $\bar{\mathbf{u}}^{n+1}$, $\hat{\mathbf{p}}^{n+1}$ and $\bar{\mathbf{p}}^{n+1}$ are

$$\frac{\hat{\mathbf{u}}^{n+1}-\mathbf{u}^{n}}{\Delta t}+\mathbf{G}(\hat{p}^{n+1})-\gamma_0\mathbf{L}(\hat{\mathbf{u}}^{n+1})=\sum_{q=1}^{J_i-1}\gamma_q\mathbf{L}(\mathbf{u}^{n+1-q})+\sum_{q=0}^{J_e-1}\beta_q\mathbf{N}(\mathbf{u}^{n-q})\ ,$$
$$\nabla\cdot\hat{\mathbf{u}}^{n+1}=0\ , \tag{3.72}$$

and

$$\frac{\bar{\mathbf{u}}^{n+1}}{\Delta t}+\mathbf{G}(\bar{p}^{n+1})-\gamma_0\mathbf{L}(\bar{\mathbf{u}}^{n+1})=\mathbf{e}_x\ ,$$
$$\nabla\cdot\bar{\mathbf{u}}^{n+1}=0\ . \tag{3.73}$$

Since equation (3.73) is time-independent it is solved only once, whereas equation (3.72) is solved at every time step to determine $\hat{\mathbf{u}}^{n+1}$ and $\hat{p}^{n+1}$. α^{n+1} is then calculated by solving

$$\alpha^{n+1}=\frac{Q-\int_y\hat{\mathbf{u}}^{n+1}\cdot\mathbf{e}_x\,\mathrm{d}y}{\int_y\bar{\mathbf{u}}^{n+1}\cdot\mathbf{e}_x\,\mathrm{d}y} \tag{3.74}$$

and used to find the final solution from equation (3.71). When this technique is used for a divergence-free coordinate system together with explicit treatment of the super-term $\mathbf{A}$, then the solution to $\bar{\mathbf{u}}^{n+1}$ is the same as in the Cartesian case.

Chapter 4

Laminar channel flow over active wall deformation

In this chapter the response of laminar channel flow to predetermined and discrete active wall deformation is analysed.

The overall aim of this research is to actuate turbulent flow, but it is difficult to distinguish between flow structures caused by the actuator and those arising naturally in turbulent flow. To eliminate this problem the flow response is studied in laminar flow which delivers a clear picture of the fundamental flow perturbations WDAs can induce.

Since one of the cases analysed in this chapter has parameter values which largely correspond to the ones used by Carlson *et al.* [12], the analysis will also reveal the impact of the mathematical terms that were omitted in their equations according to Luo *et al.* [73].

The response of laminar channel flow to wall deformation can also be studied using tools other than DNS. The highly-efficient triple-deck theory based on asymptotic analysis has been used by Sobey [96] to compute the flow in channels over static deformations. However, one condition for the application of asymptotic theory is that the deformation length is much larger than the channel height. In the present work it is desired to avoid this constraint so as not to restrict the explorable shape-parameter space.

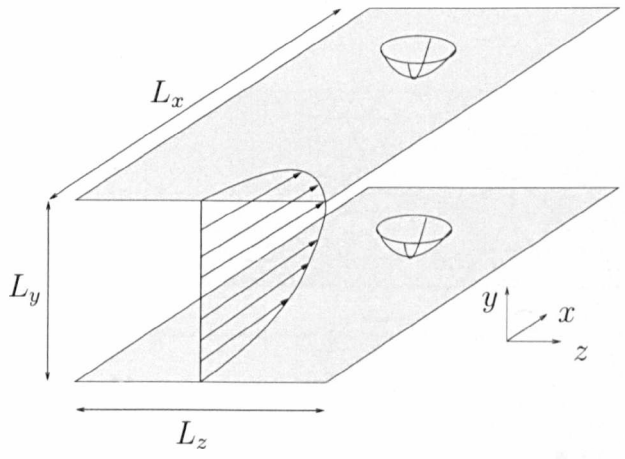


Figure 4.1: Geometry of laminar channel flow with wall actuators

All simulations feature one actuator on each wall, an active dimple at the lower wall and an active bump at the upper wall. The two actuators are identical in shape at any given time. This configuration is depicted in figure 4.1. Choosing this specific geometry facilitates usage of the highly-efficient scheme presented in section 3.1.3 since the identical shapes guarantee that the local Jacobian of a coordinate system fitted to this domain is unity everywhere. Accordingly, the y-displacement of the wall boundaries is given by

$$f := f(x, z, t) \ , \tag{4.1}$$

where the streamwise, wall-normal, and spanwise directions are denoted by x, y, and z, respectively. Note that equation (4.1) is independent of y which is a consequence of the decision that shapes of lower and upper wall must be identical.

The h-method of section 3.2.2 is applied in the (x,y)-planes by using the mesh shown in figure 4.2. It was created using the mesh generation software FELISA and consists of 1126 elements. The mesh is finest in the regions where the dimple and the bump are located. In the spanwise direction the solution is Fourier-discretised as demonstrated in section 3.3. This results in periodicity of the flowfield in the spanwise direction.

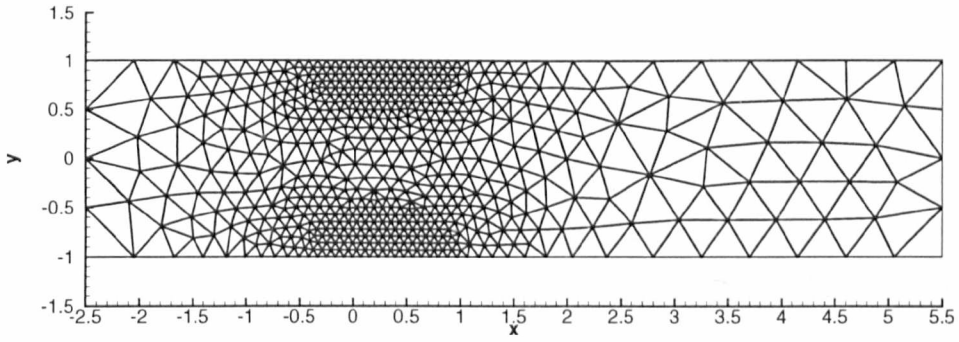


Figure 4.2: Computational mesh.

4.1 Parameters

In this section the parameters that govern the channel flow around WDAs are characterised and assigned values. In canonical channel flow the only dimensionless coefficient is the Reynolds number which can be defined in various ways. If the flow is laminar it is common to use

$$Re_{\mathrm{C}} = \frac{u_{\mathrm{C}}^* L_c^*}{\nu^*} \ , \tag{4.2}$$

with u_{C}^* and L_c^* being the streamwise velocity at mid-channel and the channel half-height, respectively. Units of velocity, length, and time are then normalised by u_{C}^*, L_c^*, and L_c^*/u_{C}^*, respectively, where the * denotes a dimensional quantity. The flow geometry has dimensions $L_x = 8$, $L_y = 2$, $L_z = \pi$, where the undeformed bottom wall is located at $y = -1$ and the undeformed top wall at $y = 1$. All other parameters are related to the wall deformation and must be defined with respect to the shape of the actuator.

The variables in the wall obstacle surface function $f(x, z, t)$ of expression (4.1) shall be separated, so that

$$f(x, z, t) = \epsilon\, T(t) X(x) Z(z) \ , \tag{4.3}$$

where ϵ is the amplitude and $h(x, z, t) = T(t)X(x)Z(z)$ the normalised shape.

The normalised time-independent shape, $X(x)Z(z)$, can be defined in various ways but depending on the treatment of the irregular boundaries, restrictions apply.

For example, the function consisting of a discrete sinusoidal wave embedded in a flat wall that was used by McKeon *et al.* [74] is discontinuous in its second-order differentiation. As will be seen in section 4.4.1, this violates the condition that the boundary is C^3-continuous when the method of section 3.1.3 is applied. To avoid this problem it was opted for Gaussian-shaped actuators which are smooth, hence infinitely differentiable. Also, figure 2.5 shows that this shape is similar to what is currently developed at the FCG, Imperial College. Moreover, it is also popular with other investigators for its smoothness [12].

The Gaussian shape is defined by

$$X(x)Z(z) = e^{\left(-\sigma_x^{-2}(x-x_0)^2-\sigma_z^{-2}(z-z_0)^2\right)} , \tag{4.4}$$

where σ_x and σ_z are the standard deviation in x- and z-direction respectively. The parameters x_0 and z_0 set the centre of the obstacle and are chosen to be $x_0 = 0.25$ and $z_0 = \pi/2$. That means the centre of the actuators is located in the middle of the domain in the spanwise direction and slightly upstream of the middle in the streamwise direction.

Of the infinite number of possible time functions two are selected for this study. One is oscillatory and given by

$$T(t) = 0.5(1 - \cos(2\pi\, Str_c\, t) , \tag{4.5}$$

where

$$Str_c = \frac{fr^* L_c^*}{u_c^*} \tag{4.6}$$

is the dimensionless frequency or Strouhal number and fr^* the dimensional frequency. An example of this motion and its first two derivatives is shown in figure 4.3 a. Often, oscillatory motion of actuators is used to create quasi-static perturbations as in the case of synthetic jets.

Alternatively, an actuator can perform individual upward or downward motions, that will be called transient motion hereafter. An analytical time function describing transient motion is

$$T(t) = 1 - e^{-\sigma_t^{-3} t^3} \tag{4.7}$$

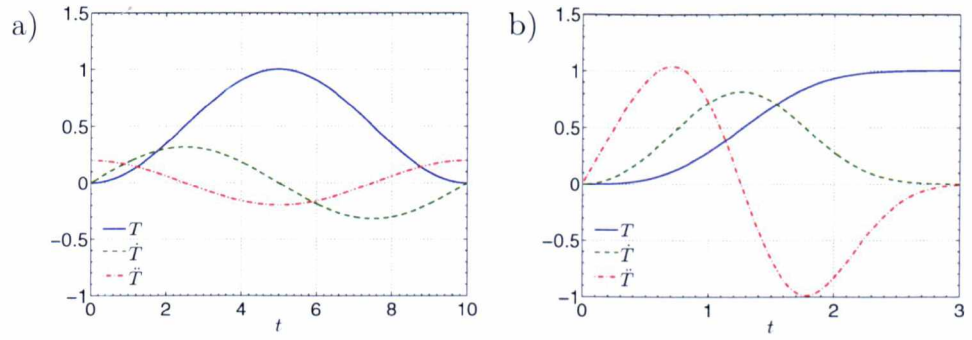


Figure 4.3: Time-dependent height $T(t)$, velocity $\dot{T}(t)$, and acceleration $\ddot{T}(t)$. a) Oscillating actuator with $Str_{\mathrm{C}} = 0.1$. b) Transient actuator with $\sigma_{t,\mathrm{C}} = 1.44$.

where

$$\sigma_{t,\mathrm{C}} = \frac{\sigma^*_{t,\mathrm{C}} u^*_{\mathrm{C}}}{L^*_c} \tag{4.8}$$

is a non-dimensional motion parameter and $\sigma^*_{t\mathrm{C}}$ a dimensional motion parameter. For the obstacles to have zero deflection, velocity, and acceleration at $t = 0$, the exponent of t in expression (4.7) was set to three. An example of this motion is shown in figure 4.3 b.

To summarise, five dimensionless parameters for channel flow over Gaussian WDAs were defined: Re, ϵ, σ_x, σ_z, and depending on the time function, Str_{C} or $\sigma_{t,\mathrm{C}}$.

Values were assigned to those parameters for three cases which are given in table 4.1. In choosing these values three issues had to be taken into account. First, parameter values had to correspond roughly to what could be necessary for skin-friction control. This requirement is difficult to quantify but it will be seen in Chapter 7 that it was achieved. Secondly, the parameter values should be such that non-linear effects take place so that linear and non-linear boundary treatment can be compared. The technique necessary for the former will be introduced in section 4.3.1 whereas the latter can be facilitated through the use of boundary-fitted coordinate systems. And finally, they should allow comparison with previous research.

The first case, Case 1, is similar to the one that was investigated by Carlson *et al.* [12]. The obstacles are transient, which means they pop down (dimple) or up

(bump) and then turn inactive, as defined in expression (4.7). With $\sigma_t = 1.44$ the actuator reaches 99% of the maximum deflection after $t = 2.4$ time units. If the time period $0 \leq t \leq 2.4$ is considered as an excursion from a minimum to a maximum of a periodic cycle then the motion of Case 1 is comparable to an oscillating motion with a frequency of $Str_C = 0.21$. The amplitude, $\epsilon = 0.12$, is sufficiently large to cause a severe test of the linearised boundary condition. With $\sigma_x = \sigma_z = 0.18$ the radius is roughly $r = 0.27$ in both directions. The other two cases, Case 2 and Case 3, are identical to Case 1 except for the form of motion. They have actuators that oscillate at Strouhal numbers of $Str_C = 0.1$ and $Str_C = 1$, respectively, as defined by expression (4.5). Further analysis of the these parameter values is provided in section 4.3.1 using the linearisation technique.

All cases share the same Reynolds number, that is $Re_C = 2000$, and the same resolution. With a 6^{th}-order polynomial expansion basis approximating the solution in each of the 1226 elements, the discretisation is sufficiently fine to achieve good accuracy. Increasing the polynomial order through the p-type method generated the same results. The order of the Adams-Bashforth time integration scheme that was used for the explicit terms was set to one, which is equivalent to an explicit Euler scheme. The viscous terms were also integrated in first order, though implicity. The large diffusive error caused by such integration was contained by keeping a very small time step.

Because the spanwise direction is Fourier-discretised, it is by definition periodic. This implies that the presence of one actuator in the computational domain translates into an infinite array of actuators in physical space. In practical terms, however, the discrete obstacles studied in the present work can be considered quasi-solitary. This is because the width of the domain is almost six times larger than the diameter of the actuators, which prohibits significant interaction between adjacent flow perturbations. In simulations not presented in this thesis it was found that in domains of reduced width the flow structures are qualitatively the same albeit more compact.

An interesting question that is not investigated in this work is the sensitivity of the flow response to the shape of the actuator. The exponential function (4.4),

Flow param		Resolution			Box size	Time integration		Flow State
Re_τ	Re_C	Nel	P	Z		Order	Δt	
63.2	2000	1126	8	36	8 x 2 x π	1	0.001	Laminar

Case	Actuator parameters									
	ϵ	σ_x	σ_z	$\sigma_{t,C}$	$\sigma_{t,\tau}$	Str_C	Str_τ	$v_{W,rms,C}$	$v_{W,rms,\tau}$	f_{rms}
1	0.12	0.18	0.18	1.44	0.05	(0.21)	(6.64)	0.060	1.9	0.071
2	0.12	0.18	0.18			0.1	3.16	0.027	0.85	0.073
3	0.12	0.18	0.18			1.0	31.6	0.267	8.44	0.073

Table 4.1: Simulation parameters. Parameter values in the upper table are common for all cases. rms values are taken at the centre of the actuators. For Case 1 rms values are computed for the time period $0 \leq t \leq 2.4$. Parameters with the symbol τ in the subscript use the friction velocity u_τ^* (expression 5.3) as reference velocity and serve comparison with table 6.1.

which was chosen for its differentiability, also offers great flexibility for modifications in shape. With σ_x and σ_z the dimensions of the actuator can easily be altered. Moreover, by changing the numeric value of the exponents one can control the steepness which probably influences the point of separation.

4.2 Vorticity generation

In the literature review actuation methods were presented that are based on cancelling vorticity flux at the wall [63] or cancelling streaks by creating streamwise vortices away from the wall [50]. One of the ideas outlined in section 2.3 was to use actively deformed walls to create such actuation. To evaluate the feasibility of this idea, the generation of streamwise vortices away from the wall and vorticity flux at the wall by actuation through WDAs is analysed. In this section the analysis is performed analytically.

First, the vorticity flux from the surface of a WDA is investigated. The analytical theory for this flow quantity was pioneered by Lighthill [68]. As shown in the

textbook by Batchelor [2] the viscous term in the momentum equation (3.2) can be reduced to

$$\frac{1}{Re}\nabla^2\mathbf{u} = -\frac{1}{Re}(\nabla \times \boldsymbol{\omega}) \ . \tag{4.9}$$

By substituting (4.9) into the equation (3.2) one gets the following expression for the normal flux of vorticity, σ_n, on a two-dimensional, passive, and non-porous wall:

$$\sigma_n = \frac{1}{Re}\left(\frac{\partial \omega}{\partial n}\right)_{\mathrm{w}} = \left(\frac{\partial p}{\partial x}\right)_{\mathrm{w}} \ . \tag{4.10}$$

In this case, apparently, the vorticity flux is proportional to the streamwise pressure gradient. (The term vorticity flux here is not to be confused with the surface integral of vorticity, also often referred to as vorticity flux.)

A more general theory taking into account wall acceleration, transpiration, and three-dimensional curvature was presented by Wu and Wu [111]. According to them, the vector of diffusive vorticity flux, $\boldsymbol{\sigma}^d$, can be split into the four constituents:

$$\begin{aligned} \boldsymbol{\sigma}^d_p &= \mathbf{n} \times \nabla p, \qquad \boldsymbol{\sigma}^d_a \ = \ \mathbf{n} \times \mathbf{a} \\ \boldsymbol{\sigma}^d_{\mathrm{vis}\,\pi} &= -(\mathbf{n} \times \boldsymbol{\tau}_{\mathrm{w}}) \cdot \mathbf{K} \\ \boldsymbol{\sigma}^d_{\mathrm{vis}\,n} &= -\mathbf{n}[\mathbf{n} \cdot (\nabla \times \boldsymbol{\tau}_{\mathrm{w}})] \end{aligned} \tag{4.11}$$

where $\boldsymbol{\tau}_{\mathrm{w}}$ is the wall skin-friction and $\mathbf{K}$ the curvature tensor, defined by $\mathbf{K} = -\nabla_\pi \mathbf{n}$ with ∇_π being the tangent component of the nabla operator and $\mathbf{n}$ the unit wall-normal vector pointing out of the fluid domain. More information regarding the relevance of each constituent is given in section 4.3.2 and 4.4.2 because their significance depends on the treatment of the boundary. If the wall is porous one also has to consider convective vorticity flux.

Next, the creation of streamwise vorticity away from the wall is considered. This is a phenomenon observed in flows penetrated by a cylinder in wall-normal direction. From the curl of the momentum equation (3.2) one obtains a relation for the total derivative of vorticity:

$$\frac{\mathrm{D}\boldsymbol{\omega}}{\mathrm{D}t} = (\boldsymbol{\omega} \cdot \nabla)\,\mathbf{u} + \frac{1}{Re}\nabla^2\boldsymbol{\omega} \tag{4.12}$$

Away from the wall, vorticity in one direction can be created by vorticity in another direction through inertial tilting and stretching. This process is represented by

the first term on the right hand side of equation (4.12). Considering only terms that contain ω_z or $\frac{\partial u}{\partial y}$, which are $O(1)$ and associated with the parabolic flow, the streamwise component becomes

$$\frac{\mathrm{D}\omega_x}{\mathrm{D}t} \approx \frac{\partial u}{\partial y}\left(\omega_y - \frac{\partial u}{\partial z}\right) . \tag{4.13}$$

The first term of expression (4.13) accounts for the streamwise turning of wall-normal vorticity and the second term for the streamwise turning of spanwise vorticity. The vorticity created by a cylinder in the wall-normal direction is dominated by the second term. The approximate equation (4.13) for the dynamic evolution of streamwise vorticity will be revisited in the flow analysis.

Another process which is known to create streamwise vorticity without requiring a base shear profile, is found in flows perturbed by a jet or synthetic jet. By causing a strong gradient of the wall-normal velocity in the spanwise direction, $\partial v/\partial z$, streamwise vorticity can emerge. However, it is expected that this process only plays a minor role in the flow response to the motion of smooth actuators. This is because the smooth shape prohibits large $\partial v/\partial z$.

4.3 Flow over linearised actuators

Before simulating the exact flow response to WDAs using boundary-fitted coordinate systems, an approximation can help to get a notion of the flow perturbations. For that, a caricature of the full flow response is suggested that models the time-dependent surface obstacles using transpiration applied at a flat wall. The streamwise velocity perturbations are determined from a Taylor expansion of the wall deflection which must counteract the baseflow contribution, while the normal velocity perturbations are determined by the speed of the wall deflection. This idea was first provided by Gaster *et al.* [37] and then numerically implemented in [53, 43]. It was also used by Fasel *et al.* [32] to predict actuator excitations of linearly-unstable laminar boundary layers. McKeon *et al.* [74] later used this technique to study the vorticity flux from active dimples. The strength of this approximation is that it reduces the complexity of the boundary by replacing the irregular wall with a flat

one which allows the use of a Cartesian coordinate system. It should be noted that with this technique the deformation of the upper and lower wall does not have to be identical. The reason they are, nevertheless, is that it facilitates comparison with the results of section 4.4 where this is required due to the use of a divergence-free coordinate system.

4.3.1 Linearisation

In this section it is shown how a moving wall can be approximated by wall transpiration. Let $\mathbf{f}_t$ be the velocity of the lower boundary given in equation (4.1). The boundary condition is that on the moving surface

$$\mathbf{u} = \mathbf{f}_t \tag{4.14}$$

with

$$\mathbf{f}_t = \begin{pmatrix} 0 \\ \epsilon \frac{\partial h}{\partial t} \\ 0 \end{pmatrix} . \tag{4.15}$$

Expanding the flow velocity $\mathbf{u}$ in terms of ϵ up to $O(\epsilon)$ yields

$$\mathbf{u} = \mathbf{u}_0 + \epsilon \mathbf{u}_1 \left(+ \epsilon^2 \mathbf{u}_2 + ... \right) . \tag{4.16}$$

By substituting expression (4.15) and (4.16) into equation (4.14) one obtains

$$\mathbf{u}_0(x, -1 + \epsilon h, z) + \epsilon \mathbf{u}_1(x, -1 + \epsilon h, z) = \begin{pmatrix} 0 \\ \epsilon \frac{\partial h}{\partial t} \\ 0 \end{pmatrix} \tag{4.17}$$

on the lower wall. The base velocity $\mathbf{u}_0$, which is defined by the Poiseuille profile, and the perturbation velocity $\mathbf{u}_1$ in equation (4.17) can then be expanded at the lower boundary about $y = -1 + \epsilon h$, so that

$$\begin{aligned} \mathbf{u}_0(x, -1 + \epsilon h, z) &= \mathbf{u}_0(x, -1, z) + \epsilon h \frac{\partial \mathbf{u}_0}{\partial y}(x, -1, z) \left(+ \frac{(\epsilon h)^2}{2} \frac{\partial^2 \mathbf{u}_0}{\partial y^2}(x, -1, z) + ... \right) , \\ \mathbf{u}_1(x, -1 + \epsilon h, z) &= \mathbf{u}_1(x, -1, z) \left(+ \epsilon h \frac{\partial \mathbf{u}_1}{\partial y}(x, -1, z) + ... \right) . \end{aligned} \tag{4.18}$$

Substituting expression (4.18) into equation (4.17) and equating all the terms of $O(\epsilon)$ yields

$$\mathbf{u}_1(x,-1,z) = \begin{pmatrix} -h\frac{\partial u_0}{\partial y} \\ \frac{\partial h}{\partial t} \\ 0 \end{pmatrix}_{y=-1} . \tag{4.19}$$

The velocity boundary condition to be imposed at the lower wall is thus

$$\mathbf{u}_{LW} = \begin{pmatrix} -\epsilon h\frac{\partial u_0}{\partial y} \\ \epsilon\frac{\partial h}{\partial t} \\ 0 \end{pmatrix}_{y=-1} , \tag{4.20}$$

which means that the streamwise component is proportional to shear stress and the wall-normal component equals the velocity of the actuator.

It is important to clarify what the term linearisation refers to. Because the fully non-linear Navier-Stokes equations are solved, the term does not imply linearisation with respect to velocity perturbation. Instead, it refers to linearisation regarding distance from the wall. This means that because the terms $O(\epsilon^2)$ are neglected, only the linear dependance of the perturbation on the amplitude is taken into account. Also, the term $\frac{\partial^2 \mathbf{u}_0}{\partial y^2}(x,-1,z)$ drops out because of this approximation. Therefore, another linearisation is the profile of the baseflow at the wall.

Without solving the flow equations for the cases given in table 4.1, the linearisation of the actuators can provide qualitative insight into the expected perturbations. The flowfield will depend on the strengths and scales of three components: baseflow, streamwise-velocity boundary perturbation, and wall-normal-velocity boundary perturbation. The three components are not independent. The streamwise velocity perturbation depends on the baseflow and both components of the boundary velocity perturbation depend on the same actuator characteristics.

In terms of spatial scales, it is assumed that the small size of the actuators results in perturbations to the baseflow that are strongest close to the centre of the actuators and weaken as they approach the middle of the domain. Under this presumption, the analysis of the components' strength is conducted close to the centre of the actuator. For that, the rms values of the centre deflection, f_{rms}, from

table (4.1) are used to substitute $-\epsilon h$ in the first component of expression (4.20). From the same table, the rms values of the centre vertical velocity, $v_{\mathrm{W,rms,C}}$, are used to substitute $\epsilon \partial h/\partial t$ in the second component of expression (4.20). The remaining term, $\partial u_0/\partial y$, is defined by the Poiseuille profile. As a result one obtains the rms fluctuations of the velocity boundary perturbation, $\mathbf{u}_{LW,\mathrm{rms}}$=(0.14, 0.06, 0), (0.15, 0.03, 0), (0.15, 0.27, 0), for Case 1, 2, and 3 respectively. These numbers reveal that only Case 3 has a wall-normal velocity perturbation that is stronger – in terms of average magnitude – than the streamwise velocity perturbation and the baseflow in the vicinity of the actuator.

For the analysis of temporal scales the local Strouhal number is considered. The local Strouhal number is based on the local Poiseuille velocity and the local distance from the wall. In laminar channel flow the relation is

$$Str_l(y) = Str_{\mathrm{C}} \frac{1}{1-y} , \tag{4.21}$$

which means that Str_l decreases with distance from the wall. Replacing Str_{C} in equation (4.21) by the values in provided in table (4.1) and using f_{rms} to substitute y, one obtains the local Strouhal number $Str_l(y = f_{\mathrm{rms}})$=2.96, 1.37, and 13.7 for Case 1, 2, and 3 respectively. So whereas the local Strouhal number is of $O(1)$ in Case 1 and 2, it is of $O(10)$ in Case 3.

To summarise, a complex flowfield made up of streamwise actuation, wall-normal actuation, and baseflow with overlapping time scales is expected in Case 1 and Case 2. In Case 3 the wall-normal velocity boundary perturbation dominates the flow and acts within time-scales unaffected by the baseflow. Naturally, the relative weight of each component changes over time. In Case 1, for example, the effect of wall-normal velocity perturbation is strongest near $t = 1.3$ whereas the effect of streamwise velocity perturbation dominates the flow when the obstacle reaches maximum amplitude. In Case 2 and Case 3, the importance of the components of velocity perturbation relative to each other is out of synchronisation due to the oscillatory motion of the obstacles.

4.3.2 Vorticity flux

By linearising the WDA, velocity perturbations are introduced to a flat, static wall. Thus, the WDA is replaced by wall transpiration and the viscous vorticity source due to wall curvature in expression (4.11) vanishes, so that

$$\boldsymbol{\sigma}^d_{\mathrm{vis}\,\pi} = 0 \; . \tag{4.22}$$

According to Wu and Wu [111] the three-dimensional vorticity sources $\boldsymbol{\sigma}_{\mathrm{vis}\,n}$ and $\boldsymbol{\sigma}_{\mathrm{vis}\,\pi}$ are small, except for critical points of separation. Since there is no separation when the boundaries are linearised,

$$\boldsymbol{\sigma}^d_{\mathrm{vis}\,n} = 0 \; . \tag{4.23}$$

By having replaced deformation with transpiration it is now also required that the diffusive vorticity flux from the wall is evaluated in the Eulerian frame. This means that the acceleration in $\boldsymbol{\sigma}^d_a$ must be decomposed into a local and a convective component, so that

$$\mathbf{a} = \frac{\partial \mathbf{u}}{\partial t} + (\mathbf{u} \cdot \nabla)\mathbf{u} \; . \tag{4.24}$$

By substituting expression (4.22), (4.23), and (4.24) into equation (4.11) the diffusive vorticity flux vector reduces to

$$\boldsymbol{\sigma}^d = \mathbf{n} \times \nabla p + \mathbf{n} \times \left[\frac{\partial \mathbf{u}}{\partial t} + (\mathbf{u} \cdot \nabla)\mathbf{u} \right] \quad , \tag{4.25}$$

at the wall. Decomposing equation (4.25) gives

$$\sigma^d_x = \left[-\frac{\partial p}{\partial z} - v\frac{\partial w}{\partial y} \right]_{\mathrm{w}} \tag{4.26}$$

for the streamwise direction and

$$\sigma^d_z = \left[\frac{\partial p}{\partial x} + u\frac{\partial u}{\partial x} + v\frac{\partial u}{\partial y} \right]_{\mathrm{w}} \tag{4.27}$$

for the spanwise direction. This can also be expressed in rotational form as

$$\sigma^d_x = \left[-\frac{\partial p}{\partial z} + u\omega_y - v\omega_x - u\frac{\partial u}{\partial z} - u\frac{\partial v}{\partial z} \right]_{\mathrm{w}} \tag{4.28}$$

and

$$\sigma^d_z = \left[\frac{\partial p}{\partial x} - v\omega_z + w\omega_y + u\frac{\partial u}{\partial x} + v\frac{\partial v}{\partial x^1} \right]_{\mathrm{w}} \; . \tag{4.29}$$

Equation (4.28) is more complete than corresponding ones in [74] and [12] where the local tangential velocity at the wall was neglected.

In the case of wall-normal transpiration, vorticity enters the domain not only diffusively but also through convection and tilting. Therefore, a convective vorticity flux has to be added to the diffusive vorticity flux to determine the total vorticity flux. Using the vorticity equation (4.12) the total vorticity flux in the streamwise direction is given as

$$\sigma_x = \sigma_x^d + [v\omega_x - u\omega_y]_{\mathrm{w}}, \tag{4.30}$$

and

$$\sigma_z = \sigma_z^d + [v\omega_z - w\omega_y]_{\mathrm{w}} \ . \tag{4.31}$$

in the spanwise direction.

As such, equations (4.30), and (4.31) together with (4.26) and (4.27), cannot be used to cancel vorticity flux because they lack closure. Instead they depend on flow quantities that are not known *a priori*. In order to determine the actuator parameter values necessary to induce a desired vorticity flux at the wall, an explicit closed formulation must be found. Using a formulation based on Lighthill's conceptual model of vorticity generation at the wall [68], Koumoutsakos [63] obtained the magnitude of wall transpiration necessary to manipulate the vorticity field in a desired way. In principal, an equivalent relation can also be derived for wall deformation. This is pursued next.

Following Lighthill, the generation of vorticity flux at the wall is considered in terms of a fractional step algorithm. The algorithm considers the evolution of the vorticity field in discrete viscous and inviscid substeps. The enforcement of the tangential velocity boundary condition provides a link between the inviscid and viscous descriptions of the flow in terms of the vorticity field. Specifically, vorticity appears at the surface continuously, in the right measure to maintain the tangential velocity boundary condition (without wall velocities this condition becomes the no-slip condition). A two-dimensional example is presented next.

First, the effect of the wall-normal velocity perturbation is analysed. According to Lighthill's model, there is a slip velocity $u_{\mathrm{slip}\,v}$ at the wall for an instant due to

the vertical blowing and suction. This quantity can be determined by inviscid flow theory and accounts for circulation over an elementary wall segment of $\partial\Gamma = u_{\text{slip}\,v}\partial x$. This spurious slip velocity is then nullified via the diffusive generation of vorticity at the wall. The amount of circulation that enters the flow over each time step over each segment is then $\partial\Gamma$ and is related to a vorticity flux as $\partial\Gamma = -\sigma\ \partial t\ \partial x$. Thus the instantaneous vorticity flux at each location over the wall caused by the transpiration is expressed as:

$$\sigma_v = \frac{u_{\text{slip}\,v}}{\partial t}. \tag{4.32}$$

To link the slip velocity $u_{\text{slip}\,v}$ to the vertical wall velocity, v_{W}, inviscid theory is used. According to potential theory [109], one can model the vertical wall velocity by a source sheet $q(x)$. It can be shown that the velocity directly above the source sheet is

$$v(x, 0_+) \approx \frac{q(x)}{2}\ . \tag{4.33}$$

Therefore, the strength of the source sheet has to be $q(x) = 2v_{\text{W}}$. Using this to determine the stream function, differentiating it by y, and setting $y = 0$, provides the tangential velocity on the wall induced by the source sheet:

$$u_{slip\,v} = \frac{1}{\pi}\int_{-\infty}^{\infty} \frac{v_{\text{W}}}{x-\xi}\partial\xi\ . \tag{4.34}$$

The vorticity flux over ∂t at the wall due vertical wall velocity is then

$$\partial t\ \sigma_v = \frac{1}{\pi}\int_0^c \frac{v_{\text{W}}}{x-\xi}\partial\xi\ , \tag{4.35}$$

with v_{W} given by equation (4.20).

For the case in which wall perturbation velocity represents the linearised wall motion, a slip velocity is also created by the streamwise wall velocity u_{W}. This is because u_{W} is part of the viscous substep as it would violate the impermeability condition in potential flow. Hence, the vorticity flux over ∂t at the wall due to horizontal wall velocity is

$$\partial t\ \sigma_u = u_{\text{W}}\ , \tag{4.36}$$

where u_{W} is also given by equation (4.20). Finally, by adding $\partial t\ \sigma_v$ and $\partial t\ \sigma_u$ one obtains the total incremental vorticity flux, $\partial t\ \sigma$.

Considering that this can easily be extended to three dimensions, it is obviously possible to find an explicit formulation relating wall deformation and vorticity flux. Such a formulation could be used to control turbulent flow by cancelling the vorticity flux with wall deformation. In light of the 40% drag reduction reported in [63], this seems to be a promising approach at first. But, as mentioned in section 2.3, significant problems arise. One problem is that a baseflow, which is necessary to determine the streamwise velocity perturbation, does not exist in turbulence due to the instantaneous nature of the flow. Approximations, which could be made by using time-averaged profiles, would introduce additional errors. Another problem is that the linearisation of wall deformation is only valid for very small deflections.

4.3.3 Flow analysis

The flow response to transient as well as oscillating motion of WDAs was simulated using the linearising technique presented in section 4.3.1. Whereas the results of the transient case, Case 1, are presented in detail the discussion of the oscillating cases, Case 2 and Case 3, is brief and limited to time-averaged structures. A more comprehensive analysis of laminar channel flow over oscillating WDAs is given in the next chapter, where the obstacles are treated exactly through using boundary-fitted meshes. In general the analysis is focused on the region close to the actuators. It will be shown in Chapter 7 that this is the region the actuator is supposed to control. For another analysis of vorticity and vorticity flux over oscillating dimples approximated by the linearised velocity boundary condition, the reader is referred to McKeon *et al.* [74].

4.3.3.1 Case 1: Transient motion

The results for Case 1 of table 4.1 are shown as time sequences in figures 4.5 to 4.11. The last picture of each sequence depicts the flow perturbation at $t = 7$, which represents the quasi-static case of a passive obstacle where transient effects have widely decayed, especially in close proximity to the actuator. The percentage beneath each frame refers to how far the actuator has moved relative to final deflection. Because of

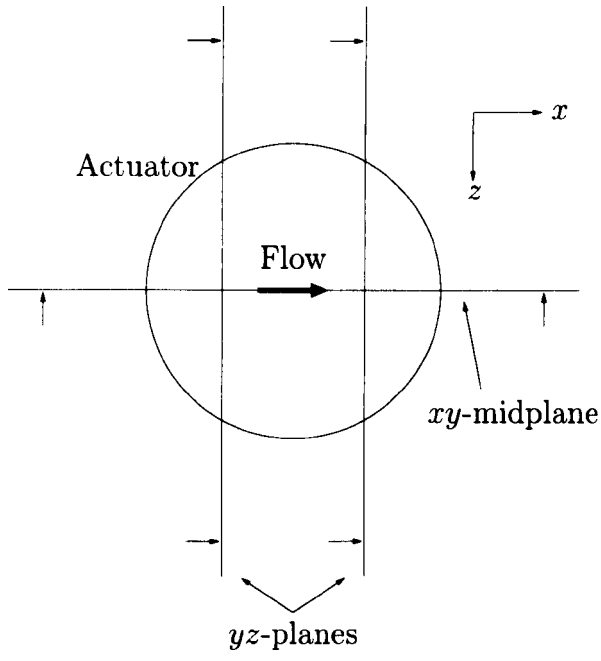


Figure 4.4: Planes of flowfield.

the three-dimensionality of the problem the general flow-perturbation structures are analysed using iso-surfaces. These surfaces are shown for streamwise, wall-normal, and spanwise velocity in figures 4.5, 4.7, and 4.9, respectively. For a more quantitative analysis, velocity contours in planes cutting through the flowfield are plotted in figures 4.6 and 4.8. These planes either extend into the x and y-directions and go through the centre of the obstacles or they extend in the y and z-directions at some location in x. The location of these planes is shown in figure 4.4. Apart from velocity plots, streamwise-vorticity iso-surfaces are shown in figure 4.11, spanwise-vorticity flux in figure 4.11, and wall pressure in figure 4.10.

For the sake of brevity most figures only show the flow around the active dimple, which is located on the lower wall. Some of the contour plots, however, extend over the whole y-range and therefore also include the region around the active bump. The reader should also note that in most cases it is the perturbation streamwise velocity from the baseflow, u', that is analysed and not the total streamwise velocity u.

The most general observation in the analysis of Case 1 is that two fundamental

states can be distinguished. One is where the vertical movement of the actuator dominates the flow, as seen in the third picture of each sequence, and the other is where the static deformation dominates the flow, as seen in the last picture of each sequence. Heuristically, the response in-between those states can be considered as a combination of the responses at those states.

The first state can be clearly recognised in the third frame of figure 4.7, which is showing an iso-surface of v. Due to the downward motion a single lobe of negative wall-normal velocity develops around the dimple. Because of the simplicity of this nearly-spherical shape, the structure holds promise as a possible actuation mechanism for intuition-based flow control. In the third frame of figure 4.8, which shows contours of v in the midplane, the same shape can be observed for a range of contour levels. The frame also reveals that the perturbation is largest close to the wall as was expected from the scales of the obstacle. Symmetry and continuity demand that during the motion phase the flow is drawn into the dimple not only from above but also from the sides. Looking at the third frame in figure 4.9, which is showing iso-surfaces of w, this appears to be the case. The same applies to streamwise velocity in figure 4.5 albeit superposed by some early effects of deformation.

The second state can be well identified in the last frame of figure 4.5 where $t = 7$. At this time, four time units have elapsed since the obstacles reached maximum deflection. As a result, transient flow structures around the actuators have widely decayed. The dimple is surrounded by a single lobe of positive u' which can be anticipated from the boundary condition. Accordingly, the lobe is largest at this time because it grows with deformation. The contour plots in figure 4.6 show the streamwise velocity in the mid-plane. In the last frame the most perturbed area is again, as expected, close to the wall. The sequence shows how towards the static case the structure is stretched in the streamwise direction reflecting the baseflow profile. Iso-surfaces of v in the last frame of figure 4.7 confirm the intuitive notion that the fluid is going in and out of the dimple as it flows downstream. At the same time the fluid is drawn in from the sides upstream of the centre and expelled to the sides downstream of the centre, as shown by iso-surfaces of w in the last frame of figure 4.9. This dynamical behaviour is also in accordance with intuition. For

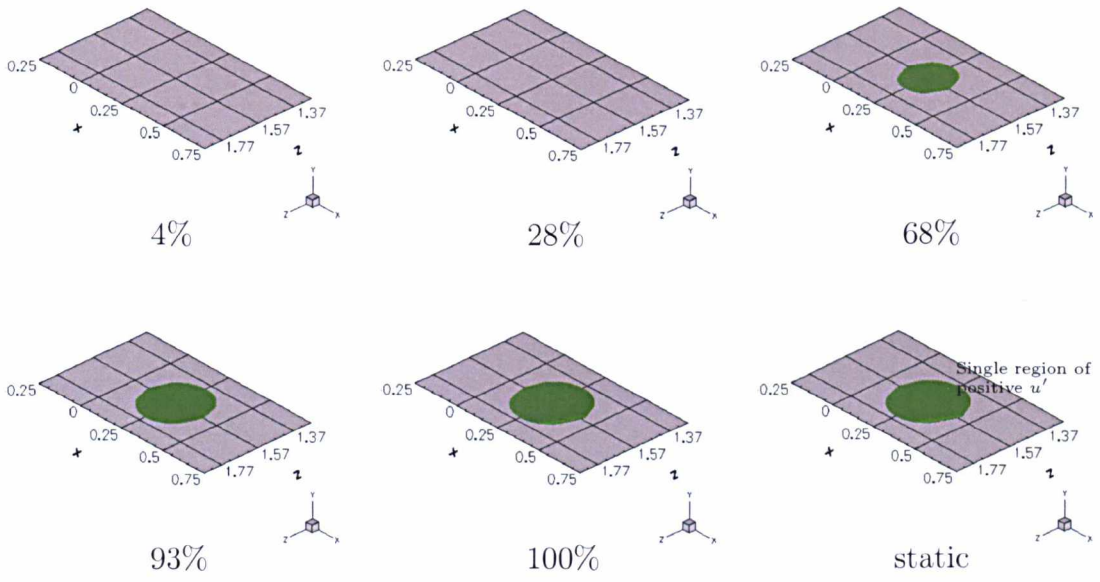


Figure 4.5: Case 1: (u'=0.1)-iso-surfaces around dimple. t = 0.5, 1, 1.5, 2, 3, 7.

reasons of symmetry there is no spanwise flow across the midplane.

In the contour plots of figures 4.6 and 4.8 it can be seen that the bump creates a similar disturbance of opposite sign. The differences can be attributed to the non-linearity in the Navier-Stokes equation.

Contours of constant pressure on the lower wall are shown in figure 4.10 for the motion and the static case. In the latter, shown on the right, the pressure is dropping upstream, rising fast over the front of the dimple, reaching a maximum just behind the lowest point and then dropping back to zero downstream. To the sides of the peak line the same trend emerges, but is less accentuated. In the motion case the pressure perturbation is significantly higher. It is negative upstream of the centre and positive downstream with peaks located close to the edge of the dimple.

In general, intuition and simple arguments of symmetry and continuity suffice to predict velocity reasonably well. Streamwise vorticity, on the other hand, is more complex and less intuitive. Figure 4.11 reveals a pattern of two strong pairs of counter-rotating streamwise vorticity regions, one upstream and one downstream of the centre. While the dimple is moving down, the upstream region of streamwise

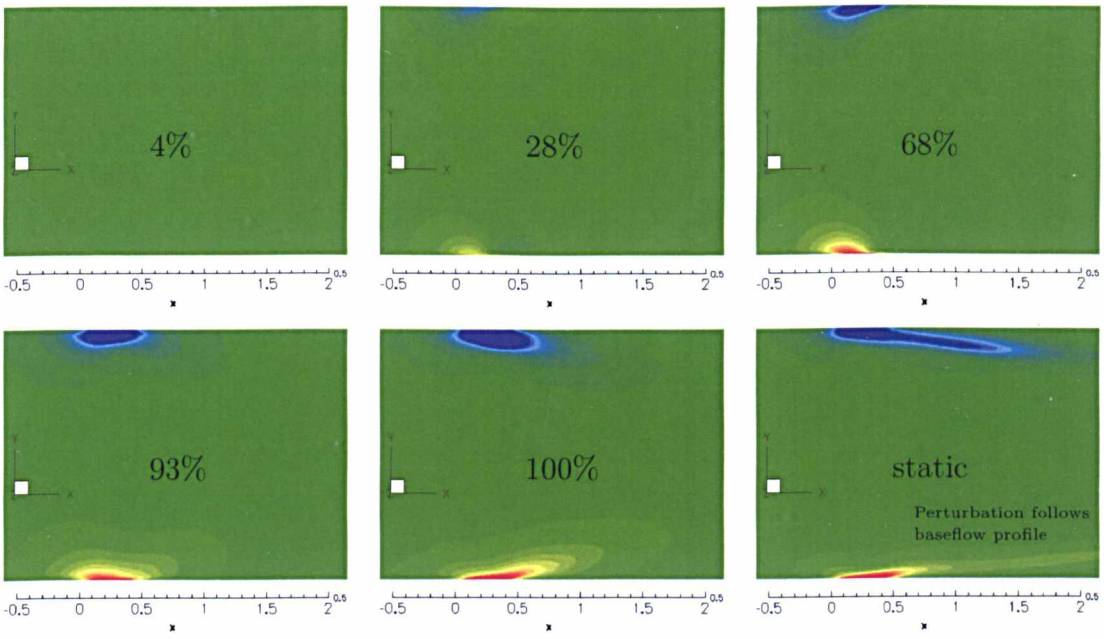


Figure 4.6: Case 1: (-0.1≤u'≤0.1)-contours in xy-midplane. t = 0.5, 1, 1.5, 2, 3, 7.

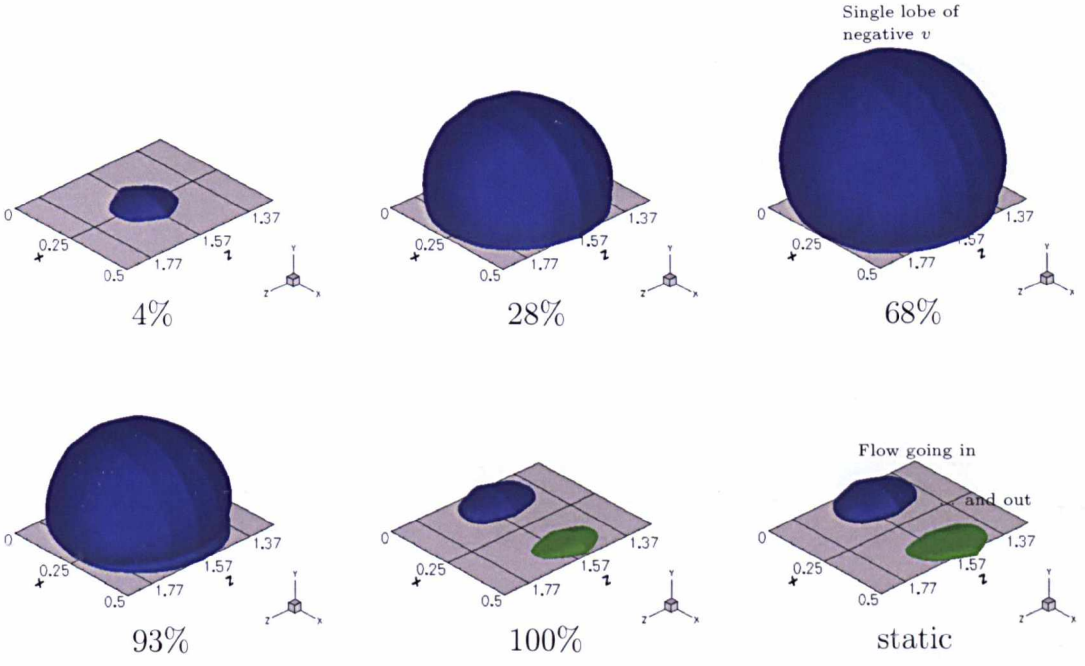


Figure 4.7: Case 1: (v=±0.01)-iso-surfaces around dimple. t = 0.5, 1, 1.5, 2, 3, 7.

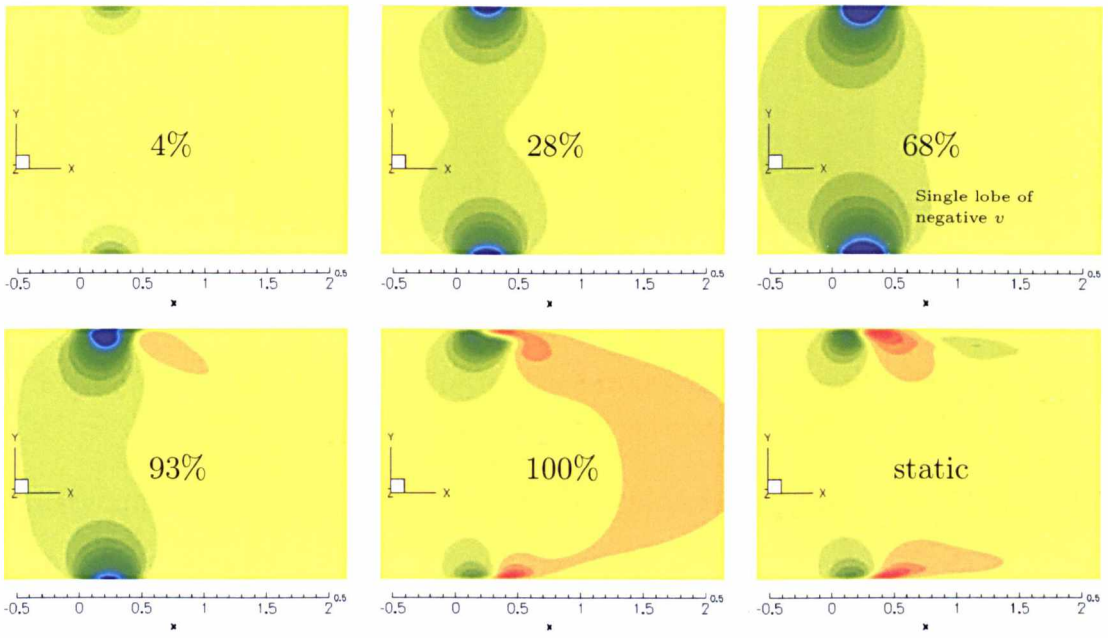


Figure 4.8: Case 1: (-0.07≤v≤0.02)-contours in xy-midplane. t = 0.5, 1, 1.5, 2, 3, 4, 5, 6, 7.

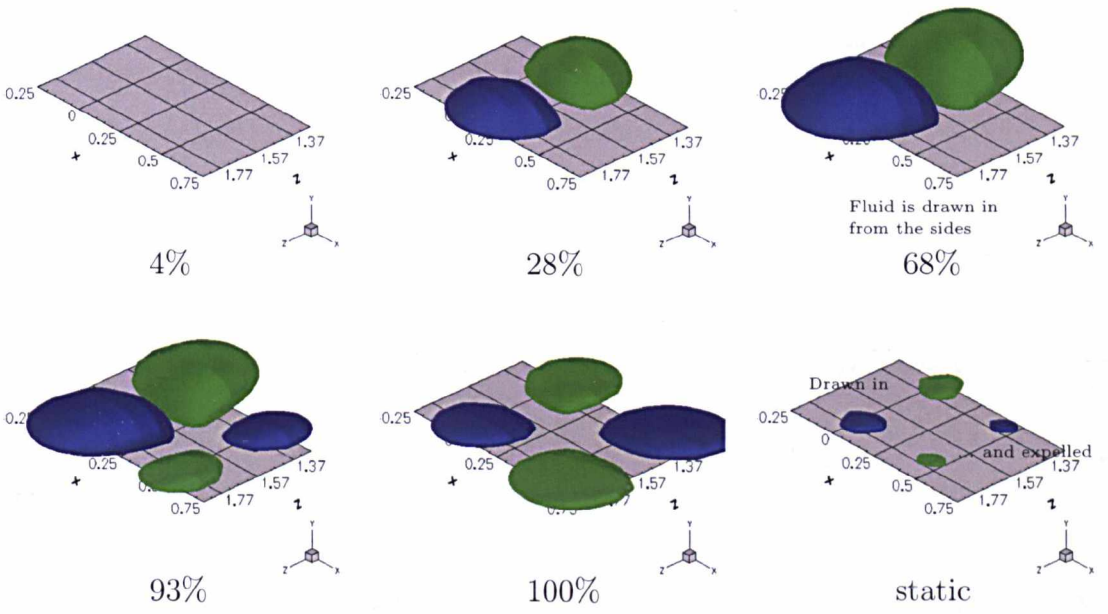


Figure 4.9: Case 1: (w=±0.01)-iso-surfaces around dimple. t = 0.5, 1, 1.5, 2, 3, 7.

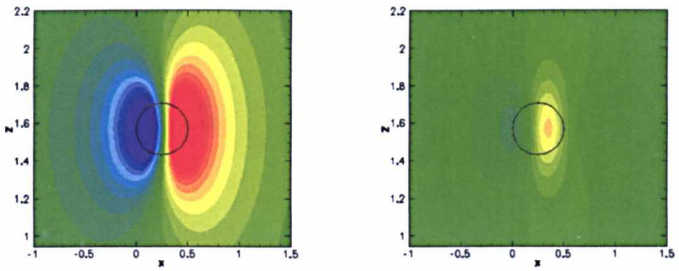


Figure 4.10: Case 1: (-0.01≤p≤0.01)-contours on lower wall. Circle shows approximately where dimple is located. $t = 1.5$ and 7.

vorticity appears first and is then followed by the downstream region. Both regions result from vorticity transport through the wall.

At all times the perturbation of streamwise vorticity is located very close to the wall. To reveal the structures in the plots it was necessary to stretch them by a factor of three in normal direction. Also, the perturbation extends further tangentially than vertically. Both features are noticeably different to the perturbation caused by a strong jet which mainly comprises a compact streamwise vortex pair away from the wall. The reason for this difference lies in the distribution of the actuation. Whereas a strong jet has a velocity profile that is almost uniform and has strong gradients at the edges, the profile generated by a smooth WDA is also smooth. The resulting gradient is weaker but of larger extent and causes the streamwise vorticity to be near the wall and to be spread out.

In section 4.2 a mechanism was discussed by which a cylinder placed normal to the flow turns existing spanwise vorticity in the streamwise direction. Though dimples also generate vorticity through turning, the effect is relatively weak. The little lobes away from the wall appearing at $t = 2$ (93%) are due to this process but negligible compared to the vorticity coming from the wall. The sign of these lobes reflect that the flow is accelerated over the dimple.

From this discussion it can be concluded that the transient Gaussian actuators of Case 1 cannot be used to create pairs of streamwise vorticity the way jets or cylinders do. It must be inferred that such observations are less likely for non-smooth actuators for which generation of vorticity is dominated by the sharp edges. It must

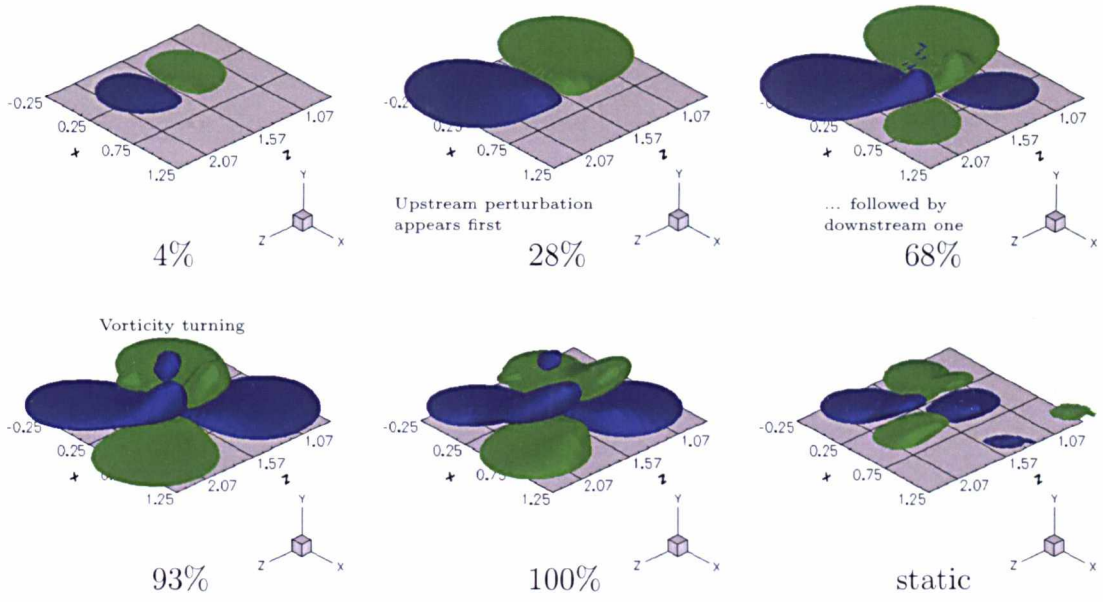


Figure 4.11: Case 1: (ω_x=$\pm$0.1)-iso-surfaces around dimple. $t = 0.5, 1, 1.5, 2, 3, 4, 5, 6, 7$. The y-axis has been stretched by a factor of three.

be stressed that such observations are less likely for non-smooth obstacles. For example, passive spherical dimples have been shown to create streamwise vortices [69].

The contours of streamwise vorticity also show the influence of the baseflow and the deformation at the moving state, despite the dominance of the wall-normal-velocity perturbation. If the same experiment was conducted without baseflow, the ω_x-structure at $t = 1.5$ (68%) would reduce to a single counter-rotating streamwise vorticity pair.

In section (4.3.2) it was shown how an explicit formulation of the vorticity flux from linearised deformed boundaries can be derived that could be used for control based on the cancellation of vorticity flux at the wall. Since it is unknown how such a formulation could be obtained for accurately modelled boundaries, it is investigated how the well the linearised case predicts the vorticity flux in the non-linear regime. Figure 4.12 shows the total spanwise vorticity flux from the dimple as defined in equation (4.31). In the dynamic evolution of this quantity a simple time-dependent pattern transpires : First there is a negative region upstream and positive one

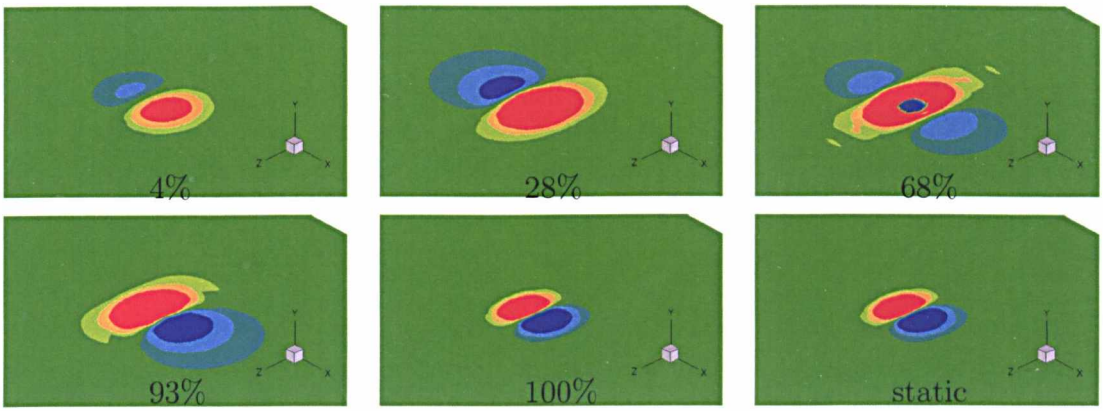


Figure 4.12: Case 1: Contours of total spanwise vorticity flux, σ_z, between -0.04 and 0.04 in the xy-midplane. $t = 0.5, 1, 1.5, 2, 3, 4, 5, 6, 7$.

downstream of the centre of the dimple. At $t = 1.5$ (68%) this pattern is extended by another negative region downstream of the positive region. The upstream negative region then vanishes at $t = 2$ (93%). To determine the accuracy of this result, these contours will be compared to the contours of another simulation in section 4.4.3.1, where the parameter values are identical but the boundaries are treated exactly through application of a boundary-fitted mesh.

4.3.3.2 Case 2 and 3: Oscillating motion

High-frequency oscillation of actuators often aims at introducing quasi-static structures into the flow. In the case of synthetic jets this is a pair of streamwise vortices which can be used for control purposes. An interesting question is whether oscillating WDAs can also produce quasi-static flow features.

Figure 4.13 shows time-averaged streamwise-vorticity iso-surfaces around dimples. The middle frame corresponds to Case 2 ($Str_C = 0.1$) and the right frame to Case 3 ($Str_C = 1.0$). For comparison the result from another simulation is shown in the left frame, where the dimple is fixed at half the amplitude. This shape is equal to the time-averaged shape of Case 2 and Case 3. The qualitative ω_x-structures in the left and the middle frame are alike. As described in the last section, it consists of two pairs of counter-rotating streamwise vorticity regions stacked on top of each other, one beginning upstream and the other downstream of the centre of the dimple.

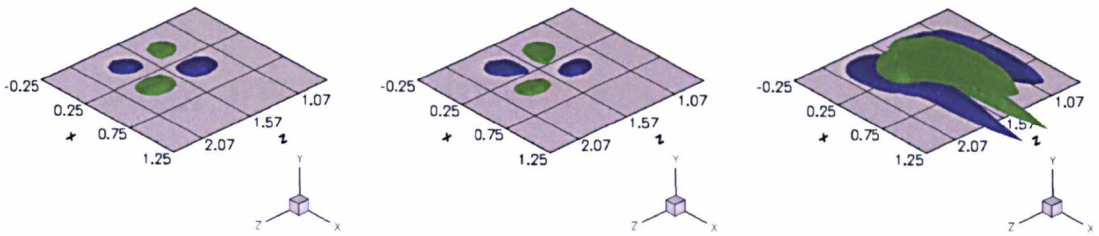


Figure 4.13: Case 2 and 3: Time-averaged (ω_x=$\pm$0.2)-iso-surfaces around dimple for different frequencies. The y-axis has been stretched by a factor of three.

This qualitative similarity is not surprising considering that the flow into the dimple and the flow out of the dimple are governed by the same physical processes. This implies that structures created by the downward motion cancel structures created by the upward motion. As a result, the net effect of the active dimple in Case 2 is mainly attributable to its time-averaged deflection.

In the right-hand frame, where the dimple is oscillating at ten times the frequency of Case 2, a different structure emerges which can be best described as a pair of counter-rotating streamwise vorticity regions. It seems that with the increased frequency the outflow has become more directed than the inflow, similar to a synthetic jet. An alternative explanation for this phenomenon could be stronger turning of pre-existing spanwise vorticity.

A time-resolved analysis of flow over oscillating dimples is given in section 4.4 where the boundaries are treated exactly. The principal reason for using linearised boundary conditions to study the quasi-steady structures is that the fixed domain allows easy computation of time-averaged flowfields.

4.4 Flow over non-linear actuators

Having studied the approximate effect of time-dependent WDAs on laminar channel flow it is now attempted to study this problem without linearising the WDAs. A technique for exact treatment of time-dependent curvilinear boundaries is the use of boundary-fitted coordinate systems. The general mathematical frame for this technique was presented in section 3.1.2. As laid out at the beginning of this chapter, the problem is studied efficiently by placing identical and synchronised WDAs at the upper and lower wall. Each mesh element size then equals its Cartesian counterpart. As a result, the Jacobian of the coordinate system is unity everywhere and the use of the scheme presented in section 3.1.3 becomes possible.

The question that arises when actuators are placed on both walls is how much the perturbation created at one wall affects the perturbation on the other wall. If this effect is considerable, then the results could not be extrapolated to single-sided channel control which approximately resembles the case of boundary-layer control. To answer this question, two-dimensional simulations are presented in section A.3 where the actuator at the upper wall is removed. As will be seen, interaction does occur but is modest relative to the perturbation.

4.4.1 Coordinate system

This section contains the expansion of the super-term A^i of expression (3.34) for the geometry shown in figure 4.1. The transformation is defined by the relations

$$\begin{aligned} \tau &= t \\ \xi &= x \\ \eta &= y - f(x,z,t) \\ \zeta &= z\,. \end{aligned} \tag{4.37}$$

As mentioned before, f is independent of y due to the identical and synchronised deformation of upper and lower wall. The contravariant velocities then transform

according to

$$\begin{aligned} u &= U \\ v &= V - f_x U - f_z W \\ w &= W \ . \end{aligned} \tag{4.38}$$

Figure 4.14 shows an example of this vector transformation for the geometry under investigation.

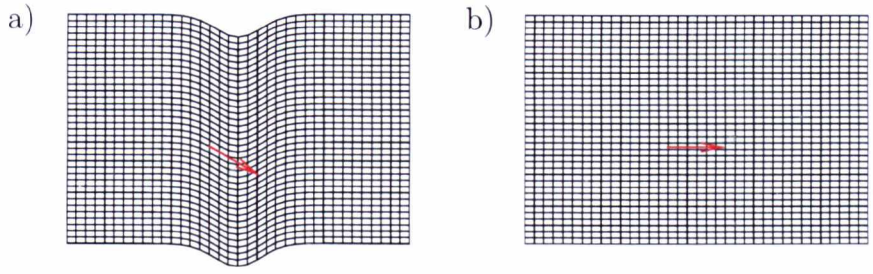


Figure 4.14: Transformation of a vector in the xy-midplane. a) Cartesian coordinate system. b) Boundary-fitted coordinate system.

In a general time-dependent curvilinear-coordinate system the velocity of the moving coordinates would need to be specified at the boundaries. This means that the left-hand sides of the elliptic equations of the splitting scheme would have to be updated every time step. This would inherently slow down the computation. To avoid these extra costs the vertical contravariant velocity in the curvilinear system, V, is transformed to the new velocity $\tilde{V}$ according to

$$\tilde{V} = V - f_t \ . \tag{4.39}$$

By using this new velocity $\tilde{V}$, which is zero at the wall, updating the left-hand-side of the elliptic equations is not required anymore. Moreover, this transformation leaves the continuity equation unaffected as the coordinate system is divergence-free. Transforming equation (3.22) by substituting according to expression (4.39) one obtains for A^i:

$$A_\xi = p_\eta f_\xi + \frac{1}{Re}(- 2U_{\xi\eta} f_\xi - U_\eta f_{\xi\xi} + U_{\eta\eta} f_\xi^2 - 2U_{\zeta\eta} f_\zeta - U_\eta f_{\zeta\zeta} + U_{\eta\eta} f_\zeta^2) \tag{4.40}$$

$$A_\zeta = p_\eta f_\zeta + \frac{1}{Re}(- 2W_{\zeta\eta} f_\zeta - W_\eta f_{\zeta\zeta} + W_{\eta\eta} f_\zeta^2 - 2W_{\xi\eta} f_\xi - W_\eta f_{\xi\xi} + W_{\eta\eta} f_\xi^2) \tag{4.41}$$

$$\begin{aligned} A_\eta = {} & p_\xi f_\xi - p_\eta f_\xi^2 + p_\zeta f_\zeta - p_\eta f_\zeta^2 \\ & - U^2 f_{\xi\xi} - W^2 f_{\zeta\zeta} - 2UW f_{\xi\zeta} \\ & - 2U f_{\tau\xi} - 2W f_{\tau\zeta} - f_{\tau\tau} \\ & + \frac{1}{Re}(-2\tilde{V}_{\xi\eta} f_\xi - \tilde{V}_\eta f_{\xi\xi} + \tilde{V}_{\eta\eta} f_\xi^2 + U f_{\xi\xi\xi} + 2U_\xi f_{\xi\xi} \\ & \quad - 2U_\eta f_\xi f_{\xi\xi} + W f_{\xi\xi\zeta} + 2W_\xi f_{\xi\zeta} - 2W_\eta f_{\xi\zeta} f_\xi \\ & \quad - 2\tilde{V}_{\zeta\eta} f_\zeta - \tilde{V}_\eta f_{\zeta\zeta} + \tilde{V}_{\eta\eta} f_\zeta^2 + W f_{\zeta\zeta\zeta} + 2W_\zeta f_{\zeta\zeta} \\ & \quad - 2W_\eta f_\zeta f_{\zeta\zeta} + U f_{\zeta\zeta\xi} + 2U_\zeta f_{\xi\zeta} - 2U_\eta f_{\xi\zeta} f_\zeta \\ & \quad + f_{\tau\xi\xi} + f_{\tau\zeta\zeta}) \, . \end{aligned} \tag{4.42}$$

By writing out the components it becomes apparent how many more terms there are in the equations compared to the ones for Cartesian coordinates. The terms highlight the more intricate coupling compared to the linearised analysis. It also shows that the surface should be C^3 continuous to avoid discontinuities in A which explains the preference for Gaussian functions. In terms of numerical implementation it should be noted that some terms are cubic which needs to be considered with respect to dealiasing.

4.4.2 Vorticity flux

When the irregular boundaries are treated exactly, no constituents of diffusive vorticity flux vanish. This means that all terms in expression (4.11) are non-zero. According to Wu and Wu [111] the three-dimensional vorticity sources $\boldsymbol{\sigma}_{\text{vis}n}$ and $\boldsymbol{\sigma}_{\text{vis}\pi}$ are small, except for critical points of separation. But apart from this hint, it

is difficult to predict the weight of each term since they are not independent of each other. For instance, a change in acceleration, which only features in $\boldsymbol{\sigma}_a$, will also affect the pressure, which features in $\boldsymbol{\sigma}_p$.

Special attention must be paid to the acceleration term. Because the actuator is moving relative to the rest of the domain, it is the equation in Lagrangian frame that should now be used to find the vorticity flowing from its surface. Therefore, the acceleration, $\mathbf{a} = \partial \mathbf{u}_W / \partial t$, must not be further decomposed into local and advective acceleration, as was done in equation (4.24) for the case of linearised actuators.

An exact analytical explicit formulation linking actuation strength and vorticity flux from the moving boundary, as derived in section 4.3.2 for linearised boundaries, could not be found with exact treatment of the boundaries.

4.4.3 Flow analysis

The same cases as in section 4.3 are analysed with the parameter values given in table 4.1. The actuators are Gaussian in shape and either oscillatory or transient in motion. The results should help identify features of the flow response that could prove useful in finding control methods. Moreover, comparison with results by Carlson *et al.* [12] will highlight the importance of the mathematical terms describing the motion of the coordinate system that they omitted according to Luo *et al.* [73].

Oscillating actuators are revisited despite the lack of quasi-static perturbation structures observed in the previous simulations. The reason for this is the attention these type of actuators continue to receive in numerical [74] and experimental [65, 17] investigations .

4.4.3.1 Case 1: Transient motion

Recall that Case 1 of table 4.1 is similar to the problem studied by Carlson *et al.* [12] where the actuator was in transient motion. One difference is that in the present case the acceleration is smooth and does not exhibit any jumps, as shown in figure 4.3. This avoids discontinuities in the forcing terms (4.40), (4.41), and (4.42), and reduces the truncation error. In simulations not presented here it was verified that

smoothing the acceleration makes no substantial difference to the results. Another difference in the configuration of Carlson *et al.* was their flow geometry which was periodic in the streamwise direction and featured an obstacle on the lower wall only.

Results are shown in figures 4.15 to 4.29. As before the frames in each sequence refer to different points in time and the percentage next to each plot refers to how far the actuator has moved relative to final deflection. The quantity u' denotes again the perturbation streamwise velocity from the baseflow.

In general the results are strikingly similar to the ones shown in figures 4.5 to 4.11 where the actuators were linearised. In particular, the moving state and the stationary state, which were introduced in section 4.3.3.1, can still be recognised. This observation justifies retaining the distinction of these two states.

The moving state represented by the third picture of each sequence and characterised by a dominant vertical velocity is much less influenced by exact boundary treatment than the passive state, shown in the last picture of each sequence. A new non-linear effect is the appearance of a separation bubble inside the static dimple. This can be seen in the last frame of figure 4.18 where the separation prevents downward motion of the fluid upstream of the centre. The bubble can be best recognised in the right frame of figure 4.20, where the streamlines curl up inside the static dimple. Naturally, this type of separation cannot exist in the moving state as the moving boundary acts as a sink of streamlines. The exact treatment of the boundaries in the passive state also manifests itself in higher u' downstream of the dimple, less upward movement after the peak of the bump, and less spanwise flow around the dimple. In the moving state differences are so little that a discussion is omitted. But the differences would be expected to strengthen with increasing actuation velocity.

Similar to the dimple, the bump exhibits separation only in the stationary but not in the moving state, see figure 4.21. The streamlines around the passive bump reveal the same pattern as described by Carlson *et al.* [12] in figure 6. This is expected as their missing terms did not affect simulations in fixed coordinate systems.

By calculating the product

$$\boldsymbol{\tau}_{\mathrm{W}} = \mathbf{n} \cdot [\boldsymbol{\tau}] \tag{4.43}$$

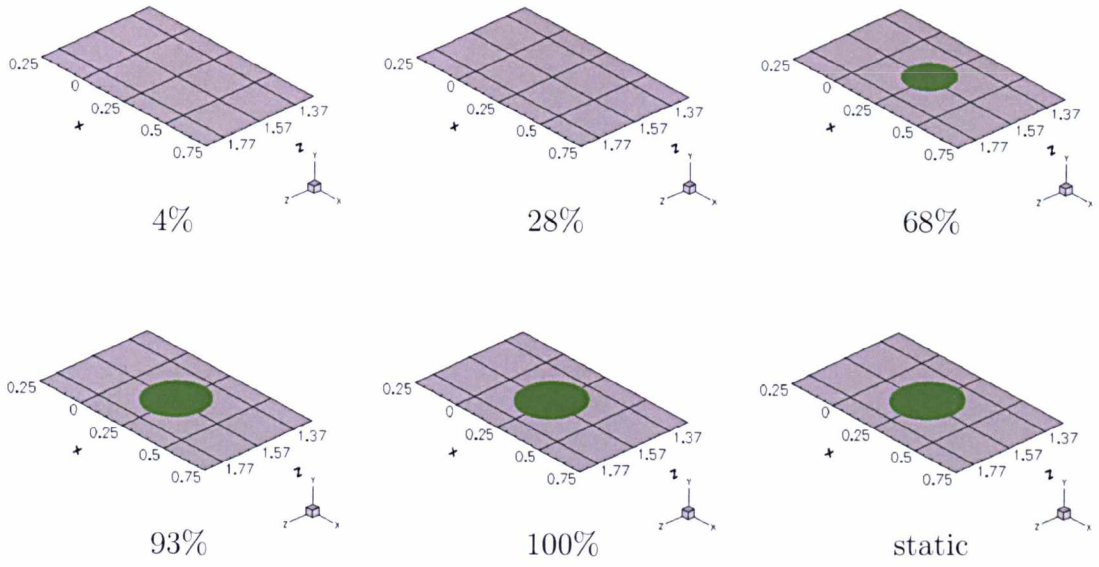


Figure 4.15: Case 1: ($u'=\pm 0.1$)-iso-surfaces around dimple. t = 0.5, 1, 1.5, 2, 3, 7.

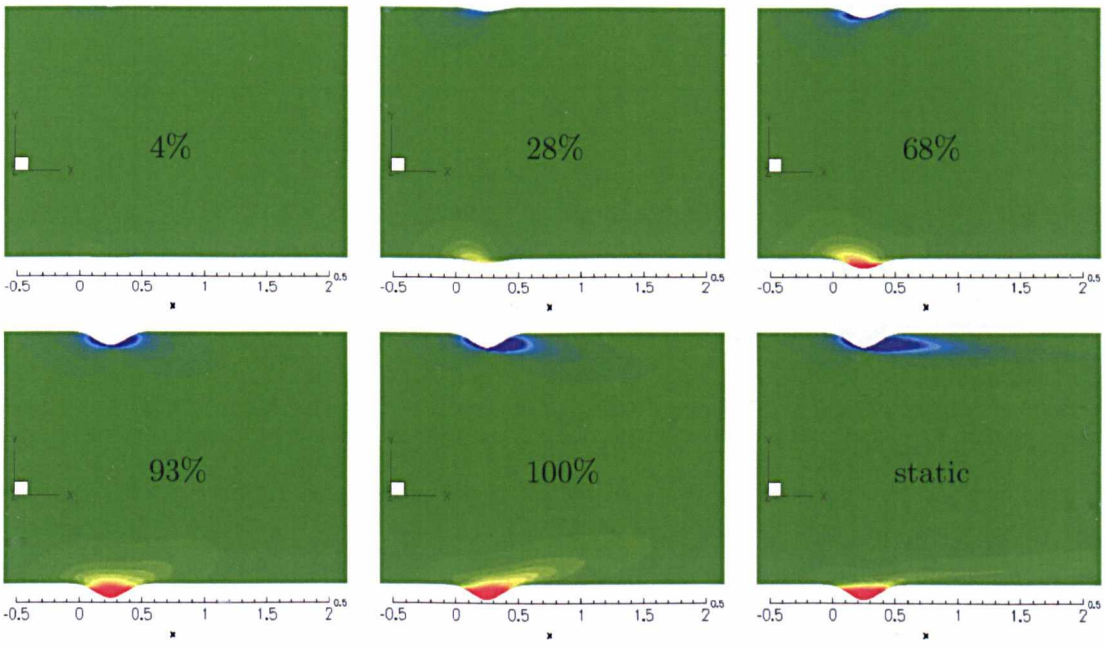


Figure 4.16: Case 1: ($-0.1 \leq u' \leq 0.1$)-contours in xy-midplane. t = 0.5, 1, 1.5, 2, 3, 7.

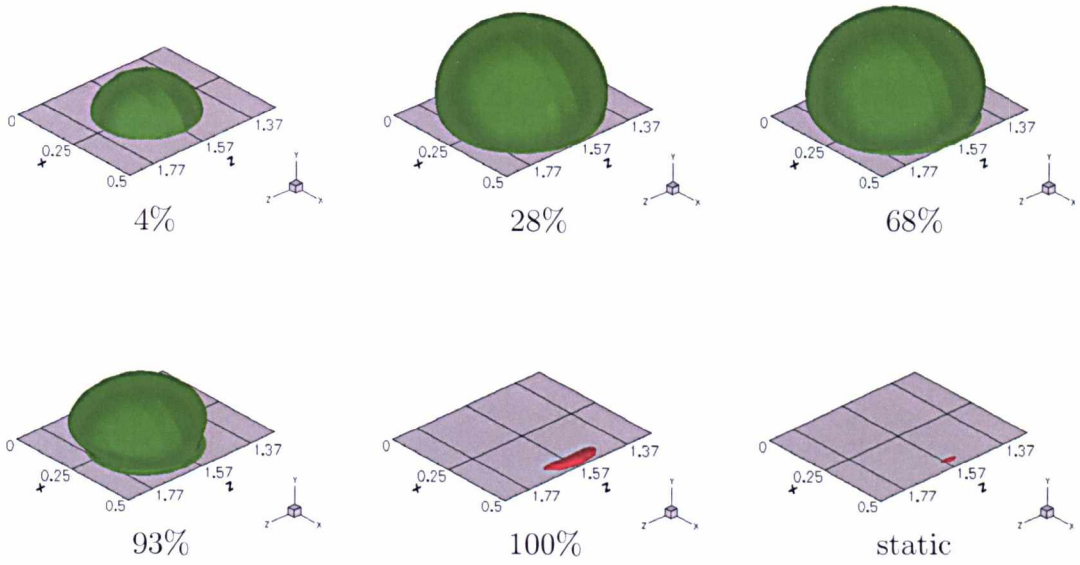


Figure 4.17: Case 1: (v=±0.01)-iso-surfaces around dimple. t = 0.5, 1, 1.5, 2, 3, 7.

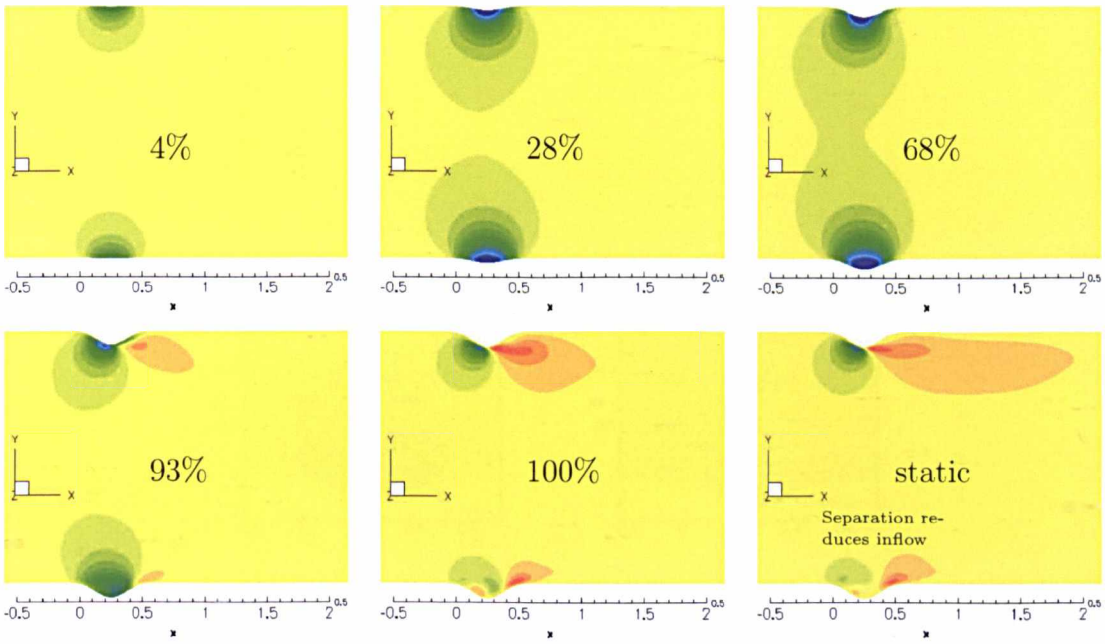


Figure 4.18: Case 1: (-0.07≤v≤0.02)-contours in xy-midplane. t = 0.5, 1, 1.5, 2, 3, 4, 5, 6, 7.

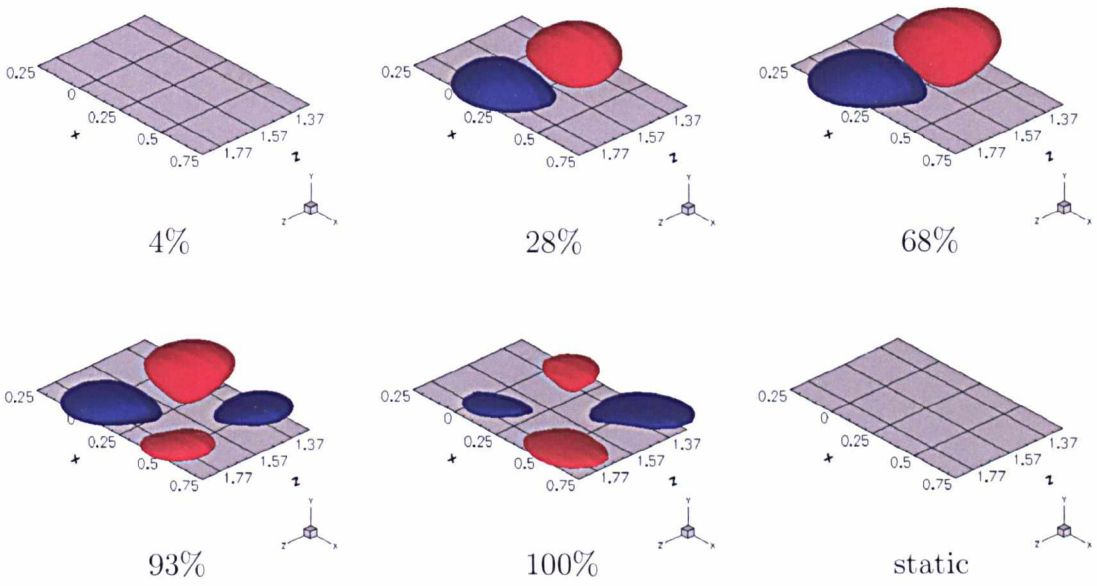


Figure 4.19: Case 1: ($w'=\pm 0.01$)-iso-surfaces around dimple. $t = 0.5, 1, 1.5, 2, 3, 7$.

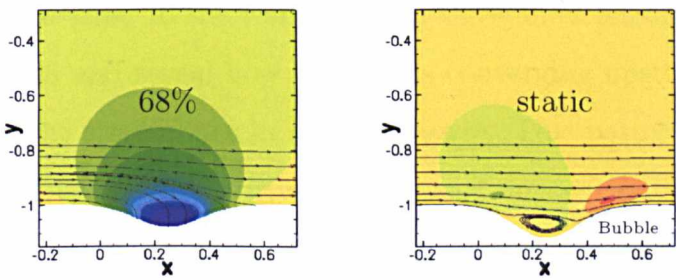


Figure 4.20: Case 1: Streamlines and (-0.07$\leq v \leq$0.02)-contours in xy-midplane around dimple. $t = 1.5$ and 7.

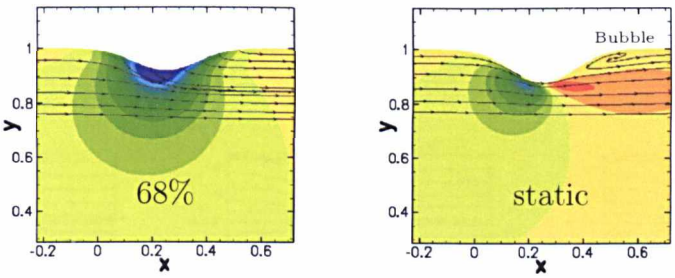


Figure 4.21: Case 1: Streamlines and (-0.07≤v≤0.02)-contours in xy-midplane around bump. $t = 1.5$ and 7.

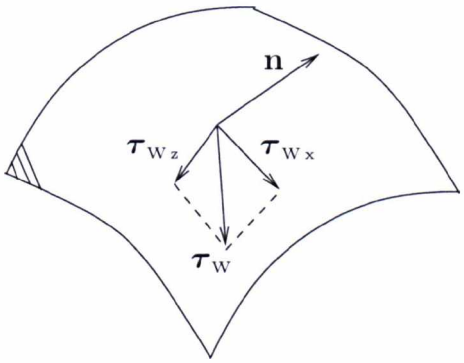


Figure 4.22: Shear stress at the irregular channel wall.

one finds the shear stress vector, $\boldsymbol{\tau}_W$, on the deformed wall as shown in figure 4.22. The quantity can then be decomposed to construct the stress lines which indicate the direction of flow close to the wall. Plots of those lines on the active dimple are shown in figure 4.23 and reveal how the flow is converging upstream and diverging downstream, like the streamlines in a Laval nozzle. This pattern is only disrupted by the re-circulation zone which drives the surrounding streamlines apart.

One would expect to see the opposite phenomenon in flow over bumps, that is stress lines that are first diverging and then converging. Figure 4.24 confirms this intuition. Also, the stress lines on the passive bump agree well with the results reported by Carlson *et al.* [12].

Figure 4.25 shows iso-surfaces of streamwise vorticity over the dimple. The largest perturbation appears towards the end of the motion at around $t = 2$ (93%).

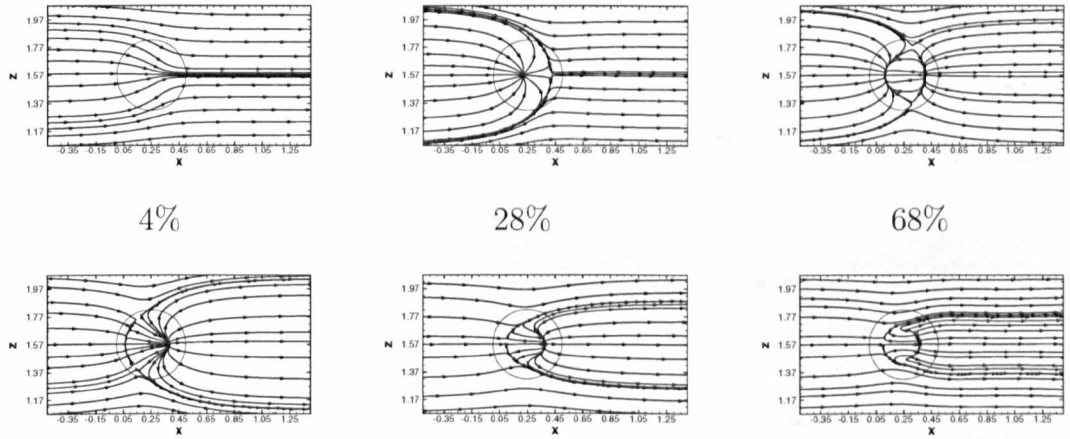


Figure 4.23: Case 1: Stress lines on the dimple. $t = 0.5, 1, 1.5, 2, 3.5, 7$.

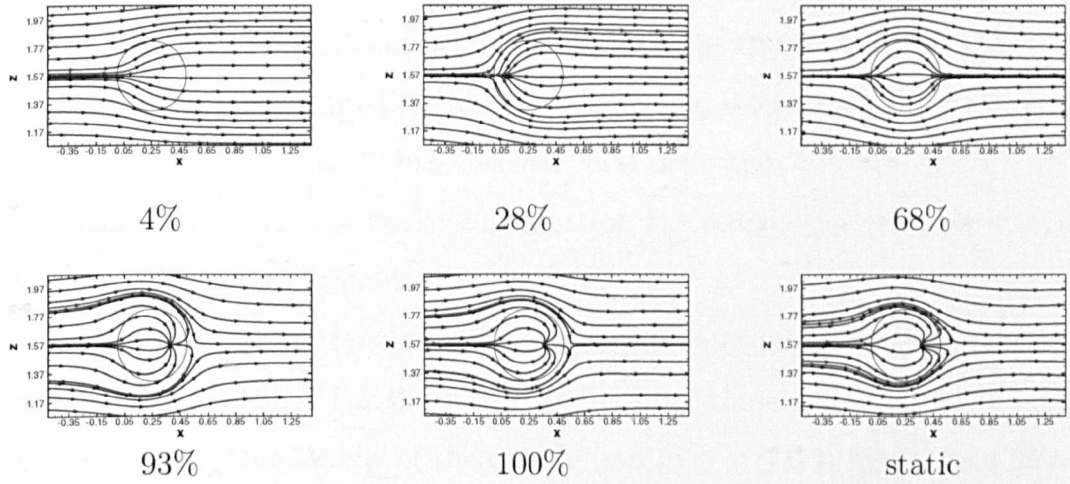


Figure 4.24: Case 1: Stress lines on the bump. $t = 0.5, 1, 1.5, 2, 3.5, 7$.

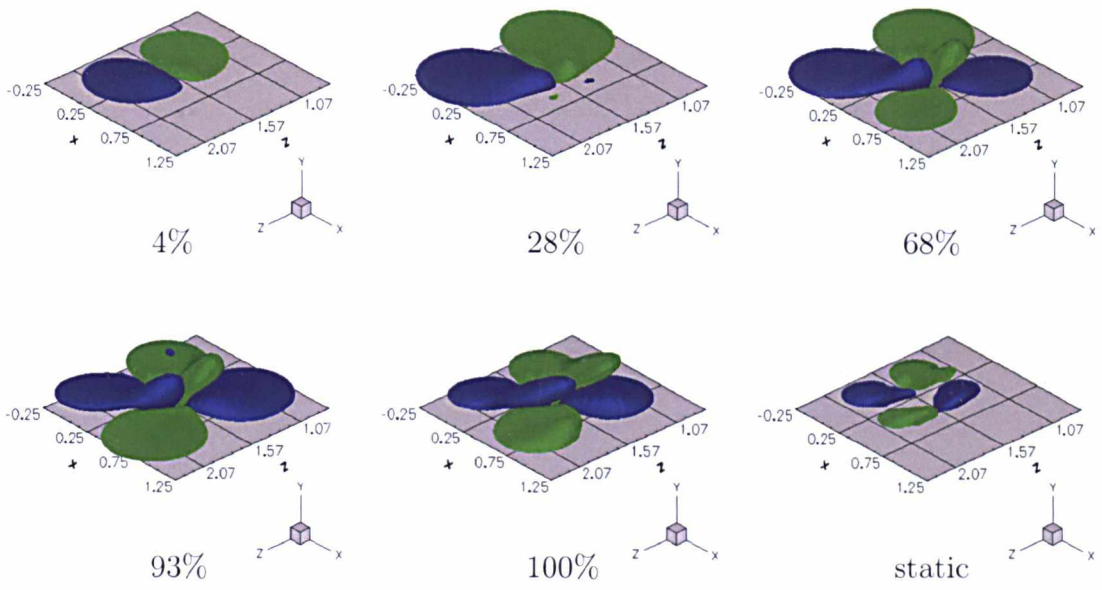


Figure 4.25: Case 1: (ω_x=$\pm$0.1)-iso-surfaces around dimple. $t = 0.5, 1, 1.5, 2, 3, 4, 5, 6, 7$. The y-axis has been stretched by a factor of three.

The maximum streamwise vorticity at that point is about 1.6 times larger than in the static case. The pattern of two strong pairs of counter-rotating streamwise vorticity regions, one upstream and one downstream of the centre that was seen in figure 4.11 is also present in this figure. While the dimple is moving down, the upstream region of streamwise vorticity appears first, followed by the downstream region. The weak region that is accounted for by inertial turning, see expression (4.13), is more pronounced after the dimple has reached final deflection. In the static case the separation seems to have a weakening effect on the streamwise vorticity compared to the case of linearised boundaries.

More information is revealed by overlaying streamwise-vorticity contours with streamlines in yz-planes. For the static case at $t = 7$ these plots are shown in figure 4.26. Upstream of the middle of the dimple ($-0.15 \leq x \leq 0.1$; first row) a sink-like trend develops that draws fluid in from all sides. Hence, vorticity is diffused from the wall. Trailing downstream, this is followed by major adjustments. First, fluid near the surface is pushed to the sides at the centre of the dimple ($x = 0.25$) which causes vorticity of the opposite sign to be diffused. Then, on the downstream side

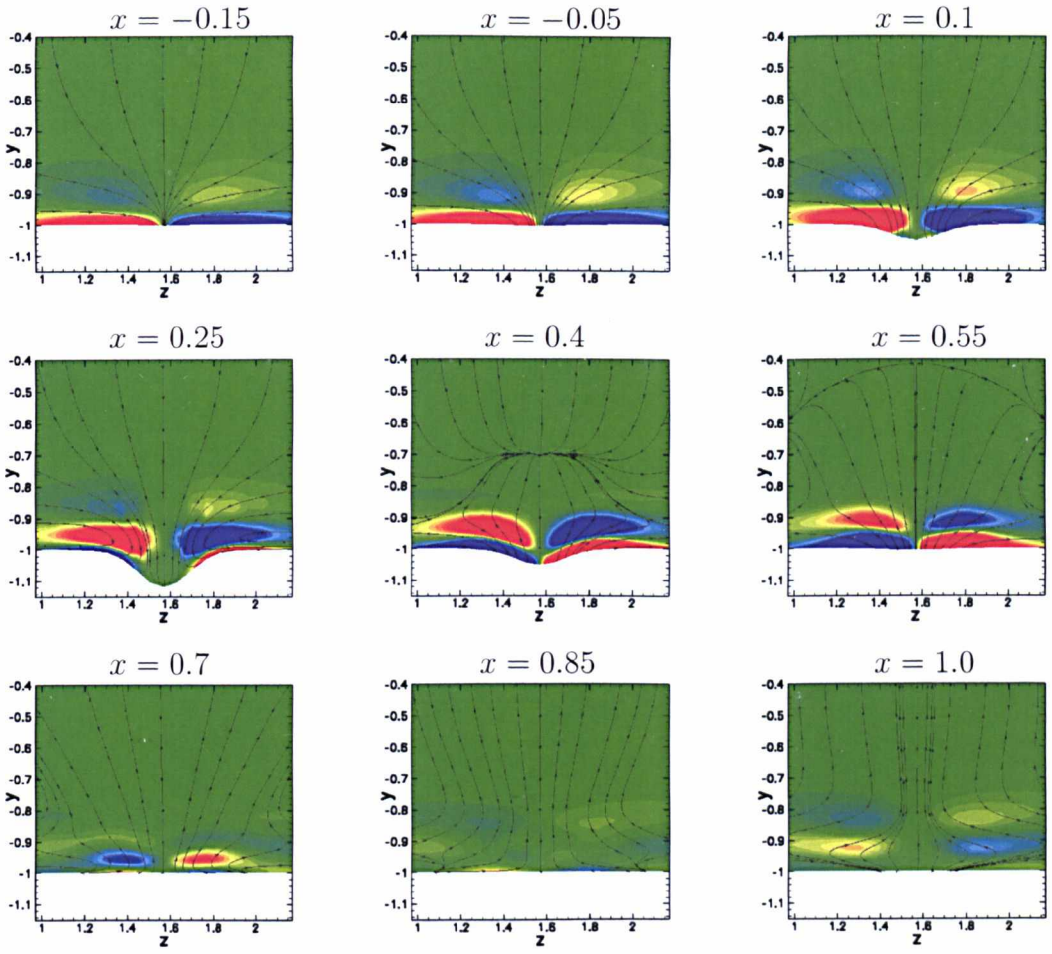


Figure 4.26: Case 1: Streamlines and (-0.05≤ω_x≤0.05)-contours in yz-planes around static dimple at $t = 7$.

of the centre of the dimple ($0.4 \leq x \geq 0.55$), a source-like form appears intensifying the vorticity diffusion. Downstream of the dimple's edge ($0.7 \leq x \geq 1.0$) the sign of the streamwise vorticity at the wall changes once again. The fact that ω_x at the wall changes sign three times in the streamwise direction was also observed in figure 4.25. Also, a stagnation point appears at $x = 0.4$ and $x = 0.55$.

The equivalent plots for the motion case ($t = 1.5$) are shown in figure 4.27. On the downslope of the dimple the qualitative structure is very similar to the static case, which is sink-like. After the trough at $x = 0.25$, the fluid is not expelled but keeps being drawn in because of the downward motion of the dimple. Downstream of the dimple the fluid coming from above is pushed aside and streamwise vorticity diffusion of opposite sign develops. As a result, there are only two noticeable changes

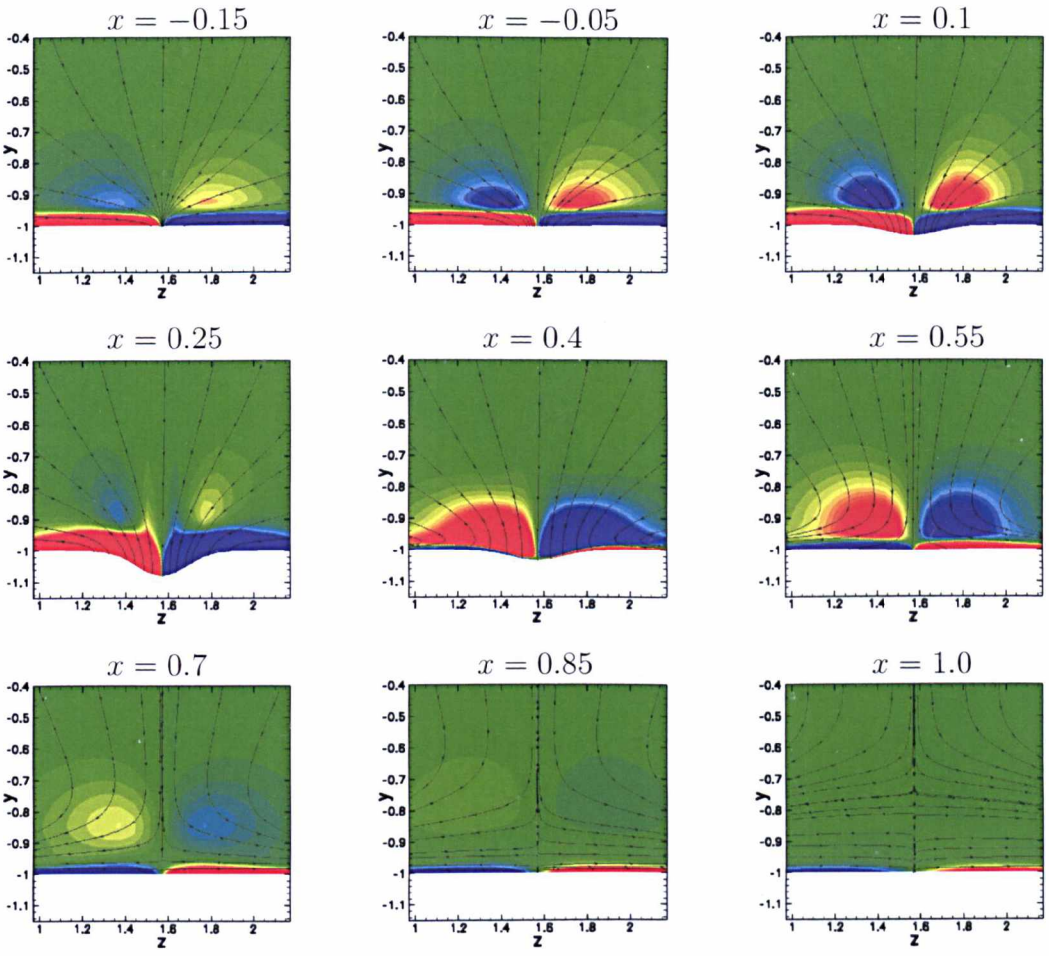


Figure 4.27: Case 1: Streamlines and (-0.05≤ω_x≤0.05)-contours in yz-planes around moving dimple at $t = 1.5$.

of sign in ω_x in the streamwise direction at the wall. Again, a stagnation point emerges.

Figure 4.28 shows iso-surfaces of streamwise vorticity around the moving bump. A comparison with figure 4.25 reveals that active dimples and bumps generate similar streamwise-vorticity contours but of opposite sign. This highlights the linear nature of the processes involved during this stage. But once the maximum deformation has been reached the two fields diverge. Most notably the perturbation caused by the bump decays much less. This leads to a static ω_x-perturbation that is significantly larger than that around the dimple, while the general pattern consisting of four regions is retained in both. In conclusion, it is suggested that dimples do not necessarily generate more localised vorticity than bumps, as was suggested in [74].

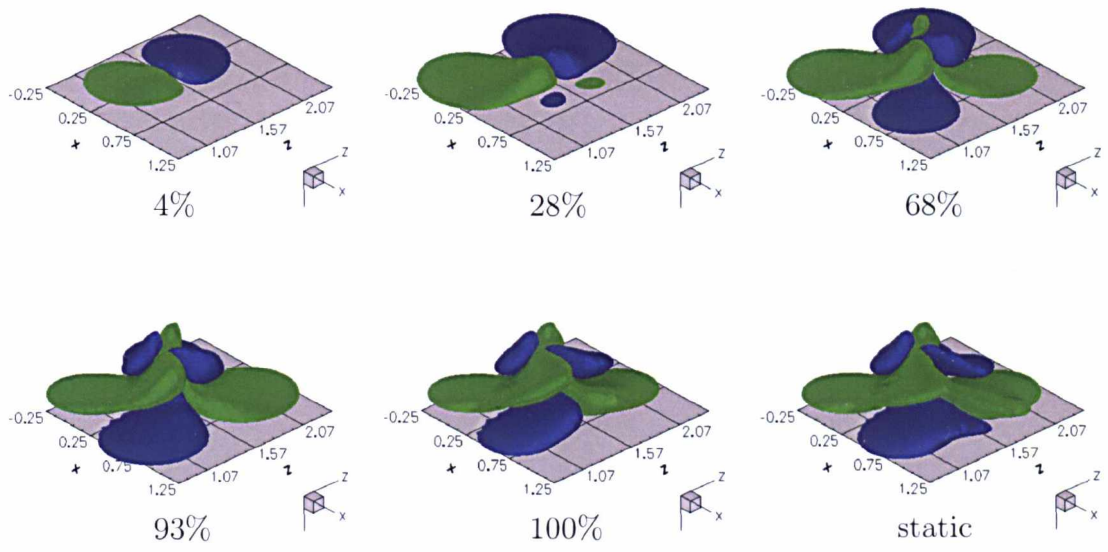


Figure 4.28: Case 1: (ω_x=±0.1)-iso-surfaces around bump. t = 0.5, 1, 1.5, 2, 3, 7. Flow structures have been stretched by a factor of 3 in the wall-normal direction.

The iso-surfaces in figure 4.28 can be directly compared to those in figure 2 of Carlson *et al.* [12]. In the present results the strong vortex shedding event reported by them cannot be observed. On the contrary, the streamwise vorticity structure seems to build up smoothly to its steady form. It is considered entirely possible that the large shedding in their results is due to the omission of acceleration terms in the transformed equations [73]. Supporting this claim is the fact that the vorticity patterns do correspond around the static bump where the acceleration terms are zero.

The total spanwise-vorticity flux from the dimple is shown in figure 4.29. This flow quantity was defined in expression (4.31) and can be used as a target in cancellation techniques [63]. The plots have to be compared to those shown in figure 4.12 where the boundaries were linearised. When the dimple is in motion the patterns agree reasonably well, at least for the selected contour levels. But in the passive stage strong non-linear effects are involved and the results compare poorly. This means that the closed expression for the vorticity flux generation from a linearised dimple, (4.35), cannot be used for stationary actuators. It is tempting to suggest

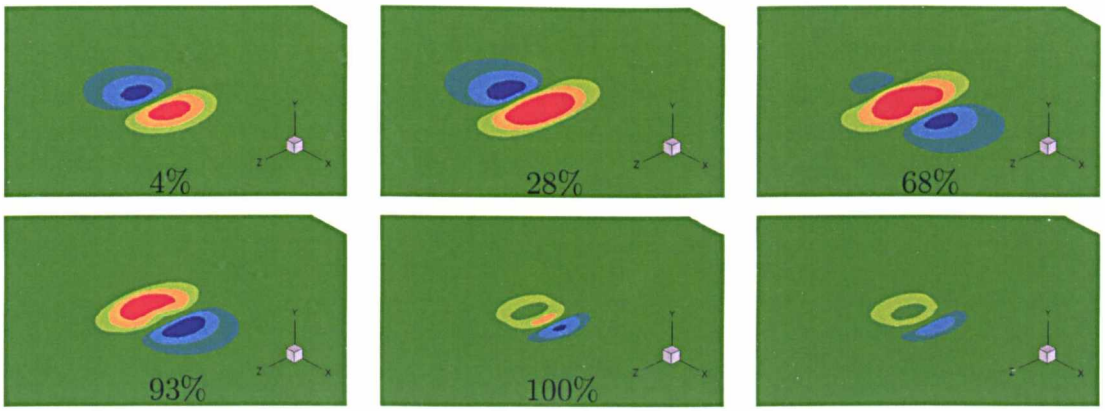


Figure 4.29: Case 1: Contours of total spanwise vorticity flux at -0.04:0.01:0.04. $t = 0.5 : 0.5 : 2.5, 3.5$, and 7.

that this technique could still be employed if permanent motion of the actuators is assumed. Though this might work in laminar flow, another problem remains in turbulence which is that the baseflow must be known *a priori*. For this, the turbulent mean velocity profile could be used as an approximation but that would lead to a more erroneous implementation.

4.4.3.2 Case 2: Slow oscillating motion

The second case to be analysed are actuators oscillating at $Str_c = 0.1$. The parameter values, which are unrelated to the time function, are taken over from Case 1. To ensure absence of the initial transient, the obstacles are oscillated ten times before results are taken.

The analysis is confined to vertical velocity, streamwise vorticity, and stress lines. The first sequence in figure 4.30 shows contours of vertical velocity in the xy-midplane. Up to the point of maximum deflection at $t = 0.5$, the perturbation is qualitatively the same as in the transient case shown in figure 4.18. This is unsurprising as the walls move on similar time scales, something that was already noted in section 4.3.1. Accordingly, the dimple acts again as a sink during the downward motion and as a source during the upward motion. At the end of a cycle, when the actuator is back in the flush position, the v-perturbation is small relative to the v-perturbation at other points in the cycle.

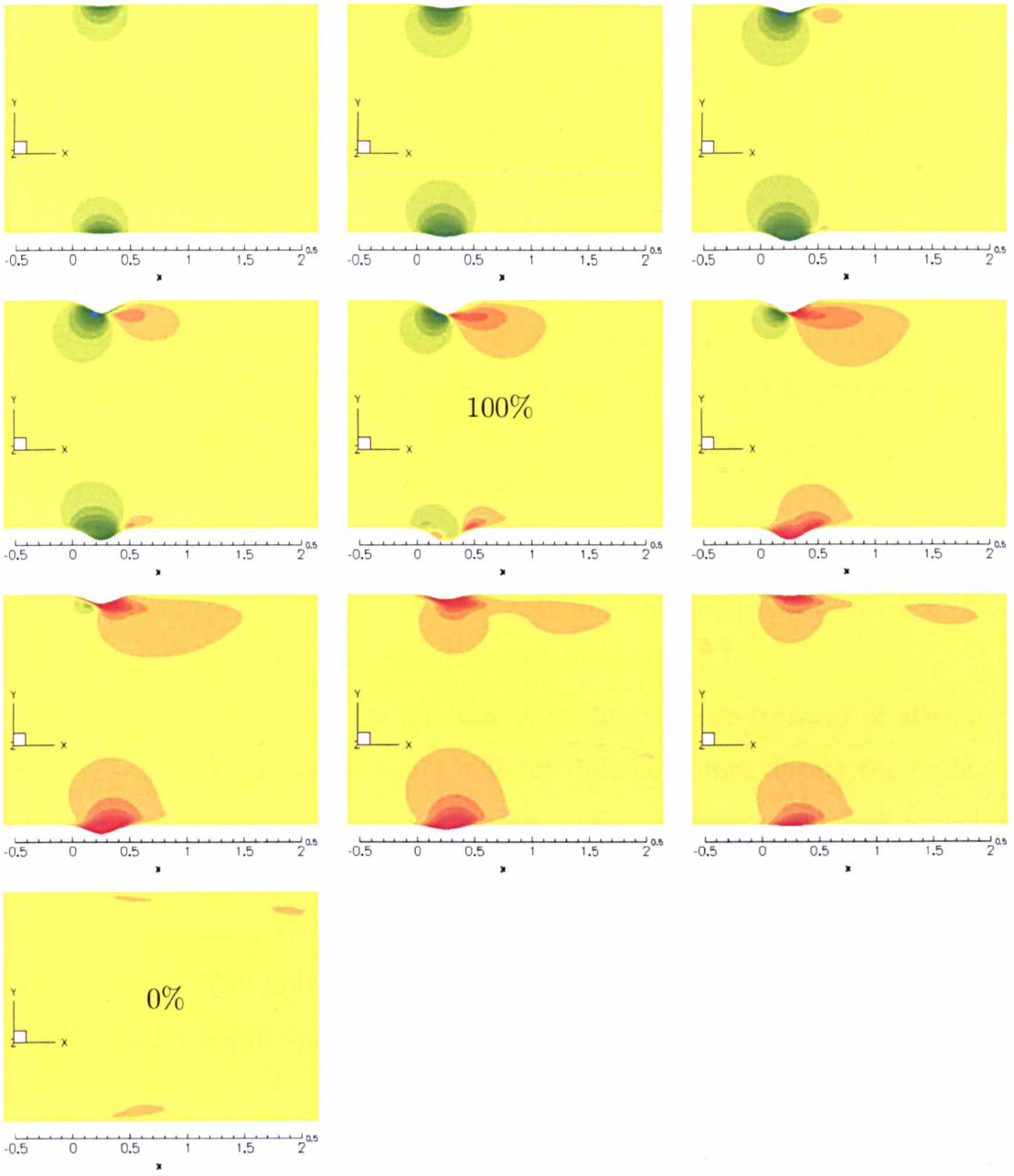


Figure 4.30: Case 2: (-0.07≤v'≤0.02)-contours in xy-midplane. t = 1, 2, 3, 4, 5, 6, 7, 8, 9, 10.

Streamwise-vorticity iso-surfaces are shown in figure 4.31. During the downward motion they resemble the ones of Case 1 in figure 4.25. Similar to the wall-normal velocity a change of sign is observed in the middle of the cycle. At the end of the cycle the ω_x-perturbation remains strong relative to the ω_x-perturbation at other points in the cycle.

The similarities between Case 1 and 2 also include the presence of a separation bubble. This is revealed by the stress lines shown in figure 4.32. In the oscillatory case, however, the bubble quickly disappears once the actuator starts retracting.

All results show that the physical processes in up- and downward motion are, as predicted, fundamentally the same but of opposite sign. This is also the reason why the time-averaged responses, that were analysed in section 4.3.3.2, were so weak.

4.4.3.3 Case 3: Quick oscillating motion

To explore a regime where the perturbation flow is less influenced by the baseflow convection but more by the motion of the actuator, the frequency is raised to $Str_c = 1$. The other parameter values remain, again, unchanged.

For the sake of brevity the analysis is confined to iso-surfaces of streamwise vorticity, which are shown in figure 4.33 for different times during the cycle. By increasing the Strouhal number, the pattern of four regions at the wall is replaced by a pattern of just two regions. Again, the change in direction of motion in the middle of the cycle is accompanied by a change in sign of perturbation but not a change in shape. This indicates that despite the time-averaged structures observed in section 4.3.3.2 it is still the same physical process that govern upward and downward motion.

To create stronger quasi-static structures another approach would be the introduction of asymmetries in the time function. This means upward and downward motion would take place on two different time scales. For example, the actuator could move downward quickly and retract slowly. Another option would be the sharpening of the actuator's edges. This would also prevent the vorticity from being located too close to the wall. By sharpening the edges the actuators would resemble more closely synthetic jets.

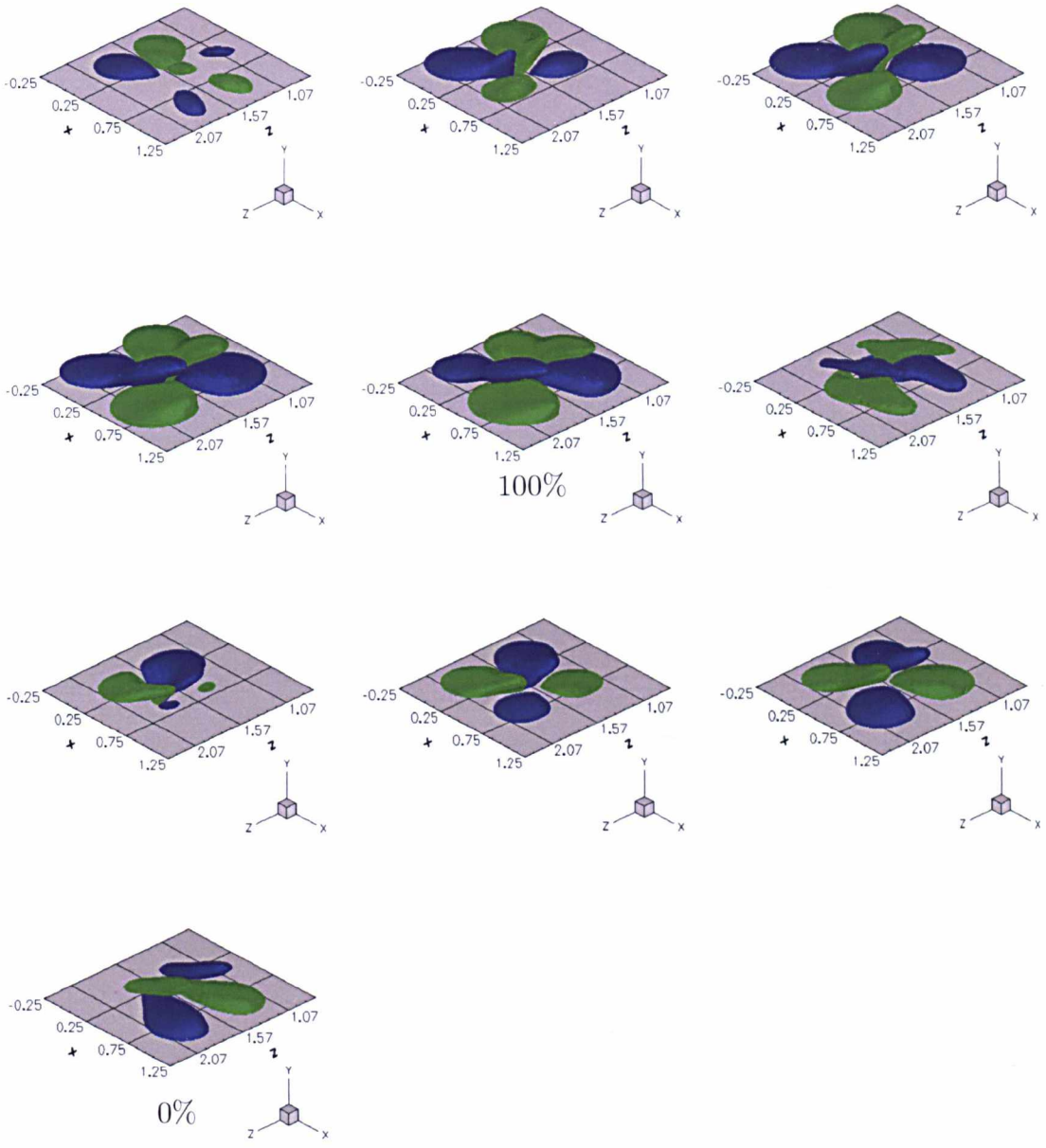


Figure 4.31: Case 2: (ω_x=$\pm$0.1)-iso-surfaces around dimple. $t = 1, 2, 3, 4, 5, 6, 7, 8, 9, 10$. The y-axis has been stretched by a factor of three.

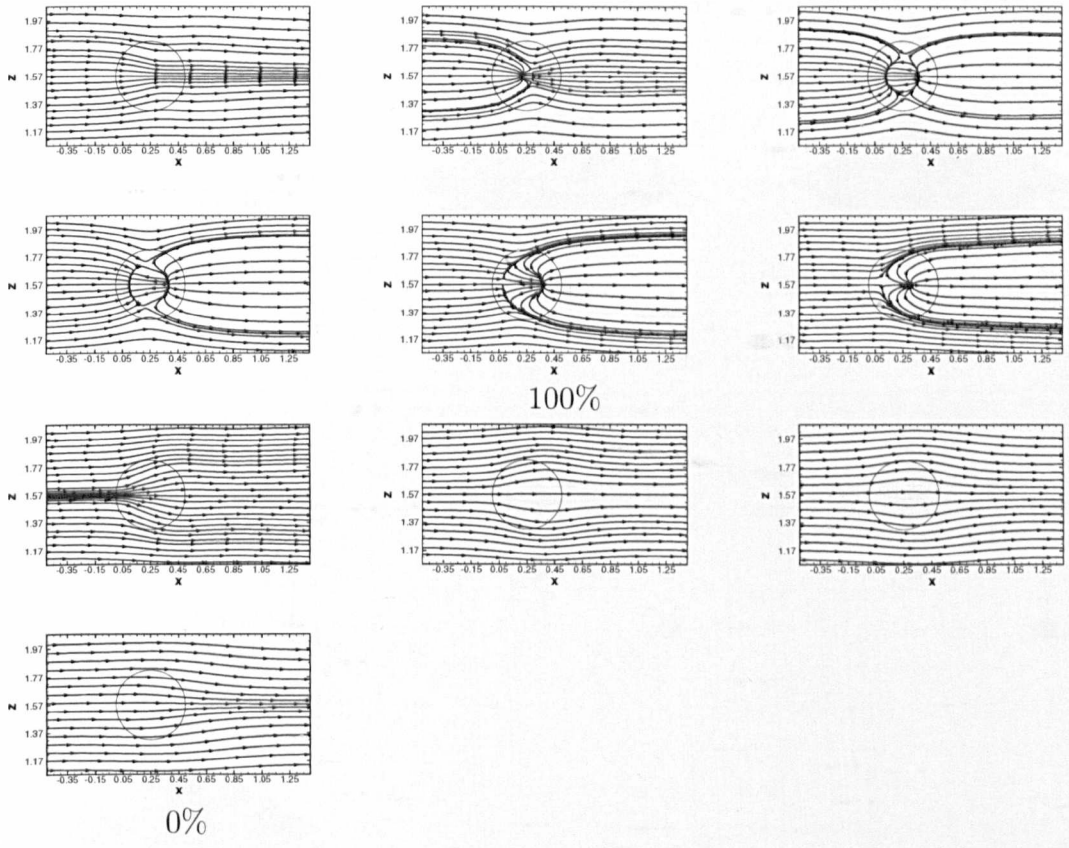


Figure 4.32: Case 2: Stress lines on the dimple. $t = 1, 2, 3, 4, 5, 6, 7, 8, 9, 10$.

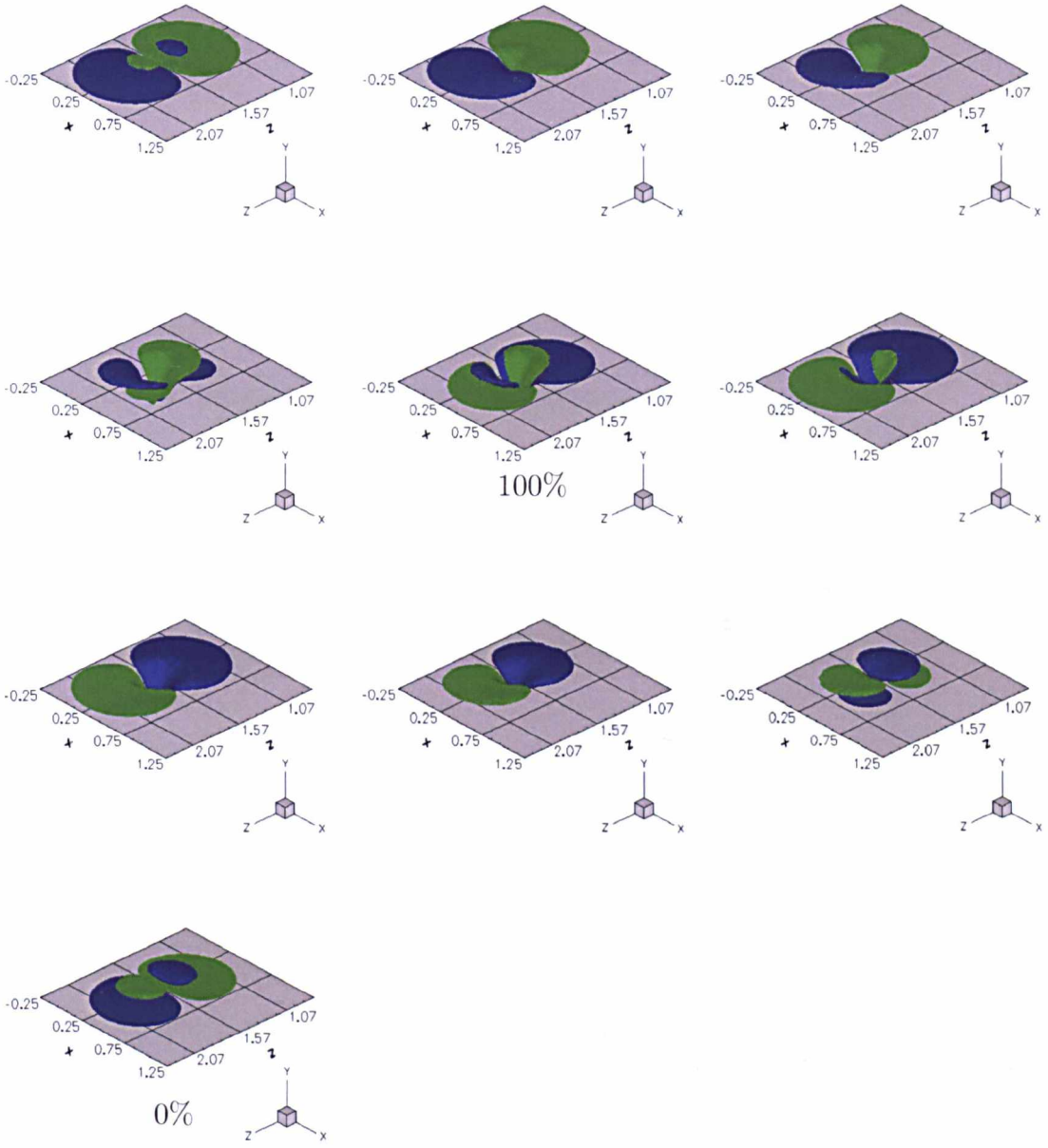


Figure 4.33: Case 3: (ω_x=$\pm$1)-iso-surfaces around dimple. t = 1, 2, 3, 4, 5, 6, 7, 8, 9, 10. The y-axis has been stretched by a factor of three.

Chapter 5

Turbulent channel flow

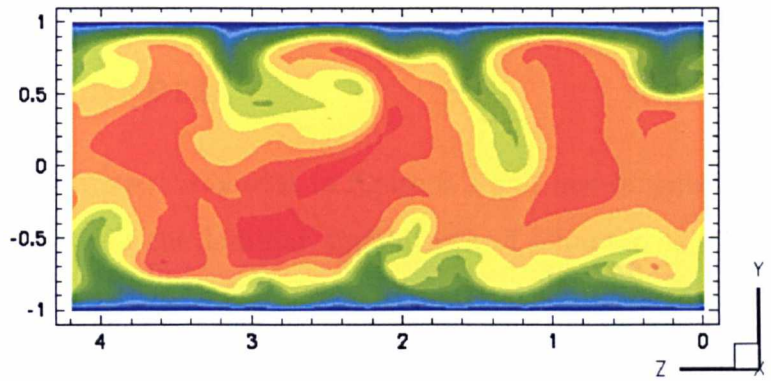


Figure 5.1: Instantaneous streamwise velocity contours in a cross plane at $Re_\tau = 100$.

The main objective of the work presented in this chapter is to calculate a field of wall turbulence which could serve as a platform for control studies. In DNS, wall turbulence is commonly studied in a straight channel. The high regularity of this geometry facilitates spectral computations of high polynomial order that show good agreement with experimental results. The predominant global spectral method for channel flow involves Chebyshev polynomials in the inhomogenous wall-normal direction and Fourier expansions in the homogenous streamwise and spanwise directions [15, 44, 46, 63, 64, 67, 79]. The convergence order of a combined *hp*-method is generally lower than of a pure *p*-method, i.e. global spectral method, but can be sufficient to obtain accurate statistics of turbulent channel flow at low

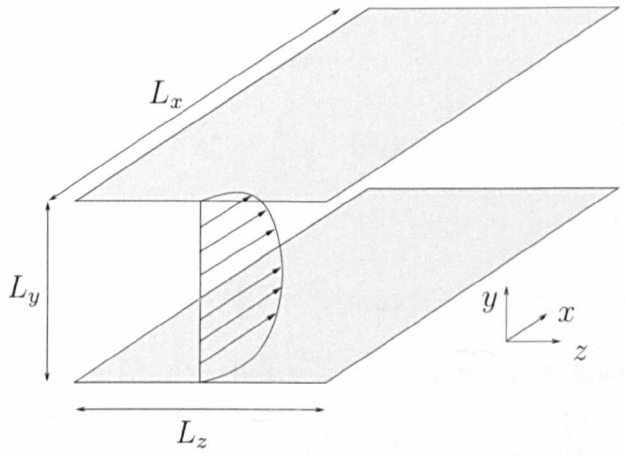


Figure 5.2: Geometry of turbulent channel flow.

Reynolds numbers [19, 26, 42, 55, 57].

5.1 Parameters

The flow geometry used is shown in figure 5.2 and has dimensions $L_x = 4\pi$, $L_y = 2$, $L_z = 4/3\pi$. As in the laminar simulations of Chapter 4, the spectral element discretisation is applied in the streamwise and wall-normal plane, xy, while the solution in the spanwise direction, z, is approximated using Fourier expansions. A difference to those previous laminar simulations is that the inflow is not prescribed by an analytical function but set to the outflow in order to enforce periodicity in x.

When comparing the present discretisation scheme to the one used in recent simulations of turbulent channel flow with $Nεκταr$, one notices the different choice of Fourier direction. Whereas usually it is the streamwise direction that is Fourier-discretised [19, 26, 42, 55, 57] it is the spanwise direction in the present study. Since Fourier discretisation is global spectral, it offers a higher convergence order than the spectral element discretisation. Hence, a Fourier discretisation should be chosen for the homogenous channel direction that requires the higher resolution. But since many experienced investigators use an equivalent number of Fourier modes in both homogeneous directions [5, 15, 64], it is considered unlikely that the choice of the Fourier direction has a significant effect on the efficiency of the discretisation scheme.

Turbulent channel flow can be non-dimensionalised using outer or inner scales.

Possible outer scales are the bulk velocity

$$u_{\mathrm{B}}^* = \frac{1}{2}\int_{-1}^{1} \overline{u^*}\partial y \ , \tag{5.1}$$

the centreline velocity

$$u_{\mathrm{C}}^* = \overline{u^*}_{(y=0)} \ , \tag{5.2}$$

and the channel half-width L_c^*. Possible viscous, inner scales are the friction velocity

$$u_\tau^* = \left(\frac{\overline{\tau_{\mathrm{W}}^*}}{\rho^*}\right)^{\frac{1}{2}} \tag{5.3}$$

where $\overline{\tau_{\mathrm{W}}^*}$ is the average wall shear stress, and the viscous lengthscale

$$L^{+*} = \frac{\nu^*}{u_\tau^*} \ . \tag{5.4}$$

As before, the symbol $*$ in the superscript denotes that the quantity is dimensional and the bar denotes that the quantity is averaged in time and the homogenous directions.

To adhere to the most common convention for simulations of turbulent channel flow, the new Reynolds number

$$Re_\tau = \frac{u_\tau^* L_c^*}{\nu^*} \ . \tag{5.5}$$

is used to characterise the flow. Units of velocity, length, and time are then normalised by u_τ^*, L_c^*, and L_c^*/u_τ^*, respectively. Measures of length that feature a $+$ in the superscript are exceptions to this rule. The $+$ indicates normalisation with L^{+*} rather than L_c^*.

The difference between the non-dimensionalisation presented above and the one used for the laminar simulations in Chapter 4 is that velocity is normalised by u_τ^* rather than u_{C}^*. To compare velocities of laminar and turbulent simulations one can convert them by using the two Reynolds numbers Re_{C} and Re_τ whose values are provided in tables 4.1, 5.1, 6.1, and 7.1 for the simulations under discussion.

In the work presented in this chapter three cases of different resolution were simulated. According to the polynomial order, P, and the number of Fourier modes, M_z, they are termed P6Z32, P7Z48, and P8Z64, where P7Z48 is also referred to

as baseline case. The discretisation and flow characteristics of these cases are summarised in table 5.1. In addition, the table provides details of three simulations from literature, wherein global spectral methods were used to simulate turbulent channel flow. The first literature reference, KK, is a simulation performed by Kuroda and Kasagi [64] and qualifies as a benchmark due to its high resolution. The other two, BMT and CMK, are well-known control simulations conducted by Bewley *et al.* [5] and Choi *et al.* [15], respectively. The former established a control benchmark by presenting a controller that is capable of relaminarising channel flow at low Reynolds numbers and the latter introduced the opposition control scheme. Both studies were mentioned in the literature review of Chapter 2. The numbers in table 5.1 relating to these two studies refer to the unmanipulated channel flow without control.

	Flow Parameters			Spatial discretisation						Box Size	Time integration	
	Re_τ	Re_B	Re_C	N_{el}	P	M_z	Δx^+	Δy^+	Δz^+		Explicit scheme	Δt
P6Z32	100	1410	1698	15x30	6	32	35.07	0.61-4.94	13.09	12.6x2x4.2	AB3	1E-3
P7Z48*	100	1410	1681	15x30	7	48	30.42	0.53-4.28	8.73	12.6x2x4.2	AB3	8E-4
P8Z64	100	1416	1688	15x30	8	64	27.69	0.48-3.9	6.55	12.6x2x4.2	AB3	5E-4
				M_x	M_y	M_z						
KK [64]	100	1445	1740	64	64	64	19.69	0.12-4.9	9.84	12.6x2x6.3	AB2	
BMT [5]	100	1429	1712	42	65	42	30	0.7-5.8	10	12.6x2x4.2	RK3	
CMK [15]			1800	32	65	32				12.6x2x4.2	RK3/AB3	

** Baseline case*

Table 5.1: Simulation parameters.

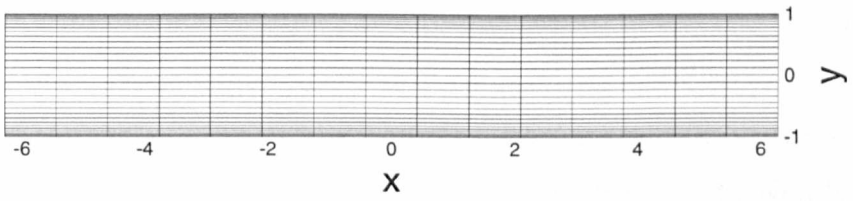


Figure 5.3: Mesh in the streamwise ,x, and wall-normal, y, direction.

In all simulations presented in this chapter, the turbulent channel is driven at a constant force to maintain a Reynolds number of $Re_\tau = 100$. By all standards, this is a very low Reynolds number which can give rise to so-called low-Reynolds-number effects, an issue addressed in section 5.3. Although nowadays, such a low Reynolds number is unusual for studies of unmanipulated channel flow, it is not for studies where some sort of flow control is involved. For example, table 5.1 shows that BMT and CMK also conducted experiments in this regime. The reason for choosing a low Reynolds number is that the implementation of a control algorithm will render the computation more expensive. This applies in particular, when the flow is actuated by wall deformation, as noted by Carlson *et al.* [13].

In DNS all relevant energy scales should be resolved. Because the domain is periodic in x and z the box dimensions have to be large enough to include the largest scales. With $L_x = 4\pi$, $L_y = 2$, $L_z = 4/3\pi$, the size of the domain is the same as BMT and CMK used and considerably larger than the minimal flow unit [51]. At the other end of the range the Kolmogorov length scale is commonly quoted as the smallest scale that needs to be resolved. However, Moin and Mahesh [77] noted that this is probably too stringent because DNS have shown very good agreement with experiments even though the Kolmogorov length scale was not resolved. Hence, resolutions were picked that did not resolve the Kolmogorov scale but were in line with the studies by BMT and CMK. These discretisations are explained in the next paragraph.

The h-type method was equally applied to all cases by subdividing the (x,y)-planes into quadrilaterals using the software GID. The resulting mesh is shown in figure 5.3 and contains 15 elements along the x-direction and 30 elements along the y-direction. The spacing of the elements in the y-direction was chosen so that it

mimicked a Chebyshev distribution, as is recommended in textbook by Karniadakis and Sherwin [57]. Such a discretisation of the wall-normal direction allows higher resolution in the region close to the wall where small-scale features are dominant. In the x-direction the homogeneity of the flowfield dictated an equidistant spacing. With this discretisation of the (x,y)-planes the grid provided a resolution of $\Delta x^+ = 83.78$ and $1.45 < \Delta y^+ < 11.8$. Applying the p-type method then refined this resolution by representing the solution in each element through a polynomial expansion. The polynomial order of this expansion was set to $P = 6$, 7, and 8, for cases P6Z32, P7Z48, and P8Z64, respectively. The global distance of quadrature points, which indicates the resolution, can be calculated based on these polynomial orders and the mesh of figure 5.3. Compared to the case of BMT in table 5.1, Δx^+ and Δy^+ of the baseline case are almost equal and hence the resolution of this case in the x and y-directions is considered sufficiently high. In contrast, case P6Z32 offers a resolution in the x and y-directions that is lower than in the simulations by BMT. This could lead to an insufficient representation of turbulence. In the highest-resolved case, P8Z64, both directions are finer resolved than in the case of BMT. It should be remembered though that since the p-method delivers higher convergence than the h-method, a global spectral scheme will generally provide higher accuracy for the same number of degrees of freedom, i.e. same resolution, than a spectral element scheme. The validation of statistics will reveal which case provides not only sufficient resolution but also sufficient accuracy.

In the spanwise direction, the flowfield was resolved by 32, 48, and 64 Fourier modes for cases P6Z32, P7Z48, and P8Z64, respectively. The number of modes resolved in the spanwise direction by CMK, BMT, and KK are also within the range from 32 to 64.

To time-march the flowfield, a third-order Adams-Bashforth scheme was used for the non-linear terms. Increasing the order of the explicit time integration compared to the laminar simulations in Chapter 4 was necessary since first-order integration proved too diffusive, effectively lowering the Reynolds number. This choice of an Adams-Bashforth scheme is common for turbulent channel flow simulations but other options such as Runge-Kutta exist. Specific reasons for using a multi-step

method and not a one-step method will be given in Chapter 7. In the simulations the CFL number was in general greater than unity thus violating the CFL condition. This can produce incorrect instantaneous results but the turbulence statistics proved to be invariant to smaller time steps. In flow simulations where the accurate prediction of transient flow events was necessary, such as in the control simulations of Chapter 7, it was ensured that the CFL number stayed below one.

To generate and verify a fully-developed turbulent channel flow, the following steps were undertaken. First a parabolic flow was randomly perturbed over a couple of time steps. The fields were then integrated over time until full development of the flow and absence of large transients due to initial excitation were achieved. This equilibrium state was identified through its characteristics, which are a linear profile of stress, symmetrical second-order profiles and zero skewness of w in the y-direction. From this statistically steady state, the equations were integrated for more than 200 time units to obtain a time average of the statistical variations. The results of these statistics are presented and verified next.

5.2 Statistics

In this section the turbulent statistics of cases P6Z32, P7Z48, and P8Z64 are presented and verified. An analytical verification is not possible due to the chaotic nature of turbulent flow. Instead, the flow statistics obtained are compared to an established reference, as is common practice. For the low Reynolds number that was chosen here, $Re_\tau = 100$, only few databases are widely available. One of them is provided by KK for the simulation listed in in table 5.1. Since they used a relatively high resolution their results are well suited for comparison.

In table 5.1 it can be seen that Re_B and Re_C vary from case to case. This is because in DNS of turbulent channel flow the flowrate is not known *a priori* when a fixed driving force is specified. Hence, the two Reynolds numbers can be considered as gross statistical figures of the flow that also measure accuracy. But interestingly, the discrepancy of Re_B and Re_C relative to the values provided by KK shows no significant improvement with increasing resolution. This indicates that the two

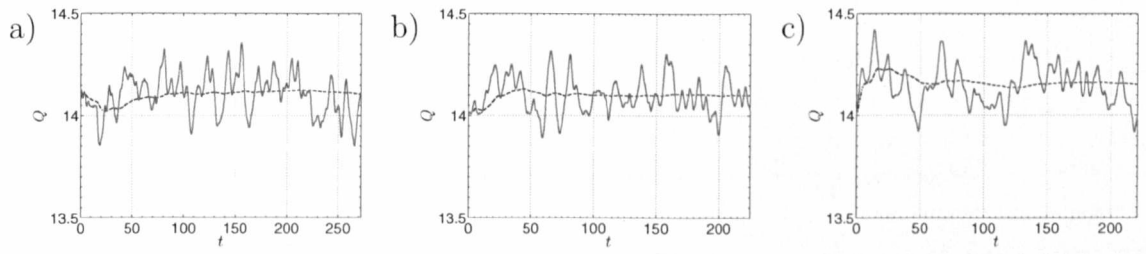


Figure 5.4: Flowrate and its running time average. a) P6Z32; b) P7Z48; c)P8Z64.

Reynolds numbers are not sufficient to measure general accuracy and points to a need to analyse the flow locally. To demonstrate that the time-averaged flowrate, on which Re_{B} is based, has converged over time, the flowrate and its running time-average are shown in figure 5.4.

To investigate local accuracy, the statistics of variation of turbulence with distance from the wall or a point in the domain are examined. The quantities under investigation are listed in table 5.2 where a W in the subscript always denotes a quantity at the wall.

To enhance the time-averaged statistical sample it was also averaged in the horizontal plane. In the following discussion an overbar generally indicates an average over x, z, and t, and a prime indicates perturbation from this average. One exception is $\overline{\tau \mathrm{w}}(t)$ which is averaged in space only, because this quantity measures the evolution of skin friction in time. Other exceptions are one-dimensional spectra and two-point correlation which are averaged in time and a single homogenous direction.

Before comparing to the database by KK the local statistical properties that are known analytically are verified with the results of the baseline case. In the fully-developed channel flow considered here, the total shear-stress profile must be a straight line, that is $\overline{\tau(y)} = 1 - y$. The graph in frame 'e' of figure 5.7 clearly demonstrates that this is the case. The graph also shows that $|\overline{\tau_W}| = 1$ which is required for the global balance of forces. For the box size to be sufficiently large two-point correlation must fall off to zero for large separations. The two-point correlation in z at $y^+ = 5.4$ shown in figure 5.7 f does fall off for large z . This trend is flawed

First order	$\overline{u}$		
	$\overline{\omega_z}$		
	$\overline{\tau_W}$	$=$	$\frac{1}{Re}\frac{\partial \overline{u}_W}{\partial y}$
RMS	$u_{i,\mathrm{rms}}$	$=$	$(\overline{u_i' u_i'})^{1/2}$
	$\omega_{i,\mathrm{rms}}$	$=$	$(\overline{\omega_i' \omega_i'})^{1/2}$
	$\overline{\tau_{Re}}$	$=$	$-\overline{u'v'}$
Total stress	$\overline{\tau}$	$=$	$-\overline{u'v'} + \frac{1}{Re}\frac{\partial \overline{u}}{\partial y}$
Skewness	$u_{i,\mathrm{skew}}$	$=$	$(\overline{u_i' u_i' u_i'})^{1/3} / {u_{i,\mathrm{rms}}}^{3/2}$
Kurtosis	$u_{i,\mathrm{flat}}$	$=$	$(\overline{u_i' u_i' u_i' u_i'})^{1/4} / {u_{i,\mathrm{rms}}}^{2}$
Energy spectra over k_x and k_z at $y^+ = 5.4, 10, y_{\mathrm{LW}}$	$E_{u_i u_i}(k_x)$	$=$	$\overline{\frac{1}{L_x}\int_{L_x} e^{(-ik_x x)} \frac{1}{2} u_i' u_i' \partial x}$
	$E_{u_i u_i}(k_z)$	$=$	$\overline{\frac{1}{L_z}\int_{L_z} e^{(-ik_z z)} \frac{1}{2} u_i' u_i' \partial z}$
Two-point correlation over z at $y^+ = 5.4$	$R_{u_i u_i}(z)$	$=$	$\frac{\overline{u_i(0)' u_i(z)'}}{u_{i,\mathrm{rms}}(0) u_{i,\mathrm{rms}}(z)}$

Table 5.2: Quantities for the statistical analysis of turbulence.

by a kink in the graph at $z = 2$, which results from an insufficient sample size. A known analytical relationship is that the skewness of w must be zero over the entire y-range because the z-direction is homogenous. As can be seen in frame 'a' of figure 5.8, this holds for the baseline, again with an error due to insufficient sampling. Finally, the energy spectra in frames 'c', 'd', 'e', and 'f' of figure 5.8 illustrate that the grid resolution is adequate, since the energy density associated with the high wavenumbers is several decades lower than the energy density corresponding to low wavenumbers. Moreover, there is no evidence of energy pile-up.

In the next three sections the different cases are compared individually to the database by KK. Given that these turbulent simulations are meant to provide a platform for control of wall turbulence, intuition suggests that the viscous layer should be the focus of this verification analysis. In particular, it is the vertical velocity at $y^+ = 10$ that is of interest because the sensor picks up these values and feeds them to the controller in the control simulations of Chapter 7. Because this vertical motion close to the wall is widely attributed to coherent structures in the shape of streamwise vortices, it is also essential to accurately predict the average size and location of these vortices. Two-point correlation and energy spectra are mainly shown for $y^+ = 5.4$ which marks the approximate location of the so-called "virtual wall", a concept explained in Chapter 7. Finally, it should be noted that logarithmic plots of the mean flow are left out as the buffer-layer extends to the centre of the channel for Reynolds numbers as low as $Re_\tau = 100$.

5.2.1 Case P6Z32

The first case to be analysed is labelled P6Z32 as the flow field is discretised by polynomials of sixth order in each element over 32 Fourier modes in z. In general, the turbulence statistics shown in figure 5.5 and 5.6 are of modest accuracy.

First, the graphs in figure 5.5 are examined. In frame 'a', the mean flow is shown. In line with Re_B, the mean flow is under-predicted. To the right, in frame 'b', profiles of rms fluctuations of all the velocity components collapse for most of the y-range, apart from the peak in u_{rms}. In the next frame, c, a good agreement is

found for the profile of mean spanwise vorticity. The rms fluctuations of vorticity in contrast, which are depicted in frame 'd', agree less well. This lack of accuracy disqualifies P6Z32 as a potential basis for flow control since collapsing rms profiles are generally considered as a minimum requirement for accurate representation of turbulence. The Reynolds stress profiles in frame 'e' are sufficiently well predicted. For the two-point correlation no quantitative reference data are available but the graphs in frame 'f' correspond qualitatively to the graphs found in literature [5, 15]. The minimum of R_{uu} around $z = 50$ equals half the spanwise spacing of streaks.

More graphs follow in figure 5.6, starting with profiles of higher-order statistics in frame 'a' and 'b'. The most visible flaws are the under-prediction of u_{skew} away from the wall and the under-prediction of kurtosis of all velocity components near the wall. Energy spectra are shown in frame 'c' and 'd'. No quantitative reference data is available but the graphs are qualitatively correct. Reflecting the discretisation scheme, the streamwise energy spectra bottoms out for scales that are not resolved whereas the energy spectra in the Fourier-discretised z direction is cut-off at the highest-resolved wavenumber. Since E_{vv} is still relatively high at the highest spanwise wavenumber, a finer resolution should be applied in the z-direction.

Clearly, the accuracy of this case is insufficient for rigourous conclusions to be drawn from possible control experiments. It should be said though that preliminary flow control simulations at this resolution have predicted drag reductions remarkably well. Performing these simulations was part of the development process and their results are not presented here. But they served well in providing directions.

5.2.2 Case P7Z48

The abbreviation P7Z48 stands for a polynomial discretisation up to seventh order and 48 resolved Fourier modes in z. This is the second-highest resolution studied here and is comparable to the one in the simulations by CMK and BMT. Based on a good compromise between speed and accuracy, this case was chosen as baseline case and hence requires special attention in the analysis.

First, the graphs in figure 5.7 are analysed. As in the case of P6Z32, the mean

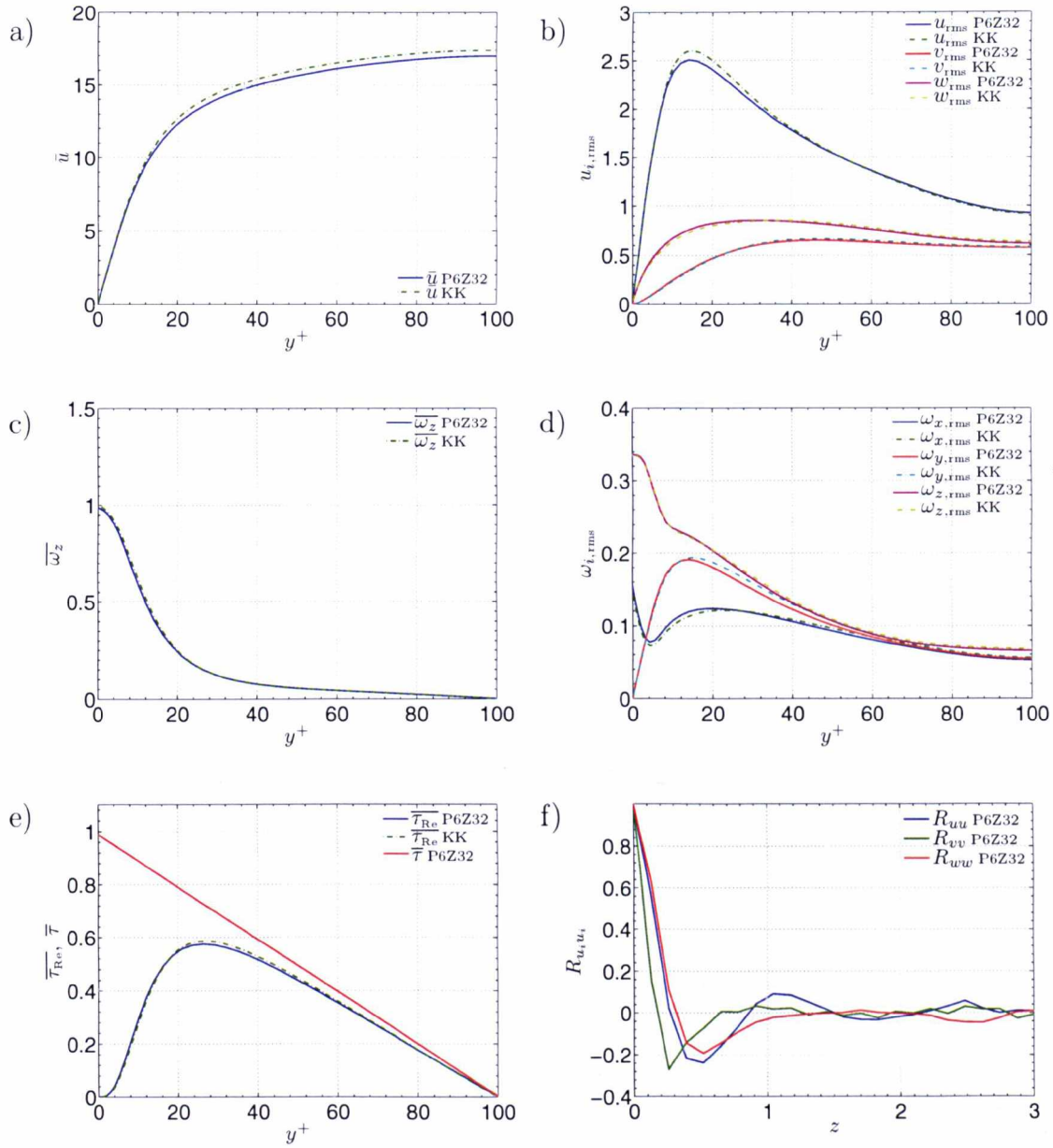


Figure 5.5: P6Z32: a) mean velocity; b) rms velocity fluctuations; c) mean vorticity; d) rms vorticity fluctuations; e) Reynolds stress and total stress; f) spanwise two-point correlation at $y^+ = 5.4$

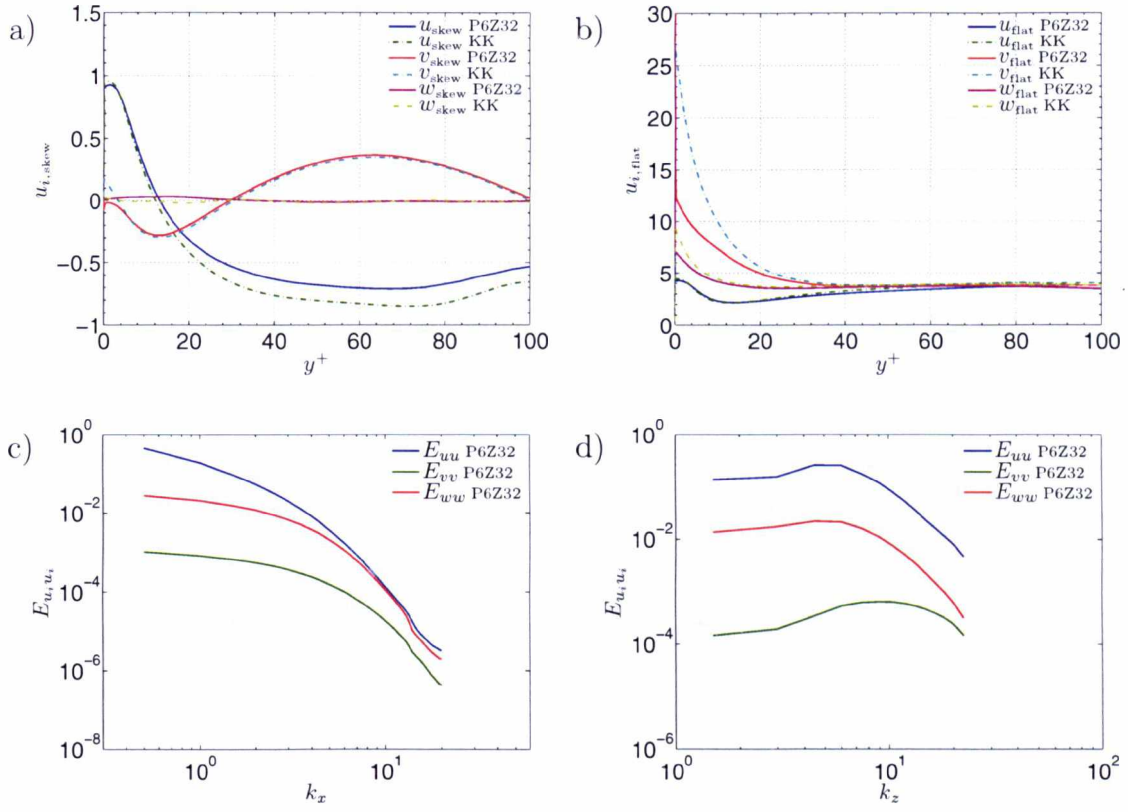


Figure 5.6: P6Z32: a) skewness of velocities; b) kurtosis of velocities; c) streamwise energy spectra at $y^+ = 5.4$; d) spanwise energy spectra at $y^+ = 5.4$

flow shown in frame 'a' is under-predicted, not benefiting from the increase in resolution. Second order profiles, however, have improved noticeably. The rms velocity fluctuations in figure b now collapse, including the peak in u_{rms}. This means that the local distribution of kinetic energy is correctly predicted. Equally well predicted are the mean vorticity in frame 'c', the rms vorticity fluctuations in frame 'd', and the Reynolds stress in frame 'e'. The latter implies that the simulation also predicts the location of the peak of maximum turbulence production correctly because it corresponds to the location of the peak of Reynolds stress. The two-point correlation in frame 'f' follows the correct pattern but no database is available to compare it to. Most importantly, it trails off to zero for large separations and R_{uu} has a local minimum at $z^+ = 50$, reflecting half the spanwise spacing of the streaks. Again, the accuracy of this graph is noticeably impeded by the number of samples.

Next, the graphs in figure 5.8 are analysed. Unfortunately, significant discrepancies remain for the skewness of velocity in frame 'a' and the kurtosis of velocity in frame 'b'. But the increase in resolution has reduced the error, most notably the kurtosis close to the wall has become more accurate. The energy spectra in frames 'c' and 'd' resemble the ones found for case P7Z48, although now the lines extend further as higher wavenumbers are resolved. Most importantly, E_{vv} at the highest spanwise wavenumber is now lower than E_{vv} at the lowest spanwise wavenumber. Given the good overall agreement, a further increase in resolution will only aim at improving the prediction of the mean flow, the skewness, and the kurtosis.

The existence of streaks is commonly attributed to streamwise vortices. Should this be the case, an accurate reproduction of streamwise vorticity is paramount. The average magnitude of streamwise vorticity fluctuation has one local maximum and one local minimum. The location of the local maximum corresponds to the average location of the centre of the streamwise vortices. The local minimum is caused by the opposite streamwise vorticity created at the wall so as to enforce the no-slip condition [60]. The collapse of profiles of $\omega_{x,\,\text{rms}}$ in frame 5.7 d implies that both the average location and the average size of streamwise vortices are correctly predicted.

Strong events in the flow are of the utmost importance to flow control. Some studies, such as the opposition control experiment by CMK, suggest that the strong

events must be nullified to achieve significant skin-friction reduction. Statistically, the kurtosis of the velocity profile represents the relative fatness of the tails of the probability distribution. Hence, the observed under-prediction of velocity kurtosis close to the wall is equivalent to an under-prediction of strong events. In considering the importance of strong events, this discrepancy is most undesirable but it is possible that the increase in resolution of Case P8Z64 will further correct this.

5.2.3 Case P8Z64

At a polynomial order of eight and with 64 Fourier modes resolved, P8Z64 presents the highest-resolved case to be tested. Though good agreement was found for most statistics with the previous resolutions, the accuracy of mean flow and higher-order statistics left room for improvement.

The new results shown in figures 5.9 and 5.10 are disappointing in this respect. While $\bar{u}$ has slightly increased towards the mean flow of the benchmark simulation, the skewness and kurtosis have not improved at all. This lack of convergence gives rise to the unsettling thought that the accuracy of these statistical quantities cannot be improved. Whether that is so requires more investigation but, for the mean flow at least, similar observations using *Nεκταr* have been made elsewhere [57]. Be that as it may, the additional computational expense caused by the increase in resolution did not pay off sufficiently. Hence, it is justified to use case P7Z48 as a baseline case for control simulations.

5.3 Reynolds number effects

Having produced good results for a turbulent channel simulation at $Re_\tau = 100$ ($Re_C = 1688$) the question is whether the results of control simulations conducted with this baseline case may be extrapolated to a higher Reynolds number regime. Without doubt, simulations at $Re_\tau = 10^5$, which corresponds to flows around commercial planes, would be preferred. But with the current limit in computational power and the time constraints of this project, high-Reynolds-number control simulations were not feasible. Although the present Reynolds number is clearly

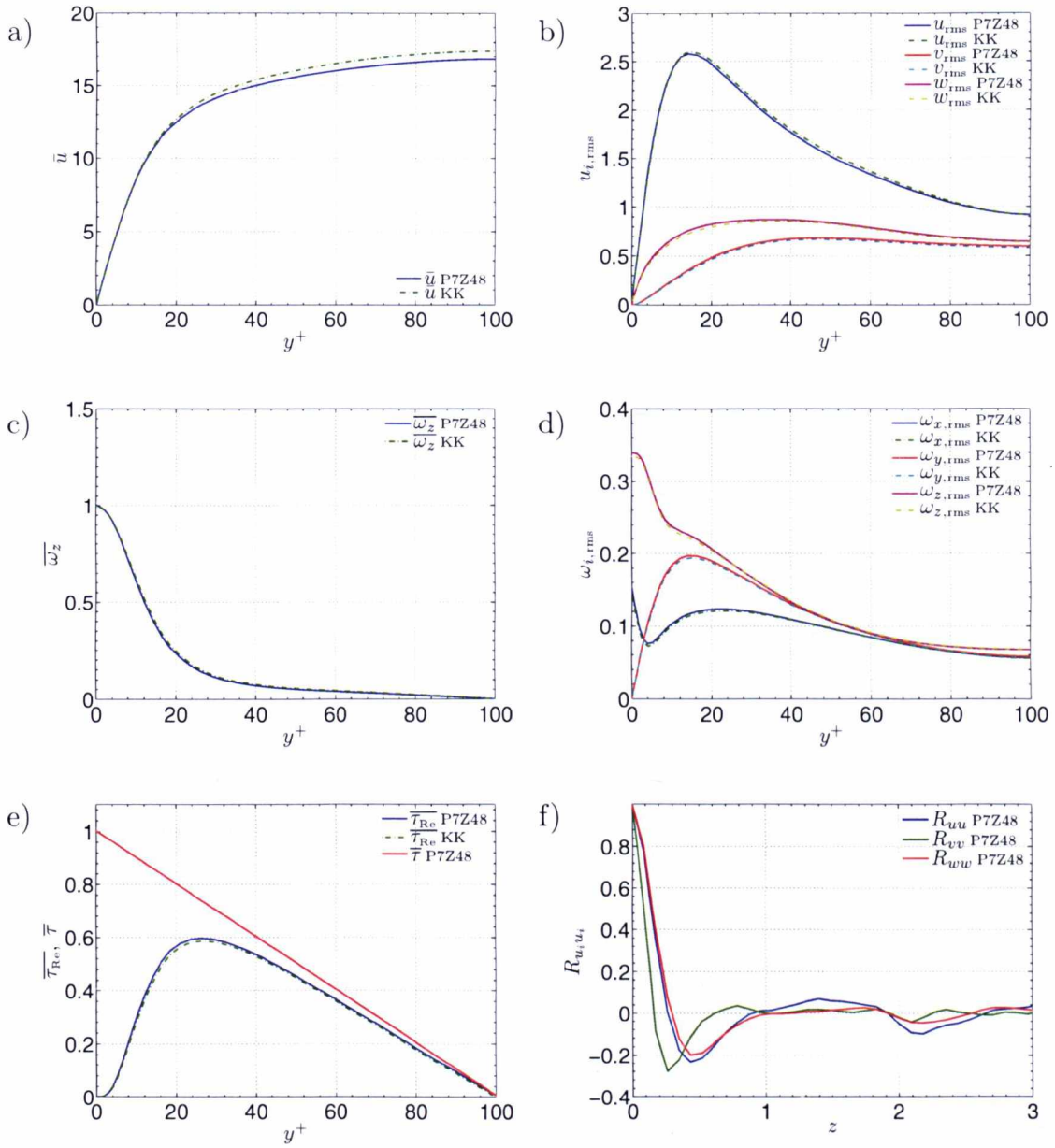


Figure 5.7: P7Z48: a) mean velocity; b) RMS velocity fluctuations; c) mean vorticity; d) RMS vorticity fluctuations; e) Reynolds stress and total stress; f) spanwise two-point correlation at $y^+ = 5.4$

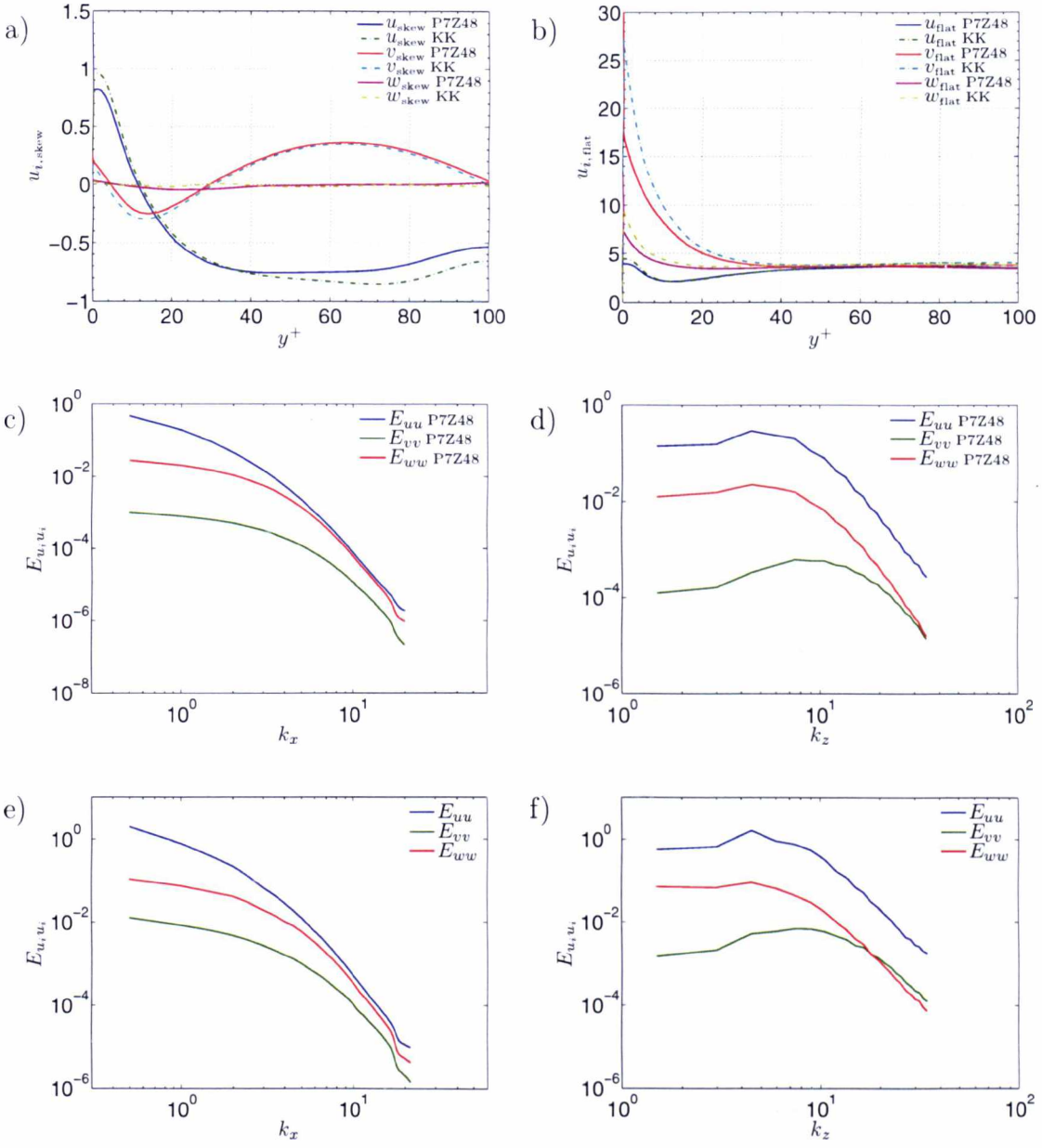


Figure 5.8: P7Z48: a) skewness of velocities; b) kurtosis of velocities; c) streamwise energy spectra at $y^+ = 5.4$; d) spanwise energy spectra at $y^+ = 5.4$; e) streamwise energy spectra at $y^+ = 10.1$; f) spanwise energy spectra at $y^+ = 10$

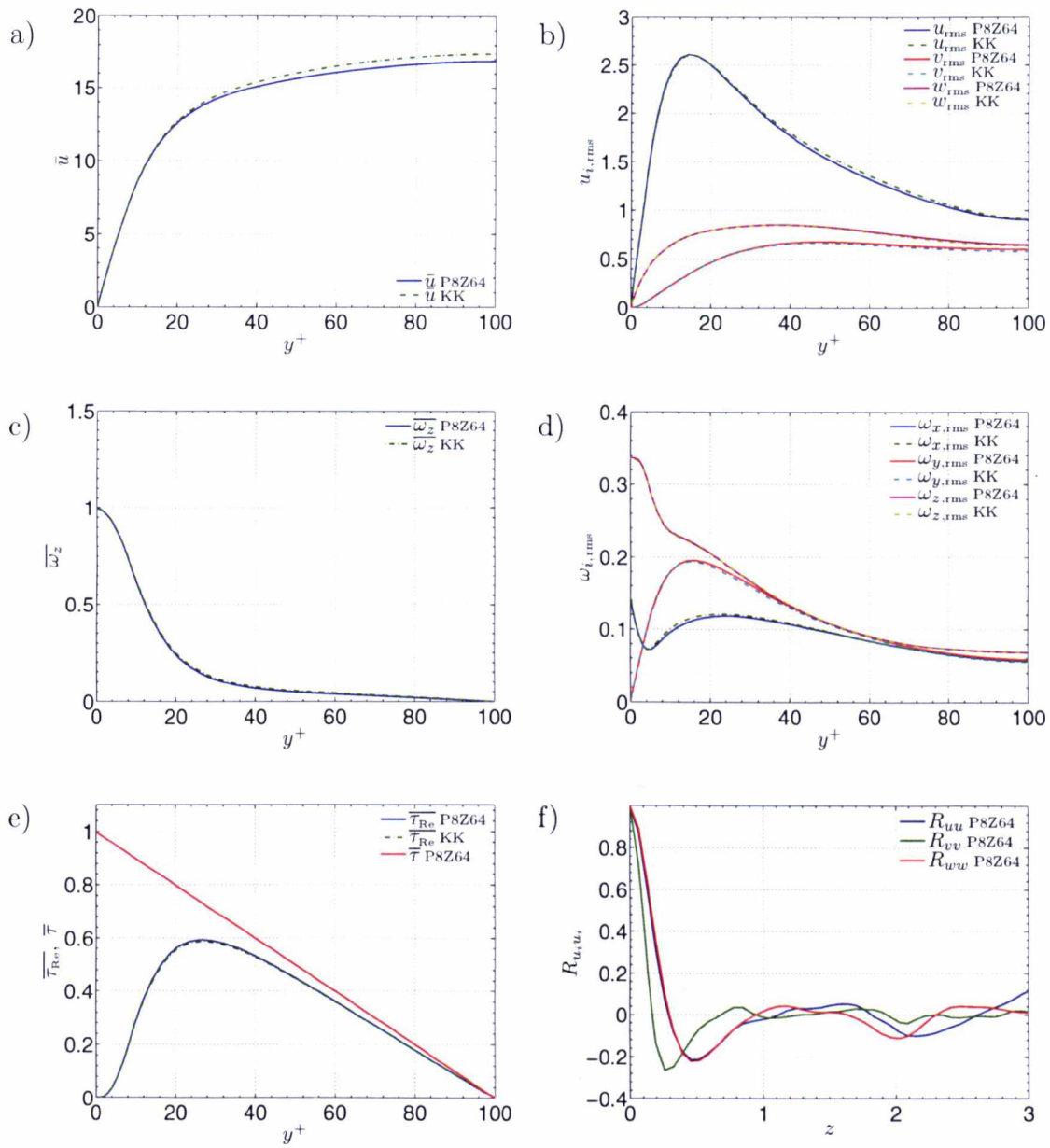


Figure 5.9: P8Z64: a) mean velocity; b) RMS velocity fluctuations; c) mean vorticity; d) RMS vorticity fluctuations; e) Reynolds stress and total stress; f) spanwise two-point correlation at $y^+ = 5.4$

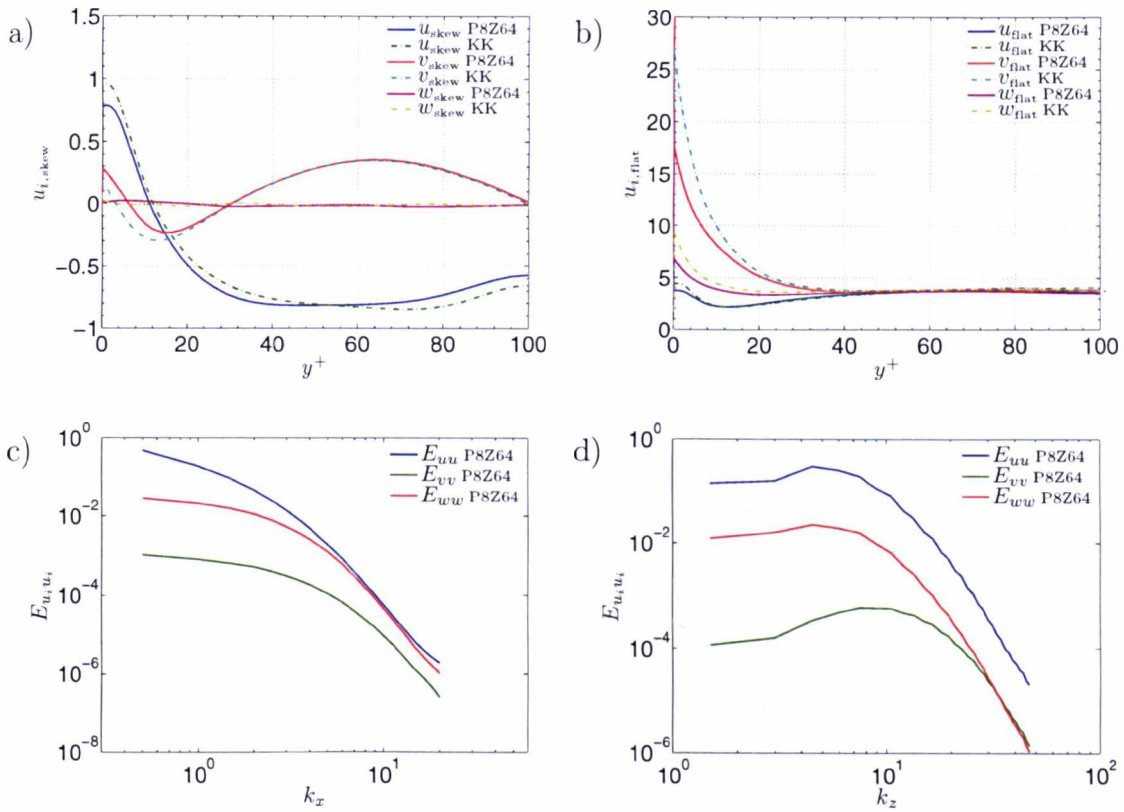


Figure 5.10: P8Z64: a) skewness of velocities; b) kurtosis of velocities; c) streamwise energy spectra at $y^+ = 5.4$; d) spanwise energy spectra at $y^+ = 5.4$

higher than $Re_C = 900$, above which the flow is considered fully-turbulent [80], low-Reynolds-number effects are expected to be present. In fact, Moser *et al.* [79] maintain that such effects persist up to $Re_\tau = 395$. This raises the question whether control simulations above a critical Reynolds number could produce results of universal validity. By combining the most recent insights into turbulence scaling with certain assumptions about the workings of drag control, light is shed on this problem.

First, it should be noted that these effects depend on the distance from the wall because the physics do so, too. It is heuristically assumed that for actuation applied at the wall the correct representation of turbulence close to the wall is most important. Under this presumption, the focus is on the viscous region $0 \leq y^+ \leq 10$. To analyse this region for different Reynolds numbers, the flow is non-dimensionalised with viscous scales, that is the friction velocity, u_τ^*, and the viscous lengthscale, L^{+*}. The Reynolds number is then absorbed into y^+. Thus, for the region $0 \leq y^+ \leq 10$, where the flow is dominated by viscous effects, profiles of different Reynolds numbers should in theory collapse.

For the comparison datasets from four different Reynolds numbers, Re_τ =100 [64], 180 [45], 650 [48], and 2000 [45], are taken. Profiles of statistical variations from the wall are shown in figure 5.11 for all four sets. Frame 'a' reveals that the mean velocity profiles collapse for $y^+ < 10$. As expected the departures from the linear relation $u^+ = y^+$ are negligible in the viscous sublayer ($y^+ < 5$). So in terms of the mean velocity profile in the viscous region, low-Reynolds number effects are absent and $Re_\tau = 100$ is an adequate Reynolds number to produce typical wall turbulence.

The profiles of rms velocity fluctuations are depicted in frame 'b'. These statistical quantities are important because they determine the kinetic energy and are known to be sensitive to Reynolds number effects [79]. The near-wall peaks of u_{rms} increases steadily with Reynolds number. Even more striking are the profiles of rms vorticity fluctuations in frame 'c'. In the case of the streamwise and spanwise component, not even the values at the wall agree. This contradicts the belief that the flow close to the wall is only influenced by viscous effects. The phenomena can only be explained by near-wall modes interacting with modes residing away from the wall. In conclusion, all results in this work are affected by Reynolds number effects,

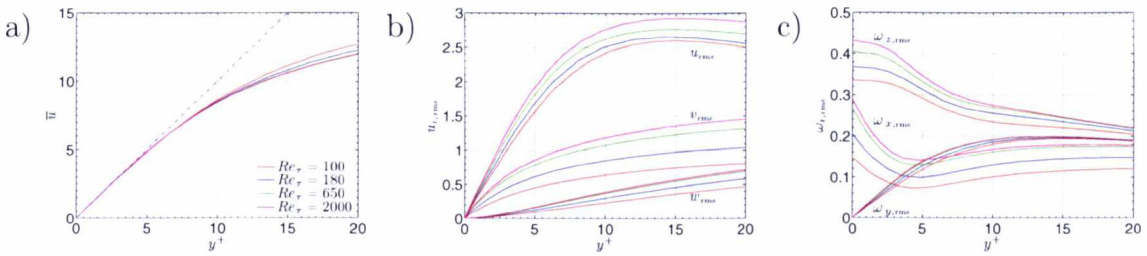


Figure 5.11: Comparison of near-wall turbulence at different Reynolds numbers: $Re_\tau = 100$ (red), 180 (blue), 650 (green), 2000 (magenta). a) mean velocity; b) rms velocity fluctuations; c) rms vorticity fluctuations. All rms values increase with Reynolds number.

in particular statistics of order greater than one. But can these effects be overcome in simulations in the foreseeable future? Recent experiments suggest otherwise. For example, Morrison *et al.* have shown that the Reynolds-number-dependence of the streamwise velocity fluctuations in the viscous layer persists at least up to $Re_\tau = 10^4$ [78]. This has lead some researchers to suggest a logarithmic dependence of the peak value in the rms streamwise velocity profile on Reynolds number [75].

Given the results from this analysis, there appears to be no immediate necessity to study control algorithms at higher Reynolds numbers. The increased computational costs would bring little benefit in the sense of reduced Reynolds-number effects. Simulations at $Re_\tau = 100$ might not be ideal but, at this stage, justifiable. Besides, it is not proven that a control algorithm's performance will vary with Reynolds number. In fact, opposition control delivers constant performance for Reynolds numbers ranging from Re_τ =110 to 650 [47], which is an interesting result that will be discussed in section 7.1.1. Another example for Reynolds-number independence of control strategies are riblets, which also affect near-wall turbulence and have shown to reduce skin-friction drag during a test flight of a commercial aircraft, despite being mainly tested at low Reynolds numbers, both numerically and experimentally [59].

To get an idea of the computational load involved one should consider that, at the time of writing, the highest Reynolds numbers ever achieved are Re_τ =

650 in controlled channel DNS [46] and $Re_\tau = 2000$ in unmanipulated channel DNS. The latter was performed independently on the Earth Simulator [49] and the Marenostrum computer [45]; currently two of the most powerful computer sites in the world [101].

On a positive note, there is an obvious Reynolds-number invariance of the wall-normal-vorticity profiles in frame 'c' of figure 5.11. Close to the wall this quantity is dominated by the streaks through the term $\frac{\partial u}{\partial z}$. Accordingly, the invariance of $\omega_{y,\mathrm{rms}}$ implies a constant spacing of streaks, an observation that is consistent with experimental results. Even for very high Reynolds number flows such as in the atmosphere streaks are spaced 100 wall units apart [75]. With these structures widely seen at the core of turbulent drag this invariance could prove significant for the scaling of control performance and support the use of low-Reynolds number simulations.

Chapter 6

Turbulent channel flow over active wall deformation

In this brief chapter it is examined how a moving dimple interacts with wall turbulence. For laminar flow a similar study was presented in Chapter 4 where the absence of background turbulence allowed clear identification of the disturbances created by the actuators. Here, the differences that arise when the flow is turbulent are described.

The main finding in the laminar-flow simulations was that moving obstacles create complex vorticity perturbations whereas the velocity structures are intuitively predictable. In particular, an actuator that is in motion is surrounded by a single lobe of wall-normal velocity. This perturbation penetrates far into the domain compared to the streamwise-velocity perturbation. In turbulent flow one would expect the penetration length to be more clearly defined as the turbulent fluctuations increase with distance from the wall, eventually overshadowing the actuator-induced perturbation. This postulate is verified in this chapter.

Instantaneous shots of flowfields from three different simulations are analysed. In Case 1 transient actuators pop down (dimple) and up (bump) once in a fully-turbulent flow. In Case 2 the same initial turbulent flowfield as in Case 1 is stepped forward in time but in absence of actuators. In Case 3 the flow is laminar and actuated in the same way as in Case 1. Each case was simulated only once using the

domain and resolution of Case P8Z64 of table 5.1. For the turbulent cases, Case 1 and Case 2, P8Z64 also provided the initial field.

The same Reynolds-number value was chosen for all simulations, but based on friction velocity rather than centerline velocity. The reason for this choice is that the flow close to the wall should be similar for all cases since this is the region where the actuator has the strongest effect. When linearising the flowfields around the near-wall baseflow, this similarity implies that the overall perturbation in Case 1 is a superposition of the turbulence fluctuations of Case 2 and the actuator-induced perturbation of Case 3. The validity of this rough approximation worsens with increasing actuation strength, time horizon, and distance from the wall.

To cope with the irregular walls, the flow was solved in a boundary-fitted coordinate system. Again, identical actuators were placed on lower and upper wall to make the Jacobian universally one. This geometry, which was already shown in figure 4.1, facilitated the use of the equations presented in section 3.1.3. In the present study, the expanded form of the extra term A^i of expression (3.34) is identical to the one given in section 4.4.1. Because this analysis is constrained to active dimples, only the flow region close to the lower wall is analysed.

6.1 Parameters

The parameter values of the cases under investigation are given in table 6.1. Case 1 and Case 3 share the same values for the actuator parameters. The amplitude, ϵ, is 8 wall units which should be enough to trigger non-linear boundary effects. The spatial mean variation of the obstacles, σ, is 0.33 in both homogenous directions. The time-motion parameter based on friction velocity, $\sigma_{t\tau}$, is 0.14. The centre of the obstacles is now located at $(x_0, z_0) = (0.25, 2.094)$ which is close to the middle of the walls.

Table 4.1, which provided the actuator parameter values for the laminar-flow simulations, can be compared to table 6.1. This comparison reveals that the amplitude is now smaller and the radius is larger. Also, the value for σ_t is larger which means that the obstacles are moving more slowly. Another difference to the laminar

flow study is that the domain is now periodic in the x-direction. As a result, the flow perturbations due to the actuation are flowing back into the domain. However, the streamwise length of the domain is large and the simulation time is short. Therefore, the difference compared to a simulation with in- and outflow conditions is assumed to be small.

In section 4.1 it was mentioned that the actuator parameters should roughly correspond to what would be necessary for skin-friction control. In Chapter 7 it is found that the average magnitude of the normal wall velocity for standard opposition control is $v_{\mathrm{W\,rms}} = 0.072$. To compare this to the obstacle motion in the present chapter, the average magnitude of the obstacles' velocity at the centre point, $v_{\mathrm{rms}}(x_0, y_{\mathrm{W}}, z_0)$, is calculated for the time period $0 \leq t \leq 0.23$, where $t = 0.23$ is the time the obstacles reach 99% of their deflection. This calculation yields $v_{\mathrm{rms}}(x_0, y_{\mathrm{W}}, z_0) = 0.413$. Hence, the actuation at the centre of the obstacles can be considered strong relative to the average actuation strength found in opposition control. It should be noted though that according to Choi *et al.* [15] the strong events are of particular importance in opposition control. At $\sigma_z = 0.33$, the diameter of the actuator is larger than half of the streak spacing but of the same order. This discrepancy is probably less significant since no attempt will be made to place the dimple directly under a streak.

6.2 Flow analysis

Turbulent flows are vastly more complex than laminar ones. To derive information from the available data, the flow quantities to be analysed must therefore be chosen carefully. To focus on the interaction between the actuator and the adjacent flow, the quantitative analysis is restricted to streamlines and contour plots of wall-normal velocity and streamwise vorticity. Those plots are shown for planes located in xy- and zy-direction, as was schematically depicted in figure 4.4.

In Chapter 4 it was discovered that a transient dimple is characterised mainly by two distinct states, the moving state when the dimple is at full speed and the stationary state where most transients have decayed. Based on this finding, only

Case	Flow param		Flow State
	Re_τ	Re_C	
1	100	1680	Turbulent
2	100	1680	Turbulent
3	100	5000	Laminar

Case	Actuator parameters							
	ϵ	σ_x	σ_z	$\sigma_{t,C}$	$\sigma_{t,\tau}$	$v_{W,rms,C}$	$v_{W,rms,\tau}$	f_{rms}
1	0.08	0.33	0.33	2.33	0.14	0.025	0.413	0.047
2	-	-	-	-	-	-	-	-
3	0.08	0.33	0.33	6.94	0.14	0.008	0.413	0.047

Table 6.1: Simulation parameters. rms values are calculated for $0 \leq t \leq 0.23$.

two-points in time are studied, $t = 0.15$ and $t = 0.6$, at which the flow response represents the aforementioned states. The results at these two time instants are plotted in figures 6.1 to 6.4. In each row the left picture corresponds to Case 1, the middle one to Case 2, and the right one to Case 3. Note that these images make the amplitude of the obstacles appear larger since the y-direction is stretched by a factor of 3 for viewing purposes.

Figure 6.1 shows streamlines and v-contours of the moving state in the xy-midplane. As expected from the motion of the dimple, the wall-normal-velocity perturbation is clearly dominating the surrounding flow. But in the turbulent flow of Case 1, it appears that the perturbation reaches further into the domain than in the laminar flow, Case 3. Qualitatively, the wall-normal-velocity perturbation induced by the moving dimple in Case 1 and Case 3 is comparable to the observations made in Chapter 4, as can be seen for example in the frame of figure 4.8 where $t = 1.5$. This also holds for the streamlines which, as shown in figure 4.20, turn into the dimple from above.

Figure 6.2 shows the same plots as figure 6.1 but for the quasi-static case at

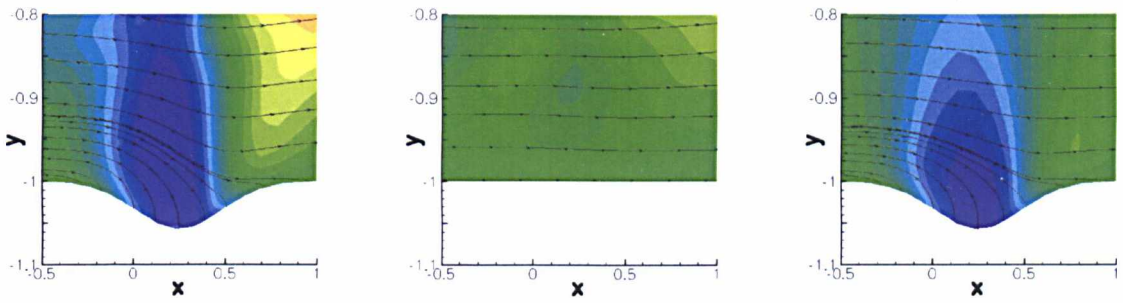


Figure 6.1: Streamlines and (-0.5≤v≤0.5)-contours in xy-midplane around dimple at t = 0.15 (72%). Left: Case 1. Middle: Case 2. Right: Case 3. For viewing purposes flow structures have been stretched by a factor of 3 in the wall-normal direction.

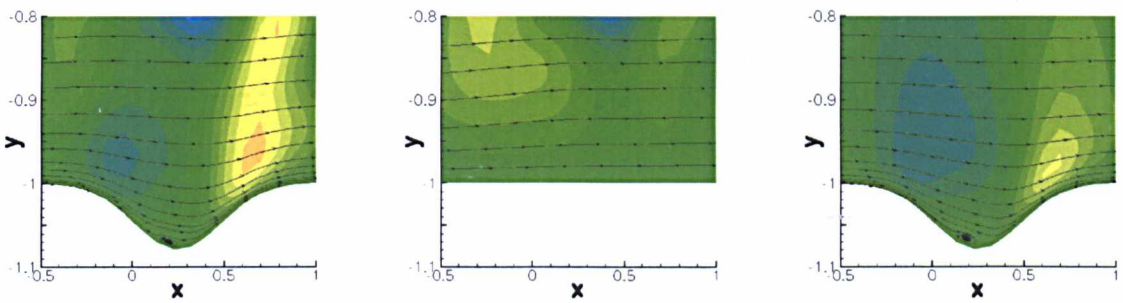


Figure 6.2: Streamlines and (-0.5≤v≤0.5)-contours in xy-midplane around dimple at t = 0.6 (100%). Left: Case 1. Middle: Case 2. Right: Case 3. For viewing purposes flow structures have been stretched by a factor of 3 in the wall-normal direction.

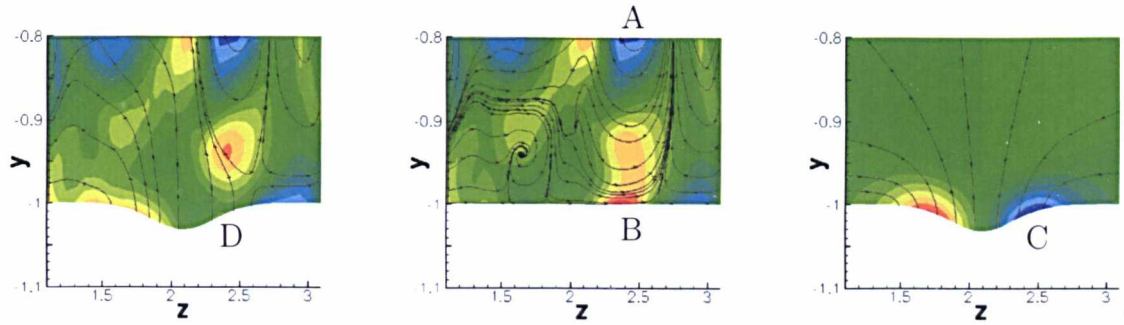
t = 0.6. Since the dimple has stopped moving the wall is no more a sink for streamlines. As observed in the laminar simulations of Chapter 4, the fluid goes in and out of the dimple as it flow downstream. Since the ratio between amplitude and radius is less than in the laminar simulations, the separation bubble is smaller. It is located at the very bottom of the dimple. At this point in time, the streamlines in Case 1 and Case 3 are almost identical. There is also little difference in the wall-normal velocity contours between these two cases. As in the moving state there is stronger vertical component of the flow downstream of the dimple when the flow is turbulent which seems also to effect disturbances found 20 wall units away from the wall in the upper-right corner.

Having analysed the flowfield in the xy-midplane we now turn to (y,z)-planes. Figure 6.3 shows streamlines and ω_x-contours in these planes for the moving state at different locations in x. Because there is no mean flow in the z-direction the structures are now significantly more complex than in the xy-midplane. Most notably, the dimple motion has great effect on little vortical structures close to the dimple. Whereas many little vortices exist in this region in the unactuated Case 2, none can be found in Case 1. An example of a near-wall vortical structure that is annihilated by the actuator-induced perturbation can be found at point E in Case 2. The streamlines suggest that the little vortical structures are overwhelmed by the gross down-flow region the dimple creates. As a result, the flow around the dimple becomes more regular. As expected, this effect is of limited extent: at $y>-0.9$ the flow remains largely unaffected by the moving obstacle. This is very important with respect to wall-based control and will be discussed in more detail later.

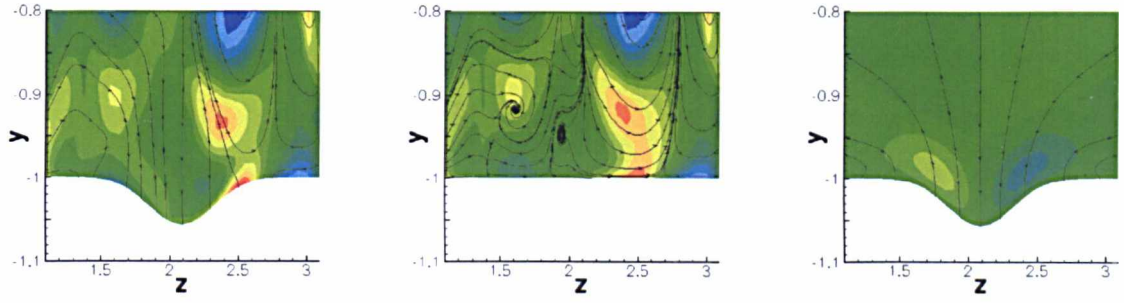
The streamwise-vorticity patterns in figure 6.3 agree with previous observations in Chapter 4. Case 1 shows that the vorticity generated by the actuation is roughly of the same order as the natural structures in the near-wall region. This suggests that, in theory at least, wall deformation actuators could be used to cancel vorticity flux, as proposed by Komoutsakos *et al.* [63]. For example, in Case 2 there is a negative ω_x-region at point A. The no-slip condition causes flux of positive ω_x at point B. At the same location in Case 3, point C, the dimple generates flux of negative ω_x which, in effect cancels the pre-existing one in Case 1, as seen at point D.

Figure 6.4 shows the same plots as figure 6.3 but for the stationary state. Coincidentally, there is generally more streamwise vorticity due to background turbulence than at the moving state. The streamlines of Case 3 reveal the usual pattern of fluid going in and out of the dimple as it flows downstream. Close to the wall this pattern can also be found in the turbulent Case 1. Since more time has evolved Case 1 and 2 are now less comparable. Despite this, similar structures are still apparent in both cases, in particular at some distance away from the dimple. In Case 2 a little vortical structure is found at point F that does not appear in Case 1. It is possible that this structure is overshadowed by the downward movement at the leading edge

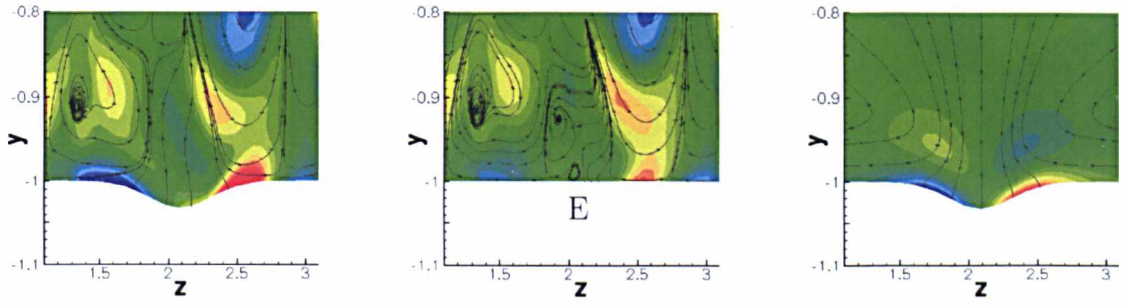
$x = 0.0$: upstream of centre



$x = 0.25$: centre



$x = 0.5$: downstream of centre



$x = 1.0$: far downstream of centre

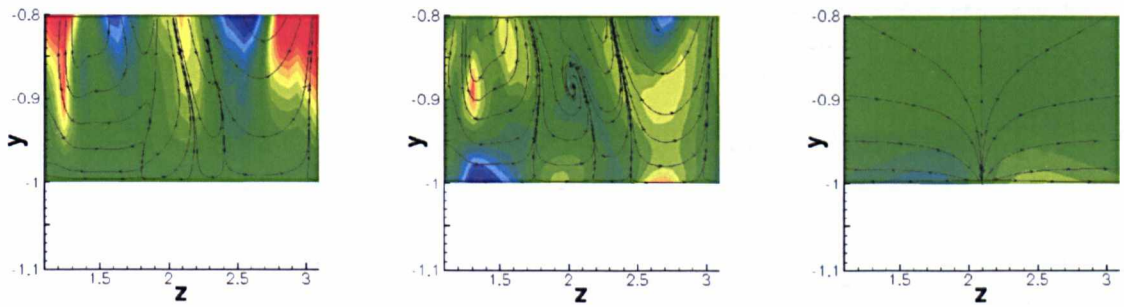


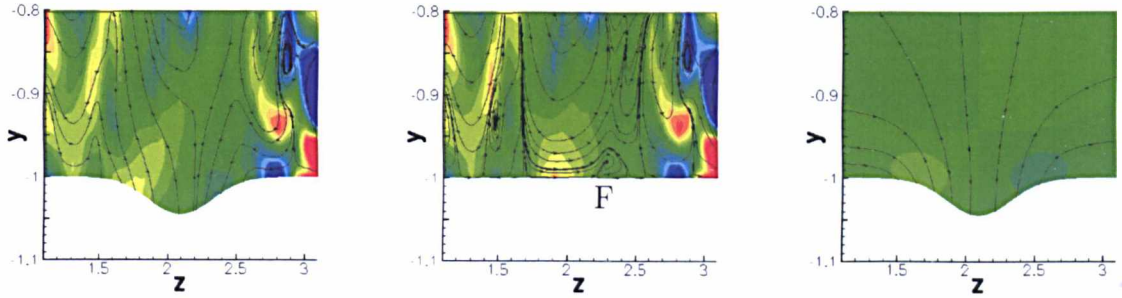
Figure 6.3: Streamlines and (-30≤ω_x≤30)-contours in (y,z)-planes at t = 0.15 (72%). Left: Case 1. Middle: Case 2. Right: Case 3. Domain stretched by a factor of 3 in the wall-normal direction.

of the dimple. The opposite is found in Case 1 at point G (inside the image) where a new vortical structure is formed inside the domain by the same downward flow. But this structure does not persist far downstream as the the wall-normal flow changes direction downstream of the centre.

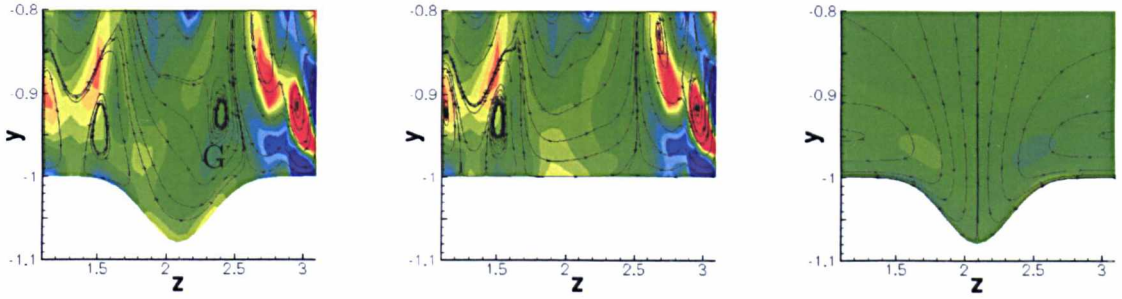
To summarise the analysis of the flow visualisation, it was found that for these specific parameter values the actuator has a strong influence on the surrounding wall turbulence with a clear limit to the extent of its influence. Often smaller structures close to the wall vanish by being overridden by the induced perturbation. In particular, the actuator can impose a wall-normal velocity of a certain strength and direction which could be used as a means to control the flow. The results also show that vorticity flux could potentially be manipulated if only the necessary strength of actuation for a certain flux could be estimated. This problem was addressed in section 4.2.

The reach of the actuation, that is the perturbation length, is now investigated in a quantitative matter. For this purpose the velocity values above the centre of the dimple, $(x, y, z) = (x_0, y, z_0)$, are extracted from Case 3 at the moving state, $t = 0.15$, and the quasi-static case, $t = 0.6$. These values are then compared to the rms velocity fluctuations, $u_{i,\,\mathrm{rms}}$, of the turbulent channel of Case 2, which were already presented in figure 5.9. This comparison is shown in figure 6.5. In frame 'a' ($t = 0.15$) the dimple of Case 3 is in full motion and has already deflected by 72% of its amplitude, hence the streamwise velocity, u, as well as the wall-normal velocity, v are perturbed. As was already observed in Chapter 4 these perturbations of u and v drop monotonically for increasing wall distance, but far steeper for u than v. As opposed to the actuator-induced perturbations of Case 3, the turbulent fluctuations of Case 2 strengthen monotonically with increasing wall distance in the near-wall region. Therefore, at a specific distance from the wall the perturbation due to actuator movement and the turbulent fluctuations must be of equal magnitude. We shall denote this distance as penetration length. In frame 'a' ($t = 0.15$) the point of equal magnitude is located around 5 wall units from the wall in the case of u and 15 wall units in the case of v. Both points are indicated by small circles in the plot. By that token – and under the assumption that the control should target

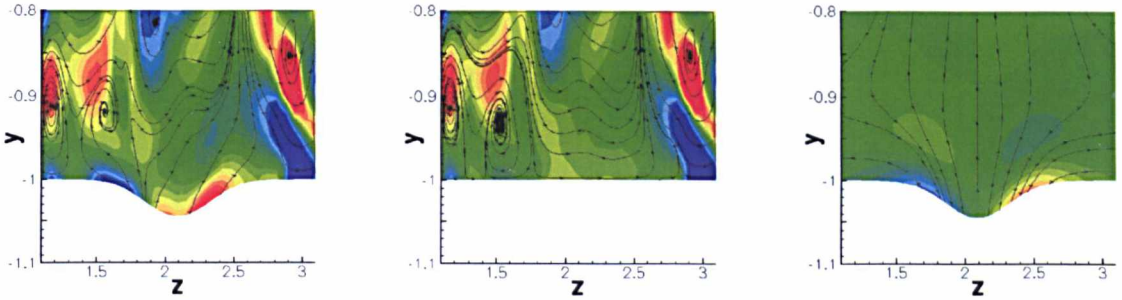
$x = 0.0$: upstream of centre



$x = 0.25$: centre



$x = 0.5$: downstream of centre



$x = 1.0$: far downstream of centre

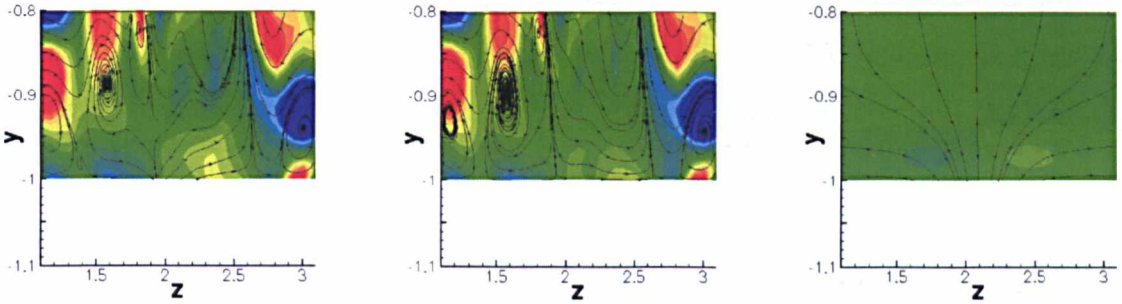


Figure 6.4: Streamlines and (-30≤ω_x≤30)-contours in (y,z)-planes at t = 0.6 (100%). Left: Case 1. Middle: Case 2. Right: Case 3. Domain stretched by a factor of 3 in the wall-normal direction.

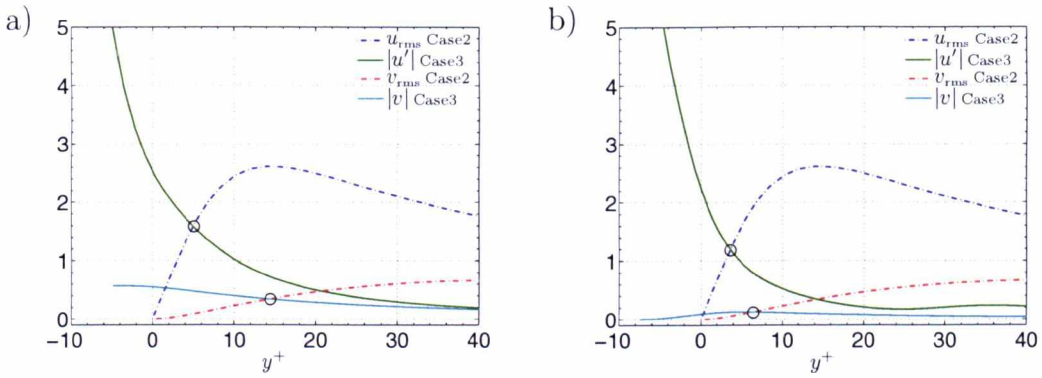


Figure 6.5: Comparison of root-mean-square velocity fluctuations in Case 2 and absolute velocity perturbations above the centre of the dimple in Case 3. a) $t = 0.15$ (72%); b) $t = 0.6$ (100%).

the turbulent velocity fluctuations – the vertical velocity perturbation has a much higher penetration ability than the streamwise one.

The same analysis is conducted in frame 'b', where the actuator has stopped moving and most of the transients around it have decayed. One could expect the penetration length of u' to be larger since the deflection has increased which in turn has increased the perturbation at the wall. But in fact, the penetration length of u' has even decreased by one wall unit.

The issue of penetration ability has some important ramifications. One is that the high decay in the case of u' would require very high actuation strength for u' to manipulate u away from the wall. This is unfavourable because for reasons of practicality and efficiency strong actuation should be avoided. Also, there is a high risk that strong perturbations close to the wall could trigger unwanted side effects. Another ramification is that the high gradient of the decay translates to a higher sensitivity to y. As a result, inaccuracies in the location of the detection plane could lead to large errors.

From the quantitative analysis of penetration length, it can be concluded that wall deformation actuators are best used to impart wall-normal momentum rather than streamwise momentum. Control algorithms based on such actuation are available. An example is opposition control, which is introduced in the next chapter.

Chapter 7

Opposition control in turbulent channels by wall deformation

Chapter 5 described the process of creating a simulation of turbulent channel flow as a precursor for control studies. Reasonable computational costs combined with good overall agreement of turbulence statistics were found for case P7Z48, thereby making it the right candidate for a series of flow control experiments that are presented in this chapter.

This series contains simulations that are linked by a single logical thread: starting from standard opposition control by wall transpiration, it is developed to the ultimate goal, opposition control by wall deformation. The intermediate experiments were conducted to extract additional information and to set the parameter values in a way to maximise the rate of drag reduction, also referred to as controller performance.

Opposition control is only one option among a wide choice of control methods. It was selected for its ease of implementation and for its popularity in the flow control community. Introduced in 1993 by CMK (Choi *et al.* [15]), it has established itself as a benchmark for physically-intuitive control methods. A brief introduction to opposition control was given in Chapter 2 but the next section will review the literature on opposition control in more detail, in particular with respect to the present study. This is followed by a number of sections explaining the various

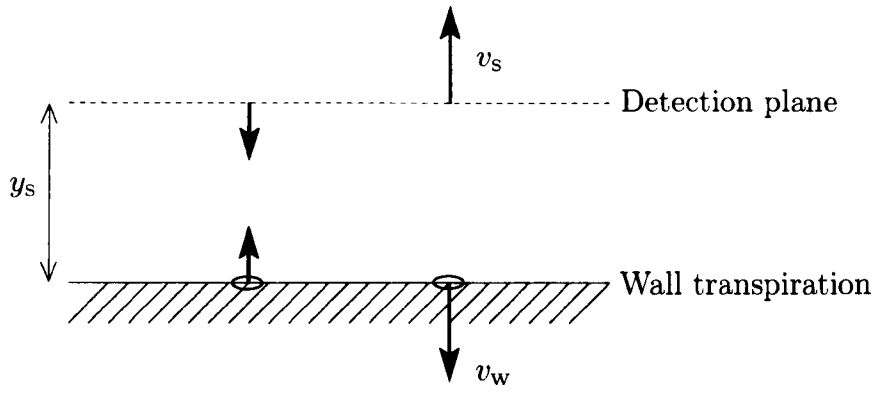


Figure 7.1: Schematic diagram of opposition control by wall transpiration.

complications in using wall deformation for opposition control. The chapter ends with the discussion of the results retrieved from the flow control experiments.

Turbulent channel flow at a certain Reynolds number can be driven by either a constant driving force or a variable driving force keeping the flowrate constant. With a constant driving force the flowrate is not known *a priori* and *vice versa*. In order to measure a reduction in drag, which is the aim of implementing a controller, the flowrate must be held constant. A method to calculate the necessary driving force for a constant flowrate was explained in section 3.4.

7.1 Standard opposition control

The v-out-of-phase control scheme by CMK, also known as opposition control [41], senses the wall-normal velocity in a plane some small distance from the channel wall and then opposes with transpiration at the channel wall such that

$$v_w(x,z,t) = -v_s(x,z,t) = -v(x,y=y_s,z,t) \tag{7.1}$$

where v_w is the wall velocity, v_s is the wall-normal velocity at the detection plane, and y_s is the location of the detection plane. In graphical form this scheme is explained in figure 7.1.

Using this scheme, CMK achieved about 25% reduction of skin-friction, accompanied by weakened turbulence intensities and Reynolds shear stress throughout the flow. They also observed a general outward shift of turbulence statistics and

attributed the drag reduction to the opposition and stabilisation of streamwise vortices.

Regarding the location of the detection plane, they found $y_s^+ = 10$ to be optimal whereas in another study Hammond *et al.* [41] report the optimal location to be $y_s^+ = 15$. Later, Chung and Sung [18] argued that the drag reduction is not influenced by the position of the detection plane as long as it is located within $10 < y_s^+ < 20$. For observation locations above this range increases in drag were reported [15].

In reality, sensing inside the flow is not practical as MEMS sensors generally only have access to information at the wall. However, it has been shown that there is a correlation between spanwise shear $\partial w/\partial y$ at the wall and turbulent coherent structures in the near-wall region [66, 67, 27]. In theory, this correlation can be used to estimate the flow inside the domain. For this approach, the sensing layer should be as close to the wall as possible because correlations decrease with distance from it. Adhering to this idea, the detection plane was placed 10 wall units away from the wall in the present simulations which is the lowest value attainable without impeding the controller performance.

Chung and Sung [18] also introduced an additional parameter to opposition control. They manipulated the amplitude of the actuation, A, and found that in the range $0.5 \leq A \leq 1$ the rate of drag reduction stayed almost constant. This relationship opens the prospect of reducing the overall energy balance by actuating at lower strength.

The outward shift of turbulence observed by CMK indicated a displaced virtual origin of the boundary layer. This feature of the flow was later coined "virtual wall" by Hammond *et al.* [41]. It prevents the vertical motion of flow while allowing slip. They showed that this phenomenon does not occur when the detection plane is at a large distance ($y_s^+ \approx 25$), concluding that it must be the characteristic feature of flows subjected to this form of control.

Physical explanations for the reduction in drag were given by CMK. The mechanisms were studied with two different approaches: a minimal flow unit and an isolated vortex pair interacting with a wall. By studying time sequences, two mechanisms were identified. First, within a short time after control is applied, drag

is reduced mainly by the deterring of sweep motion. Secondly, the active control changed the evolution of the wall vorticity layer by stabilising and preventing uplift of the vorticity near the wall. The absence of this lifting process weakens a source of new streamwise vortices near the wall.

It is interesting to note that the first mechanism makes no assumption about the cause of vertical motion. Even if vortices played no significant role in the formation of streaks [14], the sweep motion could still be deterred in this manner, no matter if it were organised or not. One result that supports this possibility is that the scheme works well for detection planes at $y_s^+ < 10$ which is a value much lower than the average centre of streamwise vortices, $y^+ = 20$.

A mathematical explanation for the workings of opposition control was given by Kim and Lim [61]. Combining the Orr-Sommerfeld-Squire equations (see section 8.1) with the non-linear terms, they found that both the non-linear terms and the linear coupling term, L_C, are necessary for the formation and maintaining of coherent structures at their proper scale. The non-linear terms are necessary for the formation of streamwise vortices and the coupling term is necessary to generate the wall-layer streaks, the instability of which in turn drives the streamwise vortices through the non-linear terms. In the absence of either mechanism, turbulence ceases to exist. Considering that the vertical velocity, v, and the vertical vorticity, ω_y, are coupled through the term $k_z(\partial U/\partial y)\hat{v}$, the opposition control scheme can be viewed as a control scheme trying to reduce the effect of coupling by suppressing the spanwise variation of v in the wall region.

In terms of energy balance it must be remembered that as an active control strategy, opposition control adds energy to the flow. However, it modifies the perturbation structures in such a way that interaction of the mean flow and the perturbation reduces Reynolds stress.

7.1.1 Reynolds number effects

In section 5.3 the issue of Reynolds-number-dependence of unmanipulated turbulent channel flow was addressed. It was argued that for the purpose of turbulence control

in the viscous layer, the use of low-Reynolds-number simulations can be justified. This conclusion is confirmed by results from Iwamoto *et al.* [47], who performed opposition control experiments at $Re_\tau = 110$ to 650 and found that the scheme offered almost constant drag reduction (19-22%) for all Reynolds numbers examined. This promising results indicates that, indeed, the drag reduction found at lower Reynolds numbers might persist into higher regimes.

Yet, drag reduction is not the most relevant measure. More important is the total power gain which determines the effectiveness of the control algorithm. To compute this quantity, Iwamoto *et al.* define the power input as

$$P_{\text{in}} = \overline{p_{\text{W}} v_{\text{W}}} + 0.5\rho\overline{v_{\text{W}}^3} \tag{7.2}$$

and the pumping power as

$$W = -\frac{\partial \bar{P}}{\partial x} u_{\text{B}} \ , \tag{7.3}$$

where $-\partial P/\partial x$ is the averaged streamwise pressure gradient. Then, the power gain G is defined as the ratio of pumping power saved to control power input, so that

$$G = \frac{W_0 - W}{P_{\text{in}}} \ , \tag{7.4}$$

where W_0 is the pumping power in the unmanipulated case. Using this expression, Iwamoto *et al.* reported that the power gain dropped from 260 at $Re_\tau = 110$ to 60 at $Re_\tau = 650$ but converged at higher Reynolds numbers. They attribute this phenomenon to the increase of pressure fluctuations. Arguing on the basis of these results, simulations at very low Reynolds numbers cannot predict total power gain in laboratory environments but at such high levels this can be tolerated. In fact, the theoretical values are so high that one could justify simplifying the design goal to a maximisation of drag reduction. But issues of power requirement can be expected to resurface in the construction of actuators where energy losses will need to be addressed.

7.2 Opposition control by wall deformation

The opposition control scheme discussed in the last section uses wall transpiration as a means of actuation. Instead of this, momentum in the y-direction may also be

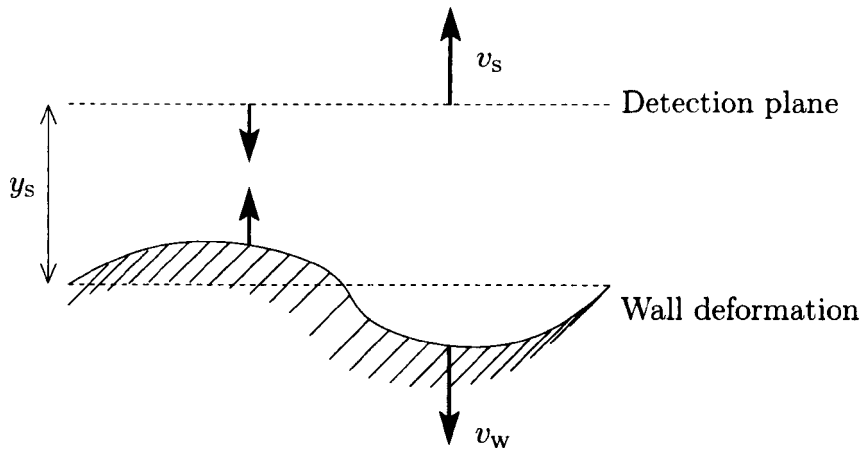


Figure 7.2: Schematic diagram of opposition control by wall deformation.

added by deforming the channel wall itself. This scheme, which is depicted in figure 7.2, was used to various degrees of success in studies by Kang and Choi [54], Endo *et al.* [27], and Kellogg [58] – all published in the year 2000. Drag reductions were reported throughout but never reached more than 17%. To date, this significant drop in performance compared to opposition control by transpiration has not been studied in detail but it is commonly attributed to the deformation restriction.

This restriction says that the wall is not allowed to deflect above a certain limit. Failing to do so, will eventually cause the wall to penetrate the sensing plane, leaving an ill-posed problem. But the significance of this constraint reaches further. Most certainly, any actuator in the laboratory will be of limited deflection, making such a restriction a necessity for any real-world experiment. Imposing this restriction is a delicate matter and has not received enough attention. Section 7.2.1 attempts to explore this issue in more detail.

Another difference to wall transpiration which has drawn little attention is that wall deformation cannot perfectly replicate wall transpiration. Secondary effects will occur that are not taken into account by the control algorithm. Their influence can be demonstrated by expanding the perturbation to the order of the amplitude, as outlined in section 4.3.1. This approximation decomposes the actuation into wall motion and wall deformation. The wall motion can mimic transpiration but the deformation is left unaccounted for. Some argue that the deformation is negligible when it is small enough to be considered hydraulically smooth but this is not

straightforward when time-dependence is involved. Also, it is unknown what effect deformation has when it is coordinated with the adjacent flow events, that means correlated with the measurements at the detection plane. The issue of secondary effects will be revisited in section 7.2.2.

Apart from these general difficulties encountered, the implementation of wall deformation also raises specific numerical issues. One issue is that in the present code the bandwidth of the actuation must be restricted at the top to achieve numerical stability. This restriction is a nuisance but has its benefits. Actuators cannot be built infinitely small and, thus, results of simulations with large-scale actuation have more practical relevance. This matter is subject to further discussion in section 7.2.3. Another numerical issue is the choice of coordinate system. As a matter of convenience the one used for the laminar simulations is slightly modified in the way it is presented in section 7.2.5. These changes do not affect the Jacobian of the system which must remain one throughout the domain. For control simulations this has an important consequence: Only one wall at a time can be controlled whereas the other wall must replicate the same motion irrespective of the adjacent turbulent events. The ramifications of this constraint are discussed in section 7.2.4. On the same subject it should be remembered that the mean location of each wall remains constant throughout the simulation as this is required by the incompressible flow assumption.

7.2.1 Restriction in wall deformation

If the opposition control method is used in conjunction with active wall deformation the wall cannot breach the sensing plane. Since the deformation of the wall is determined by integrating the wall velocity, the condition can be enforced by restricting the wall velocity so that

$$v_{\mathrm{w}}(x,z,t) = A(x,z,t)\hat{v}_{\mathrm{w}}(x,z,t)\ , \tag{7.5}$$

where $\hat{v}_{\mathrm{w}}$ denotes the uncorrected actuation velocity and $A := A(x,z,t)$ is a spatially and temporally varying amplitude. Regardless of its formulation, A is likely to have some influence on the rate of reduction.

Chung and Seng [18] have investigated the effect of constant-amplitude modification. They found that the effectiveness of opposition control is almost constant for $0.5 < A < 1$. This low sensitivity to changes in strength implies that the control is "robust" and allows for inaccuracies. Moreover, the energy input can be lowered by lowering the amplitude, should this be required. Another piece of information about the effect of amplitude modification was provided by CMK who also tried v-in-phase control, that is $A = -1$. They reported a significant increase of drag before the simulation broke down. This is consistent with the intuition that in-phase control enforces the sweep and ejection events.

In the present work, the amplitude modificator, A, varies in both homogenous directions and in time. It also depends on the local state of flow which means that it is not known *a priori*. Regardless of this non-uniformity of A, it is assumed that the aforementioned findings still apply, albeit locally. Arguing on the basis of these results, the formulation of A should be designed such that its resulting distribution function is clustered in the insensitive range of $0.5 < A < 1$ to maintain the control character. Also, the distribution must be kept at a minimum around $A = -1$ to avoid local increase in drag which would negate the control objective. Before formulating an expression for A based on these considerations, choices that are obvious or were used by other investigators in the past are discussed.

An obvious choice is to define a maximum deflection for the deformation so that when a certain location of the wall reaches or approaches the maximum amplitude, it becomes inactive. This means that $A := 0 \wedge 1$. Numerically, this method is very problematic since a binary amplitude function causes discontinuities in time and space that the boundary-fitted coordinates system is not suited for. Also, discontinuities in the actuation allow for high truncation errors impeding the accuracy of the results. With other, safer options available this method is not taken into consideration.

Kellogg [58] also defined a maximum amplitude but enforced it differently. In his simulation the entire vertical velocity field was modified once a point had reached

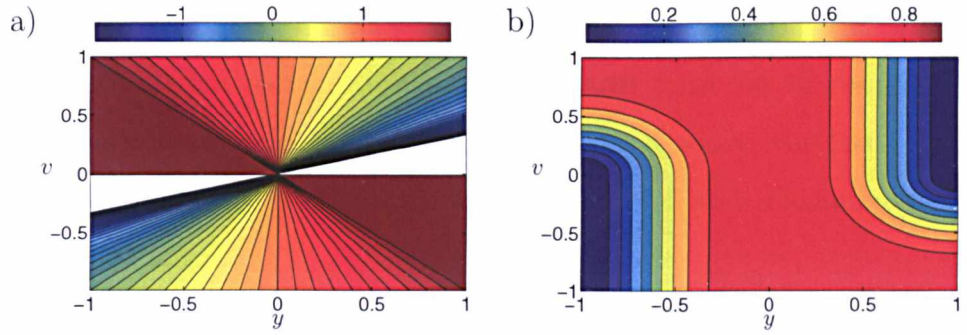


Figure 7.3: Amplitude A for different values of $\hat{v}_{\mathrm{w}}$ and y_{w}: a) expression (7.9) at $\chi = 0.01$; b) expression (7.11) at $\kappa_y = -5$, $\kappa_v = -5$, and $f_{\max} = 1$.

maximum wall deformation, so that

$$v_{\mathrm{w}}(x, z, t) = \hat{v}_{\mathrm{w}}(x, z, t) - \hat{v}_{\mathrm{w}}(x_m, z_m, t) \ , \tag{7.6}$$

where m denotes the point in space an time where maximum deformation was reached. In terms of amplitude function, expression (7.6) is equivalent to

$$A(x, z, t) = 1 - \frac{\hat{v}_{\mathrm{w}}(x_m, z_m, t)}{\hat{v}_{\mathrm{w}}(x, z, t)} \ . \tag{7.7}$$

Contrary to the previous method, this formulation of A ensures that the actuation remains smooth in space. In time, however, discontinuities can still occur. Furthermore, the amplitude can adopt values close to $A = -1$.

Endo *et al.* [27] opted for an entirely different technique where the wall velocity is constantly damped depending on the wall deflection. This condition is formulated as

$$v_{\mathrm{w}}(x, z, t) = \hat{v}_{\mathrm{w}}(x, z, t) - \chi y_{\mathrm{w}}^{+}(x, z, t) \ , \tag{7.8}$$

where χ is a penalty parameter to be assigned. Using again the amplitude function, equation (7.8) can be expressed as

$$A(x, z, t) = 1 - \chi \frac{y_{\mathrm{w}}^{+}(x, z, t)}{\hat{v}_{\mathrm{w}}(x, z, t)} \ , \tag{7.9}$$

which is shown in frame 'a' of figure 7.3. This is a formulation where smoothness is guaranteed in both space and time. But the amplitude can attain again $A = -1$, thereby increasing drag.

With these apparent insufficiencies in previous formulations it is evident that a better formulation can be designed. The goal must be to combine numerical robustness with optimal distribution. As explained above, the latter is defined as a distribution that has little weight around $A = -1$ and maximum weight in the range $0.5 \leq A \leq 1$.

In a first attempt to achieve this, expression (7.9) is slightly modified by introducing the factor ϖ so that

$$A(x,z,t) = \varpi \left(1 - \chi \frac{y_{\mathrm{w}}^{+}(x,z,t)}{\hat{v}_{\mathrm{w}}(x,z,t)}\right) \quad 0.5 < \varpi < 1.0 \; . \tag{7.10}$$

This attenuates the actuation strength so that the wall deflects less which in turn reduces the penalty.

But negative amplitudes can also be avoided altogether in the following way. The general concept comprises again the definition of a deformation limit. But instead of abrupt changes, the wall is forced to slow down as it approaches the defined maximum. Mathematically, such an amplitude function can be formulated as

$$A(x,z,t) = \begin{cases} 1 - e^{\left(\kappa_y |y(x,z,t) - f_{\max}|^2 + \kappa_v \hat{v}_{\mathrm{w}}^2(x,z,t)\right)} & y(x,z,t)\hat{v}_{\mathrm{w}}(x,z,t) < 0 \; , \\ 1 - e^{\left(\kappa_y |y(x,z,t) - f_{\max}|^2\right)} & y(x,z,t)\hat{v}_{\mathrm{w}}(x,z,t) > 0 \; , \end{cases} \tag{7.11}$$

where $f_{\max}$ is the deformation limit and κ_y and κ_v are parameters to be defined. This formulation is graphically represented in frame 'b' of figure 7.3. It can be seen how the amplitude converges to zero as the wall approaches its maximum allowable deformation while remaining positive throughout. According to the present theory, higher drag reductions could potentially be achieved with this formulation compared to earlier ones. Whether this is the case will be clarified in the analysis of results.

7.2.2 Secondary effects of deforming walls

The idea behind replacing wall transpiration with wall deformation is that both impart momentum in wall-normal direction. But a deforming wall does more than that – it alters the flow by introducing secondary effects that are not accounted for in the control algorithm. It is unknown how these affect the flow. Kang *et al.* [54] , for example, believe these effects to be negligible for deflections smaller than $y^{+} < 5$,

as such a surface can be considered hydraulically smooth. Certainly this is true for passive obstacles, such as riblets, but is it also for active wall deformations? An attempt to answer this questions using approximate analysis is made next.

In section 4.3.1 it was shown how to approximate a deforming wall for very small deflections. According to this method, the deformation is replaced by wall-normal and streamwise velocity applied at a flush wall. The former represents the effect of vertical velocity and the latter the effect of deformation. In the case of small deflections the streamwise velocity at the wall would be negligible. This means that the approximation of a moving obstacle would reduce to wall transpiration and the approximation of a passive obstacle would reduce to a flat wall. But the threshold for considering deflection small enough might not be the same for active and moving obstacles due to one crucial difference: in the active case the streamwise velocity imposed at the wall is time-dependent and in the passive case it is not. Assuming that the two are equally insignificant for small values is not straightforward and will be verified in the discussion of results.

The strength of the streamwise component can be estimated from a simple numerical example using expression (4.20). When the deformation in opposition control is replaced by a velocity boundary condition then the vertical wall velocity, v_{w}, corresponds to the one measured at the sensing plane, v_{s}, whereas the streamwise wall velocity corresponds to $u_{\mathrm{w}} = \epsilon \frac{\partial u_0}{\partial y}|_{\mathrm{w}}$, with ϵ being the deflection and u_0 a known base profile. Turbulent flows are time-dependent so a baseflow as such does not exist. But in order to estimate the strength it seems legitimate to use the average velocity profile shown in frame 'a' of figure 5.7.

v_{w} seeks to cancel v_{s} so by definition they are of equal magnitude. But it can be shown that u_{w} and the streamwise velocity at the detection plane, u_{s}, are roughly of the same magnitude, too. If the sensing plane is located at $y_{\mathrm{s}}^+ = 10$ then $u_{\mathrm{s\,rms}} \approx 2$. And if the rms deflection is assumed to be two wall units then $u_{\mathrm{w},rms} \approx 2$. Hence, $u_{\mathrm{w},rms} \approx u_{\mathrm{s\,rms}}$.

This implies that, assuming sufficient penetration length, the wall deformation could be employed to manipulate the streamwise velocity in the detection plane. In fact, such an experiment was performed by CMK where the streamwise velocity

in the detection plane was applied at the wall, thereby reducing the drag by 10%. From that crude calculation one can conclude that the secondary effects of wall deformation are not negligible.

A very interesting question is whether it might be possible to account for these effects in the control method to achieve higher drag reduction. Since the wall velocity is the time derivative of the wall deformation the response of the v-perturbation is much quicker than the response of the u-perturbation. In order to control u the wall would have to move so quickly that the effects on v would be unpredictable. From this perspective, it seems that the secondary effects are a burden that cannot be avoided when flow velocities are to be controlled. But even if it were possible to control u using wall deformation, it might not be a good strategy. The reason is that perturbations of u close to the wall do not penetrate far into the domain, something that was discovered in section 6.2. Without a certain penetration length in relation to the turbulent fluctuations, it is questionable if significant drag reductions can be achieved.

7.2.3 Actuation bandwidth

In standard opposition control the number of modes that are actuated equals the number of modes that are resolved. This is because the actuation is determined by the unfiltered measurements taken in the detection plane.

Alternatively, the signal may be filtered to retain a certain bandwidth. If turbulent regeneration cycle is truly dominated by a limited number of modes, then this restriction must not necessarily impede the performance. On the contrary, less energy input improves the net energy balance and might also prevent unwanted side effects. And to perform such an experiment in the laboratory, bandwidth restrictions are inevitable in any event. For all the progress made on the downscaling of actuators, even actuators the size of coherent structures remain a distant goal.

In the present work the actuation bandwidth is capped for all control simulations that use wall deformation as a means of actuation, but not for the aforementioned reasons. Here, it became a matter of necessity as it was observed that strong high

wavenumber forcing lead to instability. This phenomenon is purely numerical and as such can be avoided but, unfortunately, no solution was found for the implementation considered. Common issues such as aliasing were found not to be the cause.

But before the full actuation bandwidth is reduced to a selective one, it must be understood how this affects the performance. To gain such insight, experiments are conducted using opposition control by wall transpiration where the bandwidth is gradually reduced. The results of this study are presented in chapter 7.3.3. Apart from providing guidelines, they also reveal the relevant scales of the physical mechanism.

7.2.4 Ramifications of using a divergent-free coordinate system

In divergent coordinate systems, as the ones used in [12, 27, 70], upper and lower walls of a channel can be deformed independently of each other. In divergent-free coordinate systems in contrast, this is not possible. To ensure that the divergence is zero, which is equivalent to constant element sizes, lower and upper wall displacement must be equal in space and time. In terms of flow control this has significant implications. Essentially it means that one wall can be controlled while the other has to replicate the same deformation irrespective of the adjacent flow. Consequently, the drag reduction achieved by control is not reflected in the pressure drop in the channel but in the average skin friction on the wall that is controlled.

The benefit of such studies relies on an important assumption – that the two walls do not communicate in terms of skin friction. If that were the case, the results from such experiments could not be extrapolated to turbulent boundary layers. The study by CMK supports this assumption. They performed opposition on one wall as well as both walls and found that the skin-friction reduction of the single controlled wall was identical to that obtained on one wall when control was applied at both walls. This indicates that, in terms of skin friction , there is indeed little communication between the two walls. The question of whether the same holds for

the present configuration, that is both walls actuated but only one controlled, is to be investigated in section 7.3.2. Apart from the practical advantage, the result by CMK also gives interesting physical insight. Intuitively, one would expect the skin friction in the single controlled case to be larger because of the energy flux across $y = 0$ that is caused by the different levels of turbulence intensity. However, this seems not to be the case.

Although it was said that these different configurations yield similar results in skin friction, it is still interesting to ask which one is best suited to produce results as applicable as possible to real-world problems. In general, it could be argued that channel flow with control applied to a single wall is advantageous as it retains almost full turbulence in one half of the channel, thus better mimicking the control of a turbulent boundary layer.

Arguing on this basis, divergent-free coordinate systems become a true alternative to divergent ones. While providing results of equal, if not, greater applicability they come at much lower computational costs. It makes them an attractive choice and presents a novel approach to the study of control by wall deformation.

7.2.5 Coordinate system

As in section 4.4.1, the extra term A^i of expression (3.34) is expanded. Again, the coordinate system is chosen to have zero divergence so that the problem simplifies to the equations given in section 3.1.3. The transformation is defined by the expressions (4.37) where the velocities transform as in (4.38). Here, however, the secondary transformation (4.39) is omitted. Thus, time-dependent boundary velocities have to be imposed.

Expanding the extra term A^i yields

$$A_\xi = U_\eta f_\tau + p_\eta f_\xi + \frac{1}{Re}(- 2U_{\xi\eta} f_\xi - U_\eta f_{\xi\xi} + U_{\eta\eta} f_\xi^2 - 2U_{\zeta\eta} f_\zeta - U_\eta f_{\zeta\zeta} + U_{\eta\eta} f_\zeta^2) \tag{7.12}$$

$$A_\zeta = W_\eta f_\tau + p_\eta f_\zeta + \frac{1}{Re}(- 2W_{\zeta\eta} f_\zeta - W_\eta f_{\zeta\zeta} + W_{\eta\eta} f_\zeta^2 - 2W_{\xi\eta} f_\xi - W_\eta f_{\xi\xi} + W_{\eta\eta} f_\xi^2) \tag{7.13}$$

$$\begin{aligned} A_\eta \;=\; & p_\xi f_\xi - p_\eta f_\xi^2 + p_\zeta f_\zeta - p_\eta f_\zeta^2 \\ & - U^2 f_{\xi\xi} - W^2 f_{\zeta\zeta} - 2UW f_{\xi\zeta} \\ & - U f_{\tau\xi} - W f_{\tau\zeta} + f_\tau V_\eta \\ & + f_\xi f_\tau U_\eta + f_\zeta f_\tau W_\zeta \\ & + \frac{1}{Re}(-2V_{\xi\eta} f_\xi - V_\eta f_{\xi\xi} + V_{\eta\eta} f_\xi^2 + U f_{\xi\xi\xi} + 2U_\xi f_{\xi\xi} \\ & \quad - 2U_\eta f_\xi f_{\xi\xi} + W f_{\xi\xi\zeta} + 2W_\xi f_{\xi\zeta} - 2W_\eta f_{\xi\zeta} f_\xi \\ & \quad - 2V_{\zeta\eta} f_\zeta - V_\eta f_{\zeta\zeta} + V_{\eta\eta} f_\zeta^2 + W f_{\zeta\zeta\zeta} + 2W_\zeta f_{\zeta\zeta} \\ & \quad - 2W_\eta f_\zeta f_{\zeta\zeta} + U f_{\zeta\zeta\xi} + 2U_\zeta f_{\xi\zeta} - 2U_\eta f_{\xi\zeta} f_\zeta \\ & \quad + f_\xi f_\zeta W_{\xi\eta} + f_\zeta f_\xi U_{\zeta\eta}) \end{aligned} \tag{7.14}$$

The most noticeable difference between expression (4.42) and (7.14) is the presence and absence, respectively, of the acceleration term $f_{\tau\tau}$.

The addition of the extra term to the Cartesian equations increases the computational load significantly. The term requires the calculation of 22 derivatives of the primitive variables and 12 derivatives of the wall deformation. This increases the computational expense by a factor of more than two – not taking into account tighter time restrictions. In order to integrate at high order it is thus better to use previous values that are stored rather than calculating new values inside the time-stepping interval. This makes multi-step methods such as the Adams-Bashforth scheme more efficient than one-step methods such as Runge-Kutta.

Some terms in expressions (7.12), (7.13), and (7.14) contain a multiplication of more than two variables, which produces Fourier modes of very high order. The

resulting aliasing problem can be dealt with in two ways. One is to modify the de-aliasing rule (3/2) by increasing the physical space of the non-linear operations. Another is to actuate the flow in a bandwidth smaller than the resolved one. The latter method does not bring additional computational costs and is pursued in any event, as explained in section 7.2.3. It was found that ignoring aliasing can lead to significant numerical instabilities.

7.3 Results

This section is divided into five parts, each of which presents a different set of experiments. All details of those simulations are are given in table 7.1 and in the schematic diagrams shown in figure 7.4.

Cases 7, 8, and 9 are the goal of this study: one-sided opposition control by restricted wall deformation at small wavenumbers. The control is required to be one-sided, because the divergence-free coordinate system dictates equal displacement at upper and lower wall. The restriction to small wavenumbers is required, because at high wavenumbers instabilities were encountered. The restriction of deformation is required, because the wall must not penetrate the detection plane.

The idea behind this series of experiments is to progress step-wise from standard opposition control to Cases 7, 8, and 9. This facilitates studying the effect of each modification independently. The first experiment, Case 1, depicted in frame 'a' of figure 7.4, is a repetition of the original opposition control study by CMK, that is opposition control applied on both walls. In Case 2 (frame 'b') the control is confined to the lower wall with equal actuation at the upper wall. In Cases 3, 4, and 5 (frame 'c') control is reduced to small wavenumbers. In Case 6 (frame 'd') the velocities are damped by a penalty function which is equivalent to the deformation restriction. And finally, in Cases 7, 8, and 9 (frame 'e'), actuation by wall deformation is introduced.

Each of these steps is documented in an individual section but the parameter values and the most important results, skin-friction reduction at upper and lower wall as well as rms of wall velocity, can be found in table 7.1. The flows are anal-

ysed by the examination of changes in turbulence statistics averaged over 42.4 time units. Structures in space and time are identified in the classical way by performing Fourier analysis. The label P7Z48 in the following discussion always refers to the unmanipulated baseline case introduced in Chapter 5.

Case	Control		τ_w		F_x, F_z	Transp	Deform	A			v_{LW}			f		
	LW	UW	LW	UW				χ	ϖ	f^+_{max}	RMS E1	Skew	Flat E−1	RMS E2	Skew	Flat E−1
1	x	x	-24.7%	-21.2%	11.5, 34.5 (all)	x					0.71					
2	x		-23.9%	1.6%	11.5, 34.5 (all)	x					0.72	-0.50	0.98			
3	x		-21.3%	-3.6%	5, 15	x					0.73	-0.13	0.64			
4	x		-22.5%	-4.5%	3.5, 10.5	x					0.61	-0.14	0.50			
5	x		-19.2%	-2.4%	2.5, 7.5	x					0.51	-0.09	0.36			
6	x		-12.0%	-6.5%	2.5, 7.5	x		0.1			0.46	0.03	0.35			
7	x		-12.8%	-7.5%	2.5, 7.5		x	0.1			0.50	0.03	0.40	0.71	-0.28	0.31
8	x		-15.1%	-5.0%	2.5, 7.5		x	0.08			0.53	0.00	0.45	0.77	-0.25	0.33
9	x		-12.4%	-5.3%	2.5, 7.5		x	0.07	0.6		0.41	0.05	0.40	0.87	-0.28	0.30
10	x		-11.8%	-6.2%	2.5, 7.5	x				2.5	0.40	0.06	0.71			

UW =Upper wall

LW =Lower wall

Table 7.1: Opposition control experiments. Measurements taken over 42.4 time units.

7.3.1 Standard opposition control: Case 1

To start with, the repetition of the standard opposition control experiment by CMK is discussed. As defined in table 7.1, control is applied on both walls. The actuation is performed by means of wall transpiration and covers all resolved wavenumbers. As expected, the skin-friction reduction on both walls is between 20 and 25%, which is consistent with the result by CMK and suggests that this is an appropriate platform for the following experiments. The difference in drag reduction on the two walls is 3.5% which shows that the measurement period of 42.4 time units is only marginally sufficient.

7.3.2 Effect of limiting control to lower wall: Case 2

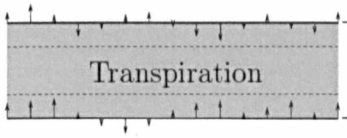
As in the previous case, opposition control is applied using wall transpiration at all wavenumbers. Now, however, only the lower wall is controlled whereas the upper wall replicates the transpiration at the lower one, irrespective of the surrounding flow events. Hence, the upper wall can be considered as actuated but not controlled. In table 7.1 this is marked by a missing cross in the UW field of Case 2. This restriction on a single wall will later be necessary for the control simulations involving divergence-free coordinate systems.

Before it was mentioned that the two walls hardly communicate in terms of skin-friction drag according to CMK. Assuming this to be the case, it would be expected that the friction drag on the lower wall is reduced by the same amount as in the previous case, that is between 20% and 25%.

This is confirmed by the drag reduction given in table 7.1. Frame 'a' of figure 7.5 shows a plot of the skin friction on the lower wall which is on average 23.9% lower than the skin friction on the same wall in an unmanipulated channel. This reduction translates into an effective Reynolds number of $Re_\tau = 76$. The initial sharp decrease in drag is often attributed to immediate prevention of ejection and sweep events [15]. After this transient stage, the flow settles to a new quasi-steady state.

Frame 'b' shows a plot of the skin friction at the upper wall. Apparently, the

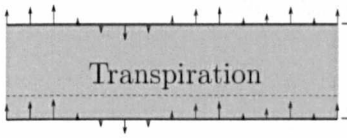
a) Case 1:



$$\rightarrow v_{\mathrm{UW}} = -v(x, y = 0.9, z, t)$$

$$\rightarrow v_{\mathrm{LW}} = -v(x, y = -0.9, z, t)$$

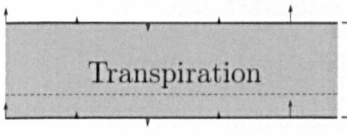
b) Case 2:



$$\rightarrow v_{\mathrm{UW}} = v_{\mathrm{LW}}$$

$$\rightarrow v_{\mathrm{LW}} = -v(x, y = -0.9, z,)$$

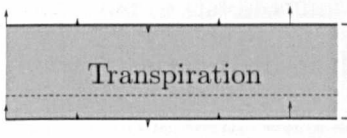
c) Cases 3, 4, 5:



$$\rightarrow v_{\mathrm{UW}} = v_{\mathrm{LW}}$$

$$\rightarrow v_{\mathrm{LW}} = -\sum_{m_x=-\frac{N_x}{2}-1}^{\frac{N_x}{2}-1} \sum_{m_z=0}^{\frac{N_z}{2}-1} v_{m_x,m_z}(x, y = -0.9, z, t)$$

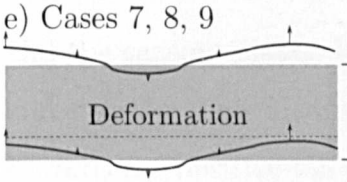
d) Case 6:



$$\rightarrow v_{\mathrm{UW}} = v_{\mathrm{LW}}$$

$$\rightarrow v_{\mathrm{LW}} = A(x, z, t) \left(-\sum_{m_x=-\frac{N_x}{2}-1}^{\frac{N_x}{2}-1} \sum_{m_z=0}^{\frac{N_z}{2}-1} v_{m_x,m_z}(x, y = -0.9, z, t) \right)$$

e) Cases 7, 8, 9



$$\rightarrow v_{UW} = v_{LW}$$

$$\rightarrow v_{LW} = A(x, z, t) \left(-\sum_{m_x=-\frac{N_x}{2}-1}^{\frac{N_x}{2}-1} \sum_{m_z=0}^{\frac{N_z}{2}-1} v_{m_x,m_z}(x, y = -0.9, z, t) \right)$$

Figure 7.4: Case1: Two-sided opposition control using transpiration. Case 2: One-sided opposition control using transpiration. Cases 3, 4, 5: One-sided opposition control using transpiration at small wavenumbers. Case 6: One-sided opposition control using restricted transpiration at small wavenumbers. Cases 7, 8, 9: One-sided opposition control using restricted deformation at small wavenumbers.

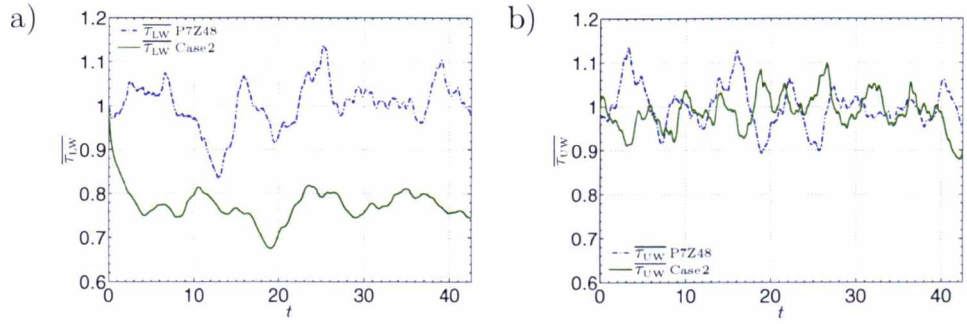


Figure 7.5: Case 2 and P7Z48: a) skin-friction drag at lower wall; b) skin-friction drag at upper wall.

uncoordinated blowing and suction has no gross effect on the skin friction as it remains at the same level. In fact, there is a little increase of 1.6% but for the selected sample size this is believed not to be a conclusive result.

The essential features of opposition-controlled flow are found close to the wall. In figure 7.6 rms, skewness, and kurtosis of v are shown for the first 20 wall units away from the lower wall. The dashed lines refer to the same quantities in unmanipulated flow. Due to the blowing and suction, v_{rms} in frame 'a' is not zero but around 0.72 at the wall. From there it drops to almost zero in a zone between $-0.97 < y < -0.95$. This is consistent with observations by CMK and Hammond *et al.* [41] which say that opposition control establishes a virtual wall half-way between the actual wall and the sensing plane. Inside this layer, both skewness and kurtosis, grow rapidly and linearly. This means that for increasing distance the fluctuations quickly shift towards the positive tail of the distribution before the virtual layer breaks down. In general, these figures illustrate how the vertical motion close to the wall is completely restructured by the action of opposition control.

Contrary to the effect of riblets [16], opposition control not only alters the statistical quantities close to the wall but also in the rest of the domain – possibly a consequence of the higher drag reduction. This is clearly visible in figure 7.7 which shows plots for various statistical properties over the entire y-range. In the lower half of the domain, which is dominated by opposition control, all rms profiles have dropped, of the velocity in frame 'b' as well as of the vorticity in frame 'd'. In ac-

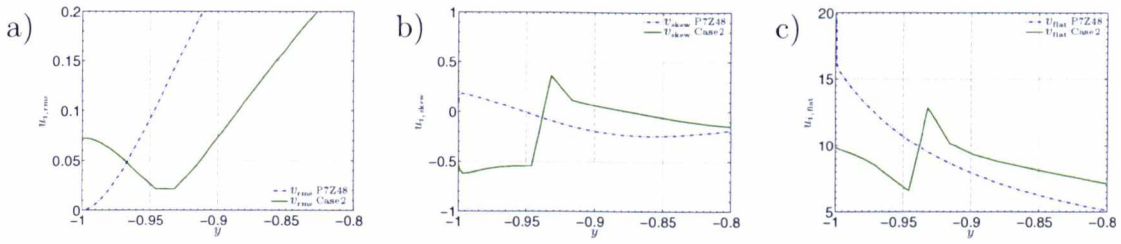


Figure 7.6: Case 2 and P7Z48: comparison of v statistics close to the controlled wall and uncontrolled wall. a) rms; b) skewness; c) flatness.

cordance with the rms profiles, the Reynolds stress in frame 'e' has been weakened, too. Furthermore, all profiles seem to have shifted towards the centre of the channel which is the effect of the displaced or virtual wall. This shift also affects the local maximum in streamwise vorticity, indicating that the average centre of the streamwise vortices has been pushed away from the wall. This feature of the flow can also be observed in instantaneous shots of the flowfield, as the one shown in figure 7.9. Another striking effect of opposition control is revealed by the rms profile of spanwise vorticity close to the wall. Instead of falling monotonously, it now displays a local maximum about 20 wall units from the wall. The global effect of control on the mean flow, shown in frame 'a', is predictable. Near the lower wall it has slowed down due to the reduced wall shear stress. At the same time the mean flow has accelerated towards to the middle of the channel so as to keep the flowrate constant. The spanwise two-point correlations in frame 'f' exhibit strong oscillations. This is less a physical phenomenon than a consequence of an insufficient sample size. Further statistics are shown in figure 7.8. The profiles showing skewness of the velocity in frame 'a' also lack samples. But they suffice to reveal complex profiles in the vicinity of the wall. Whereas in the unmanipulated case skewness profiles are smooth and monotonous, they now exhibit peaks and troughs. The same applies to the kurtosis in frame 'b'. The energy spectra in frame 'c' and 'd' have dropped throughout the entire bandwidth, while the energy in vertical motion is reduced the most, relative to its unmanipulated value.

The figures also underline the importance of coordinating the actuation. This can

be seen close to the upper wall where the actuation is the same as on the lower wall but uncoordinated with wall turbulence. There, the rms profiles are left unchanged away from the wall as is the skin friction. Even the higher-order statistics show almost no difference apart from the region very close to the wall. This suggests that "random" mass-less transpiration at all scales of the present strength cannot alter turbulence statistics away from the wall.

7.3.3 Effect of restricting control to small wavenumbers: Case 3, 4, and 5

In section 7.2.3 it was explained that the actuation bandwidth must be restricted in the present numerical code to achieve numerical stability in simulations that involve wall deformation. However, this restriction is also motivated for other reasons. For example, it closes the gap between simulation and laboratory experiment because it is difficult to actuate at very small scales in the real world. On the downside, however, any restriction of actuation reduces the degrees of freedom that are available to actuate and hence decreases the potential for drag reduction. The extent to which this adverse effect applies is studied in this section. Apart from supplying guidelines for efficient control the results will also provide physical insight into the drag-reducing mechanisms and wall turbulence itself.

Little has been published on the characteristic scales of opposition control. CMK mention having studied selective bandwidth actuation. They only report that up to 10% drag reduction was obtained by applying the control to only one streamwise Fourier coefficient corresponding to the largest wavenumber ($k_x = 0.5$) and all the spanwise waves. This significant reduction could suggest that the reduction of skin friction in opposition control is more sensitive to spanwise rather than streamwise wavenumber manipulation. In the present work, however, actuation always covers the same number of Fourier modes in both homogenous direction. This is an arbitrary decision that was made to reduce the parameter space under investigation.

To investigate the effect of bandwidth restriction, opposition control is applied again on the lower wall only. The resulting actuation is then replicated on the

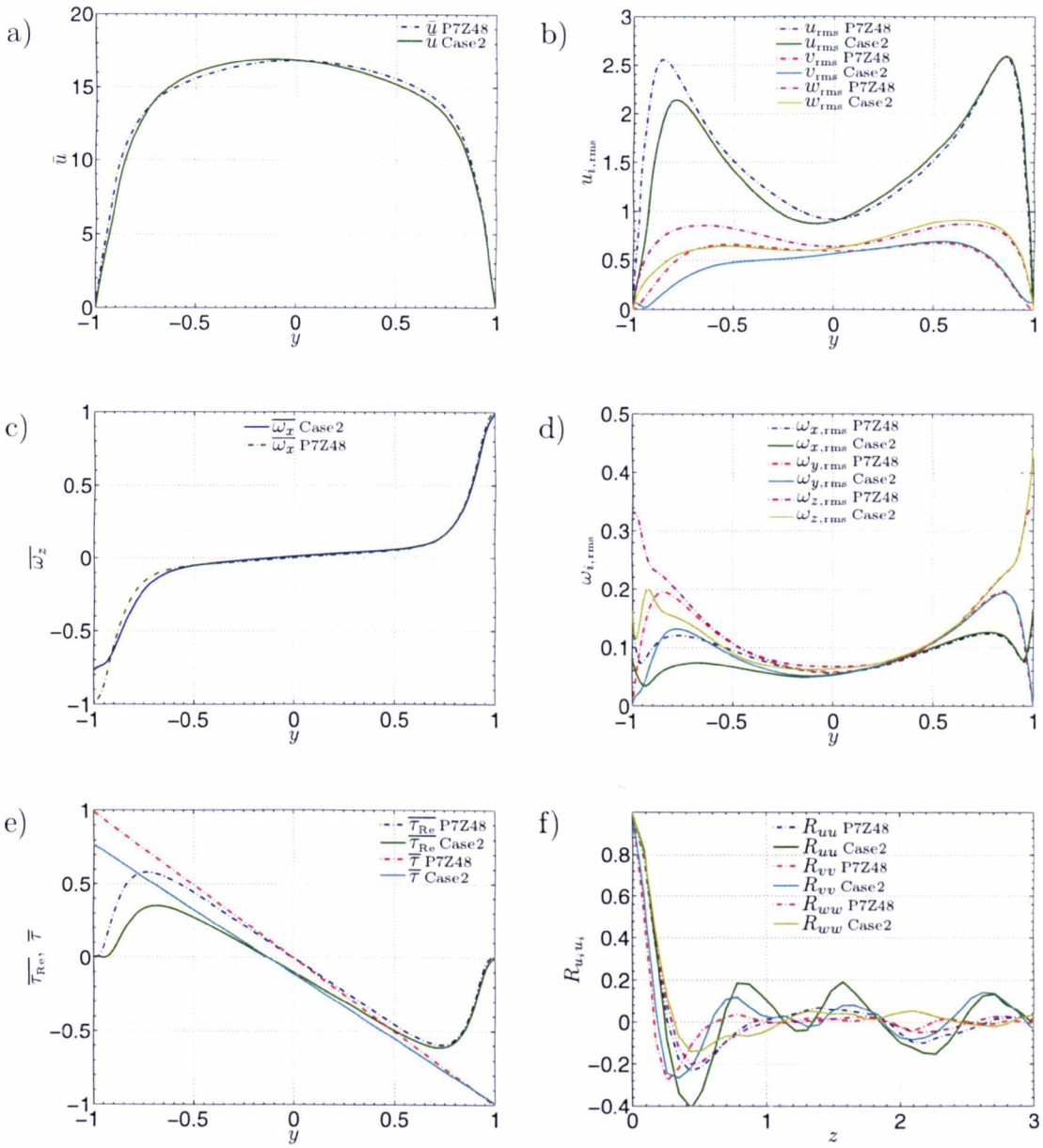


Figure 7.7: Case 2: a) mean velocity; b) rms velocity fluctuations; c) mean vorticity; d) rms vorticity fluctuations; e) Reynolds stress and total stress; f) spanwise two-point correlation at $y^+ = 5.4$.

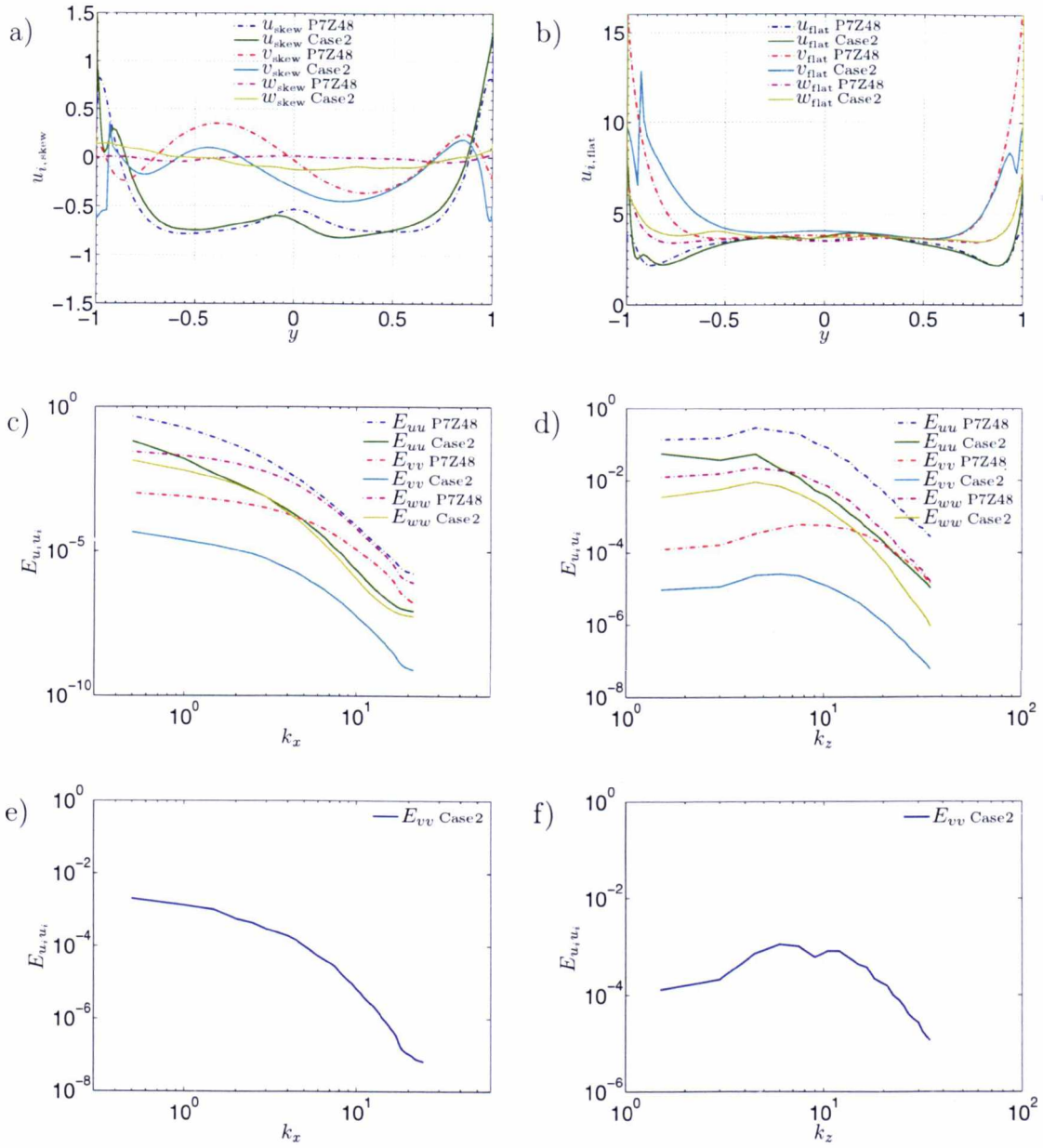


Figure 7.8: Case 2: a) skewness of velocities; b) kurtosis of velocities; c) streamwise energy spectra at $y^+ = 5.4$; d) spanwise energy spectra at $y^+ = 5.4$; e) streamwise energy spectra at wall; f) spanwise energy spectra at wall

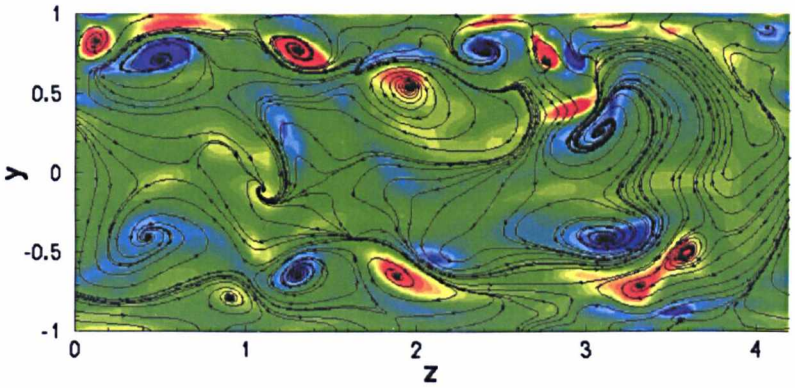


Figure 7.9: Case 2: (-20≤ω_x≤20)-contours and streamlines in (y,z)-plane. The control action at the lower wall has weakened the streamwise vortices and pushed them away from the wall.

upper wall which means that it is actuated but uncoordinated with the adjacent flow events. Four bandwidths are studied: Case 3 with $(F_x, F_z) = (5, 15)$, Case 4 with $(F_x, F_z) = (3.5, 10.5)$, and Case 5 with $(F_x, F_z) = (2.5, 7.5)$, where F_i denotes the largest actuated wavenumber in the i-coordinate direction. The relation between F_i and the largest actuated Fourier mode, N_i, is $F_i = \frac{2\pi}{L_i}\left(\frac{N_i}{2} - 1\right)$. The actuation is then defined according to the expression in frame 'c' of figure 7.4 where

$$v_{m_x,m_z}(x, y = -0.9, z, t) = \hat{v}_{m_x,m_z}(y = -0.9)e^{\left[2\pi i\left(\frac{m_x x}{L_x} + \frac{m_z z}{L_z}\right)\right]} . \tag{7.15}$$

The average skin-friction reductions of each case are given in table 7.1. For the lower, actuated wall, graphs of time-resolved skin-friction are shown in figure 7.10. The best result is obtained by controlling all modes, that is $(F_x, F_z) = (11.5, 34.5)$. Yet, an astonishing 19.2% reduction is achieved by controlling the bandwidth $(F_x, F_z) = (2.5, 7.5)$ only. The result shows that significant bandwidth restriction does not negate the opposition control mechanism and is an appropriate tool to achieve more feasible laboratory experiments.

The results also provide interesting physical insight. In figure 7.11 statistical quantities of Case 2 and Case 5 are compared. Frame 'a' shows profiles of rms fluctuations of the velocity components. The profiles of the two cases almost collapse. But in the region close to the wall, magnified in frame 'b', differences arise, in particular for v_{rms}. Most notably, there seems to be no clearly-defined virtual wall in

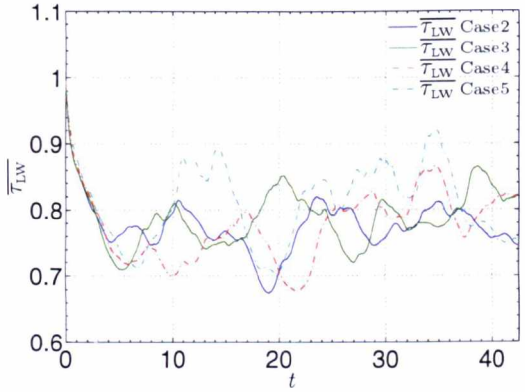


Figure 7.10: Cases 2, 3, 4, and 5: Skin-friction on lower wall for different actuation bandwidths.

Case 5. Instead, v_{rms} of this case almost stays constant for some distance away from the wall before it starts rising again. However, the steepness of the profile after this point is about equal in the two cases. This suggests that the profile shift might be less important than the profile tilt. The reason why v_{rms} remains large in the wall region is obviously that high wavenumbers remain unaffected by the actuation. This is shown vividly in frame 'd' which reveals a kink in the one-dimensional energy spectra in spanwise direction. It is located exactly at the spanwise wavenumber where the actuation ends. Using this information, a modified virtual-wall concept is proposed to explain the skin-friction reduction in Case 5. It says that the controlled flow is characterised by the existence of a layer half-way between the wall and the detection where only little vertical motion in the actuated wavenumber regime is permitted.

This study is not only useful in finding good control techniques but also provides interesting physical insight into wall turbulence itself. One field of interest in turbulence research is the cause of near-wall streaks. Instantaneous shots of these structures are shown in figure 7.12 for unmanipulated flow (frame 'a'), Case 2 (frame 'b'), and Case 5 (frame 'c'). Clearly, the actuation results in the weakening of streaks in both cases, although more so in Case 2 than in Case 5. According to a widespread theory, the streaks are caused by streamwise vortices. Since the streaks are known to be spaced 100 wall units away from each other, these streamwise vortices

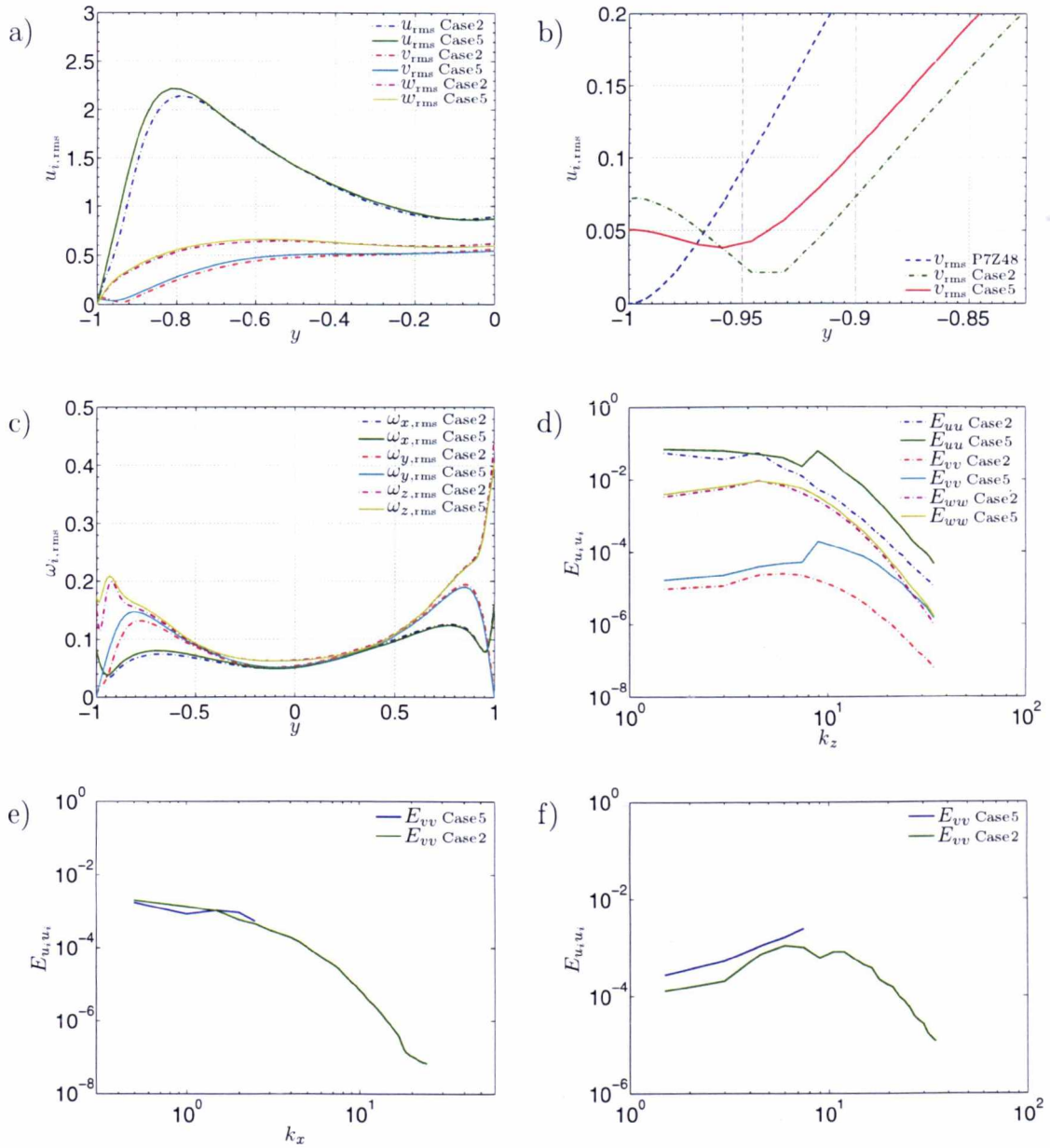


Figure 7.11: Cases 2 and 5: a) rms velocity fluctuations; b) close-up of vertical rms velocity fluctuations at the wall; c) rms vorticity fluctuations; d) energy spectra in spanwise direction at $y^+ = 5.4$; e) energy spectra in streamwise direction at lower wall; f) energy spectra in spanwise direction at lower wall.

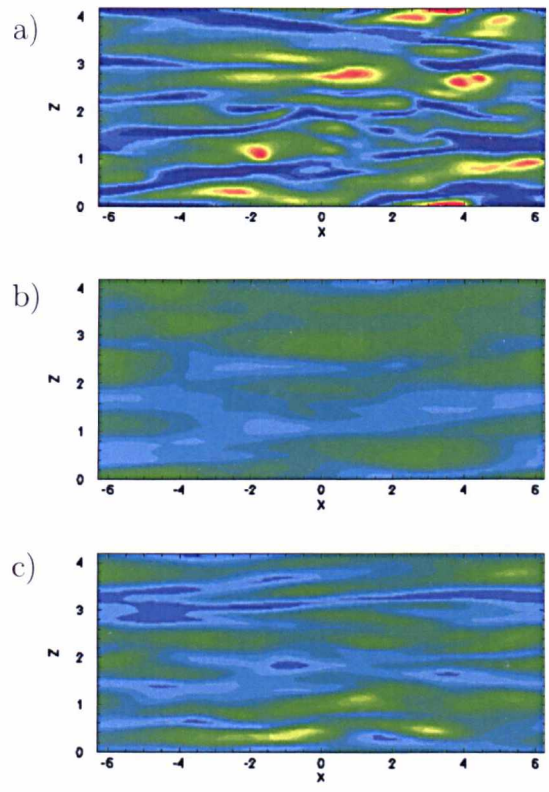


Figure 7.12: Streaks at $y^+ = 5.4$ depicted by contours of streamwise velocity between -2. and 5. a) P7Z48; b) Case 2; c) Case 5.

would have to be spaced so as to create wall-normal-velocity with a characteristic length scale of 100 wall units (or 50 wall units in terms of energy). This spacing corresponds to a wavenumber of $k_z = 4.5$ which is within the actuation bandwidth of Cases 2 and 5. In this situation, the theory would predict that both cases equally reduce the streamwise vortices and hence the streamwise-vorticity fluctuations. As can be seen in frame 'c' of figure 7.11, this is exactly the case, as the profiles of $\omega_{x,\,\mathrm{rms}}$ almost collapse. This result indicates that streamwise vortices are indeed the cause of streaks. Such a relationship supports the idea of using streamwise vortices in a laminar channel – rather than expensive DNS of fully-turbulent flow – to study control methods aimed at destroying streaks. Whether this control goal is the best way to achieve high drag reductions is an entirely different question that will be addressed in Chapter 8 where the formation of streaks is prevented by modifying the flow equations directly.

The findings above are also consistent with the report by CMK. They identified

two mechanisms for drag reduction by opposition control. One was simply the deterrence of sweep motion and the other the prevention of secondary vortices at the wall from lifting up. Both mechanisms can be put into direct relationship to streamwise vortices.

Bandwidth restriction has two other advantages. One is that it lowers energy input. As can be seen in table 7.1, the rms of vertical wall velocity is about 30% lower when the actuation is limited to the bandwidth $(F_x, F_z) = (2.5, 7.5)$. Another advantage is the possibility of using reduced order models, such as LES, without having to model the actuation.

In the last section it was found that at the upper wall, where uncoordinated wall transpiration is applied, a slight increase in skin friction occurred. Interestingly, this increase turns into a decrease when the bandwidth is restricted. The best result was obtained in Case 4 where the skin friction was reduced by 4.45 % at the upper wall. This is an interesting result showing that even uncoordinated time-dependent wall transpiration can reduce skin-friction drag, albeit marginally.

7.3.4 Effect of restricting the deformation: Case 6

Before the blowing and suction devices can be replaced by a moving wall, one last modification has to be made. This is the introduction of a restriction function. The functions' purpose is to prevent the wall from penetrating the detection plane. With wall transpiration such a restriction is theoretically not necessary. But to study the effect it has on the performance, actuation restriction is applied to control by transpiration in Case 6.

Using the same set-up as in Case 5, the actuation is now multiplied by an amplitude function $A(x, z, t)$, as shown in frame 'd' of figure 7.4. As restriction function, equation (7.9) is chosen with the parameter set to $\chi = 0.1$.

For the analysis, the results of Case 5 and Case 6 are compared. The average skin-friction reductions, listed in table 7.1, reveal that on the lower wall the reduction has dropped to just 12%, whereas on the upper wall it has improved to 6.5%. This result is also reflected in the turbulence statistics shown in figure 7.13. In the lower half

of the domain all rms fluctuations have increased relative to Case 5, of the velocity in frame 'a' as well as of the vorticity in frame 'c'. Frame 'd' shows that the energy spectra in k_z close to the lower wall has increased throughout the wavenumber space and that the kink observed in Case 5 has almost disappeared. The close-up view of the lower wall in frame 'b' shows how the v_{rms}-profile of Case 6 is closer to the unmanipulated profile while the value of v_{rms} at the wall has almost stayed constant. Around the upper wall it is the opposite. There, turbulence intensities have dropped in accordance with the lower drag.

The less favourable results at the lower wall, in terms of drag reduction, are intuitively obvious. The restriction function alters the amplitude to an extent where the actuation becomes less coordinated with the flow. This can be seen in frame 'a' of figure 7.14 which shows the probability distribution of A. When $A(x, z, t) > 0$ the sensed velocities are opposed, otherwise they are enforced. Since the average amplitude is positive, one is justified to call it opposition control. But a significant part of the distribution is found in the negative range. This could be counterproductive as it was reported by CMK that in-phase control significantly increases the drag. They also found that the stronger events are most important for opposition control. Defining strong events as $v_{\text{rms}\,W} > 0.006$, their distribution is more skewed to the positive range as shown in frame 'b'. But even for this selected range the amplitude can attain values of around $A(x, z, t) = -1$. This means that the retracting force sometimes enforces a strong event.

The situation is less clear on the upper wall. There, the drag dropped by restricting the strength of random blowing and suction. It could be speculated that the restriction introduces structure in the actuation thereby making it less random. This could be remotely related to studies involving structured open-loop actuation such as transverse travelling waves [26]. Reductions in drag due to structuring of the actuation were already observed in section 7.3.3.

All in all, the results signify the susceptibility of opposition control to manipulation of amplitude. Hence, the formulation of A presents an important design criterion for the optimisation of performance.

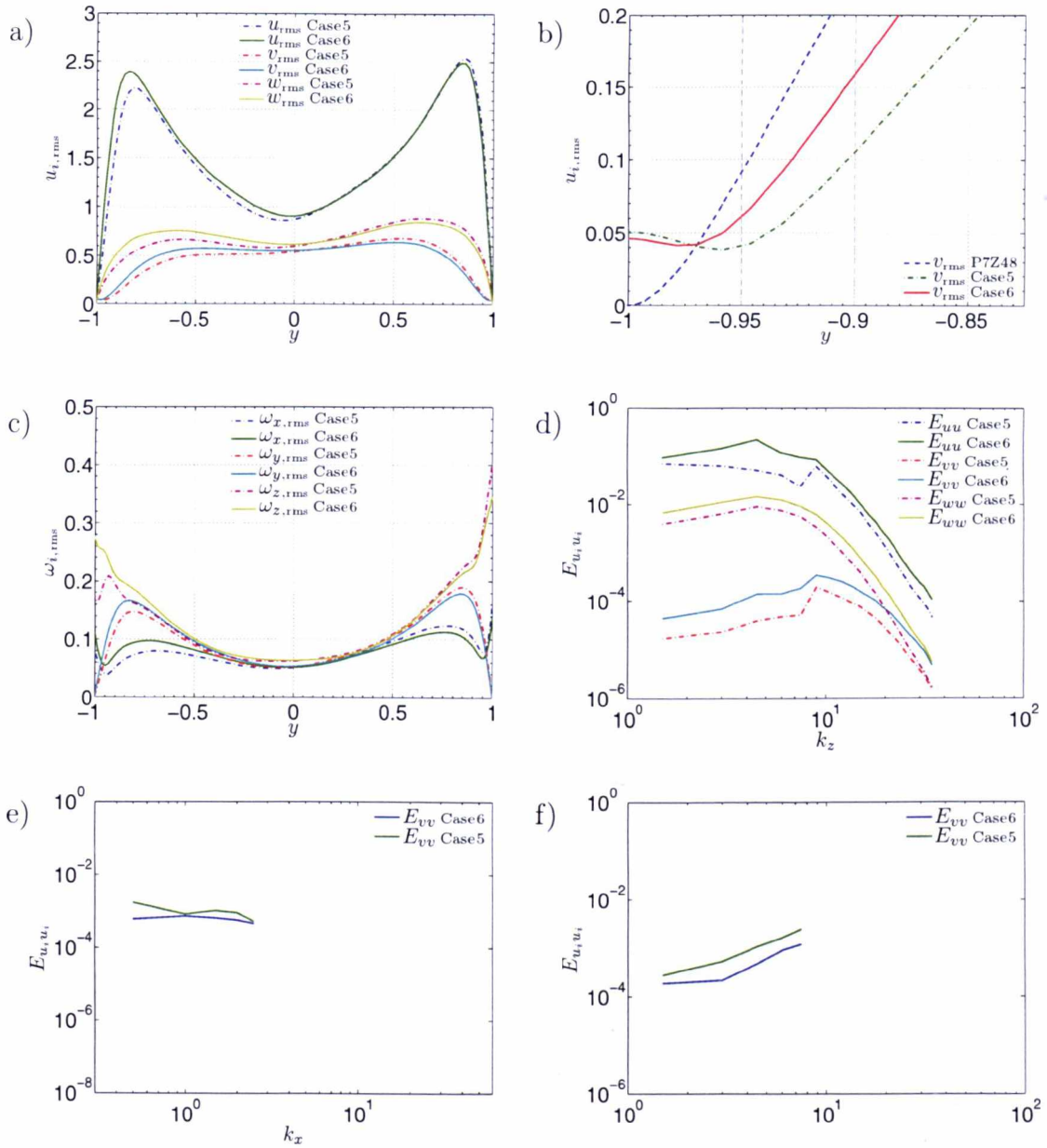


Figure 7.13: Cases 5 and 6: a) rms velocity fluctuations; b) close-up of vertical rms velocity fluctuations at the wall; c) rms vorticity fluctuations; d) energy spectra in spanwise direction at $y^+ = 5.4$.

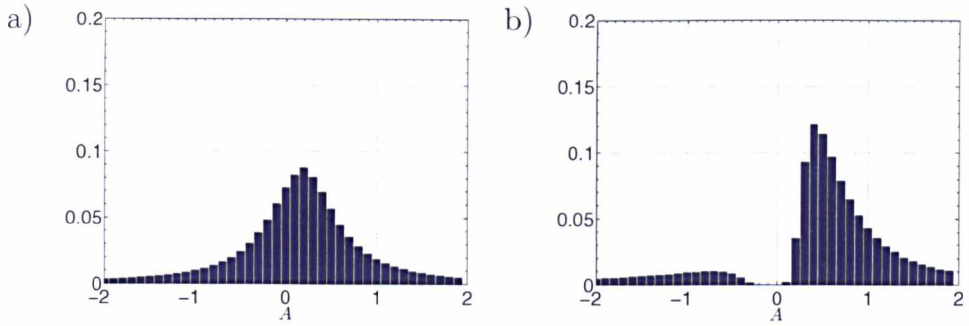


Figure 7.14: Case 6: probability distribution function of A. a) All events; b) strong events ($v_{\mathrm{rms,W}} > 0.06$).

7.3.5 Effect of using wall deformation to actuate: Case 7

In Case 7 the blowing and suction devices of Cases 6 are replaced by a moving wall. To facilitate this, a number of restrictions have to be imposed that were studied in the previous experiments. First, control must be limited to a single wall to be able to use divergence-free coordinate systems. Secondly, the actuation bandwidth has to be capped to avoid numerical instabilities. And thirdly, an amplitude function must be introduced that prevents the wall from touching the detection plane. The latter two were both found to affect the controller's performance.

The experimental set-up is shown in figure 7.2. It is the same as in Case 6 but with deformation instead of transpiration. As before the vertical velocity is measured in a flat detection plane inside the flow. This plane is located 10 wall units off the undeformed lower wall which means that the local distance between the plane and the deformed wall varies in time and space. The measured signal is then filtered to retain a small bandwidth of $(F_x, F_z) = (2.5, 7.5)$. Furthermore, the signal is multiplied by the amplitude function given in expression (7.9) with $\chi = 0.1$ before it is imposed as wall velocity. From the wall velocity, the surface can then be determined by integration according to

$$f^{n+1} = f^n + \sum_{q=0}^{J-1} \beta_q v_{LW}^{n-q} \,, \tag{7.16}$$

where β_q are the Adams-Bashforth coefficients.

The wall-averaged skin friction is shown in figure 7.15 and the time-averaged

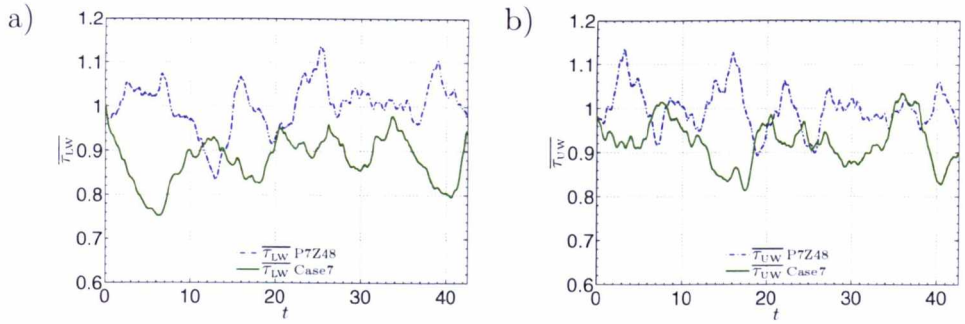


Figure 7.15: Case 7 and P7Z48: a) skin-friction drag at lower wall; b) skin-friction drag at upper wall.

values are again found in table 7.1. Compared to the last experiment, which was identical apart from the mode of actuation, the drag reduction has changed little. In fact, it even improved to 12.8% on the lower wall and 7.5% on the upper wall, although the difference could be too small to be statistically relevant. This invariance to the mode of actuation supports the assumption by Endo *et al.* [27] that it is the deformation limiter that degrades the performance and not the wall deformation itself. They argued by referring to the hydraulic smoothness of small passive obstacles which also seems to apply to small active obstacles, a theory that was discussed in section 7.2.2. Whether active dimples also remain without effect when the wall deformation – not the wall motion – is coordinated with the adjacent wall turbulence remains an open question.

An instantaneous shot of the deformed surface is shown in figure 7.16. It is tempting to compare the deformation pattern with riblets [27, 54]. However, the wall is constantly changing in shape as opposed to the static deformation of riblets. It is quite likely that the deformation pattern is in fact a result of the restriction function. In any case, riblets of such little height have shown to have no effect on the skin friction [16].

It could be argued that the increase in surface area accounts for higher skin-friction drag. Although the surface increases, the effect is almost negligible in Case 7. As a numerical example, a wave with a wavenumber pair of $(k_x, k_z) = (0, 5)$ and an amplitude of 2 wall units is considered. Then, the surface area is only 0.5% larger

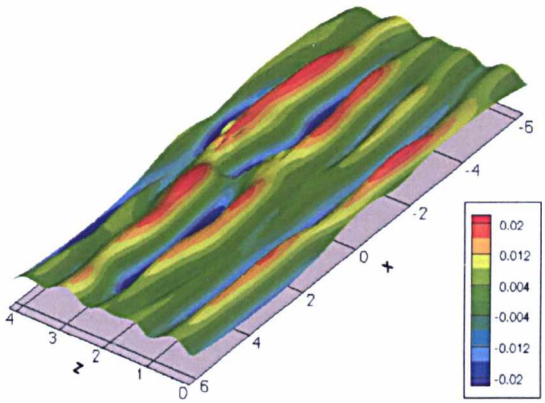


Figure 7.16: Case 7: Instantaneous wall deformation. Scaling in y is exaggerated to show wall structure.

than in the undeformed case. Compared to the impact of other factors, such as the restriction function, this is marginal.

When calculating the turbulence statistics of flows over complex surfaces one faces the dilemma of statistical inhomogeneity. A point in space can be inside the flow domain at one instant and outside the domain at another. This problem can be circumvented by computing all statistics in computational space, that is in the time-dependent curvilinear coordinate system, because any weakening in turbulence will manifest itself in any space. Comparison with statistics taken in the Cartesian systems is then of course flawed, but for a rms deflection of less than one wall unit the error is marginal.

The profiles of statistical variations of Case 7 and Case P7Z48 (unmanipulated flow) are compared in figures 7.17, 7.18, and 7.19. The rms fluctuations of velocity in frame 'b' of figure 7.17 are worth noting. In both halves of the domain the reduction in drag manifests itself in a reduced turbulence intensity of the wall-normal and spanwise velocity. But in stark contrast to standard opposition control, the peak in u_{rms} remains unaltered. The other profiles follow the trend of opposition control if much less pronounced. Most notably, the energy in frames 'a' and 'b' of figure 7.19 is much closer to the unmanipulated levels, in particular at low wavenumbers. This holds to an extent where the relative reductions at high, uncontrolled wavenumbers are equal if not larger than the ones for low, controlled wavenumbers.

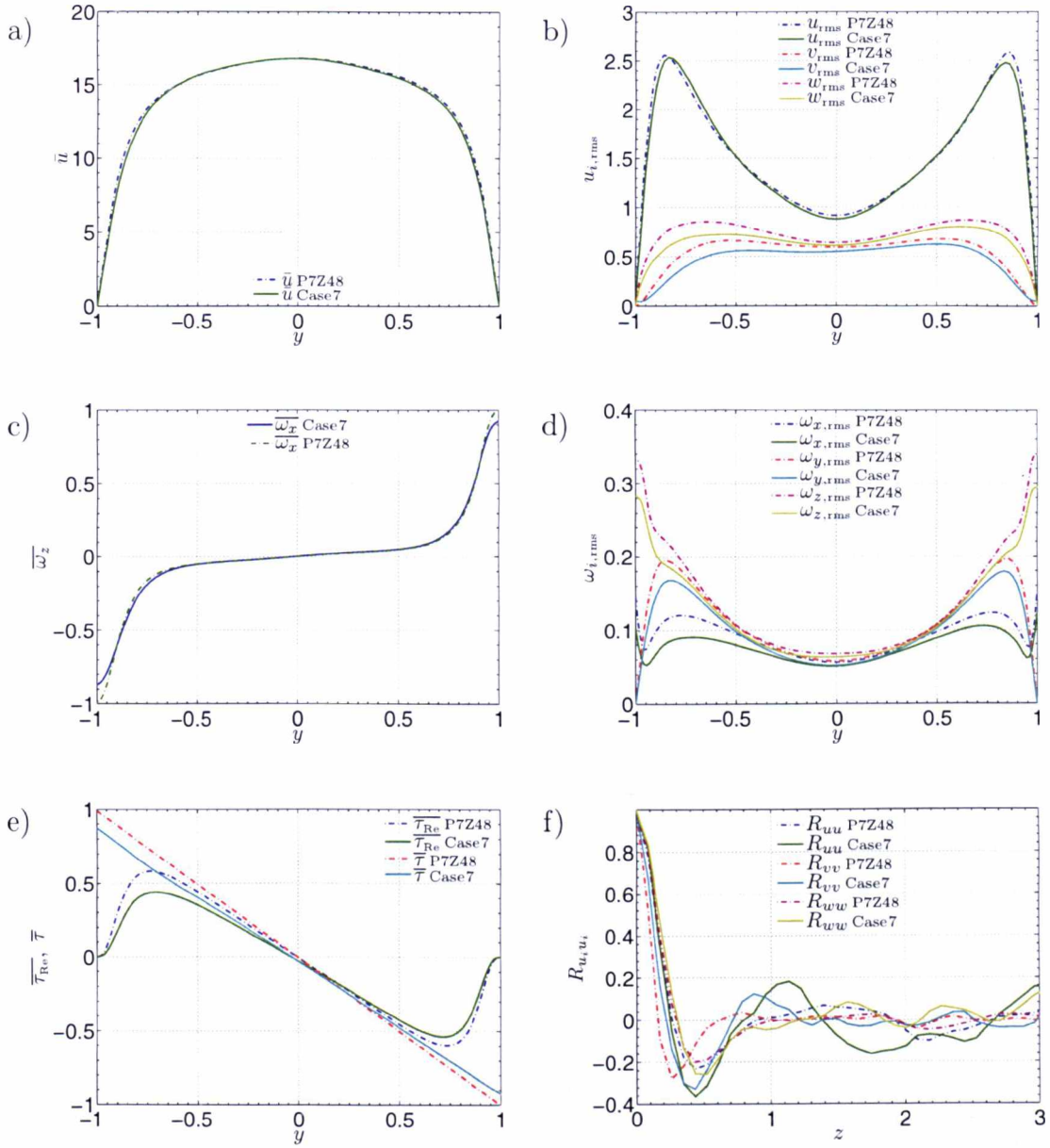


Figure 7.17: Case 7 and P7Z48: a) mean velocity; b) rms velocity fluctuations; c) mean vorticity; d) rms vorticity fluctuations; e) Reynolds stress and total stress; f) spanwise two-point correlation at $y^+ = 5.4$.

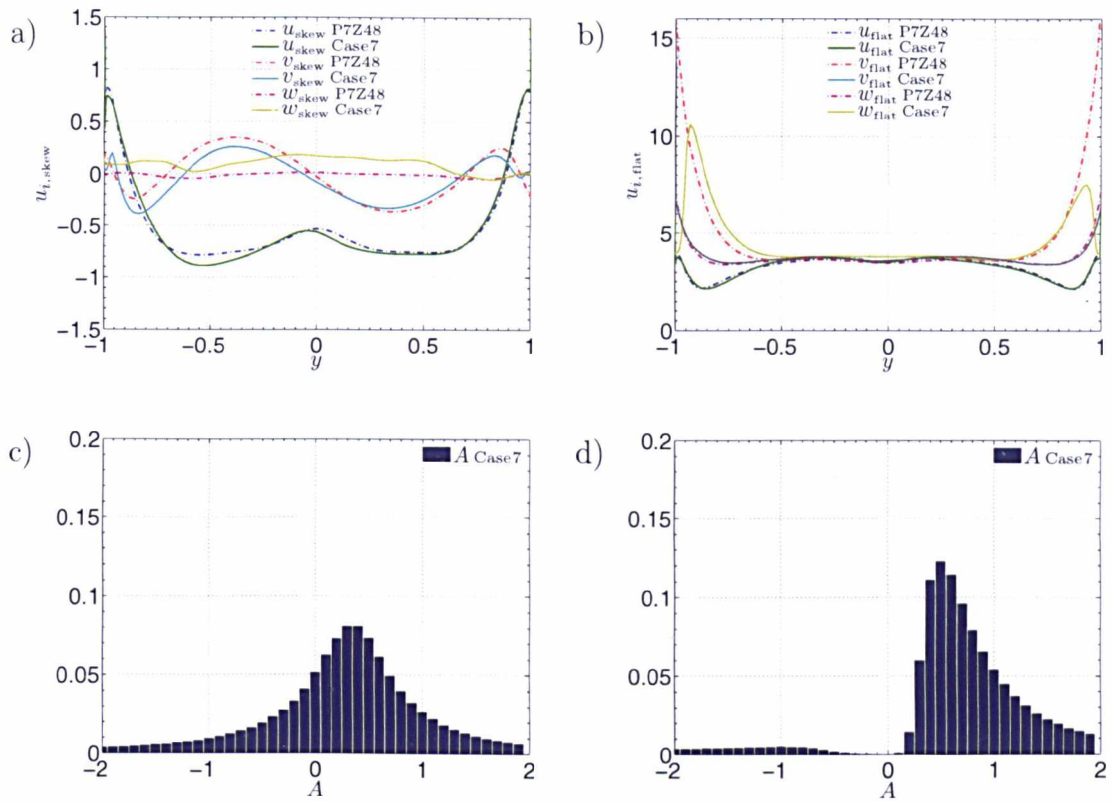


Figure 7.18: Case 7 and P7Z48: a) skewness of velocities; b) kurtosis of velocities. Case 7: c) probability distribution of A for all events; d) probability distribution of A for strong events ($v_{\mathrm{rms,W}} > 0.06$).

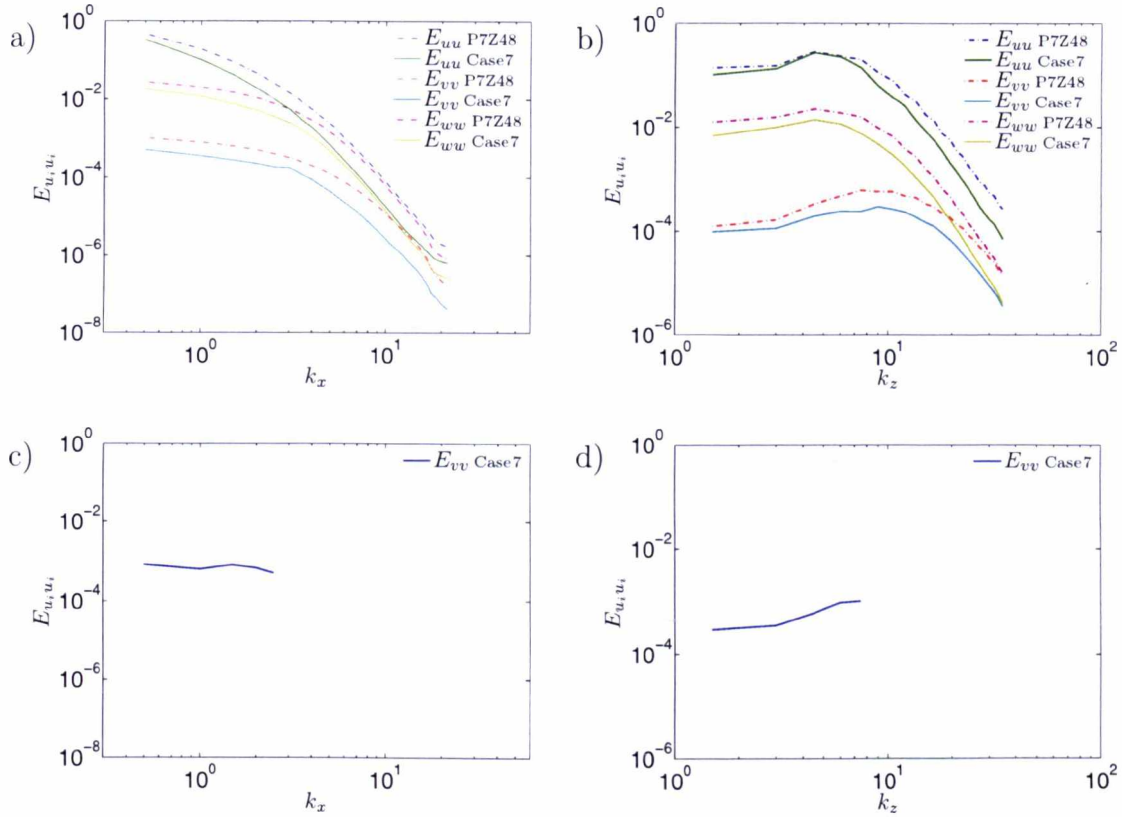


Figure 7.19: Case 7 and P7Z48: a) streamwise energy spectra at $y^+ = 5.4$; b) spanwise energy spectra at $y^+ = 5.4$; c) streamwise energy spectra at wall; d) spanwise energy spectra at wall.

The large computational costs of this simulation deserve attention. Compared to the unmanipulated case the computing time per time step rose from 2.5 sec to 7.5 sec, that is a factor of 3. The sources of this additional load are the calculation of metrics and the regeneration of the Helmholtz matrices. At first this might seem inefficient, but this is not unusual. Carlson *et al.* [11], for example, report a factor of 30. However, they also had to iterate the second and third step which was avoided here by using non-divergent coordinate systems.

As mentioned earlier, opposition control by deformation has been performed by other groups in the past. Table 7.2 compares the parameter values of the three studies known to the author: EKS by Endo *et al.* [27], KS by Kang and Choi [54] and K by Kellogg [58]. They achieved drag reductions of 4.3% to 17% which is also within the range that the results of this project lie. The general view is that the deformation restriction is the limiting factor which was confirmed in the present work. All results must therefore be considered in terms of the specific restriction functions that were applied. Whereas EKS used the penalty parameter χ to curtail the deformation, KS and K defined a maximum deformation amplitude. Also important is that in all previous studies the actuation extended over the entire resolved bandwidth whereas in Case 7 and 8 of the present work the actuation is restricted to $(F_x, F_z = 2.5, 7.5)$. To the author's knowledge the present investigation is the first to be based on divergence-free curvilinear coordinate systems. Whereas EKS and KS used divergent curvilinear coordinate systems K employed an immersed boundary method. In terms of spatial discretisation it should be noted that all previous studies involved spectral discretisation in the homogenous directions. Some investigators also studied an array of actuators. Although at some point such studies will be required, their immediate necessity at this stage is not obvious. An arrangement cannot be designed without first having identified the relevant scales. Lacking this knowledge, it is most surprising that EKS report no drop in performance by replacing the continuous wall deformation with discrete actuators. K however, did observe such an effect. When comparing with the results by KS it should be remembered that they omitted terms in their mathematical model that could potentially have an impact [73].

	Re_τ	Box size	Resolution			y_s^+	F_x, F_z	A		τ_w		f^+_{rms}	
			Nel	P	M_z			χ	f^+_{max}	conti.	arrayed		
Case 7	100	12.6x2x4.2	15x30	7	48	10	7.5	0.1		-12.8%		0.71	Div-free CCS
Case 8	100	12.6x2x4.2	15x30	7	48	10	7.5	0.08		-15.1%		0.77	Div-free CCS
			M_x	M_y	M_z								
EKS [27]	150	3.9x2x1.2	48	97	48	15	all	0.31		-10%	-10%	1	CCS
KS [54]	140	9.4x2x3.1	64	97	96	10	all		5	-17%		3.2	CCS
K [58]	100	12.6x2x4.2	48	68	32	16	all		1-6	-14.3%	-4.8%		IBM

CCS=Curvilinear coordinate system

IBM=Immersed boundary method

Table 7.2: Parameter-value comparison of opposition control simulations using wall deformation. Notice that the implementation of a maximum deformation, f^+_{max}, can vary.

7.3.6 Optimising the function restricting the deformation: Case 8, 9, and 10

Given the few experiments that have been conducted to date, improvements of the current performance must be possible. Thus, the important question is where to direct efforts.

A promising approach is the optimisation of the restriction function, as Case 6 demonstrated that it can have a great impact on the performance of a controller. This function is used to calculate the local amplitude modification that is to be imposed on the actuation to prevent the deflection from excessive growth. Based on the v-in-phase experiment by CMK, it was concluded that negative amplitudes are to be avoided as these can increase the drag. Amplitudes between 0.5 and 1, however, were found to be acceptable as this band delivers equal skin friction as reported by Chung *et al.* [18]. Because the probability distribution of A is not known *a priori* an appropriate formulation to achieve the desired distribution must be found through DNS.

The obvious way to get such a distribution is to decrease χ so that the deformation is less restricted. This is done in Case 8 where χ is lowered to 0.08. The results given in table 7.1 show that as a result the skin-friction reduction on the lower wall increased from 12.8 to 15.1%. The corresponding amplitude distribution in figure 7.20 shows that, indeed, the distribution has shifted in the desired way but only marginally. Further decreases of χ are likely to yield even higher reductions. But at the same time, further decreases will also produce higher actuation strength which requires more flexible actuators.

A restriction function that delivers the desired distribution without higher actuation strength can be designed based on the suggestions made in section 7.2.1.

In the first test, Case 9, the penalty factor is lowered to $\chi = 0.07$ but a damping factor is activated and set to $\varpi = 0.5$. As seen in figure 7.21, this clearly shifts weight away from both tails into the range $0 < A < 1$ while the actuation strength, $v_{\mathrm{rms,\,LW}}$, drops. This, however, is accompanied by a skin-friction reduction of just 12.4%. It is difficult to say whether this can be seen as an improvement or not,

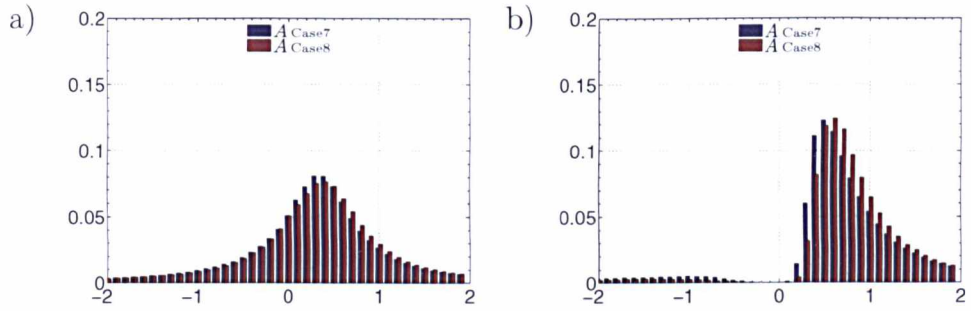


Figure 7.20: Cases 7 and 8: probability distribution of A. a) All events; b) strong events ($v_{\mathrm{rms,W}} > 0.06$).

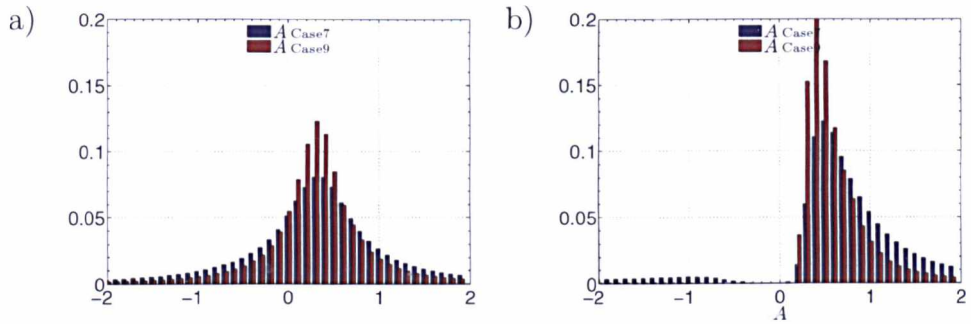


Figure 7.21: Cases 7 and 9: probability distribution of A. a) All events; b) strong events ($v_{\mathrm{rms,W}} > 0.06$).

given the minor change in results.

In the second test, Case 10, an entirely new restriction function is used that is based on expression (7.11) and defined by the parameter f^{+}_{max} given in table 7.1. In this formulation the wall slows down as it approaches a certain limit and starts moving again when the measured velocity reverses. Because of time constraints this experiment was not carried out using deformation as the mode of actuation but rather transpiration. Given the little difference between Case 6 and 7, it is assumed that the results also apply for actuation by deformation. The resulting distribution is shown in figure 7.22 and is exactly as intended: the amplitude is never negative and for strong events usually very close to 1. But other than expected, the performance at the lower wall did not improve but dropped slightly to 11.8%, if so the wall velocity fluctuations dropped slightly, too. What stands out in Case 10 is the high

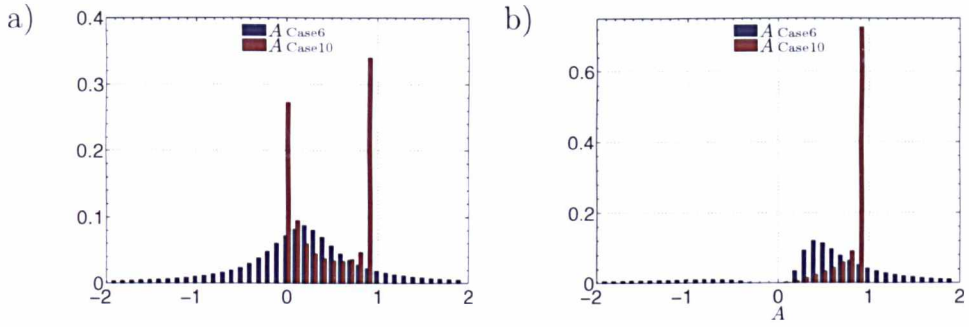


Figure 7.22: Cases 6 and 10: probability distribution of A. a) All events; b) strong events ($v_{\mathrm{rms,W}} > 0.06$).

kurtosis of the wall velocity, $v_{\mathrm{LW,flat}}$. This is because it is mostly the weak events that are affected by strong amplitudes. Because higher kurtosis means more of the variance is due to infrequent extreme deviations, as opposed to frequent modestly-sized deviations it is desirable to keep it low in terms of actuator design. The clustering of distribution close to $A = 1$ for strong events also implies that at the specified maximum deflection there is no large negative correlation between large values of velocity and deflection.

The design criterion for the restriction functions described in this section was to minimise the distribution around $A = -1$ and to maximise it for $0.5 \leq A \leq 1$. This strategy did not yield the desired effect and a possible reason could be that it is not understood how the control behaves outside these two regions.

An answer might be found in a study reported by Farrell and Ioannou [31]. They investigated opposition control not in fully-developed turbulence but in a stochastically forced non-normal dynamical system mimicking the development of coherent structures found in turbulence. The non-normal growth found in such systems will be discussed in section 8.2. In their result the suppression of turbulence energy by opposition control was confirmed. They also studied it for a range of amplitudes which revealed that the suppression became more effective at higher amplitudes. Moreover, they discovered a second control technique where the normal velocity is forced in-phase but at high amplitudes, that is around $-4 \leq A \leq -2$, which leads to similar levels of variance suppression. They refer to this as overdriving suppression.

In the approximate range $-2 \leq A \leq 1$, however, little variance suppression or even instability was found. These findings could be incorporated into a new formulation of A.

Chapter 8

Control-theoretic approach to skin-friction reduction

In the literature review of Chapter 2 various techniques for skin-friction control were discussed. Of those techniques, opposition control was used exclusively for all the control experiments in Chapter 7. Based on a simple law, this control scheme facilitated quick implementation. Moreover, its widespread use made comparison with results from literature possible. For higher drag reduction, though, it might be required not only to rely on intuition but also to use a mathematical framework for the formulation of control laws.

Building such a framework has been the goal of the FCG, Imperial College, recently. It is approached by using modern control theory to derive a controller that is capable of relaminarising turbulent channel flow. More precisely, the controller facilitates non-linear global stabilisation of the perturbed Navier-Stokes equations. It can be achieved by making the linearised part of the perturbed Navier-Stokes equations positive real, or equivalently passive. This prevents transient growth in sub-critical flow and thus eliminates turbulence production.

To derive the control algorithm, concepts of control theory such as the passivity and small-gain theorem are applied. A discussion of this is included in appendix B. Interested readers are referred to Sharma *et al.* [92].

The governing equations for the formulation of the control law are given in section

8.1 and the underlying physical concepts, transient growth and bypass transition, are subject of section 8.2. Results from the control experiments are presented in section 8.3. First, a simulation is discussed where a controller was implemented to make the linearised operator passive through full-body forcing and sensing. This is followed by the introduction of an alternative approach that aims at achieving near-passivity by cancelling the linear coupling term, L_C, throughout the domain. The viability of near-wall actuation for effective control is investigated. Moreover, it is shown how this strategy can be linked to opposition control, thereby providing a platform for the verification of the conclusions drawn in Chapter 7.

The role of non-linearities requires special mention. Transient growth occurs in the absence of non-linear effects and is believed to play a central role in the dynamics of turbulence. Given this relationship, it can be speculated that control schemes interfering with this mechanism may be successful at controlling turbulence. Based on this presumption are linear control strategies. However, this is problematic, because the linear approximation is valid only for very small perturbations. It is likely that the presence of large-magnitude exogenous disturbances will result in the terminal loss of control, if the assumption of linearity fails. Indeed, in the non-linear regime there is no guarantee that linear control strategies will not make the situation worse. Less dramatic but certain is that the neglect of non-linearities in the model will impede the accuracy of the predictions since the rms velocity is of the order of 10% of the mean in fully-developed turbulent flow. The approach taken in this work moves beyond the naive application of linear control strategies to turbulence control by incorporating particular knowledge of the non-linearity present in the governing equations. By showing that this non-linearity can be characterised as positive real, a controller is derived that works in presence of such a non-linearity [89, 98]. It makes the linearised part of the equations positive-real or equivalently passive. As a result, the strategy works for flow disturbances of any size and not just those small enough to permit linear approximation.

8.1 The Orr-Sommerfeld-Squire system

In this section the governing equations for the formulation of the two control strategies are introduced. These equations are contained in the Orr-Sommerfeld-Squire system which is used to describe the linearised behaviour of perturbations to plane Poiseuille flow. To derive the system, the Navier-Stokes equations are linearised about the parabolic steady flow solution, and projected onto a divergence-free basis. The resulting fourth-order PDEs are discretised using Fourier discretisation in the homogenous directions and rearranged into state-space form. This derivation, which is known in the literature (e.g. [8]), yields

$$\frac{\mathrm{d}}{\mathrm{d}t}\begin{bmatrix} \hat{v} \\ \hat{\omega_y} \end{bmatrix} = A \begin{bmatrix} \hat{v} \\ \hat{\omega_y} \end{bmatrix}, \tag{8.1}$$

for a temporally evolving flow with

$$A = \begin{bmatrix} L_{OS} & 0 \\ L_C & L_{SQ} \end{bmatrix} \tag{8.2}$$

where the $\hat{}$ denotes again a Fourier transformed variable and $u_0(y)$ denotes the laminar baseflow. L_{OS}, L_{SQ}, and L_C represent the Orr-Sommerfeld, Squire and coupling operators, respectively, which are

$$L_{OS} = [\nabla^2]^{-1}\left\{-ik_x u_0 \nabla^2 + ik_x \frac{\mathrm{d}^2 u_0}{\mathrm{d}y^2} + \frac{\nabla^2\nabla^2}{Re}\right\} \tag{8.3}$$

$$L_{SQ} = -ik_x u_0 + \frac{\nabla^2}{Re} \tag{8.4}$$

$$L_C = -ik_z \frac{\mathrm{d}u_0}{\mathrm{d}y}\,. \tag{8.5}$$

The Laplacian is given by

$$\nabla^2 = \frac{\partial^2}{\partial y^2} - k_x^2 - k_z^2\,.$$

The linear operator, A, is non-orthogonal which causes transient growth, a phenomenon that will be discussed in the next section.

8.2 Transient growth in sub-critical channel flow

Turbulence develops in laboratory plane Poiseuille flow at Reynolds numbers as low as $Re_C = 1000$. On the other hand, linear stability (eigenvalue) analysis predicts

that Poiseuille flow can be unstable only if $Re_C > Re_{C,crit} \approx 5772$ [31]. In recent work it has been shown that there can be substantial transient growth in the energy of small perturbations to plane Poiseuille flow if the Reynolds number is below $Re_{C,crit}$ [8, 72, 85, 102]. This growth, which may be as large as $O(1000)$, occurs in the absence of non-linear effects and is termed transient growth. Mathematically it can be explained by the non-normality of the governing linear operator. A large contributor to this non-normality is the linear coupling term, L_C, given in expression (8.5) [8]. Investigators speculate that transition may result if some initial disturbances arising from the finite level of background noise present in any flow is able to grow sufficiently to activate non-linear mechanisms which can trigger secondary instabilities.

For a given wavenumber pair one can determine a disturbance, called an optimal growth mode, which yields the greatest transient linear growth. Butler and Farrell [8] investigated these global optimal perturbations which are capable of the greatest energy growth at a specified Reynolds number. They found that in Poiseuille flow the global optimal perturbation consists of a pair of counter-rotating streamwise vortices. It is speculated that these play a dominant role in the creation of coherent structures, though the importance of other modes should not be underestimated. Some oblique waves grow less but faster.

Transient growth of a global optimal mode is demonstrated by the following simulations. Channel flow is perturbed by such a mode and stepped forward in time. The Reynolds number of the baseflow is set to $Re_C = 1500$ at which this optimal mode has the wavenumbers $k_x = 0$ and $k_z = 2$ in streamwise and spanwise direction, respectively. The results are shown in figure 8.1. In the first simulation the equations are linearised so that the perturbation decays to zero at infinity. In the second simulation, the complete non-linear equations are solved which leads to the occurrence of a secondary instability. This is caused by the vortices which generate streamwise streaks by the lift-up mechanism, and which subsequently break down due to the inflectional velocity profile, similar to a Kelvin-Helmholtz instability. In this simulation transition then occurs although, but is interrupted before sustained turbulence could be reached. To ensure the occurrence of secondary instabilities,

All simulation parameters are summarised in chapter 8.1. The baseline simulation, Case 1, is a DNS of fully-developed unmanipulated channel flow at $Re_\tau = 100$ with constant mass flux. The simulations were conducted using Channelflow 0.9.15 [38]. This code solves for the primitives variables and can advance them in time using an explicit third-order Runge-Kutta method. It can be downloaded for free and is licensed under the GNU General Public License. The number of modes is 64 x 71 x 64 (Fourier x Chebyshev x Fourier), which provides higher accuracy than the baseline case P7Z48 of Chapter 5. The size of the computational domain is, as before, 12.6 x 2 x 4.2. The time step is dictated by the condition CFL<1. The non-linear terms are computed in rotational format with 3/2 dealiasing.

Flow parameters			Resolution			Box size	Time integration		Flow State
Re_τ	Re_B	Re_C	M_x	M_y	M_z		Scheme	Δt	
100	1418	1709	64	71	64	12.6 x 2 x 4.2	RK3	0.02	Turbulent

Case	Control	Actuation domain	F_x, F_z
1	unmanipulated	all	all
2	Full passivity	all	all
3	Near passivity ($L_C = 0$)	all	all
4	Near passivity ($L_C = 0$)	$y^+ \lessapprox 20$	all
5	Near passivity ($L_C = 0$)	$y^+ \lessapprox 20$	2.5, 7.5

Table 8.1: Simulation parameters.

Using the procedure outlined in section 5.1 the statistics of unmanipulated channel flow (Case 1) are verified first. The reference for the validation is again the database provided by Kuroda and Kasagi [64]. The graphs in frames 'a', 'b', and 'c' of figure 8.2 show that the profiles are closely reproduced. The only identifiable discrepancy is found in the middle of the domain for the quantity u_{rms}. Given this accuracy, the discretisation is considered sufficient for control studies.

For the first control experiment, Case 2, a control algorithm was formulated based on making the linear part of the Navier-Stokes equations passive, as outlined

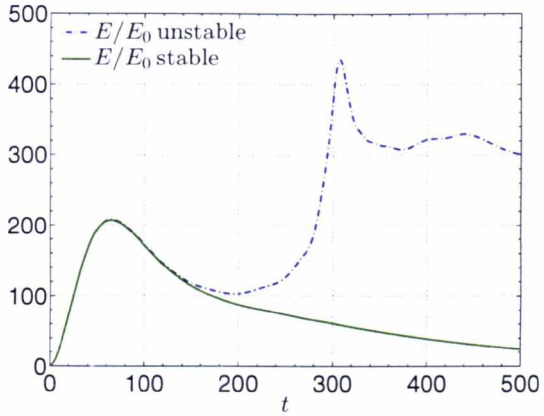


Figure 8.1: Evolution of perturbation energy density for two Poiseuille flow simulations at $Re_C = 1500$. The lower curve was obtained from linear simulation and the upper curve from a non-linear simulation.

certain requirements must be met. The first requirement is that the initial disturbance energy is sufficiently high. In the present case it is $E_0 = 7 \times 10^{-5}$. The second requirement is that streamwise noise is added to the flow to break the symmetry. This noise is set to 1% of the initial disturbance energy. Both, the level of noise and the level of initial perturbation energy, correspond to the simulations performed by Lundbladh *et al.* [72].

The connection between transient growth and near-wall streaks in turbulence was made by Butler and Farrell [8]. Adhering to this idea, the control laws in the next section attempt to destroy streaks in turbulent channel flow by preventing transient growth.

An example of control applied to transient growth was given by Farrell and Ioannou [31], which was already discussed in section 7.3.6. They applied opposition control to the evolution of optimal disturbances in channel flow and found suppression of fluctuations.

8.3 Passivity-based control in turbulent channels

This section presents the results from a number of control experiments that were conducted based on the idea of enhancing the passivity of the linearised system.

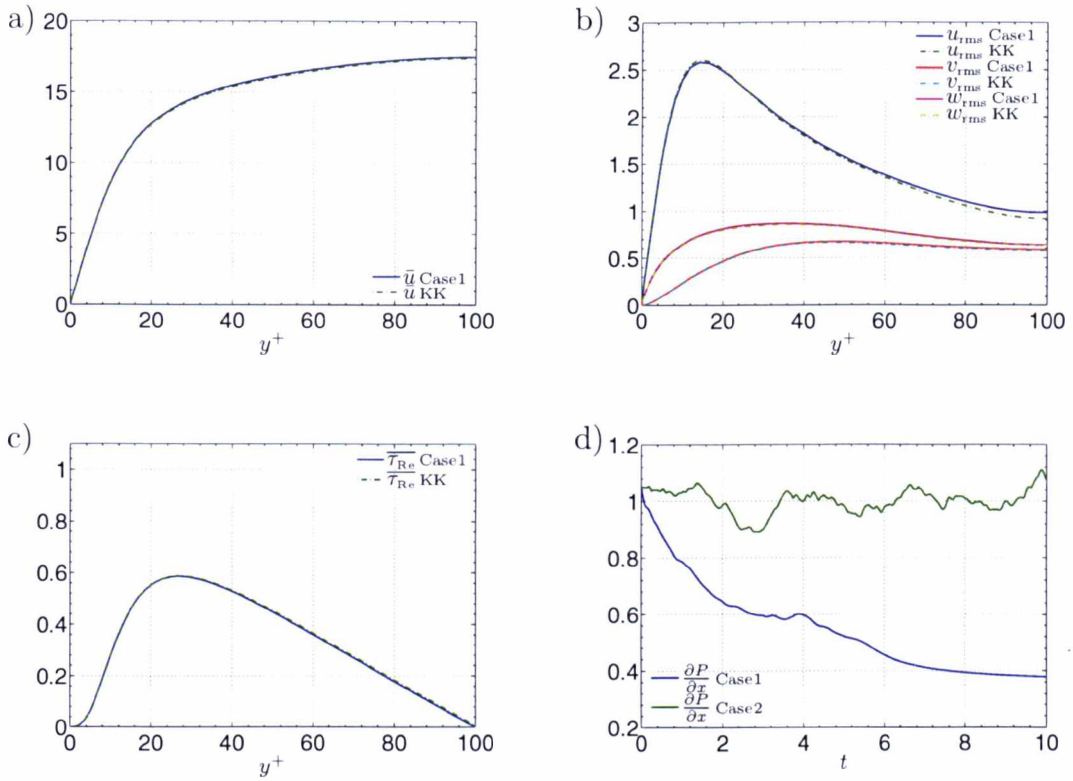


Figure 8.2: Channelflow: a) mean velocity; b) rms velocity fluctuations; c) Reynolds stress; d) drag reduction using controller.

in Sharma *et al.* [92] and appendix B. The resulting controller assumes full-domain sensing and actuating of the wall-normal velocity, v. It is applied to an initially fully-developed turbulent field taken from Case 1. Frame 'd' of figure 8.2 shows how the drag of the channel, that is the mean streamwise pressure gradient, is reduced as the flow converges to a laminar flow state.

In itself this result is trivial as it is obvious that complete cancellation is possible if the entire field can be observed and controlled. But instead, it should be regarded as the first successful test of the underlying control-theoretic model. However, an attempt to restrict the actuation to the boundary failed [92].

Alternatively, near-passivity can be pursued by cancelling the linear coupling term, L_C [92]. Within the context of transient growth, Kim and Lim [61] already showed that without this term near-wall turbulence decays. Their experiment is repeated in Case 3. Converting L_C to primitive variables, it can be cancelled by

forcing u and w through

$$f_u = -\frac{k_z^2}{k_x^2 + k_z^2} 2yv \ , \tag{8.6}$$

$$f_w = \frac{k_x k_z}{k_x^2 + k_z^2} 2yv \ . \tag{8.7}$$

As a result, the flow relaminarises, as shown by the lower graph in frame 'a' of figure 8.3.

Having found that turbulence can be reduced by interfering with L_C, the control strategy is tested to see if it is also successful for actuation confined to the near-wall region. In Case 4 the actuation of the last experiment is filtered by multiplication with the function shown in frame 'b' of figure 8.3, thereby only actuating the region close to the wall, that is $y^+ \lessapprox 20$. The resulting mean streamwise pressure gradient is shown by the middle graph in frame 'a'. Apparently, relaminarisation is not achieved. Instead, the drag reduces to less than 40% of that of the uncontrolled flow.

Clearly, opposition control would also curtail the effect of L_C, since this term is multiplied with $\hat{v}$ in the equation system 8.1. This was also noted by Kim and Lim [61]. Accordingly, one would expect the scaling laws found in Chapter 7 to apply to the last experiment. To validate this hypothesis the previous experiment is repeated in Case 5 but with the actuation confined to a bandwidth of up to $(F_x, F_z) = (2.5, 7.5)$, which corresponds to the bandwidth used in the last experiments of Chapter 7. The resulting drag is shown by the upper graph in frame 'a', where we observe that the controller loses some of its performance but the reduction in drag is still relatively high. The observation, that high drag reductions can be achieved by "low"-wavenumber forcing, agrees with the findings of Chapter 7.

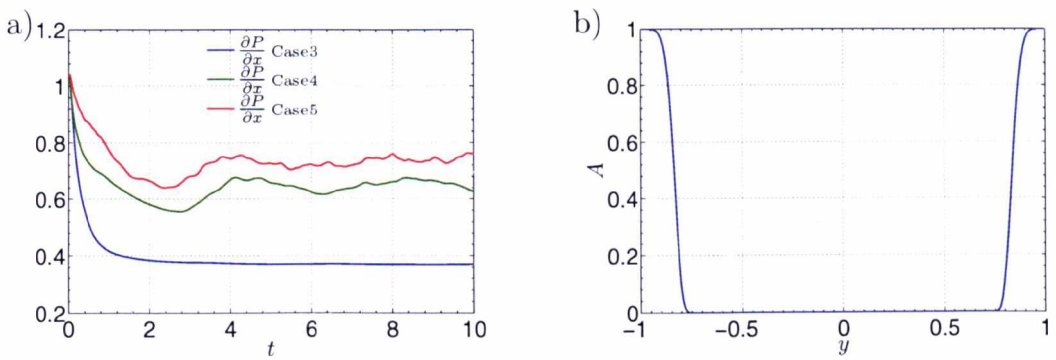


Figure 8.3: a) Drag reduction. b) Amplitude function, A, for Case 4 and Case 5.

Chapter 9

Conclusions and outlook

This thesis offers a contribution to the development of a technology for the reduction of skin friction in turbulent flow via active wall deformation. In particular, the project attempted to investigate how local wall motion alters the flow, to construct a predictive test-bed, and to correctly interpret the information derived from flow control simulations.

First, the local response to predetermined motion of Gaussian actuators was examined in laminar flow. Without turbulent fluctuations, the baseflow allowed clear identification of the flow perturbations. To make quick predictions, the irregular moving boundaries were initially approximated by velocities applied to a flat wall. For very small deflections this approximation is accurate and allows the derivation of a closed expression for the wall vorticity flux. The perturbation analysis revealed that transient Gaussian actuators are surrounded by a single lobe of vertical velocity. This important feature opens the possibility of implementing control schemes based on imparting vertical momentum, such as opposition control. Structures of streamwise vorticity, in contrast, were found to be complex and unsuitable for direct interference with the streamwise vortices occurring in turbulent flow. For oscillating Gaussian actuators, it was found that no significant quasi-static structures emerge when the time scales of the actuation are of the same order as the time scales of the baseflow. The reason for the absence of such structures is that the upward and downward motion of a smooth actuator are accompanied by the same physical

mechanisms in the flow. Next, the simulations were rerun without approximation of the boundaries. Instead, a time-dependent curvilinear coordinate system was used to represent the irregular and moving walls. Despite the considerable amplitude of the actuators, good agreement was found with the results from the approximated simulations. The main non-linear effect was the appearance of a separation bubble inside an intruding actuator and at the back of a protruding actuator.

As a preparation for investigating turbulent flow under the influence of actuation, unmanipulated fully-developed turbulent channel flow was computed and the statistical variations were compared to a database provided by Kuroda and Kasagi [64]. A suitable resolution for subsequent turbulent studies was identified on the basis of accuracy and computational costs.

Then, the response to actuator motion was studied again but with an initial field taken from the previous turbulent channel flow simulations. It was found that for the parameters under investigation, locally-varying wall motion can restructure turbulence in the near-wall region. Moreover, it was shown how the perturbation of the wall-normal velocity penetrates the flow much further than the perturbation of streamwise velocity.

In an attempt to exploit the suitability of wall deformation for the manipulation of vertical velocity in the near-wall region, the opposition control scheme by Choi *et al.* [15] was implemented. This scheme aims at opposing the velocity sensed away from the wall by imposing transpiration of opposite direction at the wall. In order to use wall deformation instead of transpiration as actuation mode, a number of modifications had to be introduced to the original scheme. First, only the lower wall was controlled – a constraint dictated by the specific coordinate system in use. Secondly, the actuation was restricted to small wavenumbers because instabilities were encountered at higher wavenumbers. And finally, the actuation was restricted in strength so as to prevent the wall from penetrating the plane where the flow measurements were taken. With each modification a new experiment was conducted to study its isolated effect.

First, the original opposition control experiment was repeated. The simulation delivered results in close agreement with the study by Choi *et al.* [15]. Next, the

control was confined to the lower wall only. The upper wall, in contrast, was left uncontrolled but was made to produce the same blowing and suction as the lower wall. The results revealed that the drag reduction on the lower wall was almost the same as in the previous experiment. This indicates little interaction between the two halves of the channel domain regarding skin friction, despite an obvious energy flux across the midplane. On the upper wall, in contrast, no drag reduction was observed. This ineffectiveness highlighted the importance of coordinating the actuation. Subsequently, the actuation bandwidth was gradually reduced. Interestingly, high reductions in drag were maintained for bandwidths that include the characteristic scale of the near-wall streaks. Considering the difficulty of producing small actuators, this quasi-invariance could prove beneficial. From there we continued by introducing a function that manipulates the actuation strength locally. As expected, this measure impeded the attainable drag reduction on the lower wall significantly. This is because the manipulation of local forcing amplitudes causes the actuation to be less coordinated with the flow. The last modification, the use of deformation instead of transpiration as actuation method, had little effect on the average wall shear stress. This suggests that for the small deflections found in this experiment (on average less than a wall unit) the secondary effects of wall motion are negligible. However, it remains unknown if this still holds when the deflection itself rather than the speed of deflection is coordinated with adjacent flow events. The study concluded with an attempt to increase the reduction in drag by optimising the formulation of the deformation restriction function. However, with the present knowledge no measurable improvements were achieved.

In this project it was shown that the flow perturbation induced by active wall deformation exhibits characteristics suitable for flow control. As a specific example, it was demonstrated how the skin friction in low-Reynolds number turbulent flow can be reduced by opposing the near-wall vertical velocity through wall deformation. Having shown the feasibility of this method, one is left with the question if further investigations in this direction are wise with the current state of knowledge. The computational costs of simulating locally-varying wall motion are considerable. Furthermore, it appears to be more profitable to first explore the vast potential for

improvement offered by simple control techniques based on the direct manipulation of individual flow quantities. The necessary adaptation to the specifics of certain actuation methods could then be pursued at an advanced stage.

As a final note it should be remembered that all simulations were conducted in a hypothetical environment. Locally controlled channel flow at very small Reynolds numbers is difficult to realise in a laboratory environment and is not really relevant for real-world applications. But given the embryonic state of research on reactive flow control and the complexity of the problem, such simplifications are currently inevitable and justified.

Appendix A

Verification of the mathematical theory and its implementation

In this chapter a number of tests are discussed that were conducted to verify the mathematical theory of Chapter 3 as well as its numerical implementation. To cover as many potential error sources as possible, test cases with a high degree of complexity were chosen.

A.1 Test 1: Passive obstacles in two-dimensional flow

An exact verification of numerical codes is possible when the solution is known analytically. To run such a test case the idea of curvilinear coordinate systems is reversed: Instead of having a flow domain that is curvilinear in Cartesian coordinates but regular in curvilinear coordinates, we now use a domain that is regular in Cartesian coordinates but curvilinear in curvilinear coordinates. An example of a domain that is regular in Cartesian coordinates is the straight channel. In the test the flow was computed for this geometry in a curvilinear system. Upon transformation into Cartesian coordinates, the flowfield should give the well-known result $u = 1 - y^2$.

The problem is solved in two dimensions and the coordinate system is chosen so that it fits the boundaries of Case 1 in table 4.1 but with two-dimensional passive

obtacles, that is $\sigma_z = 0$ and $t = t_\infty$. The mesh, consisting of 1222 Elements, is generated using FELISA and shown in frame a of figure A.1.

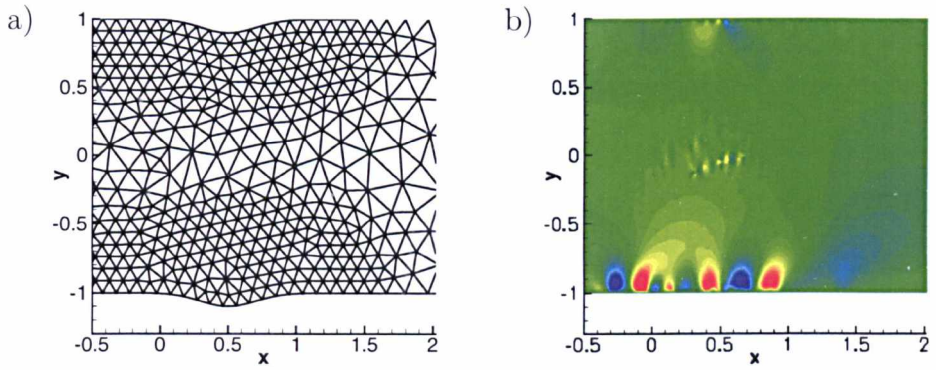


Figure A.1: a) Computational mesh around the obstacles. b) Error of the flow over passive obstacles in curvilinear coordinates: Contours of vertical velocity between -2E-5 and 2E-5.

After transients had decayed a snapshot was taken of the error in wall-normal velocity which is shown in frame b of figure A.1. In the vicinity of the dimple the error is oscillating in streamwise direction. Around the bump the pattern is similar if much less pronounced. An explanation for this phenomenon can be found in the way FELISA discretises the boundary. It uses cubic polynomials to interpolate between the data points of the Gaussian curve given as input. The resulting error converges for decreasing mesh sizes. Since the mesh is already fine, the error is small relative to the flow strength. Given this, it appears the implementation of the equations for the fixed two-dimensional curvilinear system is correct.

It can be concluded that if there is a noticeable error in the code used for the simulations in this work it must be contained in one of the two potential error sources that this test does not cover. One source is the third dimension and the other the motion of the actuator. The former is subject of the test in the next section whereas the latter is very difficult to verify unless another technique is implemented that deals with moving boundaries. Since this is too involving for the time frame of this project it was omitted. It should be noted though that the correct treatment of time-dependency in general coordinate systems has been thoroughly investigated by

Luo *et al.* [73] whose findings were paid regard to in the present work.

A.2 Test 2: Swapping of coordinate axes

In the second test case, two laminar-flow simulations over active obstacles are conducted. In the first one the mean flow is in the x-direction, which is discretised by spectral elements, and in the second one it is in the z-direction, which is Fourier discretised. With time-dependent three-dimensional effects taking place, this test case covers all potential error sources relating to three-dimensionality.

The parameters are the same as in Case 3 of table 6.1, bar the resolution. To ensure that it had as little effect on the result as possible polynomial order was increased to $P = 11$.

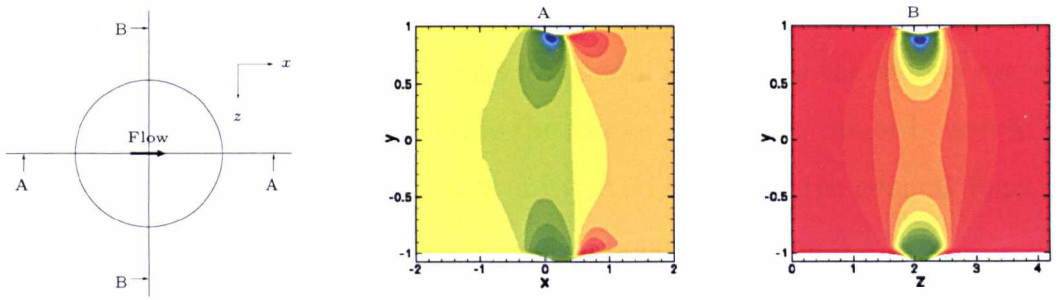
To compare the two results, the wall-normal velocity, v, is analysed. Since flow perturbations in v penetrate deep into the domain this quantity is well suited for global analysis. Contour plots of v are shown in figure A.2 and agree well for the two cases. A small difference exists that becomes larger with decreasing mesh density, that is towards the middle of the channel. This indicates that the discrepancies between the two results are caused by discretisation errors and not by an error in the numerical code. At the point $(x, y, z) = (0.25, 2.0943, 0.8)$, which is directly above the centre of the dimple, the vertical velocity is $v = -0.2956$ in the first case and $v = -0.2949$ in the second case which amounts to a 0.23% difference.

Considering the results of this test case and the previous one, it is concluded that if there is any error in this code, it is caused by incorrect representation of the actuators movement.

A.3 Test 3: Interaction between the flow responses of two actuators in two-dimensional flow

In all the channel-flow simulations presented in this work both walls were deformed. But with most practical flows being exterior, the flow around solitary actuators is of

Case 1: Flow in x-direction



Case 2: Flow in z-direction

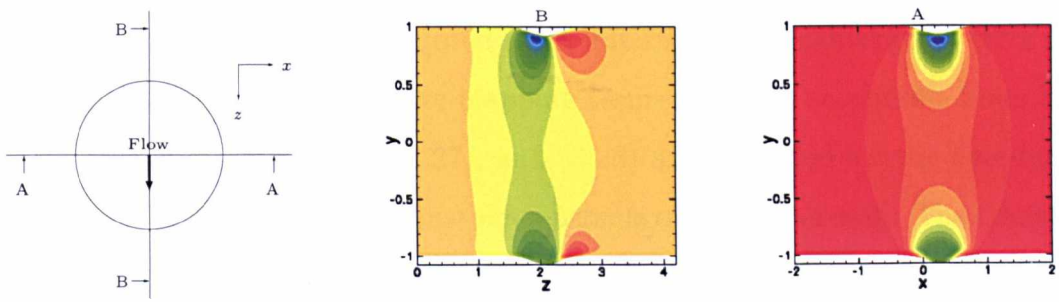


Figure A.2: (-0.4≤v≤-0.02)-contours in the middle and (-0.75≤v≤0.2)-contours on the right at $t = 0.2$.

more interest. It is only for reasons of efficiency that the simulations carried out in the last sections contained actuators on both walls. To understand how well those results apply to the case of a solitary actuator, it needs to investigated how much influence a moving obstacle has on the flow-region close to the opposite wall. This is done in this section using two-dimensional simulations. The underlying assumption is that the perturbation of a two-dimensional Gaussian obstacle will always be larger than that of a three-dimensional one.

Two simulations are carried out. Both have the parameter values of Case 1 in table 4.1 but with $\sigma_z = 0$ because of the two-dimensionality. In the first one actuators are placed again on upper and lower wall whereas in the second one only the lower wall is actuated. As opposed to the former, the latter cannot be solved in a coordinate system where the Jacobian is unity. And therefore, the general equations (3.29-3.32) must be solved instead of the special ones of section 3.1.3.

As a consequence, the pressure and viscous terms of A^i are not treated explicitly in the second case which means that the continuity equations is enforced exactly. So if the results of the two simulations correspond sufficiently well one can conclude not only that the two actuators have limited reach but also that the divergence error due to explicit treatment of the pressure mapping terms is within acceptable bounds.

Below, the operators (3.26), (3.27), and (3.28) are expanded for the coordinate stystem which fits a channel with just one obstacle on the lower wall. The transformation is defined by the relations

$$\begin{aligned} \tau &= t \\ \xi &= x \\ \eta &= f(x,y,t)\ . \end{aligned} \tag{A.1}$$

(A.2)

Note that as opposed to expression (4.37) η now depends on y. The transformation matrix (3.14) then becomes

$$c_j^k = \begin{pmatrix} 1 & \frac{\partial y}{\partial \xi} \\ 0 & \frac{\partial y}{\partial \eta} \end{pmatrix} \tag{A.3}$$

and $J = c_2^2$. Generating the metric tensor (3.17) yields

$$g_{ij} = \begin{pmatrix} 1 + \frac{\partial y}{\partial \eta}^2 & \frac{\partial y}{\partial \eta}\frac{\partial y}{\partial \xi} \\ \frac{\partial y}{\partial \eta}\frac{\partial y}{\partial \xi} & 1 + \frac{\partial y}{\partial \xi}^2 \end{pmatrix} \tag{A.4}$$

so that the Christoffel symbols become

$$\Gamma_{11}^1 = \Gamma_{12}^1 = \Gamma_{22}^1 = \Gamma_{21}^1 = 0. \tag{A.5}$$

and

$$\Gamma_{21}^2 = \Gamma_{12}^2 = \frac{\frac{\partial^2 y}{\partial \xi \partial \eta}}{\frac{\partial y}{\partial \eta}}, \quad \Gamma_{11}^2 = \frac{\frac{\partial^2 y}{\partial \xi \partial \xi}}{\frac{\partial y}{\partial \eta}} . \tag{A.6}$$

The coordinates are only moving in vertical direction so that

$$S^2 = -\frac{\partial \eta}{\partial t} = \frac{1}{J}\frac{\partial y}{\partial \tau} \tag{A.7}$$

For clarity the new transformation coefficient

$$s^{ij} = g^{jk} U^i_{,k} \tag{A.8}$$

is defined. Evaluating each component gives

$$s^{11} = \frac{\partial U}{\partial \xi} - \frac{\frac{\partial y}{\partial \xi}}{\frac{\partial y}{\partial \eta}}\frac{\partial U}{\partial \eta} \tag{A.9}$$

$$s^{12} = -\frac{\frac{\partial y}{\partial \xi}}{\frac{\partial y}{\partial \eta}}\frac{\partial U}{\partial \xi} + \frac{\frac{\partial y}{\partial \xi}^2 + 1}{\frac{\partial y}{\partial \eta}^2}\frac{\partial U}{\partial \eta} \tag{A.10}$$

$$\begin{aligned} s^{21} &= \frac{\partial V}{\partial \xi} - \frac{\frac{\partial y}{\partial \xi}}{\frac{\partial y}{\partial \eta}}\frac{\partial V}{\partial \eta} \\ &+ U\left(\frac{\frac{\partial^2 y}{\partial \xi \partial \xi}}{\frac{\partial y}{\partial \eta}} - \frac{\frac{\partial y}{\partial \xi}\frac{\partial^2 y}{\partial \xi \partial \eta}}{\frac{\partial y}{\partial \eta}^2}\right) + V\left(\frac{\frac{\partial^2 y}{\partial \xi \partial \eta}}{\frac{\partial y}{\partial \eta}} - \frac{\frac{\partial y}{\partial \xi}\frac{\partial^2 y}{\partial \eta \partial \eta}}{\frac{\partial y}{\partial \eta}^2}\right) \end{aligned} \tag{A.11}$$

$$\begin{aligned} s^{22} &= -\frac{\frac{\partial y}{\partial \xi}}{\frac{\partial y}{\partial \eta}}\frac{\partial V}{\partial \xi} + \frac{\frac{\partial y}{\partial \xi}^2 + 1}{\frac{\partial y}{\partial \eta}^2}\frac{\partial V}{\partial \eta} \\ &+ U\left(-\frac{\frac{\partial^2 y}{\partial \xi \partial \xi}\frac{\partial y}{\partial \xi}}{\frac{\partial y}{\partial \eta}} + \frac{\frac{\partial^2 y}{\partial \xi \partial \eta}(1 + \frac{\partial y}{\partial \xi}^2)}{\frac{\partial y}{\partial \eta}^3}\right) \end{aligned} \tag{A.12}$$

$$+ V\left(-\frac{\frac{\partial^2 y}{\partial \xi \partial \eta}\frac{\partial y}{\partial \xi}}{\frac{\partial y}{\partial \eta}} + \frac{\frac{\partial^2 y}{\partial \eta \partial \eta}(1 + \frac{\partial y}{\partial \xi}^2)}{\frac{\partial y}{\partial \eta}^3}\right) \tag{A.13}$$

The operators can then be written out as

$$N^1(\mathbf{u}) = U\frac{\partial U}{\partial \xi} + V\frac{\partial U}{\partial \eta} - \frac{1}{J}\frac{\partial y}{\partial \tau}\frac{\partial V}{\partial \eta} \tag{A.14}$$

$$\begin{aligned} N^2(\mathbf{u}) &= U\left(\frac{\partial V}{\partial \xi} + \Gamma^2_{11}U + \Gamma^2_{12}V\right) + V\left(\frac{\partial V}{\partial \eta} + \Gamma^2_{21}U + \Gamma^2_{22}V\right) \\ &- \frac{1}{J}\frac{\partial y}{\partial \tau}\frac{\partial V}{\partial \eta} + U\frac{\partial}{\partial \xi}\left(\frac{1}{J}\frac{\partial y}{\partial \tau}\right) + V\frac{\partial}{\partial \eta}\left(\frac{1}{J}\frac{\partial y}{\partial \tau}\right) \end{aligned} \tag{A.15}$$

$$G^1(p) = -\frac{\partial p}{\partial \xi} - g^{12}\frac{\partial p}{\partial \eta} \tag{A.16}$$

$$G^2(p) = \frac{1}{Re}\left(\frac{\partial s^{11}}{\partial \xi} + \frac{\partial s^{12}}{\partial \eta} + \Gamma^2_{21}s^{11} + \Gamma^2_{22}s^{12}\right) \tag{A.17}$$

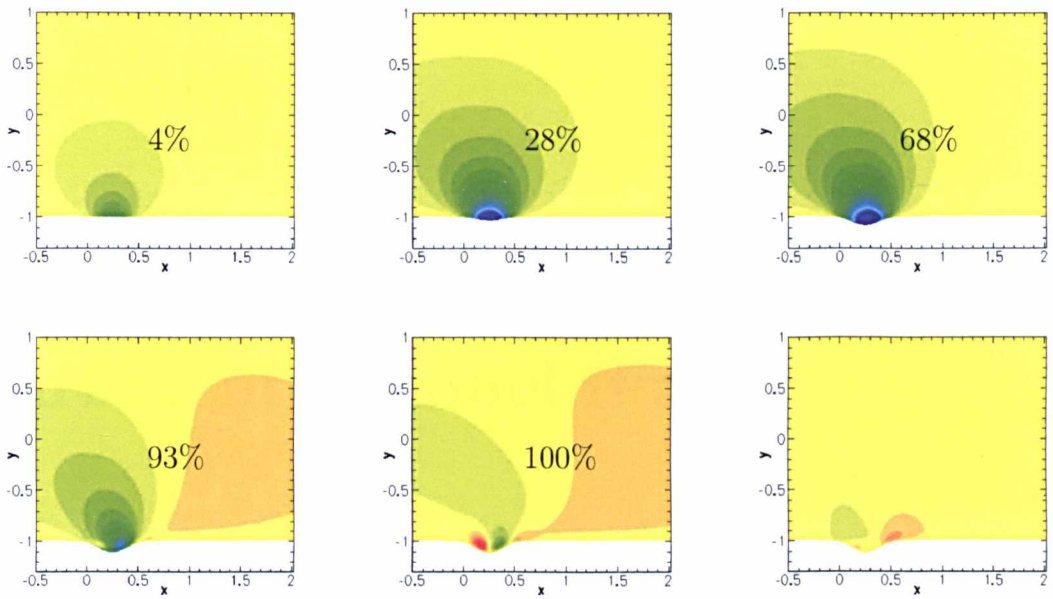
$$L^1(\mathbf{u}) = \frac{1}{Re}\left(g^{jk}v^i_{,k}\right)_{,j} \tag{A.18}$$

$$L^2(\mathbf{u}) = \frac{1}{Re}\left(\frac{\partial s^{21}}{\partial \xi} + \frac{\partial s^{22}}{\partial \eta} + \Gamma^2_{11}s^{11} + \Gamma^2_{12}(2s^{21} + s^{12}) + \Gamma^2_{22}s^{22}\right) \tag{A.19}$$

The two cases are compared using contour plots of vertical velocity. Figure A.3 reveals that the two actuators do interact. However, close the wall the active dimple at the lower wall exhibits the same flow response in both cases. In terms of skin-friction control this is the most important region. Moreover it should be noted that the amplitude is higher than anything in the control simulations in Chapter 7. Hence, it is legitimate to assume that the results obtained with one actuator on each wall can be used to predict the flow over a single actuator. This applies in particular to the finding that a downward moving wall deformation actuator is surrounded by an isolated lobe of negative vertical velocity and *vice versa*.

Comparing figure A.3 with figure 4.18 confirms the initial assumption that two-dimensional Gaussian obstacles do create larger perturbations than three-dimensional ones. This also implies that the interaction of upper- and lower-wall actuator can only be less in the three-dimensional cases analysed earlier.

Case 1: Lower wall actuation



Case 2: Lower and upper wall actuation

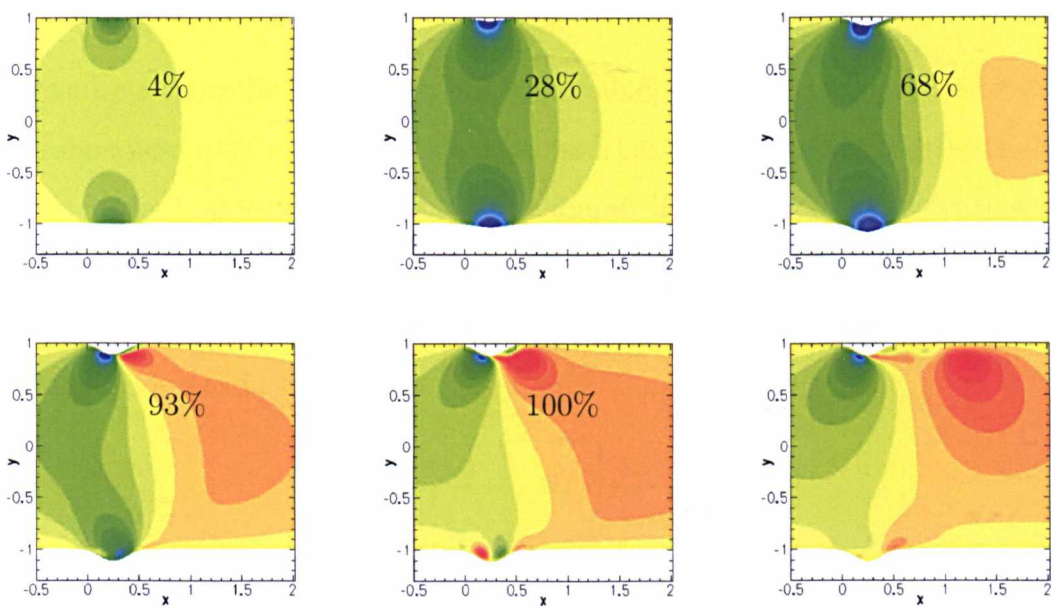


Figure A.3: (-0.07≤v≤-0.02)-contours in xy-midplane at t = 0.5, 1, 1.5, 2, 3, 7.

Appendix B

Passivity-based control of turbulent channel flow

In this chapter it is directly quoted from Sharma *et al.* [92]. It presents the theory and tools needed to derive the controller used in Chapter 8.

B.1 Theoretical foundation

We require a controlled system, as far as possible, to have the properties of stability and robustness with respect to external disturbances. These needs drive the design choices of the feedback control rule to be found. The design objectives are achieved by application of two fundamental results from control theory, which give general, open-loop conditions for closed-loop stability of two arbitrary elements connected in a feedback loop as in Figure B.1.

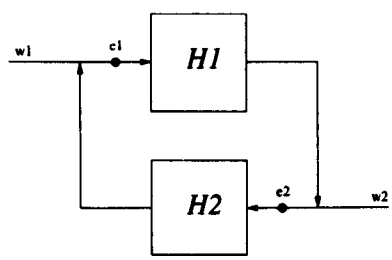


Figure B.1: A generalised feedback loop made up of two elements H_1 andH_2. This block diagram represents the equations $e_1 = H_2 e_2 + w_1$ and $e_2 = H_1 e_1 + w_2$.

The application of these results to the perturbed Navier-Stokes equations gives conditions for stability that act as a specification for the feedback control system synthesis.

The two results to be used are the small-gain theorem and the passivity theorem. One can be derived from the other by a suitable transformation, a fact we will make use of at the controller synthesis stage. They are described below.*

B.1.1 The small-gain theorem

Say U and Y are normed function spaces such as $\mathcal{L}_2[0,\infty)$ or $\mathcal{L}_2\ \mathbb{R}^3 \times [0,\infty)$. H is a system that maps U into Y, $H : U \mapsto Y$. Assume H is causal in time†, stable‡ and has no bias or offset.§

Let e be an element of U, and e_t be that same function truncated on $[0,t]$. The gain $\gamma(H)$ of H is defined via the norms on U and Y,

$$\gamma(H) = \sup_{e_t \in U} \frac{\|He_t\|_Y}{\|e_t\|_U}. \tag{B.1}$$

A feedback loop is such as that in Figure B.1 is made up of two elements, H_1 and H_2 where H_1 maps U into Y and H_2 maps Y back into U. If H_1 and H_2 have finite gains such that

$$\gamma(H_1)\gamma(H_2) < 1 \tag{B.2}$$

then for all $\mathcal{L}_2$ w_1, w_2, there are $\mathcal{L}_2$ e_1, e_2, that is, the closed loop is bounded and stable [113]. This result can be understood in terms of the contraction mapping principle [39]. The small-gain theorem is in fact the cornerstone upon which modern $\mathcal{H}_\infty$ theory is built.

B.1.2 The passivity theorem

Suppose H_1 and H_2 are square, that is, $H_1 : U \mapsto U$ and $H_2 : U \mapsto U$ also. Let $\langle \cdot, \cdot \rangle$ define the inner product on U.

*For a proof the reader is directed to [39]

†that is, the output up to time T depends only on the input up to time T, for all T

‡that is, if $e \in \mathcal{L}_2$ then $He \in \mathcal{L}_2$

§so that $Ho = o$ where o is the zero element

A system H is called passive if

$$\langle e, He \rangle \geq 0, \quad \forall\, e \in U. \tag{B.3}$$

In the case of strict inequality, H is called strictly passive.

It can be shown from the small-gain theorem that if H_1 is positive and $-H_2$ is strictly positive, with finite gain, then the closed loop system in Figure B.1 is bounded and stable [113]. In the case that H is a transfer function, then it is equivalently called positive real if and only if [39, 98]

$$H(s) + H^*(s) \geq 0, \quad \forall\, Re(s) > 0. \tag{B.4}$$

B.1.3 Application to the Navier-Stokes equations

By serendipity, the positive real result given above may be applied to the perturbed Navier-Stokes equations to give sufficient conditions for boundedness, and therefore stability of the base state, in the presence of bounded perturbations or disturbances.

We begin by writing down the equations for three-dimensional incompressible fluid flow evolving in spatial domain Ω where Ω is an open, subset of $\mathbb{R}^3$ with boundary $\partial\Omega$.

Assume that the state of the flow at an instant in time t is fully described by a time-dependent velocity vector field $V(x,t)$ and a scalar pressure field $P(x,t)$.[¶]

The relevant equations are the forced incompressible Navier-Stokes equations. A control function $f(x,t)$ and a divergence-free exogenous disturbance forcing $d(x,t)$ are introduced. The forcing resulting from the control is restricted by a linear operator B, representing physical limitations on the actuation. The range of B is the divergence-free body forcing arising from all possible control actions. Thus, $Bf(x,t)$ is the forcing arising from the control function at time t and position x.

The equations of motion are

$$\dot{V}(x,t) = -V(x,t) \cdot \nabla V(x,t) - \nabla P(x,t) + \frac{1}{Re}\nabla^2 V(x,t) + Bf(x,t) + d(x,t) \tag{B.5}$$

$$\nabla V(x,t) = 0 \quad x \in \Omega,\ t \in [0,T]. \tag{B.6}$$

[¶]so that V is mapping $\Omega \times [0,T]$ into $\mathbb{R}^3$ and P is mapping $\Omega \times [0,T]$ into $\mathbb{R}$.

The boundary conditions are prescribed,

$$V(x,t) = 0 \quad x \in \partial\Omega,\ t \in [0,T]. \tag{B.7}$$

To proceed, a time-invariant solution $\bar{v}(x)$ is assumed, that corresponds to the uncontrolled, disturbance-free situation. This steady solution may or may not be linearly stable. Perturbations $v(x,t)$ about this equilibrium are considered. This gives the net velocity vector field

$$V = \bar{v} + v. \tag{B.8}$$

The steady pressure $\bar{p}(x)$ is similarly perturbed by $p(x,t)$. We seek to find a control forcing to globally stabilise the steady solution $\bar{v}(x)$, that is to return the flow from any state to $\bar{v}$.

Substitution into (B.5) gives the perturbation equations

$$\begin{aligned}
\dot{v}(x,t) =& -\bar{v}(x,t)\cdot\nabla v(x,t) - v(x,t)\cdot\nabla\bar{v}(x,t) - n(x,t) - \nabla p(x,t) \\
&+ \frac{1}{Re}\nabla^2 v(x,t) + Bf(x,t) + d(x,t), \\
n(x,t) =& v(x,t)\cdot\nabla v(x,t), \\
0 =& \nabla v(x,t), \\
& x \in \Omega,\ t \in [0,T].
\end{aligned} \tag{B.9}$$

A substitution has been made for the nonlinear term, giving coupled linear and nonlinear equations. We do not make the linearising assumption of small perturbations.

Let $y(x,t)$ be some measurements made at time t that can be modelled by

$$y(x,t) = Cv(x,t)$$

where C is a linear operator whose range covers possible measurements. Measurement at the boundary may be modelled in a fashion analogous to the boundary control.

The equations (B.9) include pressure. The pressure term can be eliminated along with the divergence equation by projecting the equations onto the space of divergence-free functions. Invocation of the Leray projector Π achieves this [100].

Using $\Pi(\nabla p) = 0$, $\Pi(v) = v$ and the fact that Bf and d are already divergence-free gives

$$\begin{aligned}
\dot{v}(x,t) =& -\Pi\left(\bar{v}(x,t)\cdot\nabla v(x,t) - v(x,t)\cdot\nabla\bar{v}(x,t) + \frac{1}{Re}\nabla^2 v(x,t) - n(x,t)\right) \\
&+ Bf(x,t) + d(x,t), \\
n(x,t) =& \nabla \times yN(v) = v(x,t)\cdot\nabla v(x,t), \\
y(x,t) =& Cv(x,t), \quad x \in \Omega,\ t \in [0,T].
\end{aligned} \tag{B.10}$$

The perturbation equations (B.10) can be interpreted as a coupled linear system and memoryless nonlinear system. We see this by writing the system equations (B.10) in operator form as

$$\begin{aligned}
\dot{v}(x,t) &= Av(x,t) + Bf(x,t) - n(x,t) + d(x,t) \qquad t > 0 \\
y(x,t) &= Cv(x,t) \\
n(x,t) &= \mathcal{N}(v(x,t))
\end{aligned} \tag{B.11}$$

The aim is to find a control such that $v(x,t) \to 0$ as $t \to \infty$, given the measurements $y(x,t)$. The controlled system should have the properties specified in Section B.1.

To proceed, let $e = d - n$ and let G be the linear system taking n, d and f to v and y, given by (B.11). Furthermore, define K as the feedback law generating the control action f from measurements y. A linear state-space model of the flow results, with n entering as a nonlinear disturbance. The arrangement is represented graphically as in Figure B.2. The figure represents the equations

$$n = \mathcal{N}(v) \tag{B.12}$$

$$\begin{pmatrix} v \\ y \end{pmatrix} = G \begin{pmatrix} e \\ f \end{pmatrix} \tag{B.13}$$

$$f = Ky \tag{B.14}$$

$$v = Qe. \tag{B.15}$$

State-space representations of the Navier-Stokes equations are known in the literature, however this particular formulation explicitly retains the nonlinearity.

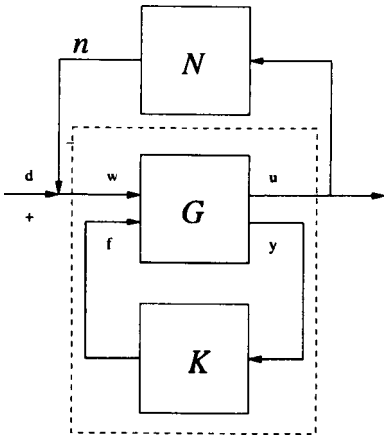


Figure B.2: The feedback loop for controlled Navier-Stokes

The nonlinearity is positive real if $\langle v, n \rangle \geq 0$ or equivalently,

$$\langle v, \mathcal{N}v \rangle = \int_0^T \int_{x \in \Omega} v^*(x,t) \cdot (v(x,t) \cdot \nabla v(x,t)) \; dx \; dt \geq 0 \quad \forall T. \tag{B.16}$$

Applying the divergence theorem and (B.6), the inner integral is equivalent to an integral over the boundary,

$$\int_{x \in \partial\Omega} (v(x,t) \cdot v(x,t)) v(x,t) \cdot \hat{\xi} \; dx \geq 0 \tag{B.17}$$

where $\hat{\xi}$ is the outward-facing unit vector perpendicular to the boundary $\partial\Omega$. Physically interpreted, (B.17) quantifies the net flux of disturbance energy out of the domain through the boundary per unit time.

The contribution from volume forcing, or forcing at the boundary in a domain with periodic boundary conditions, is necessarily zero. However, in an open domain, the flux of disturbance energy through the inlet and outlet boundaries and the net flux of disturbance energy from any boundary control both contribute. Where there is such a contribution, (B.17) enters as a nonlinear constraint on the control law. For the open-domain case where the inlet conditions are relatively undisturbed, there will be a net flux out of the domain of the disturbance energy. In these cases, the nonlinearity has a stabilising influence in the domain of study.

Next we consider the stability properties of the system as a whole. Define Q as the system with e as input and v as output corresponding to the controlled system inside the dashed box in Figure B.2, that is, the closed-loop system of G and K.

By the result in Section B.1.2, if $\mathcal{N}$ is positive real and Q is strictly positive real, then the closed loop in Figure B.2 (representing the controlled Navier-Stokes equations) is internally stable and is also strictly positive. In other words, $\langle v, d \rangle > 0$. This is simply verified; from Figure B.2 and by the strict positivity of Q and positivity of $\mathcal{N}$,

$$\begin{aligned} \langle v, d \rangle &= \langle v, n + e \rangle \\ &= \langle v, n \rangle + \langle v, e \rangle > 0. \end{aligned} \tag{B.18}$$

Note that if the uncontrolled, linearised plant is already passive, no control is required, as v is already bounded[‖]. The expression $\langle v, d \rangle$ quantifies the flow perturbation energy due to the disturbance. Physically, its positivity implies the system dissipates or does not feed the perturbations.

B.2 The controller synthesis problem

For the flow control problem to be solved by the method outlined above, the following are sufficient:

1. The desired steady flow solution must be known explicitly;
2. A linearised, state space model of the behaviour of perturbations away from that equilibrium, incorporating suitable actuation and sensing, must be found;
3. For the nonlinearity to act as a positive real disturbance on the linearised state space model, the model must have the flow state and body forcing due to the nonlinearity as an input-output pair, with units such that their inner product is defined in units of perturbation energy supply rate as in (B.16). Specifically, any grid weightings and such must be accounted for;
4. The actuation and sensing must be sufficient to ensure a solution to the algebraic Riccati equations arising from the positive real synthesis problem.

[‖]For instance, this is the case for the Stokes operator in a (xyz)-periodic or infinite domain

Where the last condition is not satisfied, a γ-minimisation approach can be used obtain the best control available given the actuation and sensing limitations described below.

Since the nonlinearity can be characterised in terms of a positive real system, the classical results can be applied to guarantee robust stability for the entire nonlinear system if the controller renders the closed loop with the linearised system strictly positive real.

There are two approaches to solving the discrete problem. One is to solve the problem directly, using state-space methods. This synthesis problem is solved in the control literature [98]. Necessary and sufficient conditions for the existence of a solution are given, which relate to the solutions of two algebraic Riccati equations (or inequalities). One Riccati equation relates to the measurement problem, and one to the control problem. It is therefore easy to see whether a solution exists and if it does not, whether this is due to insufficient control or to insufficient measurement.

Alternatively, one may transform the positive real problem into the equivalent small-gain problem [89], which may then be solved using standard loop-shifting techniques [39, 88] and Riccati-based state space methods [39, 25].

The method described by Doyle [25] in fact solves the suboptimal $\mathcal{H}_\infty$ problem for a given γ. A $\gamma < 1$ solves the small gain problem and therefore the original positive real control problem. This γ-optimisation approach is useful in the case of insufficient actuation or sensing to meet the conditions for existence of a solution to the positive real control problem. In this case, we choose a controller to reduce γ of the transformed system to get the original problem as close as possible to positive real. The guaranteed nonlinear stability is unfortunately lost, but the control does quantifiably limit the turbulent energy production. This approach is useful where there are physical or design constraints on the available measurement and actuation and is still preferable to a naive application of linear control theory, where there are no *a priori* guarantees on reduction of the turbulent energy production.

A solution of the small-gain problem ($\gamma < 1$) results in monotonous decay of the perturbation energy and thus no transient growth at all. If this occurs, the possibility of turbulence is precluded. Where there is insufficient actuation or sensing to permit

such a solution, the γ-optimisation approach provides bounds on the maximum perturbation energy production taken over all disturbances.

Recall from (B.18) that the nonlinear terms do not directly contribute to the perturbation energy production. The decay in perturbation energy due to external disturbances is given by $\langle v, e \rangle$, so we wish to maximise its lower bound. This is seen from the following argument.

Suppose we transform the problem of making a transfer function $G(s)$ strictly positive real into an equivalent problem of making H strictly bounded real, *i.e.* $\|H\|_\infty < 1$. However say we actually know $\|H\|_\infty < \gamma$. Then for $\mathrm{Re}(s) > 0$

$$\det[I - \gamma^{-1}H(s)] \neq 0, \mathrm{Re}(s) > 0.$$

From the relationship

$$H(s) = (G(s) - I)(G(s) + I)^{-1}$$

it follows that

$$H(s)H^*(s) = (G(s) - I)(G(s) + I)^{-1}(G^*(s) + I)^{-1}(G^*(s) - I) < \gamma^2 I.$$

Rearrangement gives

$$G(s) + G^*(s) > \frac{1 - \gamma^2}{1 + \gamma^2}(G^*(s)G(s) + I).$$

As $\gamma \to 1$, $G(s)$ becomes positive real. Bounding the right hand side by $-\alpha$,

$$-\alpha = \inf_{s=j\omega} \left[\frac{1 - \gamma^2}{1 + \gamma^2}(G^*(s)G(s) + I)\right]$$

means $\alpha \geq 0$ (since $\gamma \geq 1$).

If $v = Ge$, then it is straightforward to show

$$\langle v, e \rangle > -\frac{\alpha}{2} \langle e, e \rangle \ \forall e.$$

If $\|v\|_2$ is the perturbation energy, then this bounds the perturbation energy produced by any disturbance e and optimising γ improves this bound.

This expression is not equivalent to the 'optimal' in the sense of Butler and Farrel [8], which examined perturbation energy production maximised over all possible initial conditions. It is however arguably more pertinent in characterising the sensitivity of the nonlinear flow to disturbances, and thus the potential for turbulent energy production.

B.3 Application to channel flow

Again, the flow domain is a channel where periodicity is assumed for the streamwise (x) and spanwise (z) directions.

To achieve passivity of the linearised Orr-Sommerfeld-Squire system, it is sufficient to make the (independent) wall-normal velocity system passive. First consider actuation provided by simple body forcing in the wall-normal direction. The wall-normal velocity in the whole domain comprises the measurement. Such a body forcing situation is experimentally difficult but may be considered a precursor to other types of forcing.

The geometry allows Fourier transform of the linearised problem in the x and z directions which converts the (xyz)-continuous problem into a number of decoupled continuous problems at particular Fourier wavenumber pairs. Truncation at suitably high wavenumber ensures an (xz)-discrete problem with sufficient resolution. Chebyshev pseudo-spectral discretisation in the wall-normal direction results in a number of linear time invariant state-space control problems. Fortunately these problems are decoupled at the (linear) synthesis stage (a block diagonal A matrix in the state-space formulation) and only coupled (via the nonlinearity) at the full simulation stage. The controller synthesis problem is further simplified because control is only necessary at those wavenumber pairs where the linearised system is not passive, and so transient growth is possible, with attendant simplification of sensing and actuation.

The Orr-Sommerfeld-Squire formulation is used to describe the linearised behaviour of perturbations to plane Poiseuille flow. The Navier-Stokes equations are linearised about the parabolic steady flow solution, and projected onto a divergence-free basis with the resulting fourth-order PDEs discretised using a pseudo-spectral method and rearranged into state-space form. The techniques presented are known in the literature and are presented here together to clearly specify the problem as it relates to this approach. The method used avoids the spurious eigenvalues associated with other methods [6, 90].

The Orr-Sommerfeld-Squire equations can be written in state-space form as:

$$\frac{\mathrm{d}}{\mathrm{d}t}\begin{bmatrix}\hat{v}\\ \hat{\omega}\end{bmatrix} = A\begin{bmatrix}\hat{v}\\ \hat{\omega}\end{bmatrix}, \tag{B.19}$$

with

$$A = \begin{bmatrix} L_{OS} & 0 \\ L_C & L_{SQ}\end{bmatrix} \tag{B.20}$$

where v and ω are the wall-normal velocity and vorticity respectively and $\hat{\cdot}$ denotes a Fourier transformed variable. The (steady) laminar profile is $U(y)$. L_{OS}, L_{SQ}, and L_C represent the Orr-Sommerfeld, Squire and coupling operators respectively which are

$$L_{OS} = [\nabla^2]^{-1}\left\{-ik_xU\nabla^2 + ik_x\frac{\mathrm{d}^2U}{\mathrm{d}y^2} + \frac{\nabla^2\nabla^2}{Re}\right\} \tag{B.21}$$

$$L_{SQ} = -ik_xU + \frac{\nabla^2}{Re} \tag{B.22}$$

$$L_C = -ik_z\frac{\mathrm{d}U}{\mathrm{d}y} \tag{B.23}$$

where k_x and k_z are the wavenumbers in their respective directions. The Laplacian is given by

$$\nabla^2 = \frac{\partial^2}{\partial y^2} - k_x^2 - k_z^2.$$

The periodic spanwise and streamwise boundary conditions are naturally enforced by the Fourier transform. Further, any wall transpiration is necessarily divergence-free as it is expressed in a divergence-free basis. The zero net mass-flux condition of the wall transpiration is enforced by the shapes of the Fourier modes. In the wall-normal direction, the following boundary conditions must be enforced.

Firstly there are the homogenous Dirichlet boundary conditions for the wall-normal velocity and vorticity at the wall,

$$v(y=1) = v(y=-1) = 0, \tag{B.24}$$

$$\omega_y(y=\pm 1) = 0. \tag{B.25}$$

In addition there are the homogenous Neumann boundary conditions for the wall-normal velocity,

$$\frac{\partial v}{\partial y}(y=\pm 1) = 0. \tag{B.26}$$

Discretisation in the wall-normal direction is achieved using the Chebyshev transformation evaluated at the Chebyshev points. The homogenous boundary conditions are enforced automatically by using the method described in [108].

Discretised, the Orr-Sommerfeld-Squire equations have the form

$$\dot{x} = Ax + B_1 n + B_2 f \tag{B.27}$$

$$y_1 = C_1 x \tag{B.28}$$

$$y_2 = C_2 x \tag{B.29}$$

where x is the vector of v and ω evaluated at the discretisation points.

The perturbation energy at a wavenumber pair is given by [6]

$$E(t) = \frac{1}{8}\int_{-1}^{1} \hat{v}^*\hat{v} + \frac{1}{k_x^2 + k_z^2}\left(\frac{\partial \hat{v}^*}{\partial y}\frac{\partial \hat{v}}{\partial y} + \hat{\omega}^*\hat{\omega}\right) \mathrm{d}y. \tag{B.30}$$

For the discretised state the perturbation energy is approximated by the inner product on a positive-definite matrix R so that

$$E(t) \simeq x(t)^* R x(t),$$

achieving equality in the continuous limit. To satisfy the third requirement posed at the beginning of Section B.2, $E(t) \simeq y_1(t)^* y_1$. Thus we require simply $C_1^* C_1 = R$. The input matrix B_1 associated with the forcing from the nonlinearity n, is simply the inverse of C_1.

We write the system equations above in compact notation

$$G = \left[\begin{array}{c|cc} A & B_1 & B_2 \\ \hline C_1 & 0 & 0 \\ C_2 & 0 & 0 \end{array}\right]. \tag{B.31}$$

Define $Q : n \mapsto y_1$ as the finite dimensional approximation of the closed-loop transfer function from e to v, as in Figure B.2. Q is then the closed-loop of G and the controller K to be found. We wish to find a controller K such that Q is strictly positive real. Equivalently, $Q(s) + Q^*(s) > 0$ or $\langle n, y_1 \rangle_{[0,T]} > 0$, $\forall T$.

The controller that satisfies this requirement also solves a small-gain problem [89]

$$\|\tilde{Q}\|_\infty < \gamma$$

with $\gamma = 1$ and $\tilde{Q}$ given by the closed-loop of $\tilde{G}$ and K (K being the same controller). $\tilde{G}$ is given by

$$\tilde{G} = \left[\begin{array}{c|cc} A - B_1C_1 & B_1 & B_2 \\ \hline -2C_1 & I & 0 \\ C_2 & 0 & 0 \end{array}\right].$$

The resulting control problem is singular, essentially because it does not penalise the control effort. This is tackled by introducing asymptotic perturbation methods [97] or more simply by the following approach. To avoid the singular control problem and corresponding large control signals, a penalty is introduced on the control, and a model for sensor noise can be introduced. These are made orthogonal to the dynamics, by augmenting $\tilde{G}$ (to give $\tilde{G}^+$),

$$\tilde{G}^+ = \left[\begin{array}{c|c|c} A - B_1C_1 & \begin{bmatrix} B_1 & 0 \end{bmatrix} & B_2 \\ \hline \begin{bmatrix} -2C_1 \\ 0 \end{bmatrix} & \begin{bmatrix} I & 0 \\ 0 & 0 \end{bmatrix} & \begin{bmatrix} 0 \\ \epsilon I \end{bmatrix} \\ C_2 & \begin{bmatrix} 0 & \epsilon I \end{bmatrix} & 0 \end{array}\right].$$

The scalar ϵ is called the penalty weighting. The controller K is to be designed to minimise γ. In the case that the optimal γ is less than unity, the positive real control problem is solved by K. The γ optimisation is performed using loop-shifting techniques [88, 39] and the standard $\mathcal{H}_\infty$ synthesis theory [25, 39, 97].

Bibliography

[1] R. ARIS, Vectors, Tensors and the Basic Equations of Fluid Mechanics. *Prentice-Hall, Englewood Cliffs, NJ*, (1962)

[2] G.K. BATCHELOR, An Introduction to Fluid Dynamics. *Cambridge University Press*, (2000)

[3] P.W. BEARMAN, J.K. HARVEY, Golf ball aerodynamics. *Aeronaut. Q.* **112**, (1976)

[4] G. BERKOOZ, Controlling methods of the turbulent wall layer by boundary deformation. *AIAA Shear Flow Conference, Orlando, FL*, July 6-9 (1993)

[5] T.R. BEWLEY, P. MOIN, R. TEMAM, DNS-based predictive control of turbulence: An optimal benchmark for feedback algorithms. *J. Fluid Mech.* **447**, 179 (2001)

[6] T.R. BEWLEY, H. LIU, Optimal and robust control and estimation of linear paths to transition. *J. Fluid Mech.* **365**, 305 (1998)

[7] K.S. BREUER, J.H. HARITONIDIS, M.T. LANDAHL, The control of transient disturbances in a flat plate boundary layer through active wall motion. *Phys. Fluids A* **1**, 574 (1989)

[8] K.M. BUTLER, B.F. FARRELL, Three-dimensional optimal perturbations in viscous shear flow. *Phys. Fluids* **4**, 1637 (1992)

[9] D. BOND, Green is for go. *Aviation Week & Space Technology*, August 20/27 (2007)

[10] C. CANUTO, M.Y. HUSSAINI, A. QUARTERONI, T.A. ZANG, Spectral Methods in Fluid Mechanics. *Springer-Verlag, Berlin*, (1988)

[11] H.A. CARLSON, G. BERKOOZ, J.L. LUMLEY, Direct Numerical Simulation of Flow in a Channel with Complex Time-Dependent Wall Geomtries: A Pseudospectral Method. *J. Comput. Phys.* **121**, 155 (1995)

[12] H.A. CARLSON, J.L. LUMLEY, Flow over an Obstacle Emerging from the Wall of a Channel. *AIAA Journal*, 34 (5) (1996)

[13] H.A. CARLSON, J.L. LUMLEY, Active control in the turbulent wall layer of a minimal flow unit. *J. Fluid Mech.* **329**, 341 (1996)

[14] S.I. CHERNYSHENKO, M.F. BAIG, The mechanism of streak formation in near-wall turbulence. *J. Fluid Mech.* **544**, 99 (2005)

[15] H. CHOI, P. MOIN, J. KIM, Active turbulence control for drag reduction in wall-bounded flows. *J. Fluid Mech.* **262**, 75 (1994)

[16] H. CHOI, P. MOIN, J. KIM, Direct numerical simulation of turbulent flow over riblets. *J. Fluid Mech.* **255**, 503 (1993)

[17] C. KIM, W.-P. JEON, J. PARK, H. CHOI , Effect of a localized time-periodic wall motion on a turbulent boundary layer flow. *Phys. Fluids* **15**, 265 (2003)

[18] Y.M. CHUNG, H.J. SUNG, Sensitivity Study of Turbulence Control with Wall Blowing and Suction. *Proceddings of the Third International Symposium Turbulence and Shear Flow Phenomena*, Sendai (2003)

[19] C.H. CRAWFORD, G.E. KARNIADAKIS, Reynolds stress analysis of EMHC-controlled wall turbulence. *Phys. Fluids* **9**, 788 (1997)

[20] Climate Change 2007: The Physical Science Basis. Contribution of Working Group I to the Fourth Assessment Report of the Intergovernmental Panel on Climate Change. Intergovernmental Panel on Climate Change (2007-02-05). Retrieved on 2007-02-02.

[21] S.S. COLLIS, Y.C. CHANG, S. KELLOGG, R.D. PRABHU, Large Eddy Simulation and Turbulence Control. *AIAA*, 2000-2564 (2000)

[22] S.S. DEARING, J.F. MORRISON, G.G. ARTHUR, Z. CUI, Electroactive Diaphragm Actuators for Flow Control, II ECCOMAS THEMATIC CONFERENCE ON SMART STRUCTURES AND MATERIALS, C.A. Mota Soares et al. (Eds.), Lisbon, Portugal, July 18-21, 2005

[23] S.S. DEARING, Progress with EAP actuator fabrication. *Imperial College*, Presentation 27 March (2007)

[24] S. DEARING, *Personal communication*, (2007)

[25] J. DOYLE, K. GLOVER, P. KHARGONEKAR, B. FRANCIS, State-space solutions to standard H_2 and H_∞ control problems. *IEEE Trans. on Automatic Control* **34**, 831 (1989)

[26] Y. DU, V. SYMEONIDIS, G.E. KARNIADAKIS, Drag reduction in wall-bounded turbulence via a transverse travelling wave. *J. Fluid Mech.* **457**, 1 (2002)

[27] T. ENDO, N. KASAGI, Y. SUZUKI, Feedback Control of Wall Turbulence with Wall Deformation. *Int. J. Heat Fluid Fl.* **21** 568 (2000)

[28] T. ENDO, N. KASAGI, Turbulence Control in Low-to-Moderate Reynolds Number Flows. *Proc. 2nd Symp. Smart Control of Turbulence, Tokyo*, (2001)

[29] EUROCONTROL - European Organisation for the Safety of Air Navigation. *www.eurocontrol.int*

[30] B.F. FARRELL, P.J. IOANNOU, Stochastic forcing of the linearized Navier-Stokes equation. *Phys. Fluids A* **5**, 2600 (1993)

[31] B.F. FARRELL, P.J. IOANNOU, Turbulence suppression by active control. *Phys. Fluids* **8**, 1257 (1996)

[32] H. FASEL, I.J. WYGNANSKI, M. GASTER, The effectiveness of actuators used in active flow controls: numerical simulations, analysis and experiments. *The Air Force Office of Scientific Research* Final Report, (2002)

[33] F.E. FISH, Review of dolphin hydrodynamics and swimming performance. *Technical report, SSC San Diego*, August (1991)

[34] M. GAD-EL-HAK, Interactive control of turbulent boundary layers: a futuristic overview. *AIAA Journal* **32**, 1753 (1994)

[35] T. GAL-CHEN, R. C. J. SOMERVILLE, On the Use of Coordinate Transformation for the Solution of the Navier-Stokes Equations. *J. Comp. Phys.* **17**, 209 (1975)

[36] M. GAD-EL-HAK, R.F. BLACKWELDER, Selective Suction for Controlling Bursting Events in a Boundary Layer. *AIAA Journal* **27**, 308 (1989)

[37] M. GASTER, C.E. GROSCH, T.L. JACKSON, The velocity field created by a shallow bump in a boundary layer. *Phys. Fluids* **6**, 3079 (1994)

[38] J.F. GIBSON, Channelflow. A spectral Navier-Stokes simulator in C++. *www.cns.gatech.edu/channelflow/*

[39] W.J. GREEN, D.J.N. LIMEBEER, Linear Robust Control. *Prentice Hall, New Jersey*, (1995)

[40] GROUP OF PERSONALITIES, European aeronautics: a vision for 2020. *European Commission*, January 2001

[41] E.P. HAMMOND, T.R. BEWLEY, P.MOIN, Observed mechanisms for turbulence attenuation and enhancement in opposition-controlled wall-bounded flows. *Phys. Fluids* **10**, 2421 (1998)

[42] R.D. HENDERSON, G.E. KARNIADAKIS, Unstructured Spectral Element Methods for Simulation of Turbulent Flow. *J. Comp. Phys.* **122**, 191 (1995)

[43] L.M. HOFMANN, T.H. HERBERT, Disturbances produced by motion of an actuator. *Phys. Fluids* **9**, 3727 (1997)

[44] S. HOYAS, J. JIMÉNEZ, Scaling of the velocity fluctuations in turbulent channels up to $\mathrm{Re}_\tau = 2003$. *Phys. Fluids* **18**, 011702, (2006)

[45] S. HOYAS, J. JIMÉNEZ, Reynolds number effects in the Reynolds stress statistics and balances. *in preparation.*

[46] K. IWAMOTO, K. FUKAGATA, N. KASAGI, Y. SUZUKI, Friction drag reduction achievable by near-wall turbulence manipulation at high Reynolds numbers. *Phys. Fluids* **17**, 011702, (2005)

[47] K. IWAMOTO, Y. SUZUKI, N. KASAGI, Reynolds number effect on wall turbulence: toward effective feedback control. *Int. J. Heat Fluid Fl.*, **23**, 678 (2002)

[48] K. IWAMOTO, Database of Fully Developed Channel Flow. *THTLAB Internal Report*, No. ILR-0201. THTLAB, Dept. of Mech. Eng., The Univ. of Tokyo.

[49] K. IWAMOTO, N. KASAGI, Y. SUZUKI, Direct Numerical Simulation of Turbulent Channel Flow at $Re_\tau = 2320$. *Proc. 6th Symp. Smart Control of Turbulence*, Tokyo, March 6-9, (2005)

[50] S. JACOBSEN, W.C. REYNOLDS, Active control of streamwise vortices and streaks in boundary layers. *J. Fluid Mech.* **360**, 179 (1998)

[51] J. JIMÉNEZ, P. MOIN, The minimal flow unit in near-wall turbulence. *J. Fluid Mech.* **225**, 213 (1991)

[52] S. JOSHI, J. SPEYER, J. KIM, A systems theory approach to the feedback stabilization of infinitesimal and finite-amplitude disturbances in plane Poiseuille flow. *J. Fluid Mech.* **332**, 157 (1997)

[53] R.D. JOSLIN, C.E. GROSCH, Growth characteristics downstream of a shallow bump: Computation and experiment. *Phys. Fluids* **7**, 3042 (1995)

[54] S. KANG, H. CHOI, Active wall motions for skin-friction drag reduction. *Phys. Fluids* **12**, 3301(2000)

[55] G.E. KARNIADAKIS, Spectral Element-Fourier Methods for Incompressible Turbulent Flows. *Comp. Meth. Appl. Mech. Eng.* **80**, 367 (1990)

[56] G. KARNIADAKIS, M. ISRAELI, S. ORSZAG, High-order splitting methods for the incompressible Navier-Stokes equations. *J. Comp. Phys.* **97**, 414 (1991)

[57] G.E. KARNIADAKIS, S.J. SHERWIN, Spectral/*hp* element methods for CFD. *Oxford University Press*, (1999)

[58] S. KELLOGG, Immersed boundary methods with applications to flow control. *MSc Thesis, Rice University*, (2000)

[59] J. KIM, Control of turbulent boundary layers. *Phys. Fluids* **15**, 1093 (2003)

[60] J. KIM, P. MOIN, R. MOSER, Turbulence statistics in fully developed channel flow at low Reynolds number. *J. Fluid Mech.* **177**, 133 (1987)

[61] J. KIM, J. LIM, A linear process in wall-bounded turbulent shear flows. *Phys. Fluids* **12**, 1885 (2000)

[62] N. KORNEV, E. HASSEL, H.HERWIG, S. ISAEV, P. STEPHAN, V. ZHDANOV, Erhöhung des Wärmeüberganges durch Wirbelinduktion in Oberflächendellen. *Forschung im Ingenieurwesen* **69**, 90 (2005)

[63] P. KOUMOUTSAKOS, Vorticity flux control for a turbulent channel flow. *Phys. Fluids* **11**, 248 (1999)

[64] A. KURODA, N. KASAGI, Establishment of the Direct Numerical Simulation Data Bases of Turbulent Transport Phenomena: CH12_PG.WL2. *http://www.thtlab.t.u-tokyo.ac.jp/*, The University of Tokyo (1998)

[65] S. LAMBERT, B. J. MCKEON, W. H. T. KOBERG, J. F. MORRISON, Fundamental studies of active dimples. *TSFP-4, Williamsburg, VA, USA*, Vol. 1., pp 283-288, (2005)

[66] C. LEE, J. KIM, B. BABOCK, R. GOODMAN, Application of neural networks to turbulence control for drag reduction. *Phys. Fluids* **9**, 1740 (1997)

[67] C. LEE, J.KIM, H. CHOI, Suboptimal control of turbulent channel flow for drag reduction. *J. Fluid Mech.* **358**, 245 (1998)

[68] M. LIGHTHILL, Introduction. Boundary Layer Theory. *Oxford Univ. Press*, 55-61 (1963)

[69] P.M. LIGRANI, J.L. HARRISON, G.I. MAHMMOD, M.L. HILL, Flow structure due to dimple depressions on a channel surface. *Phys. Fluids* **13**, 3442 (2001)

[70] J.L. LUMLEY, P.N. BLOSSEY, Control of Turbulence. *Annu. Rev. Fluid Mech.* **30**, 311 (1998)

[71] J.L. LUMLEY, Low dimensional models of the wall region of a turbulent boundary layer, and the possiblity of control. *Proceedings of the Tenth Australasian Fluid Mechanics Conference.*

[72] A. LUNDBLADH, D.S. HENNINGSON, Threshold Amplitudes for Transition in Channel Flows. *Transition, Turbulence and Combustion, Vol. I*, 309-318

[73] H. LUO, T.R. BEWLEY, On the contravariant form of the Navier-Stokes equations in time-dependent curvilinear coordinate systems. *J. Comput. Phys.* **199**, 355 (2004)

[74] B.J. MCKEON, S.J. SHERWIN, J.F. MORRISON, Vorticity flux from active dimples. *APS, 57th Annual Meeting of the Division of Fluid Dynamics*, (2004)

[75] M.M. METZGER, J.C. KLEWICKI, A comparative study of near-wall turbulence in high and low Reynolds number boundary layers. *Phys. Fluids* **13**, 692 (2001)

[76] P. MOIN, T.R. BEWLEY, Feedback control of turbulence. *Appl. Mech. Rev.* **47(6)**, part 2, 3 (2004)

[77] P. MOIN, K. MAHESH, Direct Numerical Simulation: A Tool in Turbulence Research. *Annu. Rev. Fluid Mech.* **30**, 539 (1998)

[78] J.F. MORRISON, B.J. MCKEON, W. JIANG, A.J. SMITS, Scaling of the streamwise velocity component in turbulent pipe flow. *J. Fluid Mech.* **508**, 99 (2004)

[79] R.D. MOSER, J. KIM, N.N. MANSOUR, Direct numerical simulation of turbulent channel flow up to $\mathrm{Re}_\tau = 590$. *Phys. Fluids* **11**, 943 (1999)

[80] M.P. PATEL, G.G. SKEBE, F.J. LISY, Development of a MEMS based microvalve for flow control using active dimples. *AIAA Aerospace Sciences Meeting and Exhibit, 40th, Reno, NV*, Jan. 14-17 (2002)

[81] S.B. POPE, Turbulent Flows. *Cambridge University Press*, (2000)

[82] R.D. PRABHU, S.S. COLLIS, Y. CHANG, The influence of control on proper orthogonal decomposition of wall-bounded turbulent flows. *Phys. Fluids* **13**, 520 (2001)

[83] R. RATHNASINGHAM, K.S. BREUER, Active control of turbulent boundary layers. *J. Fluid Mech.* **495**, 209 (1990)

[84] H. REBBECK, K.-S. CHOI, Opposition control of near-wall turbulence with a piston-type actuator. *Phys. Fluids* **13**, 2142 (2001)

[85] S.C. REDDY, P.J. SCHMID, J.S. BAGGETT, D.S. HENNINGSON, On stability of streamwise streaks and transition thresholds in plane channel flows. *J. Fluid Mech.* **365**, 269 (1998)

[86] W.-E. REIF, A. DINKELACKER, Hydrodynamics of the squamation in fast-swimming sharks. *Neues Jahrb. Geol. Paläontol. Abh.* **164**, 184 (1982)

[87] S.H. RIDGWAY, D.A. CARDER, Features of dolphin skin with potential hydrodynamic importance. *IEEE Eng. Med. Biol.* **12**, 83 (1993)

[88] M.G. SAFONOV, Simplifying the H_∞ theory via loop shifting. *Proceedings of the 27th Conference on Decision and Control*, Austin (1988)

[89] M.G. SAFONOV, E.A. JONCKHEERE, M. VENNA, D.J.N. LIMEBEER, Synthesis of positive real multivariable feedback systems. *Int. J. Contr.* **45**, 817 (1987)

[90] P.J. SCHMID, D.S. HENNINGSON, Stability and Transistion in Shear Flows. *Springer*, (2001)

[91] W. SCHOPPA, F. HUSSAIN, A large-scale control strategy for drag reduction in turbulent boundary layers. *Phys. Fluids* **10**, 1049 (1998)

[92] A.S. SHARMA, B.J. MCKEON, J.F. MORRISON, D.J.N LIMEBEER, Relaminarising Control of Incompressible Flows Using the Passivity Theorem. *In Preparation*

[93] S.J. SHERWIN, G.E. KARNIADAKIS, A triangular spectral element method; applications to the incompressible Navier-Stokes equations. *J. Comp. Phys.* **123**, 189 (1995)

[94] W. SHYY, H.S. UDAYKUMAR, M.M. RAO, R.W. SMITH, Computational Fluid Dynamics with Moving Boundaries. *Taylor and Francis, Washington, DC*, (1996)

[95] F.T. SMITH, R.I. SYKES, A two-dimensional boundary layer encountering a three-dimensional hump. *J. Fluid Mech.* **83**, 163 (1977)

[96] I. J. SOBEY, Introduction to interactive boundary layer theory. *Oxford University Press*, (2000)

[97] A. STOORVOGEL, The H_∞ Control Problem: A State-Space Approach. *Prentice-Hall*, (1992)

[98] W. SUN, P. KHARGONEKAR, D. SHIM, Solution to the positive real control problem for linear time-invariant systems. *IEEE Trans. on Automatic Control* **39**, 2034 (1994)

[99] Y. SUZUKI, N. KASAGI, T. YOSHINO, R & D Study on Micro Sensors and Actuators for Active Control of Wall Turbulence. *Proc. 2nd Symp. Smart Control of Turbulence, Tokyo*, 19-26 (2001)

[100] R. TEMAM, Navier-Stokes Equations and Nonlinear Functional Analysis. *SIAM*, Philadelphia, (1995)

[101] Top 500 supercomputer sites. *http://www.top500.org/*

[102] L.N. TREFETHEN, A.E. TREFETHEN, S.C. REDDY, T.A. DRISCOLL, Hydrodynamic Stability Without Eigenvalues. *Science* New Series **261**, 578 (1993)

[103] TSAO, T. JIANG, F., MILLER, R., TAI, Y., GUPTA, B., GOODMAN, R., TUNG, S., HO, C., An integrated MEMS system for turbulent boundary layer control, In Technical Digest, 1997 Intl Conf. on Solid-State Sensors and Actuators (Transducers 97), Chicago, IL,vol. 1, pp. 315-318.

[104] Turbulence and Heat Transfer Lab, University of Tokyo. *http://www.thtlab.t.u-tokyo.ac.jp*

[105] P.R. VOKE, M.W. COLLINS, Forms of the generalised Navier-Stokes equations. *J. Eng. Math.* **18**, 219 (1984)

[106] P.W. CARPENTER, D.A. LOCKERBY, C. DAVIES, A numerical-simulation study of boundary-layer control using MEMS jet-type actuators. *Technical Report, Univ. of Warwick, Coventry Univ.*, (2001)

[107] N.P. WEDI, P.K. SMOLARKIEWICZ, Extending Gal-Chen and Somerville terrain-following coordinate transformation on time-dependent curvilinear boundaries. *J. Comp. Phys.* **193**, 1 (2004)

[108] J.A.C. WEIDEMAN, S.C. REDDY, A matlab matrix differentiation suite. *ACM Transactions on Mathematical Software* **26**, 465 (2000)

[109] D. C. WILCOX, Basic Fluid Mechanics. *DCW Industries*, (2000)

[110] S.P. WILKINSON, R. BALASUMBRIAN, Turbulent burst control through phase-locked traveling surface depressions. *AIAA, Shear Flow Control Conference, Boulder, Co*, Mar. 12-14, 16p. (1985)

[111] J.Z. WU, J.M. WU, Vorticity Dynamics on Boundaries. *Adv. Appl. Mech.* **32**, 119 (1996)

[112] C. WÜST, Dellen im Dach. *Der Spiegel* **14**, 170 (2004)

[113] G. ZAMES, On the input-output stability of time-varying nonlinear feedback systems part i: Conditions derived using concepts of loop gain, conicity and positivity,. *EEE Trans. on Automatic Control, vol. AC11* **2**, 228 (1966)